International Journal of Spectroscopy

Spectral Line Shapes in Plasmas and Gases

Guest Editors: Eugene Oks, Elisabeth Dalimier, Roland Stamm, Chantal Stehlé, and Manuel A. Gonzalez

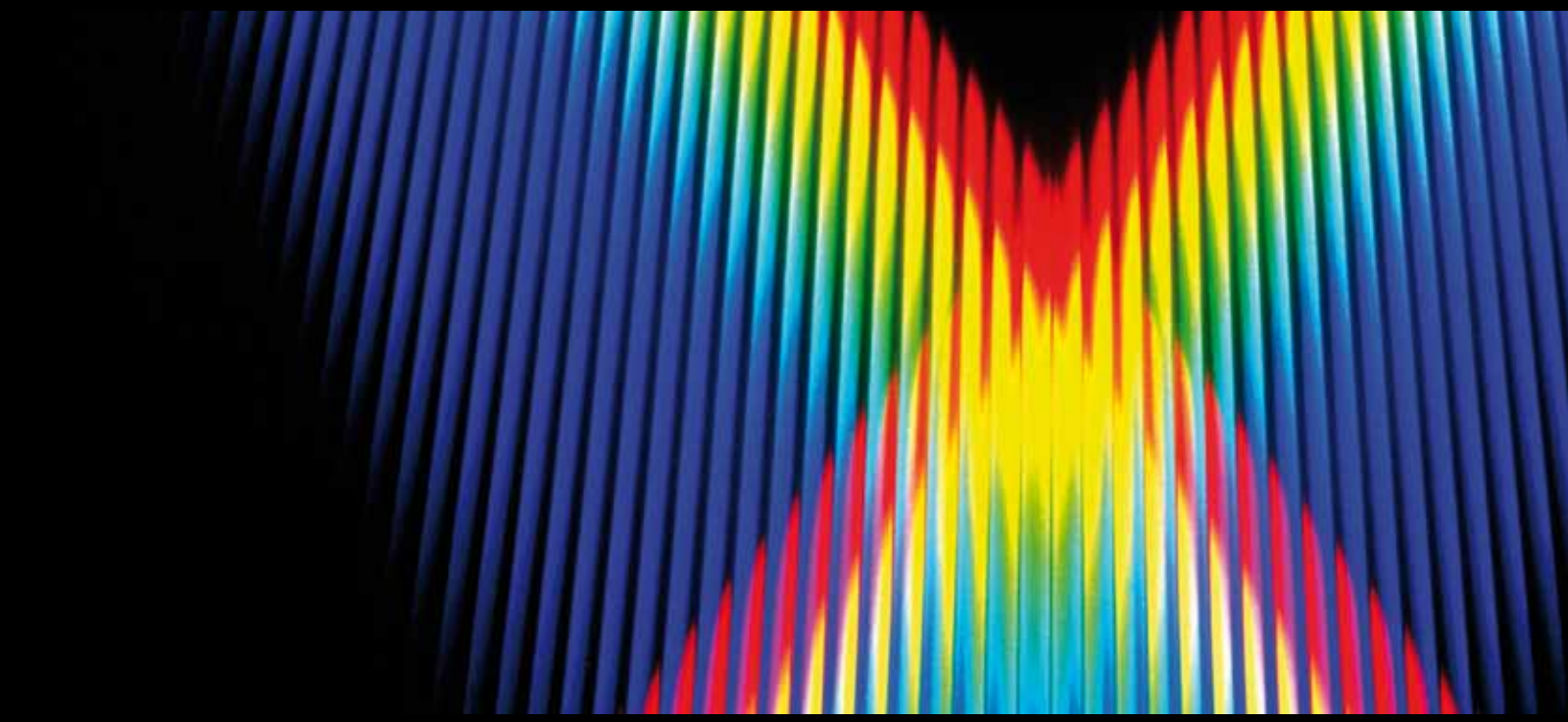

Spectral Line Shapes in Plasmas and Gases

International Journal of Spectroscopy

Spectral Line Shapes in Plasmas and Gases

Guest Editors: Eugene Oks, Elisabeth Dalimier, Roland Stamm, Chantal Stehlé, and Manuel A. Gonzalez

Editorial Board

Contents

Spectral Line Shapes in Plasmas and Gases, Eugene Oks, Elisabeth Dalimier, Roland Stamm, Chantal Stehlé, and Manuel A. Gonzalez
Volume 2010, Article ID 478539, 2 pages

Relation between Theories, Experiments, and Simulations of Spectral Line Shapes, Eugene Oks
Volume 2010, Article ID 852581, 4 pages

Optical Transitions and Charge-Exchange in Highly Charged Quasi-Molecules, A. Devdariani, E. Dalimier, and P. Sauvan
Volume 2010, Article ID 812471, 12 pages

Physical Models of Plasma Microfield, A. V. Demura
Volume 2010, Article ID 671073, 42 pages

Pressure Broadening of Some He I Lines, Banaz Omar
Volume 2010, Article ID 983578, 7 pages

Time Ordering Effects on Hydrogen Zeeman-Stark Line Profiles in Low-Density Magnetized Plasmas, J. Rosato, D. Boland, M. Difallah, Y. Marandet, and R. Stamm
Volume 2010, Article ID 374372, 5 pages

Hydrogen Stark Broadened Brackett lines, C. Stehlé and S. Fouquet
Volume 2010, Article ID 506346, 6 pages

New Statistical Multiparticle Approach to the Acceleration of Electrons by the Ion Field in Plasmas, Eugene Oks
Volume 2010, Article ID 347080, 4 pages

Elementary Statistical Models for Vector Collision-Sequence Interference Effects with Poisson-Distributed Collision Times, John Courtenay Lewis
Volume 2010, Article ID 561697, 5 pages

Time-Resolved Spectroscopy Diagnostic of Laser-Induced Optical Breakdown, Christian G. Parigger, James O. Hornkohl, and Làszló Nemes
Volume 2010, Article ID 593820, 7 pages

Unified Impact Theory for Velocity-Changing Effects and Speed Dependencies in Neutral Species Lineshapes, Roger M. Herman
Volume 2010, Article ID 306392, 9 pages

Far Wing Asymmetry of Rotational Raman Lines in Hydrogen, Magnus Gustafsson
Volume 2010, Article ID 705896, 5 pages

Laser-Induced Optical Breakdown in Methane: Diagnostic Using H-Gamma Line Broadening, Christian G. Parigger and Eugene Oks
Volume 2010, Article ID 936385, 4 pages

Collision-Induced Infrared Absorption by Molecular Hydrogen Pairs at Thousands of Kelvin, Xiaoping Li, Katharine L. C. Hunt, Fei Wang, Martin Abel, and Lothar Frommhold
Volume 2010, Article ID 371201, 11 pages

Plasma Temperature Determination of Hydrogen Containing High-Frequency Electrodeless Lamps by Intensity Distribution Measurements of Hydrogen Molecular Band, Zanda Gavare, Gita Revalde, and Atis Skudra
Volume 2010, Article ID 804506, 8 pages

Absorption Line Profile of the $^5S_2^0 - {}^5P_1$ Transition of Atomic Oxygen and Its Application to Plasma Monitoring, K. Sasaki, Y. Okumura, and R. Asaoka
Volume 2010, Article ID 627571, 6 pages

Hindawi Publishing Corporation
International Journal of Spectroscopy
Volume 2010, Article ID 478539, 2 pages
doi:10.1155/2010/478539

Editorial
Spectral Line Shapes in Plasmas and Gases

Eugene Oks,[1] Elisabeth Dalimier,[2] Roland Stamm,[3] Chantal Stehlé,[4] and Manuel A. Gonzalez[5]

[1] *206 Allison Laboratory, Department of Physics, Auburn University, Auburn, AL 36849, USA*
[2] *Université Pierre et Marie Curie, Laboratoire LULI-UMR 7605, Université Paris 6, Case 128, 4 Place Jussieu, 75252 Paris Cedex 05, France*
[3] *Universite de Provence, Physique des Interactions Ioniques et Moleculaires, Centre de Saint Jerome, case 232, 13397 Marseille Cedex 20, France*
[4] *Laboratoire d'Etudes du Rayonnement et de la Matière en Astrophysique, UMR 8112 du CNRS, Observatoire de Paris, Université Pierre et Marie Curie, 5 Place J. Janssen, 92195 Meudon, France*
[5] *Departamento de Fisica Aplicada, E.T.S.I. Informatica, Universidad de Valladolid, 47071 Valladolid, Spain*

Correspondence should be addressed to Eugene Oks, goks@physics.auburn.edu

Received 27 October 2009; Accepted 27 October 2009

The subject of spectral line shapes (SLS), a.k.a. spectral line broadening, which embraces both shapes and shifts of spectral lines, is of both fundamental and practical importance. On the fundamental side, the study of the spectral line profiles reveals the underlying atomic and molecular interactions. On the practical side, the spectral line profiles are employed as powerful diagnostic tools for various media, such as neutral gases, technological gas discharges, magnetically confined plasmas for fusion, laser- and Z-pinch-produced plasmas (for fusion and other purposes), astrophysical plasmas (most importantly, solar plasmas), and planetary atmospheres.

The research area covered by this special issue includes both the SLS dominated by various electric fields (including *electron and ion microfields* in strongly ionized plasmas) and the SLS controlled by *neutral* particles. In the physical slang, the former is called "*plasma broadening*" while the latter is called "*neutral broadening*" (of course, the results of neutral broadening apply also to the spectral line broadening in neutral gases).

The goal of this special issue is to demonstrate the most recent developments in this field. Topics presented here are basically the same as for the biannual International Conference on Spectral Line Shapes. This special issue contains 4 review articles and 11 original research papers.

The first paper is a review article discussing the role of the fully numerical simulations and complicated codes, which are important as the third powerful research methodology, with respect to experiments and theories. It shows by examples the pitfalls of the trend where the ultimate test of any theory is considered to be fully numerical simulations and complicated codes instead of experiments conducted in well-controlled conditions.

The second paper is a review article discussing the spectral profiles of the quasimolecules formed in hot and dense plasmas as two nuclei share a bound electron. The study of spectral profiles is shown to be strongly related to the collision dynamics of ions in excited states.

The third paper is a review article devoted to the current status of the concept of plasma microfield. In this review, the physical aspects of the most employed models are analyzed and some open questions are highlighted.

The fourth paper is a review article presenting a quantum statistical approach for calculating the line shape of neutral helium lines in dense plasmas. The shifts and widths of several lines are calculated and compared to experimental results and other models.

The fifth paper revisits time ordering effects in Stark profiles using simulation techniques that permit to reproduce the motion of the heavy particles in the plasma and to obtain the electric fields at the location of the emitter. By considering jointly Zeeman and Stark effects, the authors obtained valuable spectral line profiles to be used in fusion plasma diagnostics.

The sixth paper provides a coherent description of the hydrogen Brackett line shapes for plasma conditions relevant to stellar observations in the corresponding infrared range. It supplies tables of line profiles for astrophysical applications intended to gain an insight into the physical properties of stars.

The seventh paper employs a new statistical multiparticle approach to calculate the effect on spectral line caused by the acceleration of the perturbing electrons by the ion field. It shows that two totally different analytical approaches (dynamical and statistical) agree with each other by leading to the reduction of the electron Stark broadening and, therefore, disprove the corresponding recent fully numerical simulations that claimed an increase of the electron Stark broadening.

The eighth paper proposes a modelling of the distribution of collision times, and a study of their effect on collision-induced molecular spectra. The use of a Poisson distribution of velocities is shown to lead to an exactly soluble and realistic model.

The ninth paper reports experiments performed using laser-induced breakdown spectroscopy for studying the evolution of C_2 and C_3 formation. This technique also allowed the authors to study the carbon migration in the plasma cell.

The tenth paper presents a unified impact model for neutral species—the model incorporating velocity changing effects and the speed dependence of coherence destruction. Simple closed expressions are obtained for the dipole correlation function, retaining the cubic time term.

The eleventh paper presents a quantum theoretical study of the depolarized Raman spectrum of compressed hydrogen gas at low temperature with a detailed analysis of the various contributions to the line shape, as well as a comparison with the experiment at the temperature of 50 K. These calculations show the important contribution of interference and shape resonance effects.

The twelfth paper reports the measurements and analysis of Stark-broadened profiles of the H-gamma line emitted from plasma formed by laser-induced optical breakdown in a pulsed methane flow. The obtained values of the electron density are in a good agreement with the corresponding values found previously from Stark-broadened profiles of the H-alpha and H-beta lines.

The thirteenth paper presents new results on the energy and dipole surfaces of the complex H_2–H_2, allowing for the calculation of the corrsponding rototranslational absorption spectra. These spectra are of great interest for astrophysical applications as they extend the available data to higher temperatures, up to 2000 K.

The fourteenth paper explains how the spectrum of Flucher alpha diagonal band of hydrogen molecules can be prudently chosen to diagnose the temperature of hydrogen-containing high-frequency electrodeless lamps. These lamps are used for a wide range of applications.

The fifteenth paper is an experimental measure of absorption line of atomic hydrogen by diode laser spectroscopy. The fitting of the spectra by two Gaussians reveals the existence of low and high temperature components, thus allowing their ratio to be used for monitoring the dissociation of molecular oxygen.

Eugene Oks
Elisabeth Dalimier
Roland Stamm
Chantal Stehlé
Manuel A. Gonzalez

Hindawi Publishing Corporation
International Journal of Spectroscopy
Volume 2010, Article ID 852581, 4 pages
doi:10.1155/2010/852581

Review Article

Relation between Theories, Experiments, and Simulations of Spectral Line Shapes

Eugene Oks

Department of Physics, Auburn University, 206 Allison Lab, Auburn, AL 36849, USA

Correspondence should be addressed to Eugene Oks, goks@physics.auburn.edu

Received 26 April 2009; Accepted 23 June 2009

Academic Editor: Elisabeth Dalimier

Simulations of Shapes and Shifts of Spectral Lines (SSSL) are important as the third powerful research methodology—in addition to theories and experiments. However, there is a growing tendency in physics in general and in the area of SSSL in particular, to consider the ultimate test of any theory to be the comparison with results of a code based on fully-numerical simulations starting from the "scratch" rather than from some analytical advance. In this paper, we show by examples that fully-numerical simulations are often not properly verified and validated, fail to capture emergent principles and phenomena, and lack the physical insight. Physics is the experimental science. So, the ultimate test of any theory—including theories of SSSL—should be the comparison with experiments conducted in well-controlled conditions (benchmark experiments).

1. Introduction

By a commonly accepted classification, the determination of *Shapes and Shifts* of Spectral Lines (SSSL) belongs to the highest level of spectroscopy—compared to the determination of unperturbed wavelengths and frequency-integrated intensities of spectral lines. In plasmas with the high degree of ionization, SSSL are controlled primarily by various electric fields: this is the *Stark broadening* of spectral lines (the term includes both Stark shapes and Stark shifts). In weakly ionized plasmas, a significant contribution to SSSL can come from *pressure broadening by neutrals*.

The research area covered by this special issue includes both the SSSL dominated by various electric fields (including *electron and ion microfields* in strongly ionized plasmas) and the SSSL controlled by *neutral* particles. In the physical slang, the former is called "*plasma broadening*" while the latter is called "*neutral broadening*" (of course, the results of neutral broadening apply also to the spectral line broadening in neutral gases).

The subject of SSSL is a rather old field beginning about 100 years ago for plasma broadening and even earlier (about 150 years ago) for neutral broadening. Despite the age, the research area of SSSL is alive and flourishing and has a bright future.

Indeed, the growth of this field is manifested both "horizontally" (in terms of the number of publications) and "vertically" (in terms of breakthroughs to advanced approaches and better physical insights). Just over the last 5 years, there have been published several books (such as, e.g., [1–3]) and numerous papers in refereed journals and/or conference proceedings (examples of the latter are [4, 5]). Examples of vertical advances are (but not limited to):

(i) unification of the impact and one-perturber theories of line shapes [6],

(ii) QED approach to modeling spectra of isolated atoms and ions, as well as those influenced by a strong laser field [7, 8],

(iii) path integral formalism for the spectral line shapes in plasmas [9],

(iv) temperature dependence of the Stark broadening dominated by strong collisions [10],

(v) various new features in X-ray spectral lines from plasmas, such as charge-exchange-caused dips [11], Langmuir-waves-caused dips [12], and effects of external laser fields [13–16],

(vi) formalism of dressed atomic states for diagnostics (including laser-aided diagnostics) of quasi-monochromatic electric fields in plasmas [17, 18],

(vii) formalism of atomic states dressed by the broadband electric microfield in plasmas [2, 19].

Just the above incomplete list demonstrates the virility of the area of SSSL. This special issue is a further proof of this fact. There is no doubt in our mind that the field of SSSL will continue thriving. However, there is a trend, which—if continued—could jeopardize this research area. It has to do with the following.

One of the most important questions in physics in general and in SSSL in particular is what should be the ultimate test of various theories. There are two different schools of thought on this issue.

One school of thought considers the comparison with benchmark experiments as the ultimate test of the theory. Benchmark experiments are those that are conducted in well-controlled conditions, for example, for SSSL in plasmas, benchmark experiments are those, where plasma parameters are determined independently of the SSSL theory to be tested.

Another school of thought insists that the ultimate test of a particular theory is the comparison with another theory (!)—specifically, with results of a code based on fully-numerical simulations starting from the "scratch" rather than from some analytical advance.

There is no question about the importance of simulations as the third powerful research methodology—in addition to theories and experiments. Large-scale codes have been created to simulate a garden variety of complicated phenomena.

However, first, not all large-scale codes are properly verified and validated. Second, fully-numerical simulations are generally ill-suited for capturing so-called emergent principles and phenomena, such as conservation laws, the laws of thermodynamics, detailed balance, and preservation of symmetries. Third, as any fully-numerical method, they lack the physical insight. A number of physicists started warning about this several years ago. Let us present the relevant quotations.

In 2005 Post and Votta published a very insightful article [20], the main point of which was that "much of computational science is still troublingly immature" and that new methods of verifying and validating complex codes are necessary and should be mandatory. Further they wrote

> "*A computational simulation is only a model of physical reality. Such models may not accurately reflect the phenomena of interest. By verification we mean the determination that the code solves the chosen model correctly. Validation, on the other hand, is the determination that the model itself captures the essential physical phenomena with adequate fidelity. Without adequate verification and validation, computational results are not credible.*"

They described the underlying problems as follows:

> "*Part of the problem is simply that it's hard to decide whether a code result is right or wrong. Our experience as referees and editors tells us that the peer review process in computational science generally doesn't provide as effective a filter as it does for experiment or theory. Many things that a referee cannot detect could be wrong with a computational-science paper. The code could have hidden defects, it might be applying algorithms improperly, or its spatial or temporal resolution might be inappropriately coarse.*
>
> *The few existing studies of error levels in scientific computer codes indicate that the defect rate is about seven faults per 1000 lines of Fortran. That's consistent with fault rates for other complex codes in areas as diverse as computer operating systems and real-time switching. Even if a code has few faults, its models and equations could be inadequate or wrong...*
>
> *The existing peer review process for computational science is not effective. Seldom can a referee reproduce a paper's result. Generally a referee can only subject a paper to a series of fairly weak plausibility checks: Is the paper consistent with known physical laws? Is the author a reputable scientist? Referees of traditional theoretical and experimental papers place some reliance on such plausibility checks, but not nearly to the degree a computational-science referee must. The plausibility checks are, in fact, sometimes worse than inadequate.*"

This was written by two leading experts in computational science. Indeed, Post is a computational physicist at Los Alamos National Laboratory and an associate Editor-in-Chief of the journal *Computing in Science and Engineering*. Votta is a Distinguished Engineer at Sun Microsystems Inc. and an associate Editor of *IEEE Transactions on Software Engineering*. No wonder that their paper caused lots of comments published in [21]. In one of the comments, J. Loncaric from Los Alamos wrote in particular:

> "*Unfortunately, these days universities turn out users who employ codes as black boxes but do not understand what they do or when their results can be trusted.*"

Further, speaking of components of a code, he added

> "*... components can be combined, but their combination could be wrong even though the components test well individually. A combination that is insensitive to minor component errors could still give invalid results. Each component has an unstated region of applicability that is often horribly complicated to describe, yet the combination could unexpectedly exceed individual component limits.*"

Responding to the comments, Post and Votta wrote in particular [21]:

"*The second point Loncaric highlights is that a model for a natural system—physical, chemical, biological, and so forth—is often much more than the sum of the individual components. For physical systems, Robert Laughlin recently pointed out that much of science today is inherently reductionist. Present scientific research paradigms emphasize the detailed study of the individual elements that contribute to a complex system's behavior. High-energy physics, for example, involves the study of fundamental particles at progressively higher accelerator energies. Yet successful models of complex systems, such as low-temperature superconductors, are relatively insensitive to the detailed accuracy of the individual constituent effects. Laughlin stresses that successful models capture the emergent principles that determine the behavior of complex systems. Examples of these emergent principles are conservation laws, the laws of thermodynamics, detailed balance, and preservation of symmetries.*

Since a computational simulation is only a model of nature, not nature itself, there is no assurance that a collection of highly accurate individual components will capture the emergent effects. Yet most computational simulations implicitly assume that if each component is accurate, the whole code will be accurate. Nature includes all of the emergent phenomena, but a computational model may not. This perspective underscores the importance of validation of the integrated code and of individual models."

The above general deficiencies of complicated codes resulted in huge failures of important large-scaled projects. Post and Votta described the following examples [20]:

"*Examples abound of large-scale software failures in fields like information technology and aerospace. The 1995 failure of the European Space Organization's Arianne 5 rocket and the 1999 loss of NASA's Mars Climate Orbiter are still fresh in memory. After the Columbia space shuttle's ill-fated February 2003 launch and first reports of possible problems with the mission, a NASA—Boeing team's computational assessment of potential failure modes yielded misleading conclusions that may have contributed to the tragedy.*

The quest for fusion energy provides two more examples of problematic computation. By stretching boundary conditions far beyond what could be scientifically justified, computer simulations were able to "reproduce" the exciting but wrong experimental discovery of sonoluminescent fusion. With regard to the International Thermonuclear Experimental Reactor (ITER), preliminary computational predictions in 1996 of inadequate performance by the proposed facility were wrongly characterized as definitive. Those predictions contributed to the 1998 US withdrawal from that important and promising international undertaking."

As for the research area of SSSL, let us bring up just one example of the unjustifiable reliance on fully-numerical simulations that led to a conclusion contradicting first-principle-based analytical results obtained in various ways. The example concerns a *direct coupling* of the electron and ion microfields in plasmas. This coupling results from the Acceleration of the Electrons by the Ion Field (AEIF). The AEIF is a universal effect: it affects all kinds of spectral lines. The net result of the AEIF is a reduction of Stark widths and shifts.

This phenomenon was first described analytically in the binary approach in paper [22] with subsequent analytical improvements in paper [23]. Then it was also described analytically in the multiparticle approach in book [2] and paper [19].

More recently, there have been conducted fully-numerical simulations trying to "mimic" the phenomenon of AEIF [24]. Based on their fully-numerical simulations conducted for the H_α line at just one value of the electron density N_e and just one value of the temperature T, the authors of [24] claimed that the AEIF leads to an increase of the electron-caused Stark width rather than to its decrease.

It should be emphasized that those simulations [24] had lots of limitations. The primary limitation was their employment of the binary version of the AEIF. Thus, their results have no bearing on the analytical results for the AEIF obtained in the multiparticle approach [2, 19]. Nevertheless, the controversial results of simulation from [24] for the binary version of the AEIF required a resolution.

This issue has been resolved in [25] as follows. The previous analytical calculations of the AEIF [2, 19, 22, 23] were based on the *dynamical* treatment of the perturbing electrons. In other words, in [2, 19, 22, 23] there was calculated analytically how the ion microfield changes the trajectories and velocities of the individual perturbing electrons and then averaged their contribution to the broadening over the ensemble of electrons. In [25], instead of the dynamical treatment there was employed a *statistical* approach. It started from the electron velocity distribution function modified by the presence of the ion microfield—this modified electron velocity distribution function had been calculated (for a different purpose) by Romanovsky and Ebeling in the multiparticle description of the ion microfield [26]. With the help of the modified electron velocity distribution function from [26], it was then calculated in [25] the Stark broadening by electrons within the framework of the conventional theory usually assigned to Griem [27] (who is one of the coauthors of [24]). The result showed that the electron Stark broadening decreases.

Thus two totally different analytical approaches (dynamical and statistical) agreed with each other (by predicting a decrease of the electron Stark broadening) and therefore disproved the fully-numerical simulations from [24] (that claimed an increase of the electron Stark broadening).

In summary, while simulations are important as the third powerful research methodology—in addition to theories and experiments—there is a growing tendency in physics in general and in the area of spectral line shapes in particular, to consider the ultimate test of a particular theory to be the comparison with results of a code based on fully-numerical simulations. However, fully-numerical simulations are often not properly verified and validated, fail to capture emergent principles and phenomena, and lack the physical insight. The last but not least: physics is the experimental science. So, the ultimate test of any theory—including theories of spectral line shapes—should be the comparison with experiments conducted in well-controlled conditions (benchmark experiments).

References

[1] T. Fujimoto, *Plasma Spectroscopy*, Clarendon Press, Oxford, UK, 2004.

[2] E. Oks, *Stark Broadening of Hydrogen and Hydrogenlike Spectral Lines in Plasmas: The Physical Insight*, Alpha Science International, Oxford, UK, 2006.

[3] J.-M. Hartmann, C. Boulet, and D. Robert, *Collisional Effects on Molecular Spectra: Laboratory Experiments and Models, Consequences for Applications*, Elsevier, Amsterdam, The Netherlands, 2008.

[4] E. Oks and M. Pindzola, Eds., *Spectral Line Shapes, Volume 18*, vol. 874 of *AIP Conference Proceedings*, AIP Press, New York, NY, USA, 2006.

[5] M. A. Gigosos and M. A. Gonzalez, Eds., *Spectral Line Shapes, Volume 19*, vol. 1058 of *AIP Conference Proceedings*, AIP Press, New York, NY, USA, 2008.

[6] G. Peach, D. F. T. Mullamphy, and I. B. Whittingham, "Unification of the impact and one-perturber theories of line shapes," in *Proceedings of the 19th International Conference on Spectral Line Shapes*, vol. 1058 of *AIP Conference Proceedings*, pp. 234–236, 2008.

[7] A. V. Glushkov, "QED theory of radiation emission and absorption for atoms and ions in a strong laser field," in *Spectral Line Shapes, Volume 19*, M. A. Gigoso and M. A. Gonzalez, Eds., vol. 1058 of *AIP Conference Proceedings*, p. 134, AIP Press, New York, NY, USA, 2008.

[8] A. V. Glushkov, O. Yu. Khetselius, A. V. Loboda, et al., "QED approach to modeling spectra of the multicharged ions in a plasma: oscillator and electron-ion collision strengths," in *Proceedings of the 19th International Conference on Spectral Line Shapes*, vol. 1058 of *AIP Conference Proceedings*, pp. 175–177, 2008.

[9] N. Bedida, D. Boland, M. T. Meftah, and R. Stamm, "Path integral formalism for the spectral line shape in plasmas: lyman-α with fine structure," in *Proceedings of the 19th International Conference on Spectral Line Shapes*, vol. 1058 of *AIP Conference Proceedings*, pp. 366–367, 2008.

[10] M. A. Gigosos, M. A. Gonzalez, and N. Konjevic, "Temperature dependence of stark broadening dominated by strong collisions," in *Spectral Line Shapes, Volume 18*, E. Oks and M. Pindzola, Eds., vol. 874 of *AIP Conference Proceedings*, p. 35, AIP Press, New York, NY, USA, 2006.

[11] E. Dalimier, E. Oks, O. Renner, and R. Schott, "Experimental determination of rate coefficients of charge exchange from x-dips in laser-produced plasmas," *Journal of Physics B*, vol. 40, no. 5, pp. 909–919, 2007.

[12] O. Renner, E. Dalimier, E. Oks, et al., "Experimental evidence of Langmuir-wave-caused features in spectral lines of laser-produced plasmas," *Journal of Quantitative Spectroscopy and Radiative Transfer*, vol. 99, no. 1–3, pp. 439–450, 2006.

[13] N. C. Woolsey, D. M. Chambers, C. Courtois, et al., "Aluminum He-beta high resolution spectroscopy and the observation of high field processes," in *Spectral Line Shapes, Volume 18*, E. Oks and M. Pindzola, Eds., vol. 874 of *AIP Conference Proceedings*, p. 76, AIP Press, New York, NY, USA, 2006.

[14] V. P. Gavrilenko, A. Ya. Faenov, A. I. Magunov, et al., "Observation of modulations in lyman-alpha line profiles of hydrogen-like ions of oxygen in clusters irradiated by femtosecond laser pulses: effect of an oscillatory electric field," in *Proceedings of the 18th International Conference on Spectral Line Shapes*, vol. 874 of *AIP Conference Proceedings*, pp. 87–89, 2006.

[15] O. Renner, P. Sauvan, E. Dalimier, et al., "X-ray spectroscopy of hot dense plasmas: experimental limits, line shifts & field effects," in *Spectral Line Shapes, Volume 19*, M. A. Gigosos and M. A. Gonzalez, Eds., vol. 1058 of *AIP Conference Proceedings*, p. 341, AIP Press, New York, NY, USA, 2008.

[16] O. Renner, P. Sauvan, E. Dalimier, et al., "Signature of externally introduced laser fields in X-ray emission of multicharged ions," *High Energy Density Physics*, vol. 5, no. 3, pp. 139–146, 2009.

[17] V. P. Gavrilenko and E. Oks, "Use of quasienergy states for laser-aided diagnostics of oscillatory electric fields in plasmas," in *Spectral Line Shapes, Volume 18*, E. Oks and M. Pindzola, Eds., vol. 874 of *AIP Conference Proceedings*, p. 242, AIP Press, New York, NY, USA, 2006.

[18] P. Sauvan and E. Dalimier, "Floquet-Liouville approach for calculating Stark profiles in plasmas in the presence of a strong oscillating field," *Physical Review E*, vol. 79, no. 3, Article ID 036405, 2009.

[19] E. Oks, "Stark widths of hydrogen spectral lines in plasmas: a highly-advanced non-simulative semiclassical theory and tables," in *Spectral Line Shapes, Volume 18*, E. Oks and M. Pindzola, Eds., vol. 874 of *AIP Conference Proceedings*, p. 19, AIP Press, New York, NY, USA, 2006.

[20] D. E. Post and L. G. Votta, "Computational science demands a new paradigm," *Physics Today*, vol. 58, no. 1, pp. 35–41, 2005.

[21] *Physics Today*, p. 12, 2005.

[22] E. Oks, "A new spectroscopic effect resulting in a narrowing of hydrogen lines in dense plasmas," *Journal of Quantitative Spectroscopy and Radiative Transfer*, vol. 65, no. 1–3, pp. 405–414, 2000.

[23] E. Oks, "Reduction of spectral line shifts due to the acceleration of electrons by the ion field in plasmas," *Journal of Physics B*, vol. 35, no. 10, pp. 2251–2260, 2002.

[24] E. Stambulchik, D. V. Fisher, Y. Maron, H. R. Griem, and S. Alexiou, "Correlation effects and their influence on line broadening in plasmas: application to Hα," *High Energy Density Physics*, vol. 3, no. 1-2, pp. 272–277, 2007.

[25] E. Oks, "New statistical multiparticle approach to the acceleration of electrons by the ion field in plasmas," *International Journal of Spectroscopy*, vol. 2010, Article ID 347080, 2010.

[26] M. Yu. Romanovsky and W. Ebeling, "Corrections of electron impact ionization rates by plasmas electric microfield," *Physics Letters A*, vol. 317, no. 1-2, pp. 150–155, 2003.

[27] H. R. Griem, *Spectral Line Broadening by Plasmas*, Academic Press, New York, NY, USA, 1974.

Hindawi Publishing Corporation
International Journal of Spectroscopy
Volume 2010, Article ID 812471, 12 pages
doi:10.1155/2010/812471

Review Article

Optical Transitions and Charge-Exchange in Highly Charged Quasi-Molecules

A. Devdariani,[1] E. Dalimier,[2] and P. Sauvan[3]

[1] *Department of Optics and Spectroscopy, St. Petersburg University, St. Petersburg 198904, Russia*
[2] *Laboratoire pour l'Utilisation des Lasers Intenses LULI, UMR 7605, CNRS-CEA-Ecole Polytechnique-Université Paris 6, UPMC case 128, 4 Place Jussieu, 75252 Paris Cedex 05, France*
[3] *Departamento de Ingeniería Energética, E.T.S. Ingenieros Industriales, UNED, C/ Juan del Rosal 12, 28040 Madrid, Spain*

Correspondence should be addressed to E. Dalimier, elisabeth.dalimier@upmc.fr

Received 28 April 2009; Accepted 23 June 2009

Academic Editor: Roland Stamm

The interaction between quasimolecular states produces not only nonadiabatic transitions but also some exotic features in the wings of the spectral profiles emitted by the ions in collision. Although this concept has been fruitfully used for neutral species, some new highlighted experimental data on quasimolecular optical transitions in hot dense plasma have renewed the interest to the concept in the recent years. The present review deals with highly charged quasimolecules and it is dedicated specifically to quasimolecules formed by two bare nuclei and one bound electron. The reason for this choice is that, for such quasimolecules, the energy terms and the dipole moments of the optical transitions can be obtained straightforwardly in nonrelativistic case without any approximation that are typical for neutrals. Although the results obtained in the frame of the approach developed here are directly applicable to the case of single collisions or to low-density plasmas, they form a reasonable initial approximation for the problem of optical profiles in hot dense plasmas and can be regarded as a safe framework for qualitative discussions of profiles in those environments.

1. Introduction: Features of Spectral Profiles following the Interaction of Quasimolecular States

The concept of quasi-molecular (QM) states that are formed during collisions of atomic particles has proved to be successful in describing collision processes at low energies including charge-exchange processes. In frame of the QM approach, nonadiabatic transitions in collisions can be regarded as a consequence of the interaction between different QM states at some interatomic distances and can be analytically described by the Landau-Zener model or the Demkov-Nikitin model [1, 2]. However the QM states participating in collision processes are very often subjected to optical transitions. The question therefore arises whether the interaction of the states during a collision affects the spectral line shape and if so, how? An analysis based on the general theory of quasistationary states, that is, the states that are unstable due to the emission of photons or electrons during the collisions, has shown that the interaction of QM states does indeed give rise to exotic features in the profiles [3, 4]. In particular, analytical formulae have been obtained describing the features produced by the crossing of QM energy terms [5, 6]. It should be stressed that the approach proposed here has related the cross-sections of nonadiabatic transitions to the spectral features averaged over impact parameters and Maxwell's distribution.

In spite of successful applications of the elaborated theory to experiments with neutrals, for example, [6–9], attention had not been paid to ion collisions in plasma, until recent experiments in hot dense plasmas [10–14] exhibiting fine structures, that is, satellites in F Lyman β profile emitted by a fluorine plasma, dips, and bumps in the *Al* Lyman γ profile emitted by a heterogeneous *Al-C* plasma. The fine structures in *Al* Lyman γ have been connected to intersections of QM *Al-C* energy terms. This work was the first to reveal charge-exchange signature in the spectral line shape in hot dense plasmas.

The main objective of the present paper is to overview the recent theoretical and numerical developments in the specific field of spectral signatures of nonadiabatic transitions, namely, charge-exchange processes. Those processes are basic ones for plasma physics, and, among other things, they play an important role in understanding the interaction of high-temperature plasmas with cold gases [15] or the interactions at the edge plasmas in Tokamaks [16]. It is important to emphasize that the features mentioned above in the spectral profiles can be utilized as diagnostics. The whole study is complementary to the analysis of the coupling between charge-exchange processes dynamics and ionic populations dynamics in plasmas, the latter study being addressed to line intensities instead of spectral line shapes [16].

The focus of the survey is at the one-electron ionic quasi-molecule. The reason is that, in addition to hot plasma and astrophysics applications, the one-electron quasi-molecule is the unique example of quasi-molecules for which energy terms and dipole moments can be calculated straightforwardly, with any desired precision excluding uncertainties in the input data (those uncertainties on terms and dipole moments are quite typical in the calculations of profiles produced by neutrals collisions.).

2. Energy Terms and Dipole Optical Transition Moments for the Molecule Z_1eZ_2

This part is devoted to the calculation of the energy terms and the dipole transition matrix elements and related optical values, for multicharged one electron diatomic quasi-molecules with unequal nuclear charges Z_1 and Z_2 (Z_1eZ_2 notation for the quasi-molecule). The first wave of interest for such molecules was initiated by spectroscopic observations attributed to inner-shell excitations in ion-atom collisions [17, 18]. Another wave came from the hot dense plasma physics community. The excited state orbital of mononuclear ion bound electrons may be strongly disturbed by the field of the nearest-neighbor ion. Within these conditions, transitions in quasi-molecules are relevant for the interpretation of experimental results [10–14, 19, 20].

At first the exchange interaction in the quasi-molecule and its influence on the spectral profiles was considered with the rough approximations of exponential interaction energies and constant dipole matrix elements. These approximations are valid for allowed transitions produced by quasi-molecular transitions in the region of large internuclear distances. The approach is unsuitable for forbidden transitions characterized by a strong dependence of the dipole matrix elements on the internuclear distance. The need of accurate values of dipole moments over a wide range of internuclear distances rather than restricted to large ones only is then obvious.

At this step it is important to notice that the dipole matrix elements for the one-electron heterodiatomic quasi-molecules ($Z_1 \neq Z_2$), in the frame of nonrelativistic approach, had not been calculated before the work done by Devdariani et al. [21]; only the quasi-molecular energy terms had been reviewed in details by Komarov et al. [22].

In the present section we first scale the radiative characteristics of the one-electron heterodiatomic quasi-molecules, then; after summarizing the method of calculation of the energy terms and the dipole moments matrix element, we provide some results and applications to spectroscopy.

2.1. Scaling the Radiative Characteristics. We derive the formulae which relate the radiative characteristics of the one-electron diatomic quasi-molecule with nuclei charges Z_1 and Z_2 ($Z_1 \geq Z_2$) to the same characteristics of the one-electron quasi-molecule with nuclei charges $Z_1' = Z_1/Z_2$ and $Z_2' = 1$.

For an electron being in the field of two fixed nuclei Z_1 and Z_2 separated at the distance R, the matrix element of the electric dipole moment operator between states specified by quantum numbers i, m_i and j, m_j is given by the following formula:

$$\vec{d}_{im_i,jm_j}(Z_1,Z_2,R) = \int \psi^*_{im_i}(\vec{r},R)\,\vec{r}\,\psi_{jm_j}(\vec{r},R)\,\vec{dr}. \quad (1)$$

In (1) m_i and m_j stand for the magnetic quantum numbers, which determine the projection of the orbital momentum of the electron on the internuclear axis $\vec{R}$, $\vec{r}$ denotes the position vector of the electron (with origin at the middle of the internuclear axis), and ψ_{im_i} and ψ_{jm_j} are the two-Coulomb-centre wave-functions. These eigen-functions are solutions of the Shrödinger equation for the energy terms $\varepsilon_{i|m_i|}(R)$ respectively.

The oscillator strength $f_{ij}(Z_1,Z_2,R)$ corresponding to the electric dipole transition $i \rightarrow j$ is determined by means of the matrix element (1), that is,

$$f_{ij}(Z_1,Z_2,R) = -\frac{2}{3}\frac{\omega_{ij}(R)}{g_i}\sum_{m_i,m_j}\left|\vec{d}_{im_i,jm_j}(Z_1,Z_2,R)\right|^2, \quad (2)$$

where $\omega_{ij}(R) = \boldsymbol{\varepsilon}_{i|m_i|}(R) - \boldsymbol{\varepsilon}_{j|m_j|}(R)$ is the difference between the energy terms, and g_i is the degree of degeneracy or statistic weight of the initial level i ($g_i = 1$ for states with $m_i = 0$ and $g_i = 2$ for states with $m_i \neq 0$).

Finally for spontaneous emission by a quasi-molecule Z_1eZ_2 from the state i to j, the probability per time unit $A_{ij}(Z_1,Z_2,R)$ can be expressed in terms of the oscillator strength of the corresponding transition [23]:

$$A_{ij}(Z_1,Z_2,R) = 2\alpha^3\omega_{ij}^2(R)\left|f_{ij}(Z_1,Z_2,R)\right|, \quad (3)$$

where α is the fine structure constant.

Let us perform the following scale transformations:

$$\vec{r} = \frac{\vec{\rho}}{Z_2}, \quad \vec{R} = \frac{\vec{L}}{Z_2}, \quad Z_1' = \frac{Z_1}{Z_2}, \quad Z_2' = 1. \quad (4)$$

It can be shown that the normalized eigen-functions and the eigen-values of the two-center Shrödinger equation verify the following relations [24]:

$$\psi_{im_i}(\vec{r},R) = Z_2^{3/2}\varphi_{im_i}(Z_2\vec{r},Z_2R),$$
$$\boldsymbol{\varepsilon}_{i|m_i|}(R) = {Z_2}^2\boldsymbol{\varepsilon}_{i|m_i|}(Z_2R). \quad (5)$$

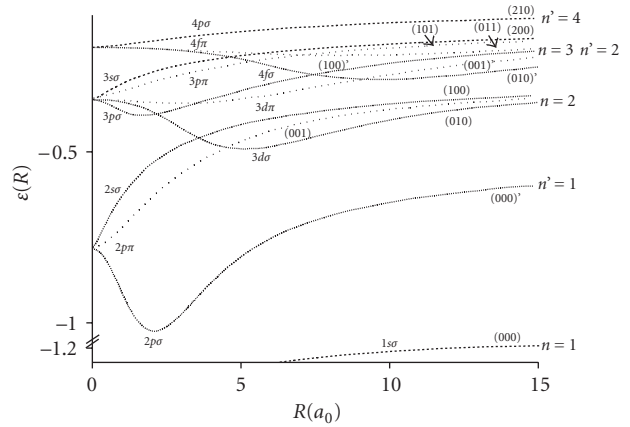

Figure 1: Molecular orbital correlation diagram for the quasi-molecule Z_1eZ_2 with $Z_1 = 1.5$ and $Z_2 = 1$. For the notation of the molecular orbitals, we use the united ion designation in the left part of the figure and the parabolic quantum numbers in brackets in the right part of the figure. n stands for the main quantum number in the separated ions limit, and the primed numbers are for the ion with $Z_1 = 1$.

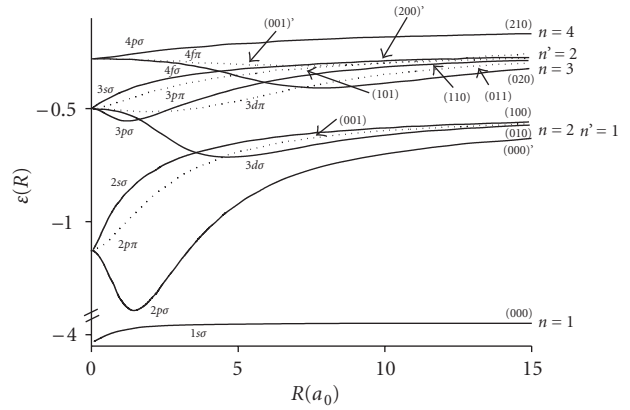

Figure 2: Molecular orbital correlation diagram for the quasi-molecule Z_1eZ_2 with Z_1= 2.0 and Z_2= 1. The notations are similar to the ones on Figure 1.

As a consequence this gives the scaling transformations for the radiative characteristics of the quasi-molecule $Z_1'eZ_2'$ experimenting the electric dipole transition $i \to j$.

$$\begin{aligned} \vec{d}_{im_i,jm_j}(Z_1,Z_2,R) &= \frac{1}{Z_2}\vec{d}_{im_i,jm_j}(Z_1',Z_2',L), \\ f_{ij}(Z_1,Z_2,R) &= f_{ij}(Z_1',Z_2',L), \\ A_{ij}(Z_1,Z_2,R) &= {Z_2}^4 A_{ij}(Z_1',Z_2',L). \end{aligned} \tag{6}$$

In the particular case of homonuclear quasi-molecules ($Z_1 = Z_2 = Z$), the radiative characteristics reduce to the ones relevant to the hydrogen molecular ion H_2^+.

The formulae obtained above reduce the calculation of the radiative characteristics of the one-electron quasi-molecules with the nuclei charges kZ_1 and kZ_2 ($k = 1,2,3,\ldots$) to the calculation of the same characteristics for a single quasi-molecule with the nuclei charges $Z_1' = Z_1/Z_2$ and $Z_2' = 1$. We emphasize that the calculation of the radiative characteristics for the quasi-molecules with smaller nucleus charges is timesaving and faced with smaller computational difficulties.

2.2. The Molecular Orbital (MO) Energy Diagrams and the Dipole Moment Matrix Elements [21]. It is well known that the Schrödinger equation of the two-coulomb-centre system is separable by using the prolate spheroïdal coordinate system (ξ,η,φ) related to the coordinates x, y, z of the electron position vector through

$$\begin{aligned} x &= \frac{R}{2}\sqrt{(\xi^2-1)(1-\eta^2)}\cos\varphi, \\ y &= \frac{R}{2}\sqrt{(\xi^2-1)(1-\eta^2)}\sin\varphi, \\ z &= \frac{R}{2}\xi\eta. \end{aligned} \tag{7}$$

The solution of this equation can then be presented as the following product:

$$\begin{aligned} \psi_{im_i}(\vec{r},R) &= \frac{1}{\sqrt{2\pi}}X_{i|m_i|}(\xi,R)Y_{i|m_i|}(\eta,R)e^{im_i\varphi}, \\ 1 \le \xi < \infty,\ -1 \le \eta \le 1,\ 0 \le \varphi < 2\pi. \end{aligned} \tag{8}$$

Here $X_{i|m_i|}(\xi,R)$ and $Y_{i\,|m_i|}(\eta,R)$ stand for the normalized two-Coulomb-centre quasi-radial and quasi-angular wave functions. After an integration over φ, the dipole matrix elements, depending on the wave-functions ψ_{im_i} and ψ_{jm_j}, can be expressed through those forms:

$$\begin{aligned} (d_x)_{im_i,jm_j} &= \pm i\left(d_y\right)_{im_i,jm_j} \\ &= \frac{R^4}{32}\left[\int_1^\infty X_{i|m_i|}X_{j|m_j|}\sqrt{\xi^2-1}\,\xi^2\delta\xi\right. \\ &\quad\times\int_{-1}^{1} Y_{i|m_i|}Y_{j|m_j|}\sqrt{1-\eta^2}\,\delta\eta \\ &\quad-\int_1^\infty X_{i|m_i|}X_{j|m_j|}\sqrt{\xi^2-1}\,\delta\xi \\ &\quad\left.\times\int_{-1}^{1} Y_{i|m_i|}Y_{j|m_j|}\sqrt{1-\eta^2}\,\eta^2\delta\eta\right], \end{aligned} \tag{9}$$

$$\begin{aligned} (d_z)_{im_i,jm_j} &= \frac{R^4}{16}\left[\int_1^\infty X_{i|m_i|}X_{j|m_j|}\,\xi^3 d\xi\int_{-1}^{1} Y_{i|m_i|}Y_{j|m_j|}\,\eta d\eta\right. \\ &\quad\left.-\int_1^\infty X_{i|m_i|}X_{j|m_j|}\,\xi d\xi\int_{-1}^{1} Y_{i|m_i|}Y_{j|m_j|}\,\eta^3 d\eta\right]. \end{aligned} \tag{10}$$

Table 1: Dipole moment matrix elements for transitions $2p\sigma \rightarrow 1s\sigma$ and $3d\sigma \rightarrow 1s\sigma$ in relation to the distance R between ions $Z_1 = 1.5, 2.0, 2.5, 3.0$ and $Z_2 = 1$, all values in atomic units.

R	$2p\sigma \rightarrow 1s\sigma$				$3d\sigma \rightarrow 1s\sigma$			
	$Z_1 = 1.5$	$Z_1 = 2.0$	$Z_1 = 2.5$	$Z_1 = 3.0$	$Z_1 = 1.5$	$Z_1 = 2.0$	$Z_1 = 2.5$	$Z_1 = 3.0$
0.25	−0.33803	−0.28907	−0.25263	−0.22412	−0.00174	−0.00303	−0.00404	−0.00485
0.50	−0.41545	−0.36026	−0.31328	−0.27264	−0.00488	−0.00885	−0.01202	−0.01446
0.75	−0.50288	−0.42748	−0.35600	−0.29371	−0.01044	−0.01920	−0.02566	−0.02989
1.00	−0.58488	−0.47277	−0.36814	−0.28570	−0.01962	−0.03555	−0.04541	−0.05021
1.50	−0.70306	−0.48210	−0.32696	−0.23558	−0.05478	−0.08810	−0.09784	−0.09613
2.00	−0.73859	−0.41656	−0.26382	−0.19231	−0.12002	−0.15697	−014965	−0.13021
2.50	−0.68315	−0.33383	−0.21462	−0.16807	−0.20965	−0.21854	−0.18207	−0.14208
3.00	−0.56969	−0.26313	−0.18281	−0.15913	−0.29820	−0.25760	−0.19418	−0.13747
3.50	−0.44511	−0.20898	−0.16470	−0.16077	−0.36338	−0.27608	−0.19380	−0.12248
4.00	−0.33529	−0.16811	−0.15710	−0.16779	−0.40070	−0.28197	−0.18663	−0.10089
4.50	−0.24687	−0.13647	−0.15830	−0.17481	−0.41596	−0.28172	−0.17467	−0.07747
5.00	−0.17850	−0.11095	−0.16738	−0.17913	−0.41672	−0.27920	−0.15713	−0.05717
6.00	−0.08884	−0.07110	−0.19803	−0.18181	−0.39782	−0.27401	−0.10127	−0.03076
7.00	−0.04175	−0.04202	−0.21427	−0.18187	−0.37434	−0.27132	−0.04739	−0.01693
8.00	−0.01880	−0.02280	−0.21733	−0.18147	−0.35788	−0.27062	−0.02052	−0.00928
9.00	−0.00821	−0.01163	−0.21755	−0.18103	−0.35023	−0.27079	−0.00893	−0.00494
10.0	−0.00352	−0.00570	−0.21727	−0.18062	−0.34912	−0.27106	−0.00390	−0.00255
12.0	−0.00062	−0.00127	−0.21655	−0.17992	−0.35424	−0.27107	−0.00074	−0.00063
14.0	−0.00010	−0.00026	−0.21591	−0.17938	−0.35822	−0.27060	−0.00014	−0.00014
16.0	−0.00002	−0.00005	−0.21537	−0.17896	−0.35959	−0.27004	−0.00002	−0.00003
18.0	0.00000	−0.00001	−0.21492	−0.17862	−0.35979	−0.26951	0.00000	−0.00001
20.0	0.00000	0.00000	−0.21455	−0.17834	−0.35957	−0.26904	0.00000	0.00000
22.0	0.00000	0.00000	−0.21423	−0.17810	−0.35922	−0.26862	0.00000	0.00000
24.0	0.00000	0.00000	−0.21397	−0.17790	−0.35883	−0.26825	0.00000	0.00000
26.0	0.00000	0.00000	−0.21373	−0.17773	−0.35844	−0.26793	0.00000	0.00000
28.0	0.00000	0.00000	−0.21353	−0.17759	−0.35807	−0.26764	0.00000	0.00000
30.0	0.00000	0.00000	−0.21336	−0.17746	−0.35773	−0.26739	0.00000	0.00000
∞	0.00000	0.00000	−0.21070	−0.17558	−0.35117	−0.26337	0.00000	0.00000

They satisfy the selection rules for the magnetic quantum number in the case of dipole transitions, that is, $m_j = m_i \mp 1$ in (9) for the radiation polarized in the plane perpendicular to $\vec{R}$ ($\sigma - \pi$ transitions) and $m_j = m_i$ in (10) for the radiation polarized along the internuclear axis $\vec{R}$ ($\sigma - \sigma$, $\pi - \pi$ transitions).

The wave functions have been expanded in various forms involving coefficients determined by recurrence relations [21] and yielding the relative accuracy of order 10^{-12} for the energy terms and the accuracy of order $10^{-8} - 10^{-10}$ for the corresponding quasiradial and quasiangular wave functions. Thus, the accuracy of the calculated matrix elements can be estimated at 10^{-8} [21].

The dipole matrix elements (and all energy terms involved) have been calculated for all transitions between the states with the principal quantum number in the united ion limit $n_u = 1, 2, 3$ and for four transitions involving $n_u = 4$. The calculations have been carried out for the quasi-molecules with the nucleus charges $Z_1 = 1.5, 2, 2.5, 3$ and $Z_2 = 1$. Some results are given in Tables 1 and 2 for the dipole matrix elements and in Figures 1, 2, and 3 for the energy terms (MO) correlation diagrams. The choice of these results gives examples relevant to the discussion of the most important new features.

In this paper we will not be concerned with the existence of extrema in the energy terms; this feature has been previously used for high-density plasma spectroscopy [10–14, 19, 20].

The most prominent other new features that can be deduced from the data are as follows: (i) the matrix elements strongly depend on the internuclear distance R; (ii) some matrix elements of the quasi-molecules, with different Z_1 at large R, exchange their limiting values; (iii) the limiting values of some matrix elements, at large R, tend in pairs to the same values or to values of equal modulus and opposite signs, and some of them are equal to zero; (iv) some of the matrix elements have zeros at intermediate R.

Below, some features are discussed qualitatively in more detail through examples.

2.2.1. The Limiting Values. A novel feature for the heteronuclear quasi-molecules is that the correlation diagram,

Table 2: Dipole moment matrix elements for transitions $3p\sigma \rightarrow 1s\sigma$ and $4p\sigma \rightarrow 1s\sigma$ in relation to the distance R between ions $Z_1 = 1.5, 2.0, 2.5, 3.0$ and $Z_2 = 1$, all values in atomic units.

R	$3p\sigma \rightarrow 1s\sigma$				$4p\sigma \rightarrow 1s\sigma$			
	$Z_1 = 1.5$	$Z_1 = 2.0$	$Z_1 = 2.5$	$Z_1 = 3.0$	$Z_1 = 1.5$	$Z_1 = 2.0$	$Z_1 = 2.5$	$Z_1 = 3.0$
0.25	−0.12796	−0.10778	−0.09289	−0.08137	−0.07421	−0.06223	−0.05341	−0.04662
0.50	−0.13743	−0.11347	−0.09481	−0.08004	−0.07673	−0.06251	−0.05167	−0.04327
0.75	−0.13436	−0.10445	−0.08230	−0.06729	−0.07096	−0.05396	−0.04225	−0.03417
1.00	−0.11617	−0.08495	−0.06615	−0.05399	−0.05717	−0.04080	−0.03165	−0.02597
1.50	−0.06109	−0.04839	−0.04293	−0.03791	−0.02412	−0.01944	−0.01814	−0.01653
2.00	−0.01617	−0.02939	−0.03216	−0.03033	−0.00027	−0.00881	−0.01182	−0.01179
2.50	0.00886	−0.02113	−0.02680	−0.02630	0.01284	−0.00385	−0.00833	−0.00881
3.00	0.01882	−0.01735	−0.02389	−0.02393	0.01881	−0.00122	−0.00606	−0.00665
3.50	0.02062	−0.01549	−0.02229	−0.02235	0.02099	0.00036	−0.00442	−0.00494
4.00	0.01898	−0.01459	−0.02142	−0.02111	0.02138	0.00139	−0.00313	−0.00352
4.50	0.01626	−0.01426	−0.02095	−0.02001	0.02096	0.00211	−0.00207	−0.00231
5.00	0.01345	−0.01431	−0.02062	−0.01897	0.02016	0.00264	−0.00114	−0.00126
6.00	0.00871	−0.01520	−0.01989	−0.01705	0.01817	0.00340	0.00044	0.00047
7.00	0.00537	−0.01666	−0.01885	−0.01537	0.01619	0.00403	0.00177	0.00182
8.00	0.00313	−0.01808	−0.01766	−0.01394	0.01447	0.00465	0.00290	0.00290
9.00	0.00169	−0.01888	−0.01646	−0.01273	0.01306	0.00529	0.00386	0.00378
10.0	0.00080	−0.01894	−0.01536	−0.01171	0.01197	0.00593	0.00469	0.00452
12.0	0.00004	−0.01787	−0.01346	−0.01007	0.01060	0.00714	0.00604	0.00568
14.0	−0.00010	−0.01641	−0.01194	−0.00882	0.01021	0.00821	0.00709	0.00656
16.0	−0.00008	−0.01504	−0.01072	−0.00785	0.01082	0.00913	0.00793	0.00725
18.0	−0.00005	−0.01383	−0.00971	−0.00707	0.01228	0.00993	0.00862	0.00781
20.0	−0.00002	−0.01277	−0.00887	−0.00643	0.01367	0.01061	0.00919	0.00826
22.0	−0.00001	−0.01186	−0.00817	−0.00589	0.01448	0.01120	0.00968	0.00865
24.0	−0.00001	−0.01106	−0.00756	−0.00544	0.01504	0.01172	0.01010	0.00897
26.0	0.00000	−0.01036	−0.00704	−0.00505	0.01552	0.01219	0.01046	0.00926
28.0	0.00000	−0.00973	−0.00659	−0.00471	0.01596	0.01260	0.01078	0.00950
30.0	0.00000	−0.00918	−0.00619	−0.00442	0.01637	0.01296	0.01107	0.00972
∞	0.00000	0.00000	0.00000	0.00000	0.02621	0.01966	0.01573	0.01311

which relates the orbitals of the isolated and united ions, now depends on Z_1. More precisely, the rearrangement for the dipole matrix elements of the Molecular Orbital (MO) correlation diagrams results in the dependence of the limiting values on Z_1, apart from the trivial scaling, and in the exchange of the limiting values. To exemplify the dependence of the limiting values on Z_1 we take the particular case of the matrix element $\langle 010|d_z|000\rangle = -128/243Z_1$ for the hydrogen-like ion (for large R the matrix elements are in parabolic coordinates). According to Figures 1–3 and Table 1 this matrix element is the limiting value for the transition between the $3d\sigma$and $1s\sigma$states in the case of $Z_1 = 1.5, 2$; but in the case $Z_1 = 2.5, 3$, this matrix element is the limiting value for the transition between the $2p\sigma$ and $1s\sigma$ states. Also Figures 1–3 shows that the $2s\sigma, 2p\pi, 3s\sigma, 3p\pi$ MO energy diagrams do not depend on Z_1.

2.2.2. The Roots of the Optical Transition Dipole Moments. When the dipole matrix element between two states of an atom or an ion is equal to zero, the transition is forbidden. Nevertheless the interaction between particles during the collisions will allow the dipole matrix elements to become functions of internuclear distance and the optical transitions to be allowed. Such optical transitions can be identified as true quasi-molecular ones, and up to now some of these transitions produced in atomic and ionic collisions have been studied [26–28].

The existence of zeros in the dipole transition matrix elements had already been pointed out for symmetrical quasi-molecules [31, 32]. In the hetero-nucleus case, the parallel transitions, having zeros in the symmetrical case, have zeros for all Z_1 values considered here, namely, $4p\sigma - 1s\sigma$; see Table 2. The matrix element for the transition $3p\sigma - 1s\sigma$ has two zeros but only for $Z_1 = 1.5$ and has no zero otherwise; see Table 2.

In the hetero-nuclear quasi-molecules there is an additional possibility for asymptotically forbidden-transitions. When at $R \rightarrow \infty$ the upper and lower states belong to different ions, the corresponding wave functions do not overlap, and therefore, the matrix element is equal to zero. At smaller R, the interaction between two different ions will allow optical transitions corresponding to the transition

of one electron from one ion to the other. Such optical transitions involve a nonresonant charge-exchange process and they correspond to asymptotically forbidden transitions. As examples the transitions $2p\sigma - 1s\sigma$ for $Z_1 = 1.5, 2$ and $3d\sigma - 1s\sigma$ for $Z_1 = 2.5, 3$ accompanying the charge-exchange between the lowest ion states with parabolic sets (000) and $(000)'$ correspond to such asymptotically forbidden-transitions (see Table 1).

The results of these calculations put forward two problems: what is the reason for the roots and how can we describe the spectral features produced?

3. Spectral Features Due to Intersection of Energy Terms

In this part we will show that the intersection of terms not only leads to the formation of extrema in energy terms but can also be responsible for the roots of dipole moments. As for the spectral features, an extremum in an energy term will then not necessarily produce a satellite. Of particular interest is the role of dipole transition moments [21, 33], which can lead, in the case of zeros, to the formation of dips in the far wing spectral profiles [21]. This phenomenon has been discussed in two limiting cases, adiabatic and diabatic [34].

3.1. The Two-State Model for the Dipole Moments. The prediction of roots and their positions can be made within the two-state model.

Let us next consider the two-state adiabatic and diabatic wave functions $|\Psi_{I,II}\rangle$ and $|\varphi_{1,2}\rangle$, for the quasi-molecule, respectively. We now follow the Nikitin model [25] that is appropriate to have an idea of all situations and can reveal the main conclusions. The model gives for the diabatic matrix elements $V_{ik} = \langle\varphi_i|V|\varphi_k\rangle$ of the interaction between the two ions:

$$V_{ik} = \delta_{ik}\left[V(x) + \frac{\Delta\varepsilon}{2}(1 - e^{-x}\cos 2\Theta_0)(-1)^{1+i}\right] + (1 - \delta_{ik})\frac{\Delta\varepsilon}{2}e^{-x}\sin 2\Theta_0. \tag{11}$$

The variable x is a dimensionless distance ($x = 0$ at the center of the considered nonadiabatic region). The parameter Θ_0 characterizes two alternative evolutions of the energy terms in the considered transition zone, namely, intersecting, $0 \le \Theta_0 \le \pi/4$, (Figure 4(a)) or nonintersecting, $\pi/4 \le \Theta_0 \le \pi/2$, (Figure 4(b)) diabatic terms. $\Delta\varepsilon$ is the splitting between the terms at large distances.

The same model leads to the following adiabatic dipole moments:

$$D = \sqrt{d_1^2 + d_2^2}\begin{vmatrix} \cos(\Theta - \Theta_d) \\ -\sin(\Theta - \Theta_d) \end{vmatrix}. \tag{12}$$

In this formula, the dipole moments for optical transitions towards the ground state $|\varphi_0\rangle$ are defined on the two wave function basis (adiabatic and diabatic) as $D_{I,II} = \langle\Psi_{I,II}|d|\varphi_0\rangle.d_{1,2} = \langle\varphi_{I,II}|d|\varphi_0\rangle$, and tg $\Theta_d = d_2/d_1$ (Θ_d varying from 0 to $\pi/2$ if $d_1 d_2 \ge 0$).

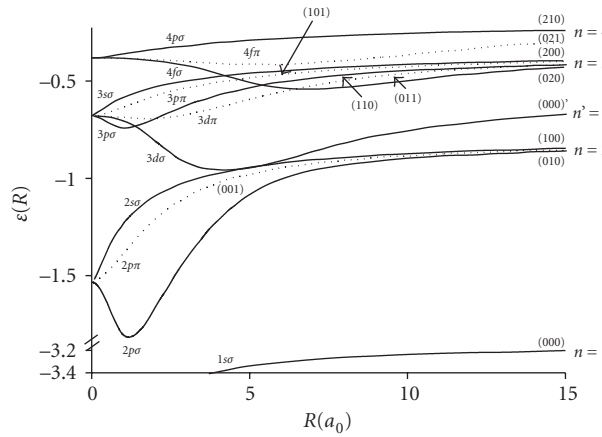

Figure 3: Molecular orbital correlation diagram for the quasi-molecule Z_1eZ_2 with Z_1= 2.5 and Z_2= 1. The notations are similar to the ones on Figure 1.

The free parameter Θ, varying from $\pi/2 - \Theta_0$ to 0, when $x$varies from $-\infty$ to $+\infty$, is defined as follows:

$$\Theta = \text{arctg}\sqrt{\frac{K - \Delta}{K + \Delta}} \quad \text{with } \Delta = V_{11} - V_{22}, \qquad K = \sqrt{\Delta^2 + 4|V_{12}|^2}. \tag{13}$$

3.2. The Roots of the Dipole Moments and the Spectral Profiles. In this section, we discuss the adiabatic dipole transition moment roots and their manifestations in the spectral profiles (satellites and/or dips). For this purpose, the relationship between Θ_0 and Θ_d turns out to be determining (see Figure 5, where all possible cases are summarized). As one can see from (12), one of the two adiabatic dipole transition moment has a root at $\Theta = \Theta_d$ and another has a maximum if the upper limiting value Θ ($x \to -\infty$) = $\pi/2 - \Theta_0 \ge \Theta_d$ (regions *III* and *IV* on Figure 5). But there are no roots in the opposite case (regions *I* and *II*). We should stress that counter-intuitively, there is a root in the former case for nonintersecting diabatic terms corresponding to $\Theta_0 \ge \pi/4$ (region *III*) but no root for intersecting diabatic terms corresponding to $\Theta_0 \le \pi/4$ (region *II*). Thus the main conclusion is that the intersection of terms is neither a necessary nor a sufficient condition for the existence of a dipole moment root.

Then we discuss the effect, on the optical spectral profiles, of the dipole transition moment rearrangement in the four regions previously discussed in the space Θ_0,Θ_d.

In the region *I* of Figure 5, the adiabatic potential energy curves (and consequently the transition energies) do not have extrema ($\pi/4 < \Theta_0 < \pi/2$, Figure 4(b)), and the dipole moments do not have any root at any allowed interatomic distances. This case leads to *a monotonous dependence of the profiles on frequency.*

In the region *II,* every adiabatic potential energy curve (and consequently the transition energy) has an extremum ($\Theta_0 < \pi/4$, Figure 4(a)), but the dipole moments have neither roots nor extrema. It is well known that an extremum

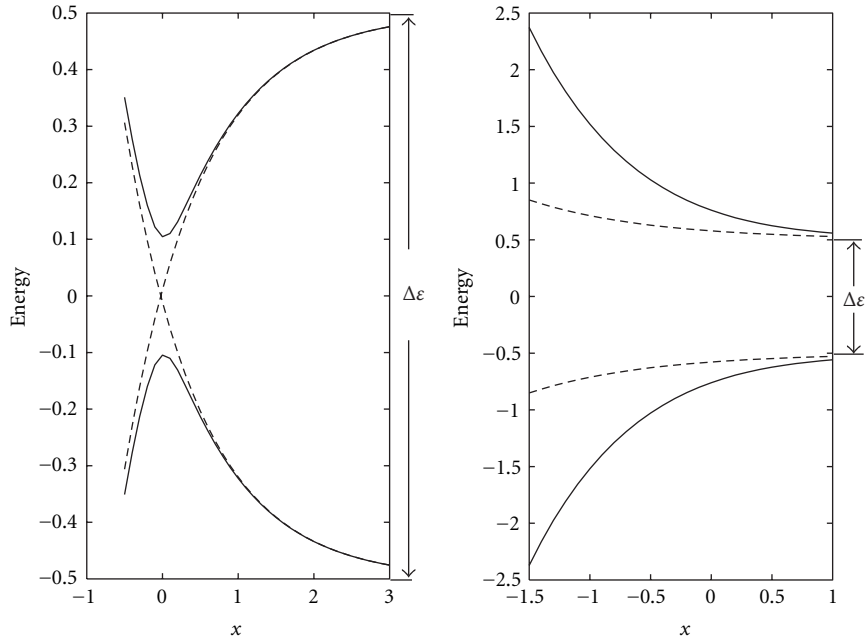

(a) Case (a): intersecting diabatic energy terms

(b) Case (b): nonintersecting diabatic energy terms

FIGURE 4: The two alternative evolutions of the diabatic energy terms V_{11} and V_{22} (the dashed lines) with respect to x (dimensionless distance), within the Nikitin's model [25]. The solid lines stand for the adiabatic energy terms. The energies are in arbitrary unit, and $\Delta\varepsilon$ is the splitting between the terms at large distances. Case (a): intersecting diabatic terms. Case (b): nonintersecting diabatic terms.

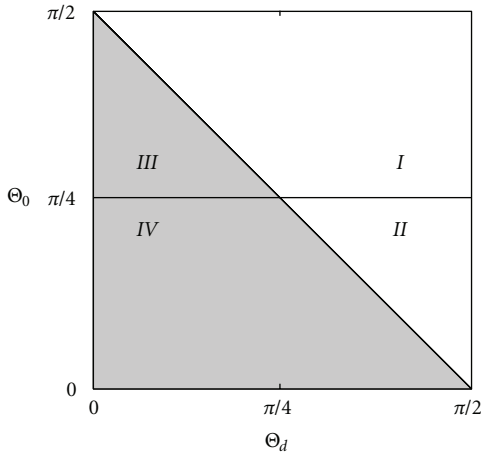

FIGURE 5: The occurrence of the adiabatic dipole transition moment roots depending on the relationship between the parameters Θ_d, Θ_0. A root exists at $\Theta_0 + \Theta_d \leq \pi/2$, that is, in the regions *III, IV*. For parameters in the regions *I, III* the diabatic potential energy curves do not cross each other contrary to the regions *II and IV*. The ordinates $\Theta_0 = 0, \pi/4$ correspond to Landau-Zener's and Demkov's models, respectively. The abscissas $\Theta_d = 0, \pi/2$ correspond to the forbidden dipole transitions, for example, [25].

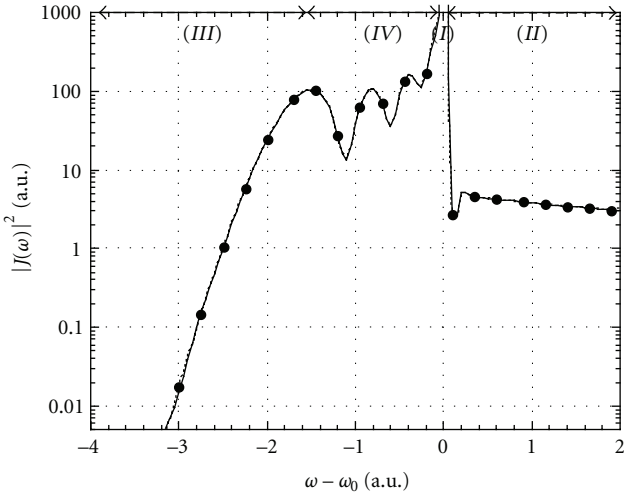

FIGURE 6: Visualization of the four regions in the line shape $|J(\omega)|^2$ of the transition $2p\pi_u \rightarrow 1s\sigma_g$ for the molecule $F^{8+} - F^{9+}$, according to (17) (dots), [29]. Results of numerical calculations for $|J(\omega)|^2$ are given by (15) and (16) for rectilinear trajectories (solid line). Parameters are $d = 2.3 \cdot 10^{-2} Z^2$, $r_{ex} = 4.2/Z, \nu = 0.035$. *I*-line core; *II*-blue wing; *III*-antistatic region; *IV*-region of quantum oscillations due to the minimum of the potential-difference.

in the transition energy produces a satellite in the spectral profile.

Region *III* of Figure 5 is completely distinctive from these two previous regions with the simultaneous existence of a

maximum of the dipole moment for the upper energy state and a root for the lower state at $\Theta_d = \text{arctg}(d_2/d_1)$, without any extremum in the potential energy (and in the transition energy) curves ($\pi/4 < \Theta_0 < \pi/2$, Figure 4(b)). Clearly *the lower state produces a dip in the profile.*

Finally, in the region *IV* there is an extremum in the two adiabatic transition energy terms at $R = R_m$ jointly with a maximum for d_I (the upper state) and a root for d_{II} (the lower state) at $R = R_d$. In general $R_m \neq R_d$, and thus *the upper state produces two satellites*, one connected with the minimum in the adiabatic transition energy curve, and another connected with the maximum in the adiabatic dipole moment. *The lower state produces a satellite* due to the minimum in the adiabatic transition energy curve *and a dip.* The spectral features are more clearly pronounced when $R_m = R_d$; this situation leads to the merging of the two satellites in one (for the upper state case) and to the merging of the dip and the satellite in some structure (for the lower state case).

4. Quasimolecular Optical Transitions Followed by Charge-Exchange

4.1. Symmetric Charge-Exchange. We start from the description of radiative transitions in symmetric quasi-molecules. The process is schematically described as follows:

$$(Ze)^* + Z \longrightarrow Z + (Ze) + \hbar\omega \tag{14}$$

and can be realized by two ways as a radiative transition between one initial quasi-molecular state and two possible final quasi-molecular states. The first way is roughly an optical transition that can be described qualitatively as a transition in an excited ion $(Ze)^*$ broadened by collisions with a charged particle Z, mainly at large interionic distances. The second way can be described as an optical transition which is followed by a jump of an electron from one charged center to another and takes place mainly at small and moderate interionic distances. It should be stressed that the probability of the reaction (14) in both ways is determined by the probabilities of the optical transitions involved. Of course the final state in a distant ion is the same for both ways, so that the correct description of the reaction (14) must take into account an interference because of the two possible reaction ways.

As it follows from the qualitative discussion, the decisive factor for the reaction (14) is the influence of "one-electron" exchange interaction. Using Ly α as an example it has been shown in [29, 35] that exchange interaction produces noticeable structures in the spectral profile of Ly α radiation. The rst indication of the structure can be obtained from the quasistatic theory [36] and the asymptotic theory of the charge exchange [37]. The interaction between ions transforms the ground ionic state into the quasi-molecular states $1s\sigma_g$ and $2p\sigma_u$, the excited $2s$ state into the quasi-molecular states $\sigma_{g,u}$, and the excited $2p$ state into the $\sigma_{g,u}$ and $\pi_{g,u}$ states. At large interionic distances the splitting of the ground states is proportional to $\exp(-Zr)$, while the splitting of the excited states is proportional to $\exp(-Zr/2)$. In addition, the splitting for π terms is opposite in sign to that for σ terms [37]. Therefore, the potential-difference curve $\Delta U_+ = U(3d\pi_g) - U(2p\sigma_u)$ experiences a maximum and the potential-difference curve $\Delta U_- = U(2p\pi_u) - U(1s\sigma_g)$ experiences a minimum, As predicted even by the quasistatic theory, these extrema lead to the formation of structures in the spectral wings of perpendicular optical transitions $3d\pi_g \to 2p\sigma_u, 2p\pi_u \to 1s\sigma_g$.

The total intensity distribution is shown to be proportional to

$$|b(\omega,t)|^2 = \frac{1}{2}\left(|J_+|^2 + |J_-|^2\right), \tag{15}$$

where $J_\pm$ are the amplitudes of the two quasi-molecular radiative transitions discussed above [29], and

$$J_\pm(\omega,t) = \int_{t_0}^{t} \langle\omega_1|V|\varphi_1\rangle \exp\left(-i\int_{t_0}^{t'}(\Delta U_\pm - \omega)dt''\right)dt' \tag{16}$$

and $\Gamma_{1,2} = 2\pi|\langle\omega_{1,2}|V|\varphi_{1,2}\rangle|^2$ are the radiative width. The reasonable approximation for $\Delta U_\pm$ by exponential functions leads to global approximation for spectral line shapes

$$\begin{aligned}\frac{J(\omega)}{\langle\omega_1|V|\varphi_1\rangle} &= j(\omega)\\ &= \frac{-i}{\alpha}(x)^{-i\Omega}\Gamma(i\Omega)D_{-i\Omega}\left(2xe^{-3i\pi/4}\right)\\ &\quad\times\exp\left(i\alpha\Omega t_0 + ix^2 + \frac{\pi\Omega}{4}\right),\end{aligned} \tag{17}$$

where $\Omega = (\Delta\omega + i(\Gamma/2))/\alpha, \Delta\omega = \omega - \Delta U(r \to \infty)$, $x = \sqrt{d/\alpha}$.

The formula (17) gives an analytical description in four different regions of the spectral profile: a Lorentzian region situated near the center $\Delta\omega \approx 0$, a blue wing with one Condon point, an antistatic region of classically forbidden transitions with no Condon point, and a region corresponding to transitions near the extrema of the potential-difference curve. Figure 6 gives the example of the Lyα profile produced in $F^{+8} - F^{+9}$ collisions.

The main conclusion of [29, 35] is that exchange interaction results in the formation of two satellites perpendicularly polarized. It is interesting to point out that the main idea of the asymptotic approach for the description of the interaction between atomic/ionic particles is to separate the effects of the long-range and the exchange parts [37]. The long-range part of the *Ze-Z* interaction produces structures that are in principle similar to structures described under the conventional Stark broadening scheme in plasmas, whereas the exchange interaction produces the features discussed above. As an example, the splitting between $3d\pi_g$ and $2p\pi_u$ terms due to exchange interaction is given by $-Z^4r^2/4\exp(-2 - Zr/2)$ according to [22]. The exchange interaction is equal to the first term of the long-range interaction $6/Zr^3$ at $r_0 \approx 16/Z$, meaning that the Stark effect dominates at $r > r_0$ and the g-u splitting can be neglected. Therefore the structures produced by the long-range part of

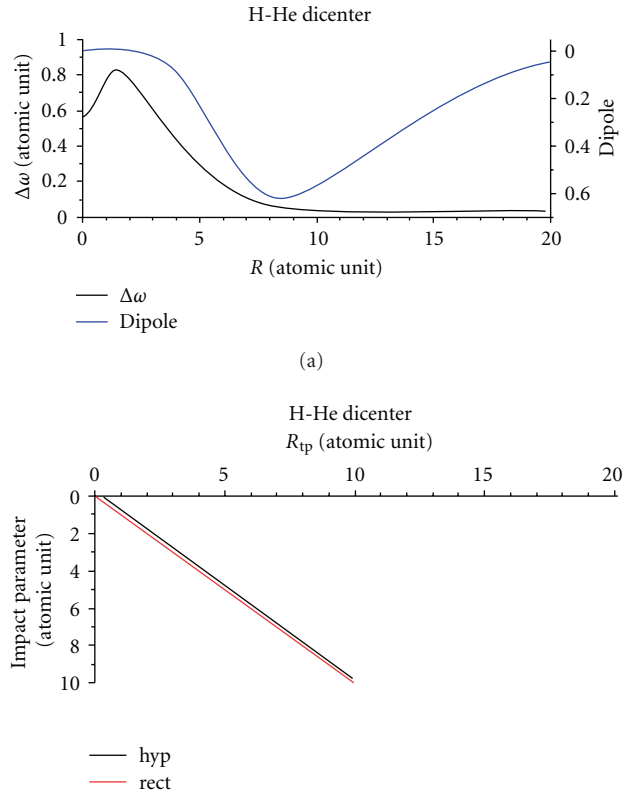

FIGURE 7: Dipole transition moment and difference potential $\Delta\omega$ for the reaction (21), (a) The dependence of the turning point position R_{tp} on the impact parameter (for collision energy 1a.u.), for rectilinear (rect), and hyperbolic (hyp) trajectories, (b).

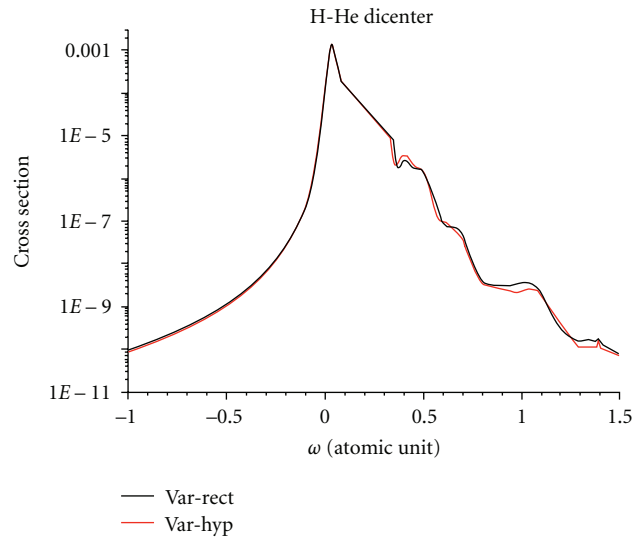

FIGURE 8: Spectral profile produced in reaction (21) for both rectilinear and hyperbolic trajectories for collision energy 1a.u., [30]. The maximum is shifted about 180Å from the center of line $H_\alpha = 1641$ Å. Some additional structures in the blue wing are due to transitions near the turning points, the extremum of the difference potential and the root of the dipole moment at $R \approx 3$.

the interaction are more sensitive to the plasma surrounding than the ones due to the exchange interaction. In connection with plasma problems, we note that the effect of charge exchange on atomic spectral line shapes in plasmas was analyzed in the frame of the asymptotic theory for exchange interaction of radiating atom with perturbing ion [38].

Equation (17) is applicable to the description of line shapes in the case of any extremum in the potential difference curves characterizing ionic or atomic quasi-molecules. Using this formula in [39] has led to a perfect agreement with experimental data on the spectral profiles produced in $Ca(4\,^1S \rightarrow 3^1D) + He$ forbidden transitions.

4.2. Nonsymmetric Charge-Exchange Involving Accidental Resonance. For nonsymmetrical quasi-molecules, and when the condition

$$\frac{Z_1}{n_{1f}} = \frac{Z_2}{n_{2f}} \quad \text{or} \quad \frac{Z_1}{n_{1i}} = \frac{Z_2}{n_{2i}} \tag{18}$$

($n_{1if,2if}$ being the principal quantum numbers of the electron in a corresponding ion) is fulfilled, then the emission of photons can be once more realized via two different optical transitions similar those described above. In ion collision physics, the condition (18) is named "swapping" [17].

The first optical transition is

$$Z_1 e(n_{1i}) + Z_2 \longrightarrow Z_1 e\left(n_{1f}\right) + Z_2 + \hbar\omega, \tag{19}$$

and the second one is an optical transition followed by nonsymmetric charge-exchange

$$Z_1 e(n_{1i}) + Z_2 \longrightarrow Z_1 + Z_2 e\left(n_{2f}\right) + \hbar\omega. \tag{20}$$

A peculiarity of the quasi-molecular optical transition (20) is that its dipole transition moment is equal to zero at large interionic distances. From this point of view, the transition must be attributed to optical forbidden transitions that are mainly concentrated near the position of the dipole moment extremum. Certainly, those two transitions (19) and (20) do not interfere with each other in contrast to the ones discussed previously, so that there will be in general only one satellite produced by the reaction (20) and shifted from the position of an optical transition in a separate ion $Z_1 e(n_{1i}) \rightarrow Z_1 e(n_{1f})$.

A typical example of the reaction (20) is the following reaction relevant to thermonuclear physics:

$$He^+(n = 3) + H^+ \longrightarrow He^{2+} + H(n = 1) + \hbar\omega, \tag{21}$$

producing a blue satellite of the $H\alpha$ transition in He^+; see Figures 7 and 8 for details.

As one can see the transitions near the position of the dipole moment extremum produce a noticeable spectral feature. The reason is clear as the position of the extremum depends neither on the impact parameter, nor on the collision energy; however the half-width of the spectral distribution on Figure 8 depends on collision energy and can be used to determine the temperature of plasma.

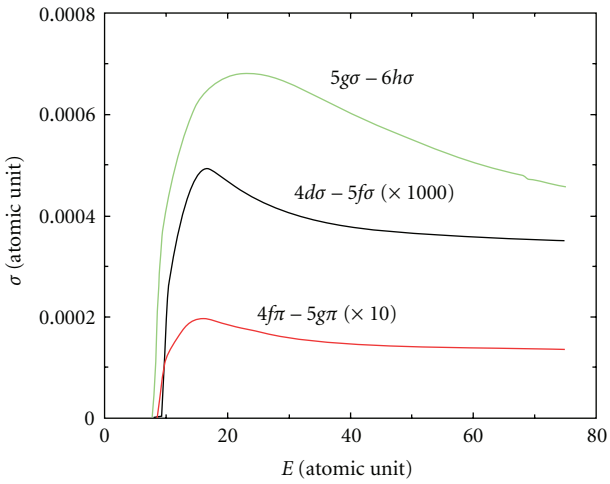

FIGURE 9: Energy evolution of charge exchange $Al^{+12}(n = 4) + C^{+6} \rightarrow Al^{+13} + C^{+5}(n = 2)$ cross sections for different channels.

4.3. Charge-Exchange in Excited States with Small Energy Defect. Let us suppose that the swapping condition (18) has been disturbed a little, for example,

$$\frac{Z_1}{n_{1i}} \geq \frac{Z_2}{n_{2i}}. \tag{22}$$

A representative example of this case is $Al^{+12}(n = 4) + C^{+6}$ collisions that have been studied in experiments on hot dense plasmas produced by laser pulses [10–14, 40]. Despite the energy splitting at large distances, two states still exist with asymptotically allowed and forbidden transitions. But the novelty, in comparison with the discussion above, is an avoided crossing between quasi-molecular terms of the two states involved. The energy separation of adiabatic terms V_{12} in the region of avoided crossing is proportional to the exchange interaction at large distances and is rather small thus making easier the diabatic scenario of collisions. In this case (14) is also true, and it predicts the occurrence of "steps" in the dependence of dipole moments on interionic distance, these "steps" occurr in the narrow regions of interionic distances about $|V_{12}|/\Delta F$, ΔF representing the difference between the forces acting on the two interacting states.

Under (22), an excited state of a separate ion $Z_1 e(n_i)$ can be depopulated by two qualitatively different ways, namely by optical transitions and by charge-exchange between two excited states. In the diabatic basis, the intersection of interacting diabatic states, one of them is populated, leads to a sudden population of the other state in the narrow region of intersection. The population of this kind can be regarded as a shake and thus produces structures in the spectral profiles similar to the ones observed in Fresnel diffraction. An example of this effect has been given in [5, 41].

As it has been discussed in Section 4.1 the interaction between excited quasi-molecular states not only produces spectral structures but also leads to nonadiabatic transitions, governed, in fact, by the same Massey parameter [3–6]. In the case under discussion, it leads to a connection between the spectral features and the cross sections of charge exchange in excited states. As an example inspired by the experiments [40], Figure 9 depicts the results of the close-coupled calculations of charge-exchange cross-sections in collisions $Al^{+12}(n = 4) + C^{+6} \rightarrow Al^{+13} + C^{+5}(n = 2)$ [42]. As one can see for this reaction, the only $5g\sigma - 6h\sigma$ channel accounts for charge exchange.

5. Conclusion

The goal of our consideration has been to clarify for ionic collisions the connection between nonelastic transitions and spectral profiles; this topic is well developed earlier in neutrals. The most distinctive collisions process involving ions is charge-exchange so that QM optical transitions have been analyzed in connection with charge-exchange process. Three typical cases have been considered, symmetric resonance charge-exchange, nonsymmetric charge-exchange involving accidental resonance, and charge-exchange in excited states with small energy defects. In all three cases, pronounced spectral structures have been exhibited. Therefore, the study of spectral profile features is intimately connected with the study of collision dynamics of ions in excited states. It is obvious that the existence of the connections between charge-exchange and spectral structures is a promising tool for plasma spectroscopy. Although the results obtained can be used directly for single collisions and low-density plasmas, they can be regarded as a reasonable starting approach and the zero-order approximation for laboratory and astrophysics hot dense plasma spectroscopy.

It has turned out that the study of the highly charged $Z_1 eZ_2$ quasi-molecule forms a foolproof and fruitful approach for analyzing different features of spectral profiles and charge-exchange processes. The main result enhanced here is that the basic characteristics of QM, energy terms and dipole moments, can be obtained in the frame of the nonrelativistic Schrödinger equation, which is justified for low and moderate Z, with any desired accuracy. Following this approach we have carefully studied the general features of the dipole moments including the roots and the extrema, the reasons, and the features of the QM asymptotically forbidden transitions. The results obtained make clear that dipole transition moments are as equally important in calculations of spectral profiles as energy terms. It must be underlined that the fundamental $Z_1 eZ_2$ problem, with its wide history [22], is of primary interest for atomic physics. So, the results discussed above can be regarded as a contribution to the study of optical characteristics of the $Z_1 eZ_2$ quasi-molecule.

Finally, we summarize the highlights in the paper. It has been demonstrated that the existence of an extremum in the difference potential energy terms is not the necessary condition for a satellite in the spectral profiles. A root of the dipole moment has transformed a maximum in the profile into a dip. A global approximation has been proposed for the first time. The approximation is valid for the central part and the wings of the profiles as well as for the region of oscillations produced by extrema in the potential energy terms differences. As this study does not include the effect of the surrounding plasma on the quasi-molecule, it must be

considered as a first step that needs to be improved, in order to be quantitatively used in plasma experiments.

It seems reasonable that the future developments of the physics of QM optical transitions will include specific calculations motivated by experiments in different kinds of plasmas as well as the study of the influence of external fields and environments. The investigations of dependencies of spectral features on external fields, temperature and density of charged particles are of the primary interest for diagnostics applications and for comparisons with experiments.

Acknowledgment

This research is supported by INTAS (Grant no. 06-1000017-9041) A. Derdariani would like also to gratefully acknowledge the hospitality of Professor E. Dalimier during his stay at Université Pierre et Marie Curie in 2009.

References

[1] E. E. Nikitin and S. Ya. Umanskii, *Theory of Slow Atomic Collisions*, vol. 30 of *Series in Chemical Physics*, Springer, Berlin, Germany, 1984.

[2] B. M. Smirnov, *Plasma Processes and Plasma Kinetics: 586 Worked Out Problems for Science and Technology*, chapter 3, Wiley-VCH, Weinheim, Germany, 2007.

[3] A. Devdariani, V. N. Ostrovskii, and Yu. N. Sebyakin, *Soviet Technical Physics Letters*, vol. 3, no. 9, p. 354, 1977.

[4] A. Devdariani, V. N. Ostrovskii, and Yu. N. Sebyakin, "Characteristics of electron and photon spectra associated with interaction between quasi-stationary states," *Soviet Physics*, vol. 49, no. 2, p. 266, 1979.

[5] A. Devdariani and Yu. N. Sebyakin, "Termperature dependence of the shape of the Landau-Zener satellite of a spectral line shape," *Optics and Spectroscopy*, vol. 48, no. 5, p. 557, 1980.

[6] A. Devdariani and Yu. N. Sebyakin, "Ionization with the participation of excited atoms," *Soviet Physics*, vol. 69, no. 7, p. 1127, 1989.

[7] M. J. O'Callaghen, A. Gallagher, and T. Holstein, "Absorption and emission of radiation in the region of an avoided level crossing," *Physical Review A*, vol. 32, no. 5, pp. 2754–2768, 1985.

[8] R. Beuc and V. Horvatic, "The investigation of the satellite rainbow in the spectra of diatomic molecules," *Journal of Physics B*, vol. 25, p. 1497, 1992.

[9] A. Gallagher, "Line shapes and radiation transfer," in *Atomic, Molecular, & Optical Physics*, G. W. F Drake, Ed., pp. 220–232, Springer, New York, NY, USA, 2006.

[10] E. Dalimier, A. Poquérusse, and P. Angelo, "Space-resolved X-ray emission from the densest part of laser plasmas: molecular satellite features and asymmetrical wings," *Physical Review E*, vol. 47, no. 3, pp. R1467–R1470, 1993.

[11] E. Oks and E. Dalimier, "Extrema in transition energies resulting not in satellites but in dips within spectral lines," *Physical Review E*, vol. 62, no. 3, pp. R3067–R3070, 2000.

[12] E. Oks and E. Dalimier, "Spectroscopic signatures of avoided crossings caused by charge exchange in plasmas," *Journal of Physics B*, vol. 33, no. 18, pp. 3795–3806, 2000.

[13] E. Dalimier, E. Oks, E. Dufour, et al., "Experimental discovery of charge-exchange-caused dips in spectral lines from laser-produced plasmas," *Physical Review E*, vol. 64, no. 6, Article ID 065401, 4 pages, 2001.

[14] E. Dalimier, E. Oks, E. Dufour, et al., "Advanced simulations of spectroscopic signatures of charge exchange in laser-produced plasmas," *European Physical Journal D*, vol. 20, no. 2, pp. 269–274, 2002.

[15] J. B. Greenwood, I. D. Williams, S. J. Smith, and A. Chutjian, "Experimental investigation of the processes determining X-ray emission intensities from charge-exchange collisions," *Physical Review A*, vol. 63, no. 6, Article ID 062707, 9 pages, 2001.

[16] F. B. Rosmej, D. Reiter, V. S. Lisitsa, et al., "Influence of charge-exchange processes on X-ray spectra in TEXTOR tokamak plasmas: experimental and theoretical investigation," *Plasma Physics and Controlled Fusion*, vol. 41, no. 2, pp. 191–214, 1999.

[17] R. Anholt, "X rays from quasimolecules," *Reviews of Modern Physics*, vol. 57, no. 4, pp. 995–1053, 1985.

[18] K. Schulze, J. Anton, T. Jacob, W.-D. Sepp, and B. Fricke, "Quasimolecular X rays in the Cl^{16+}-Ar collision system," *Physical Review A*, vol. 63, no. 2, Article ID 022503, 8 pages, 2001.

[19] P. Gauthier, S. J. Rose, P. Sauvan, et al., "Modeling the radiative properties of dense plasmas," *Physical Review E*, vol. 58, no. 1, pp. 942–950, 1998.

[20] P. Sauvan, P. Angelo, A. Calisti, E. Dalimier, and E. Minguez, "Improving the dicenter model for hot dense plasmas: molecular stark effect," *Journal of Quantitative Spectroscopy and Radiative Transfer*, vol. 71, no. 2–6, pp. 675–687, 2001.

[21] A. Devdariani, T. M. Kereselidze, I. L. Noselidze, et al., "Dipole transition-matrix elements of the one-electron heterodiatomic quasimolecules," *Physical Review A*, vol. 71, no. 2, Article ID 022512, 2005.

[22] I. V. Komarov, L. I. Ponomarev, and S. Yu. Slavyanov, *Spheroidal and Coulomb Spheroidal Functions*, Nauka, Moscow, Russia, 1976.

[23] I. I. Sobel'man, *Introduction to the Theory of Atomic Spectra*, Pergamon Press, Oxford, UK, 1972.

[24] K. Taulbjerg, J. Vaaben, and B. Fastrup, "Molecular-orbital theory of K-vacancy sharing in atomic collisions," *Physical Review A*, vol. 12, p. 2325, 1975.

[25] E. E. Nikitin and S. Ya. Umanskii, *Theory of Slow Atomic Collisions*, Springer, New York, NY, USA, 1984.

[26] A. Devdariani, in *Spectral Line Shapes*, R. Stamm and B. Talin, Eds., vol. 7, p. 235, Nova, Hauppauge, NY, USA, 1993.

[27] A. Devdariani, "Emission of quasi-molecules," *Optics and Spectroscopy*, vol. 86, no. 6, pp. 853–858, 1999.

[28] E. Bichoutskaia, A. Devdariani, K. Ohmori, O. Misaki, K. Ueda, and Y. Sato, "Spectroscopy of quasimolecular optical transitions: $Ca(4s^2{}^1S_0 \leftrightarrow 4s4p^1P, 4s3d^1D_2)$-He. The influence of radiation width," *Journal of Physics B*, vol. 34, no. 12, pp. 2301–2312, 2001.

[29] A. Devdariani, E. Dalimier, P. Sauvan, and P. Angelo, "Influence of the exchange interaction on Ly-α radiation of multicharged ions," *Physical Review A*, vol. 66, no. 5, Article ID 052703, 4 pages, 2002.

[30] A. Devdariani, T. Kereselidze, I. Noselidze, et al., "Optical transitions in one-electron quasi-molecules. The influence of the R-dependent dipole transition moments and the trajectories," in *Proceedings of the 25th International Conference on Photonic, Electronic and Atomic Collisions (ICPEAC '07)*, Freiburg, Germany, July 2007, Mo085.

[31] D. E. Remaker and J. M. Peek, "$^2H_2^+$ dipole strengths by asymptotic techniques," *Journal of Physics B: Atomic, Molucular, and Optical Physics*, vol. 5, p. 2175, 1972.

[32] D. E. Ramaker and J. M. Peek, "Dipole strengths involving the lowest twenty electronic states of H_2^+," *Atomic Data and Nuclear Data Tables*, vol. 5, no. 2, pp. 167–184, 1973.

[33] N. F. Allard, J. F. Kielkopf, G. Hébrard, and J. M. Peek, "Theoretical study of the Lyman γ line profile of atomic hydrogen perturbed by collisions with protons. Lyman γ line profile," *European Physical Journal D*, vol. 29, no. 1, pp. 7–16, 2004.

[34] A. Devdariani and E. Dalimier, "Radiative characteristics of quasimolecular state interactions," *Physical Review A*, vol. 78, Article ID 022512, 2008.

[35] A. Devdariani, *Rapport Scientifique, Laboratoire pour l'Utilisation des Lasers Intenses*, CNRS-Ecole Polytechnique-Universite Paris VI, Paris, France, 1995.

[36] N. Allard and J. Kielkopf, "The effect of neutral nonresonant collisions on atomic spectral lines," *Reviews of Modern Physics*, vol. 54, no. 4, pp. 1103–1182, 1982.

[37] B. M. Smirnov, *Asymptotic Methods in Atomic Collision Theory*, Atomizdat, Moscow, Russia, 1973.

[38] V. A. Astapenko and V. S. Lisitsa, "Effect of charge exchange on atomic spectral line shapes in plasmas: asymptotic theory," in *Spectral Line Shapes*, J. Seidel, Ed., pp. 147–149, American Institute of Physics, 2001.

[39] A. Devdariani, E. Bichoutskaia, E. Tchesnokov, et al., "Semiclassical analytical approach to the description of quasimolecular optical transitions," *Journal of Physics B*, vol. 35, no. 11, pp. 2469–2475, 2002.

[40] E. Dalimier, E. Oks, O. Renner, and R. Schott, "Experimental determination of rate coefficients of charge exchange from x-dips in laser-produced plasmas," *Journal of Physics B*, vol. 40, no. 5, pp. 909–919, 2007.

[41] A. Devdariani, V. N. Ostrovskii, I. K. Ryzhikova, and Yu. N. Sebyakin, *Vestnik LGU*, no. 22, p. 36, 1978.

[42] A. Devdariani, E. Dalimier, T. Kereselidze, I. Noselidze, F. Rebentrost, and P. Sauvan, "Characteristics of quasi-molecular state interactions," in *Proceedings of the Spectral Line Shapes: Volume 15–19th International Conference on Spectral Line Shapes*, M. A. Gigosos and M. Á. González, Eds., vol. 1058 of *AIP Conference Proceedings*, pp. 102–115, 2008.

Hindawi Publishing Corporation
International Journal of Spectroscopy
Volume 2010, Article ID 671073, 42 pages
doi:10.1155/2010/671073

Review Article

Physical Models of Plasma Microfield

A. V. Demura

Hydrogen Energy & Plasma Technology Institute, Russian Research Center "Kurchatov Institute," Kurchatov Square 1, Moscow 123182, Russia

Correspondence should be addressed to A. V. Demura, alexander.demura@hepti.kiae.ru

Received 22 April 2009; Accepted 15 July 2009

Academic Editor: Elisabeth Dalimier

The present review is devoted to the current status of microfield notion that was so successful and profitable for experimental and theoretical studies of plasma in gas discharges and thermonuclear modeling installations for many decades. The physical aspects and ideas of the main generally used microfield models are described and analyzed in detail. The review highlights the remaining vague and unclear questions in the subject.

1. Microfield Notion

1.1. The Term of Microfield. The term "microfield" was introduced to designate the electric and magnetic fields, whose action is essential on microscales intra different media [1–12]. This was done to distinguish microfield from the fields of other origin essential, for example, for macroscopic description of a medium. As a rule the average microfield over macroscopic volume is equal to zero.

Plasma on microscales is characterized by noticeable deviation from quasineutrality conditions and appearance of strong electric fields due to separation of charges [3–12]. Namely, those electric fields, essential on microscales, usually are implied under term "microfield." The magnitude of this field and its direction are subjected to fortuitous variations from point to point in space and in time.

Thus, from the very beginning, the microfield calculations represent itself challenging, complex, statistical, and kinetic problems. Being defined by the medium properties and composing it separate particles, the microfields action in its turn affects the medium characteristics and physical processes between these composing particles. Hence, the physical phenomena that somehow or other became involved and connected with microfields are very diverse. The voluminous literature [1–198], which is not confined so far by the named list and devoted to the study of various physical processes related to microfield characteristics and its affect on medium properties and composing it particles, just confirms the variety of aspects and complexity of a problem.

The characteristics of microfields could be, in principle, determined with the help of hydrogen-like atoms placed inside plasma, which experience the Stark or Zeeman effects in electric or magnetic fields correspondingly [1, 2]. Those effects lead to the line splitting into separate sublines—Stark or Zeeman components. Thereby, the simplest quantum systems could serve as some kind of microprobes for the measurements of plasma parameters on microscales and perform the role of the so-called test particles. The measured signal from these microprobes on microscales is their emission in spectral lines or other spectral characteristics, perturbed by plasma environment.

However, the emission of spectral lines practically impossible to register locally from the volume with characteristic microsizes. That is why the radiation is registered simultaneously from different microvolumes. As far as the probability of field realization with the given magnitude and direction is different in space, this is equivalent to average of observed spectral lines profiles over the field configurations with various microfield magnitudes and directions, which leads to some extent to the smoothed-broadened contour.

Basing on pointed out dependencies spectral lines of atoms, molecules and ions with simple energetic structure are used for diagnostics of plasma parameters [1, 2]. Usually the methods of measurements correspond to the

so-called passive diagnostics, when the observed quantities are the distributions of intensity and polarization in discrete spectrum, emitted by plasmas. However, as meanwhile the measurements mainly has integral character, the success of their interpretation depends on construction of adequate model notions on the interaction of radiator with plasma medium, better corresponding to observed characteristics.

The formation of spectral line contour is influenced by dynamics of interaction of radiator of the electric field with that or another frequency spectrum, and by statistics of such interactions, describing the average over probabilities of appearance of the fields in plasmas. The real problem is complicated due to the strong difference in masses of negative and positive charges in plasmas, which leads to the strongly differing characteristic time scales of corresponding electric fields alterations [3–12]. For example, in equilibrium plasmas with density in a range of 10^{17} cm^{-3} and temperature about 1 eV, the ions of the electric fields vary more slowly than the electrons ones. So, the conventional picture of spectra formation is composed by splitting the energy levels in slowly varying ion microfield into Stark sublevels, broadening of these sublevels due to transitions between them, induced by more swift electron flights, and further averaging of spectrum over ion microfield distribution in plasmas [1, 2].

Near the series limit, the lines strongly overlap, and their intensity starts to decrease due ionization in plasma microfields [1]. However, the contribution of continuum noticeably increases in this region, and that is why visually the lines, located in sequence of decreasing intensity to the series limit, look as if ascending up the hillside, describing the increasing intensity of continuum.

For emitters with more complex internal structure, the contribution of line satellites, induced by transitions from doubly excited states of ions with preceding ionization stage, becomes important. On the other hand, under plasma creation by femtosecond laser pulses ionization evolves from K—and L—atomic shells of the targets, and the ions of hole configurations are created. In this case, the observed spectrum acquires quasicontinuous character. The plasma microfield even in these more complex conditions noticeably modifies the discrete spectrum of radiation.

The plasma microfield is stipulated as by Coulomb electric fields of charged particles, as by self-oscillations of plasma, playing the decisive role in nonequilibrium conditions. These fields are subdivided by terms of "individual" and "collective" components of microfield, respectively [1, 3].

In the wide range of plasma parameters, the quasistatic approximation is efficient for the description of interactions with ion microfield. It is grounded on the notion of instantaneous static microfield distribution function [1, 2]. However, in these conditions, the broadening by some part of ions has impact character, and this is of principal significance for a family of simulation methods [13].

It would seem, from general considerations, that the solution of spectral line broadening problem in a medium could be found using only statistical, and even, moreover, thermodynamic methods. However, in truth, a phenomenon of spectral lines broadening has inseparably linked to each other dynamical and statistical aspects. For example, the processes of spectral line shape formation and population of quantum states are interrelated, and have to be considered self-consistently [108, 109]. The important factor in finding the solution is physically a correct choice of zero-order wave functions of a problem and its direction of quantization, adequately corresponding to physical observables [53].

Thus inadequacy of only statistical or only dynamical descriptions of a problem makes necessary the search of solutions based more or less on synthesis of these notions [104–109]. To a considerable extent, the necessity of such synthesis is stipulated also by actually restricted power of recent supercomputers for numerical modeling of complex multidimensional problems [14–17].

It should be noted that the whole row of phenomena exists in which microfield plays the important role but more amply its characteristics show up just in spectra of atoms and ions, immersed into plasmas. That is why in this introductory part the main attention was paid for the broadening of spectral lines.

This work presents the review of current ideas about plasma microfields, physical models, and methods for describing the quasistatic instantaneous distribution functions and temporary microfield evolution. The most ample previous reviews of this problem could be found in [1, 2, 11, 14–17] and the recently published papers [195–198].

1.2. Dipole Approximation as Basement of Microfield Formalism. So, a consideration of medium influence on test particles serves as a source of information on origin and character of interactions in various media and in its turn about the media state.

In plasmas this impact is due first of all to charged particles—plasma electrons and ions. If to expand the interaction potential of test particles with the medium into series over multipoles, assuming large remoteness of the medium (field) particles from the test ones in comparison with distances between the test particles, then the first term of expansion becomes zero due to condition of quasineutrality. (Here the case of charged plasmas, where this condition does not fulfill is not considered.)

The first not equal to zero term of this expansion just is due to the electric fields of plasma particles and proportional to the scalar product of the vector of dipole moment of a system of test particles and the summary electric field strength vector of plasma particles. This summary electric field of medium on microscales, becoming zero under average over macrovolume due to quasineutrality condition, was called microfield, as its action shows up at microscales, where the quasineutrality condition does not hold and the charge separation is essential.

Thereby, a possibility to describe the test particles interaction with environment (plasma) in terms of microfield is linked with conditions of predominance of long range components of potential over short range ones, when the distances between particles in a test system are less than the distances between particles of a medium. On the other hand, the possibility of such description depends on the

existence of dipole moment in a test system. That is why approximate representation of potential in terms of microfield corresponds to the dipole approximation.

In the case of the electric fields of collective plasma oscillations, the implementation of dipole approximation is evidently admissible, as the sizes of test systems are typically much less than the wavelength of those oscillations.

1.3. Applicability Criteria for Quasistatic Approach. Notion of quasistatic microfield is based as a rule on a simple reasoning that summary electric plasma microfield does not alter on some effective for radiation time scales [1, 2]. Within such settings, this condition turns out depending not only on microfield statistical properties but also on quantum properties of a radiator. For example, the smallness of frequency of temporary microfield changes $\vec{F}$ in comparison with the hydrogen atom dipole moment d_n (n—the principal quantum number) [1, 2] frequency precession in this field is considered as such aforementioned condition:

$$\frac{d_{nn}\, F}{\hbar} \gg \left|\frac{\dot{\vec{F}}}{F}\right|. \tag{1}$$

For the other condition of this kind, the smallness of life time of atom quantum state τ_{eff} in comparison with characteristic life time of microfield might serve or, when the characteristic frequency of atomic decay exceeds the characteristic frequency of microfield changes

$$\left|\frac{\dot{\vec{F}}}{F}\right| \ll \tau_{\text{eff}}^{-1}, \tag{2}$$

indicating that an atom could not have enough time to response to temporary microfield variation. Often both these conditions are considered in aggregate with each other.

Besides the mentioned criteria, which are called "integral," there are other types of conditions, requesting, for example, smallness of spectra variations, calculated using quasistatic microfield distribution functions $W_{st}(F)$ with small corrections $I_{st}(\Delta\omega) + \delta I(\Delta\omega)$, accounting to microfield evolution with time $W_{st}(F) + \delta\ W(F(t))$

$$\begin{aligned} I_{st}(\Delta\omega) &\gg \delta I(\Delta\omega), \\ W_{st}(F) &\gg \delta\ W(F(t)), \end{aligned} \tag{3}$$

where $\Delta\omega = \omega - \omega_0$, ω is the circular frequency of radiation, ω_0 is the unperturbed circular frequency of transition.

Per se this requires the complete solution within perturbation theory in assumption of small effective times [1, 2]. Such type of criteria dependent on circular frequency detuning from the line centers $\Delta\omega$ are used to call "spectral."

More definitive quantitative characteristics are provided by integral and spectral criteria, derived from consideration of power law potentials of binary interaction of particles with respect to problems of spectral line broadening theory (see [2]).

1.4. Quantum and Classical Theory. The necessity of quantum microfield description mainly appears in connection with degeneracy of electron plasma component [7]. That is why from practical point of view the account of "quantumness" or the extent of degeneracy of electron gas in this concrete case touches upon mainly the character of plasma ions shielding by electrons [3–12]. Prescriptively, this could be reduced to the function of plasma ions shielding by electrons, which sufficiently well describes all limiting cases (see [7–12]).

However, for example, for plasma of metals very often, the range of parameters, where the effective charge of field ions noticeably differs from the charge of bare nuclear, is of main interest. Then, the appearance of quantum exchange and correlation effects due to ion core becomes essential. Evidently, the consequent account of quantum structure of radiator also has definite contribution. The description of these effects was suggested to perform in terms of formalism of local density functional, the application of which will be discussed in Section 2.7.

Additionally, for very low temperatures, the account of quantum description might become necessary even for the translational motion.

1.5. Significance of Models. We have to comprehend that plasma is a medium with very complicated physical characteristics [3–11].

Namely, due to this complexity, it was not possible to elaborate universal rigorous and self-consistent theory of plasma microfield in spite of numerous papers published on the subject up to now [1–198]. However, each time, some tractable but limited picture is achieved only in the frames of more or less trustable assumptions, obvious physical ideas, some solvable mathematical formalism, and various approximations. All the aforementioned components together constitute that or another physical model for microfield description.

For example, plasma could be considered as continuous medium [175] or as medium, which constitutes from many separate discrete particles [18]. Indeed, the commonly used ion-sphere model for microfield description is the typical sample of continuous models (see, e.g., [11, 45, 110]). So, it is natural to divide models on continuous and discrete ones. There are also some mixed models, where continuous and discrete approaches are applied to the different subsystems (see, e.g., [9, 11, 110]). One can consider point particles [18] and particles with finite sizes as well [176].

The deviation of plasma main parameters temperature and density also provides a variety of physical conditions—weakly and strongly coupled plasmas [9, 11], nonrelativistic and relativistic plasmas [177], degenerate electron plasma component [43], and so forth.

There is also a lot of complications connected with the choice of interaction potential, that is different for weakly and strongly coupled plasmas, for movings particles and particles at rest [42, 125]. Its working form depends on effective characteristic time scales that are prescribed to the microfield action [84, 85, 135–137], which in their turn

due to Fourier transform could be determined further by detunings from the line center [83, 95].

The microfield in plasma could be due to many-body interactions with discrete charged particles, or due to plasma self-oscillations or plasma waves [18, 30, 31, 49–52]. Moreover, it is important on what space and time scales it is necessary to define microfield. The space scales could be limited by formalism as well, and introduction of additional constraints such as energy conservation law [178, 179]. Indeed, for weakly coupled plasma on the microdistances less than Debye radius, the fluctuations of energy of particles is of the order of temperature. So, there is no reason to implement energy conservation law, but on macroscales, the fluctuations are much smaller and this restriction starts to hold. Interestingly, both mentioned restrictions or usage of the formalism, which from very beginning is derived for macro scales like the formalism of dielectric functions, should lead to the different from discrete models microfield distributions. In this context, we remind the old dispute around Hunger and Larenz works [178], who obtained instead of Holtsmark distribution Gauss type distributions introducing additionally energy conservation law constraints. The illuminating analysis of these results and polemics around them is presented in the work of Kogan and Selidovkin [179], who found explicit mistakes in analytical derivations of Hunger and Larenz works.

The distribution functions of microfield conventionally are obtained in the case of the so-called thermodynamical limit for $\mathcal{N} \to \infty$ and $\mathcal{V} \to \infty$, so that $\mathcal{N}/\mathcal{V} = \text{const} = N$ ($\mathcal{N}$ is total number of particles in the system, $\mathcal{V}$ is the system volume, N is the density of particles) [14–16]. However, it is possible to introduce microfield distribution functions for the finite number of particles as well [135–137]. There are obvious contradictions between various views on microfield definitions. For example, the different notions of instantaneous static ion microfield and ion microfield, obtained as a result of thermodynamic average, appeared from the consideration of the same physical object. However, the difference between output distributions, based on the distinct initial assumptions could result only in difference of the shielding constants that had to be used in the expression of "elementary" ion microfield.

The classification of microfield models in terms of their accounting for correlations between subsystems of plasma electrons and plasma ions was presented, for example, in the work of Ortner et al. [188]. These plasma models accounting for correlations are called "Two Component Plasma" (TCP) models in distinction from "One Component Plasma" (OCP) models [9].

The microfield models are additionally subdivided on those that attempt to describe static fields and ones depending on time. Using some assumptions on microfield statistics and some other approximations, the Method of Model Microfield (MMM) [86–94], Collective Coordinates for Ion Dynamics [180], Frequency Fluctuation Model (FFM) [99, 100], and Frequency Separation Technique (FST) [181] were proposed. Also, the direct computer simulations methods were elaborated firstly for static microfield distributions like the Monte-Carlo method [27–29, 35–39, 110, 113] and after for modeling the evolution of electric microfields versus time: Computer Simulations (CS) with particles moving along prescribed type of trajectories [101–105, 142–145] and Method of Molecular Dynamics (MD) [107, 109, 135–139, 182, 183].

Thus we see that notions of microfield and models that are designed for its description are complicated and diverse, reflecting the diverse and complex plasma properties.

2. Quasistatic Distribution Functions

It is used to distinguish (although it could be done only approximately) plasma microfield additive components, having essentially different frequency and spatial characteristics. Firstly, it is possible to single out the electric fields of high and low frequency plasma collective oscillations and individual component of electric microfield, being a summary field of separate plasma particles.

Furthermore, an individual component in its turn could be divided into high frequency, induced by plasma electrons, and low frequency, induced by plasma ions, parts. Evidently, such separation should happen automatically under implementation of sufficiently adequate mathematic approaches to the complete system and specifics of that or another problem. Although such attempts were done, they did not lead to formulated goal. In fact, as was underlined in the previous subsection, the microfield theory is constructed based on model and intuitive ideas as necessary solutions for a whole row of problems could not be obtained using conventional thermodynamic methods.

The interaction of the point field ions with an emitter in dipole approximation could be represented in terms of the electric ion microfield $\vec{F}$ in assumption, that perturbing particles are situated sufficiently far from emitter, so that the radius-vector of radiating electron is much less than radius-vectors of perturbing particles with respect to the emitter nuclear. Using the condition of vector additivity of electric fields of all ions $\vec{F}_j$, we have

$$\vec{F} = \sum_{j=0}^{\infty} \vec{F}_j. \tag{4}$$

Then the statistical microfield distribution function $\vec{F}$ could be obtained from the next thermodynamic average

$$W\left(\vec{F}\right) = \left\langle \delta\left(\vec{F} - \sum_{j=0}^{\infty} \vec{F}_j\right)\right\rangle, \tag{5}$$

where symbol $\langle \cdots \rangle$ designates the average over plasma ensemble of ions. Moreover, as a rule, this average encircles passage to the limit, under which the number of particles (ions) in ensemble $\mathcal{N}_i$ and the system volume $\mathcal{V}$ are indefinitely increasing, while their ratio is kept constant and equal to the particle density $\lim_{\mathcal{N}_i \to \infty, \mathcal{V} \to \infty} \mathcal{N}_i/\mathcal{V} = \mathcal{N}_i$.

The field strength of electric microfield $\vec{F}$ and its components $\vec{F}_j$ in assumption of a point test particle is evaluated in the place of its localization, which usually is

chosen as an origin of reference frame of coordinates (in the case of test particles at rest).

The average value calculation, mentioned earlier, is a complex problem due to its many-body character, vector properties of quantities under evaluation, multicomponent system of plasma particles, correlations and interactions between them, and specific peculiarities of a test system.

It is important to comprehend what a function in the sense of performed average character would more correctly correspond to the posed problem. From the arsenal of mathematical methods of statistical physics the average over canonical or microcanonical ensembles, chaotic phases, fast subsystems, and so forth [3–12] could be recovered.

However, for obtaining such averages as a rule, the infinite time interval is needed, while the used in many physical solutions Fourier transform itself limits the effective duration of time average. For example, under Fourier transform for line profile calculation at the circular frequency detuning from the line center $\Delta\omega = \omega - \omega_0$, the effective time of profile formation is of the order $\Delta\omega^{-1}$, where ω, ω_0 are perturbed and unperturbed circular frequencies of radiation. The value $\Delta\omega^{-1}$ determines thereby the allowed characteristic scales of average over the time of stochastic variables entering expression for line contour versus the frequency detuning. As a rule, it is implicitly assumed that instantaneous distribution function of ion microfield, when the average could be performed before ions would change essentially their space configuration, is used. Here is evidently some mismatch of descriptive methods and requested from physical consideration result. However, spectra depend not only on line profiles but also on spectral lines intensities, proportional to population of excited levels. The populations in many cases are determined by the balance of thermodynamically equilibrium processes. Hence, the real situation is rather diverse. The elaborated up-to-date approaches give only approximate solutions for the aforementioned row of problems. In this paper, only those that are used more often will be enlightened.

2.1. Hotltsmark Function. Historically, the Holtsmark function [18] became the first and physically significant solution of a problem of static microfield distribution, derived for isotropic ideal gas of charged particles with the same sign of charges [1, 2, 14–21]. This function describes the probability of outcome for ions configuration for the given value of microfield module F without account of plasma ion-ion and ion-electron interactions versus the reduced dimensionless microfield value $\beta = F/F_0$, where $F_0 = 2\,\pi\,(4/15)^{2/3} eZ_i\,N_i^{2/3}$ is the normal Holtsmark field value:

$$\mathcal{H}(\beta) = \frac{2\beta}{\pi}\int_0^\infty dx\, x\, \sin(\beta\, x)\exp\left[-x^{3/2}\right]. \tag{6}$$

The important characteristic of this distribution is its asymptotic behavior at small $\beta \ll 1$ and large $\beta \gg 1$. At large β, it is proportional to $\beta^{-5/2}$ and stems to the distribution of the nearest neighbor, which corresponds to small distances between the perturbing and emitting (test) particles. At small β, this distribution is proportional to β^2, which corresponds to the many-body law of summary field formation at large distances between field particles, when the field values due to separate particles are small. Those asymptotic dependencies in fact are universal features and of more realistic microfield distributions [1, 2, 14–17]. The basic technical element for obtaining this and and other results is the Fourier-transform of δ-function, which allows to reduce the problem in the isotropic case to calculation of characteristic function $A(k)$:

$$W(\beta) = \frac{2\beta}{\pi}\int_0^\infty dk\, k\, \sin(k\beta)\; A(k),$$
$$\int_0^\infty d\beta\, W(\beta) = 1. \tag{7}$$

This expression is universal and based only on isotropy of distribution function, does not depend on density, which enters only in the definition of the normal field. At the same time, the functional dependence of $\ln A(k)$ is determined by the Coulomb law of electric field. The graph of universal Holtsmark distribution function will be given in what follows in comparison with more sophisticated distributions of Ecker-Müller [22, 23], and Hooper [27–29].

2.2. Ecker-Müller Distribution. The first step to account of plasma specifics became the Ecker and Ecker-Müller microfield distribution functions [22, 23]. In its derivation, it is assumed that the potential of plasma field ion is shielded by plasma electrons and obeys Debye law. The interaction between field ions is neglected. So, the difference from the Holtsmark distribution is only using the expression for electric field for plasma ions, shielded by plasma electrons according to Debye:

$$\vec{E}(\vec{r}) = -Z_p e\left(1 + \frac{r}{r_{\mathrm{De}}}\right)\exp\left(-\frac{r}{r_{\mathrm{De}}}\right)\frac{\vec{r}}{r^3}, \tag{8}$$

where $Z_p e$-is the charge of field ion, e is the electron charge, r_d is the electron Debye radius [3–11]. In various publications, the total Debye radius is substituted in this expression, simultaneously including the shielding by electrons and ions [14–17]. However, from physical point of view, it is not always justified.

The Ecker-Müller distribution became a function of two variables—the reduced electric field value β and dimesionless parameter δ, proportional to the number of field ions in the Debye sphere:

$$\delta = \frac{4\pi}{3}\,\mathcal{N}_i r_{\mathrm{De}}^3. \tag{9}$$

However, later, the labeling of distribution functions with the parameter

$$a = \delta^{1/3} = \frac{R_0}{r_{\mathrm{De}}} \tag{10}$$

became conventional, where R_0 is the mean distance between field ions.

For weakly coupled plasmas, only for which there is a sense to apply this distribution, the parameter value a is limited from above by unity. At $a = 0$, the Ecker-Müller distribution coincides with the Holtsmark distribution, and its maximum is shifted to the lesser reduced values of microfield while parameter a is increasing. As due to quasineutrality condition, the ion density could be expressed via electron density, and from the aforementioned, it follows that the Ecker-Müller distribution is also a function of electron temperature, of course, via dependence on parameter δ or a.

The comparison of Ecker-Müller distribution and Holtsmark function versus parameter δ and values of electric reduced field values $\mathcal{E}/\mathcal{E}_0$ is presented in Figure 1.

2.3. Baranger-Mozer Cluster Expansion. The Baranger-Mozer papers [24, 25] appeared approximately 2 years after the works of Ecker and Müller and were significant advance as according to the physical formulation as to the development of adequate mathematical formalism.

The notions of high-frequency electronic and low-frequency ionic components of plasma microfield, ion-ion correlations were introduced in [24, 25]. It was pointed out on inadmissibility of usage the total Debye radius in expression for ion microfield and was demonstrated the different character of distributions in the neutral and charged points.

The adequate formalism in [24, 25] is based on the cluster expansion methods, developed firstly for virial coefficients [7–12] and giving the possibility to represent $\ln[A(k)]$ in power series over density ordered versus the extent of correlations weakening. Let us consider in more detail the instructive derivation of these results. The summary field of ions $\vec{F}$ satisfies the vector additivity condition, that is,

$$\vec{F} = \vec{F}_1 + \vec{F}_2 + \vec{F}_3 \ + \cdots + \ \vec{F}_{\mathcal{N}}. \tag{11}$$

The distribution function of summary microfield $W(\vec{F})$ could be transformed to the form

$$\begin{aligned} W\left(\vec{k}\right) &= \frac{1}{(2\pi)^3} \int d^3k \, \exp\left(-\, i\vec{k}\vec{F}\right) A\left(\vec{k}\right), \\ A\left(\vec{k}\right) &= \int \cdots \int d^3x_1 \cdots d^3x_{\mathcal{N}} \\ &\quad \cdot \exp\left[i\,\vec{k}\left(\vec{F}_1 + \vec{F}_2 \ + \cdots + \vec{F}_{\mathcal{N}}\right)\right] \\ &\quad \cdot P(\vec{x}_1, \vec{x}_2, \ldots, \vec{x}_{\mathcal{N}}), \end{aligned} \tag{12}$$

where $P(\vec{x}_1, \vec{x}_2, \ldots, \vec{x}_{\mathcal{N}})$ designates the probability of given configuration from $\mathcal{N}$ particles.

Furher on, the standard procedure, which is performing the identical operations with each of multiplicands $\exp(i\vec{k}\vec{F}_j)$ in the integrand, is applied:

$$\begin{aligned} \exp\left(i\vec{k}\vec{F}_j\right) &= 1 + \varphi_j, \\ \prod_{j=1}^{\mathcal{N}} \left(1 + \varphi_j\right) &= 1 \ + \sum_i \varphi_i + \sum_{i,i'} \varphi_i \, \varphi_{i'} + . \end{aligned} \tag{13}$$

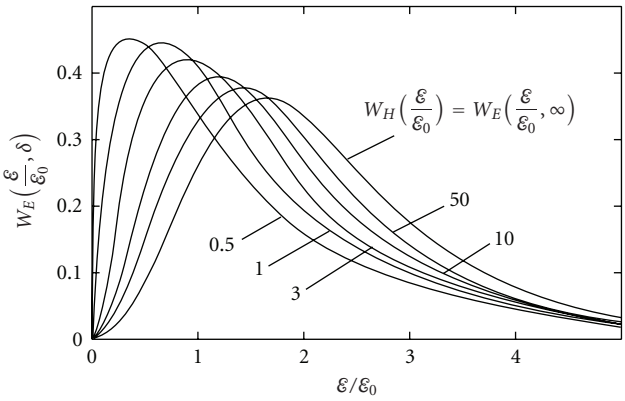

Figure 1: Comparison of Ecker-Müller microfield distribution $W(\mathcal{E}/\mathcal{E}_0)$ and Holtsmark function $W_H(\mathcal{E}/\mathcal{E}_0)$ versus parameter δ and values of reduced field $\mathcal{E}/\mathcal{E}_0$ according to [22, 23].

Then integrating over free variables, the characteristic function could be represented as a sum

$$A\left(\vec{k}\right) = \sum_{\mathcal{M}} A_{\mathcal{M}}\left(\vec{k}\right), \tag{14}$$

$$\begin{aligned} A_{\mathcal{M}} &= \int \cdots \int d^3x_i \cdots d^3x_s \ \cdot \ \varphi_i \cdots \varphi_s \\ &\quad \cdot P_{\mathcal{M}}(\vec{x}_i, \ldots, \vec{x}_s), \end{aligned} \tag{15}$$

where the summation is extended on all combinations of $\mathcal{M}$ particles from $\mathcal{N}$.

Then the idea about strong decreasing of correlations versus increasing their order is explicitly implemented:

$$\begin{aligned} &\mathcal{V}^{\mathcal{M}} \ P_{\mathcal{M}}(\vec{x}_i, \ldots, \vec{x}_s) \\ &\quad = \prod_i g_1(\vec{x}_i) + \sum_2 g_2\left(\vec{x}_j, \vec{x}_k\right) \prod_i g_1(\vec{x}_i) \\ &\qquad + \sum_{22} g_2\left(\vec{x}_j, \vec{x}_k\right) \cdot g_2(\vec{x}_l, \vec{x}_m) \prod_i g_1(\vec{x}_i) \\ &\qquad + \sum_{222} \cdots + \cdots + \sum_3 g_s\left(\vec{x}_j, \vec{x}_k, \vec{x}_l\right) \\ &\qquad \cdot \prod_i g_1(\vec{x}_i) + \sum_{33} g_3\left(\vec{x}_j, \vec{x}_k, \vec{x}_l\right) \\ &\qquad \cdot g_3\left(\vec{x}_m, \vec{x}_n, \vec{x}_p\right) \prod_i g_1(\vec{x}_i) + \sum_{333} \cdots + \cdots \\ &\qquad + \sum_{32} g_3\left(\vec{x}_j, \vec{x}_k, \vec{x}_l\right) \cdot \ g_2(\vec{x}_m, \vec{x}_n) \prod_i g_1(\vec{x}_i) \\ &\qquad + \sum_4 \cdots + \cdots , \end{aligned} \tag{16}$$

where $\mathcal{V}$ is the system volume, and the single particle probability function is

$$P_1(\vec{x}) = \frac{1}{\mathcal{V}} \, g_1(\vec{x}). \tag{17}$$

The sum $\sum_2$ designates the summation over all pairs of particles from $\mathcal{M}$ particles, the sum $\sum_{22}$ over two different pairs of particles from $\mathcal{M}$ particles. In the sum $\sum_{32}$, the summation goes over all possible combinations of different triplets and pairs of particles from $\mathcal{M}$ particles. In each term of this series, those particles, included in the product from $\mathcal{M}$ particles, do not constitute triplets, pairs, and so forth. The g functions due to the extraction of factor $\mathcal{V}^{-\mathcal{M}}$ are defined so that do not depend on volume $\mathcal{V}$ for large values of $\mathcal{V}$. Generally speaking, the cluster diagram could be confronted to each term of this expansion [7].

In the limit of large $\mathcal{N} \to \infty$ and large $\mathcal{V} \to \infty$, but for constant concentration $N = \mathcal{N}/\mathcal{V} = \text{const}$, $A(\vec{k})$ could be represented as

$$A\left(\vec{k}\right) = G_1\left(\vec{k}\right) G_2\left(\vec{k}\right) G_3\left(\vec{k}\right) \ldots, \tag{18}$$

$$\begin{aligned} G_P\left(\vec{k}\right) = {} & 1 + \mathcal{V}^{-P} \sum_P \int \varphi_i \cdots \varphi_s g_P(\vec{x}_i, \ldots, \vec{x}_s) \\ & \cdot d^3x_i \cdots d^3x_s \\ & + \mathcal{V}^{-2P} \sum_{PP} \int \varphi_i \cdots \varphi_v g_P(\vec{x}_i, \ldots, \vec{x}_s) \\ & \cdot g_P(\vec{x}_t, \ldots, \vec{x}_v)\ d^3x_i \cdots d^3x_v \\ & + \sum_{PPP} \cdots + \cdots . \end{aligned} \tag{19}$$

Here, the single sum covers all possible combinations with P particles from $\mathcal{N}$ ones, the double sum over all possible combinations of different two clusters with P particles from $\mathcal{N}$ ones, while all particles in a cluster are being different, and so forth.

The difference of expression (18) from (14) is that there are no the same particles in each term from (14), represented as the expansion according to (15)–(17), whereas according to definition (18), one particle, entering in G_P, could coincide with one of particles, that compose G_Q. That is why (18) contains a part of additional terms which do not appear in (14). However, as stated in [24, 25], the number of coinciding terms in both expansions, under the tendency of the total number of particles to infinity, is $\mathcal{N}$ times larger the number of additional terms, whose contribution to the total sum thus occurs negligible [24, 25].

If to take into account that under $\mathcal{N} \to \infty$ all terms in each sum become equal, then calculating the number of those terms, one could obtain the following closed expression for $G_P(\vec{k})$

$$\begin{aligned} G_P\left(\vec{k}\right) = {} & \exp\left(\frac{N^p}{p!}\, h_p\left(\vec{k}\right) \right), \\ h_p\left(\vec{k}\right) = {} & \int \int \cdots \int \varphi_1\ \varphi_2 \cdots \varphi_p \\ & \cdot g_p\left(\vec{x}_1, \vec{x}_2, \ldots, \vec{x}_p\right)\ d^3x_1\ d^3x_2 \cdots d^3x_p, \end{aligned} \tag{20}$$

and hence the expression for $A(\vec{k})$ takes the form

$$A\left(\vec{k}\right) = \exp\left[\sum_{P=1}^{\infty} \frac{N^p}{p!}\, h_p\left(\vec{k}\right) \right]. \tag{21}$$

In contrast to the virial expansion, the convergence of integrals $h_p(\vec{k})$ and its sum are more rapid due to the appearance of powers of additional factors $\varphi_j(\vec{k})$ in the integrands for terms of cluster expansion series, which drastically narrows the range of effective values of variables, providing the main contribution to integrals.

As the Bogolubov-Born-Green-Kirkwood-Yvon chain [7–12], the cluster expansion is based on two very significant semi-intuitive notions: (i) about monotonous decreasing of correlation functions versus increase of the correlation order; (ii) about a sufficiently rapid decrease of correlation functions versus increase of the distance between particles.

For the low-frequency distribution of ion microfield, the electric field produced by single-field ion at the origin of reference frame was taken in the form of Coulomb electric field statically shielded by plasma electrons according to Debye as was already mentioned in the previous paragraph. The Debye approximation was implemented in expressions for pair correlation functions, and calculations were limited by the pair correlations in neutral point and the triple correlations in charged point. In the case of the electric field distribution in charged point, the triple correlation function was disentangled with the help of the Kirkwood superposition approximation [7–12]. Thereby, only the two first terms of cluster expansion of $\ln[A(k)]$ were taken into account, where the second term describes ion-ion correlations. For the pair correlations function of field ions, the linearized Debye approximation was used for description of ion-ion correlations, which is the first not equal to zero term of expansion [3–12].

The high-frequency function, describing the Coulomb field of plasma electrons, practically was not used later, but the low frequency component of plasma microfield had got applications in spectroscopy.

Formally, this distribution due to ion-ion correlation additionally to the dependencies on β and T_e also is a function of ion temperature T_i through dependence on additional dimensionless parameter $R_c/R_0 = e^2 Z_p^2/T_i R_0$, which practically coincides with the definition of ionic coupling parameter Γ_i, where R_c is the ionic Coulomb radius. It should be pointed out that in the second of cited works [24, 25], the linearized Debye pair correlation function, used for description of ion-ion correlations, contains as a shielding length the total Debye radius, where the ion-ion shielding also is accounted for [24, 25].

Regretfully, in the tabulation of ion microfield distribution functions in [24, 25] the numerical mistakes were detected, which led to undeserved disavowal of developed approach. Later, Pfennig and Trefftz found and removed these inaccuracies [26] together with distrust to approach in general.

The important advantage of Baranger-Mozer formalism is the possibility of its generalization for arbitrary plasma

ionization composition, that is presented, particularly, in 2.9.1. The explicit results of 2.9.1. allow to obtain more ample apprehension on practical receipts of Baranger-Mozer approach implementations.

The graphical behavior of Baranger-Mozer distribution functions after removal of numerical inaccuracies coincides with the Hooper distributions, obtained within the different model and represented in the following subsection.

The main progress of these two works is distinguishing the high-frequency electric microfiled component, whose time variation is governed by the motion of electrons, and the low-frequency electric microfiled component, whose characteristic time scale is determined by ion motion. At the same time, it is assumed that the average of high-frequency component on the ion microfield time scale contributes to the summary low-frequency microfield component via the Debye electronic shielding of ion electric field due to the electron clouds surrounding ion charges [24, 25]. Having in mind the problem of the Stark broadening of spectral lines, the authors aimed to obtain the distribution of, namely, "instant" microfield and not the average "thermodynamic" microfield. It should be underlined, thus these declarations although quite sound and reasonable from physical sense contradict with the available formalism, which is, of course, thermodynamic in its origin [24, 25].

As the properties of correlation functions with the order larger than 2 are studied still insufficiently up to now, only the two first terms of expansion were considered in [24, 25]: the first one is being linear dependent on density and the second one is being proportional to the density squared. Thus, the first term describes certain type of independent quasiparticles, characterized by some interaction potential with the test particle, while the second term is responsible for pairwise or reduced triple correlations between field particles.

2.4. Hooper Model. The Hooper model implements Bohm and Pines "collective coordinates method" (CCM) [30, 31]. This method devoted to an attempt to separate formally Hamiltonian of the system of Coulomb particles into two Hamiltonians, characterizing almost independent subsystems one of which represents itself the plasma collective characteristic oscillations, and the other one represents the subsystem of independent quasiparticles "dressed" by the screening due to separated collective degrees of freedom [30, 31]. It was shown [30, 31] that under specific assumptions, this separation is possible to accomplish by applying the specifically defined sequence of canonical transformations of variables. These results had great impact on the further development of ideas of plasma microfield and were used later as a basis in order to determine how to separate the collective microfield component due to the plasma characteristic oscillations from many-body but "individual" microfield component due to particles or quasiparticles [48–51]. Firstly for constructing the static microfield distributions, this method was proposed by Broyles [32, 33]. The Broyles papers [32, 33] contain deep and very interesting original physical analysis of microfield problem, as well as several innovative suggestions for development of appropriate mathematical formalism.

Meanwhile, in the same period of time, the Monte Carlo (MC) procedure was formulated and published providing a powerful tool for consideration of thermodynamically equilibrium conditions and calculations of correlation functions and various static microfield distributions [110] (see [35–39, 111–113]. The overall situation at that time with the Baranger-Mozer results was not clear, and the progress in Monte Carlo and ideas of Broyles inspired Hooper to reconsider the derivation of static microfield distribution functions in some different original way [27–29]. Hooper adopted the ideas of Baranger-Mozer on the separation of high- (electron) and low-frequency (ion) microfield components, but he introduced the separation of the interaction potential into the so-called central (corresponding to the interaction with the test particle) and noncentral (corresponding to the interactions between field particles) parts [27–29]. He also formally included the scalar product of vectorial Fourier variable on the vector of elementary electric field strength of the single particle into the central part of the interaction potential. After this, Hooper constructed the analog of the two term Baranger-Mozer cluster expansion but for complex central potential, which had certain impact on the definition and determination of the correlations functions, for example. It was supposed that the screening of the ion field in the central part of potential is determined by the electronic Debye radius while the screening length for the noncentral part also is described by Debye potential but with a screening length equal to the electronic Debye radius multiplied by fitting parameter "α" to be determined later. Using the Bohm and Pines method of collective variables as a mathematical trick according to the Broyles ideas, Hooper was able to derive the formulae for the microfield distribution function that as in the case of Baranger-Mozer is expressed through the finite number of subsidiary integrals and functions [27–29]. Performing calculations along with this derivation and comparing their results with Monte Carlo method for the same values of parameters, Hooper found the rather wide ranges for the "α" parameter variation, in which the results of calculations with the prescribed accuracy practically do not alter and coincide with Monte Carlo results for the same set of plasma parameters and assumptions concerning the interaction potential. The examples presented in [27–29] showed that for the low-frequency ionic microfield component, α could change from 1.3 to 1.8 at $a = 0.8$, and from 1.8 to 4.0 at $a = 0.2$. Hence, this strangely means that in some range of fitting parameter variation, the results in question do not depend on its values. When his article was altogether in print [27–29], Hooper became aware of the article of Pfennig and Trefftz [26], and after comparison he found that the results of his calculations do not differ from the improved for digital mistake results of Baranger-Mozer [24, 25]. Thus, it was rather dramatic point because no words the Hooper's method of derivation was much more complicated and that is why, probably, lesser convincing than the Baranger-Mozer one. However, tables of microfield distributions presented in Hooper's works became widely used in practical calculations in plasma spectroscopy and thus frequently cited, although their values

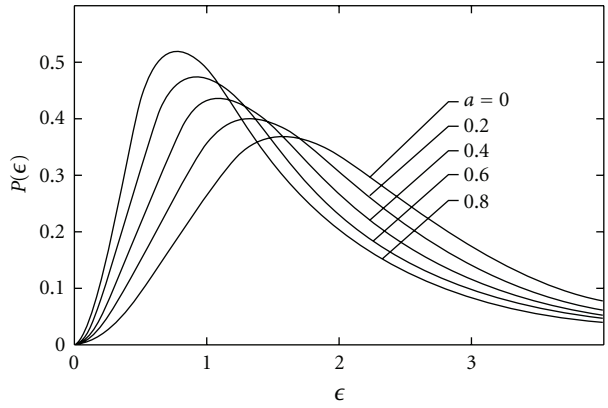

Figure 2: Microfield distribution function $P(\epsilon)$ in neutral point for several values of a from [27–29] (designations $\epsilon \equiv \beta$, $W(\beta) \equiv P(\epsilon)$ are the same as in original Hooper paper [27–29]).

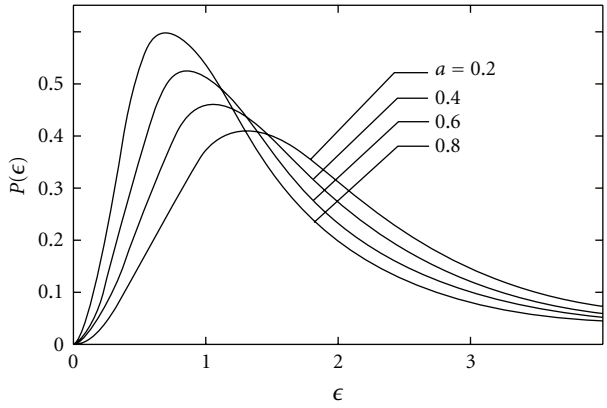

Figure 3: Microfield distribution function $P(\epsilon)$ in charged point for several a values according to [27–29] (the designations are the same as in Figure 1).

practically coincide with the values prescribed by Baranger-Mozer approach!

Alas, the derivation of Hooper results is substantially unclear [27–29] mostly due to the very complicated formalism used in [27–29], although initial settings do not differ from Baranger-Moser ones. Hooper also stated that he used nonlinear form of Debye-Hückel correlation function. However, in this case the dependence of the second term of cluster expansion starts to be more complicated and could not be reduced only to the second power of density. Regrettably, the noticeable difference of the effective shielding length from the Debye value did not get any physical treatment in [27–29] and posterior works, exploiting these initial Hooper ideas.

In Hooper works, there are no details on Monte-Carlo method used in the model. The Monte-Carlo method in its essentials corresponds to the infinite interval of time average and thus includes the total ion-ion screening, which is inadmissable in the case of its implementation for the description of quasistatic ion broadening of spectral lines in plasmas. So, now it is well known that the results of Hooper approach do not differ from corrected Baranger-Mozer results [24, 25]. At the same time Hooper approach is more laborious and could not get unequivocal interpretation. The later Hooper works with coauthors showed that the developed formalism does not have simple extension on the case of arbitrary plasma ionization composition, and even the case of binary composition needs tremendous computing efforts [34]. The Hooper distributions also are limited by values of parameter $a \leq 1$.

In Figure 2, one can see microfield distribution found by Hooper for several values of a in the neutral point, and in Figure 3 in the charged point. Both distributions are calculated for the singly charged field ions and singly charged test ion. The designations in the figures are as in the original Hooper papers. The distribution for $a = 0$ in neutral point coincides with the Holtsmark distribution. The other distributions coincide with the Baranger-Mozer ones for the same conditions as mentioned earlier.

The Hooper formalism for construction of distribution functions, based on using in mathematical calculations the collective coordinates method and cluster expansion, could not be generalized directly on quantum case or plasmas with complex ionization composition. In fact, to our knowledge, his results and formalism were never reproduced independently from the author [27–29]. However, the distribution functions presented in [27–29] and other papers are very trusted by professional community and popular in doing practical calculations.

2.5. Monte-Carlo Method. The calculation of microfield distribution functions by Monte-Carlo method (MC) is based on computer statistical sampling of probability of fall-out of various spatial configurations of field particles [35–39].

Firstly, the systematic description of Monte-Carlo method was published in [110] (see also [111–113]) and formally is not limited by only weakly coupled plasmas.

Until recently, the majority of results for microfield distribution functions for strongly coupled plasmas were obtained namely by this method [39]. The notion of strongly coupled plasmas encircles also conditions, when electronic $\Gamma_e = e^2 N_e^{1/3}/T_e$ and ionic plasma parameters $\Gamma_i = Z_p^2 e^2 N_i^{1/3}/T_i$ of coupling exceed unity not at the same time.

In the main part of MC studies up to date, the Debye form is chosen for the initial ionic potential with the effective screening length taking into account the degeneracy of electronic component. The size of the cell L is determined by the density of modeled conditions, namely, by the number of particles in MC simulations $\mathcal{N}$ plus the test particle, and connected with the ion density N_i by the relation

$$N_i = \frac{(\mathcal{N}+1)}{L^3}. \tag{22}$$

For including the influence of remote particles, the cell is reproduced by its "self-images" with step equal to L, and the total sum of potentials is evaluated by the Evald method [114, 115]. The important advantage of MC is that it easily matches any boundary conditions.

During simulations, the field ion and its location inside the cell are chosen in a random manner. If, during modeling, the ion occurs outside the cell, then it is substituted by its

image. Under the usage of powerful computers like Cray, the first 10^4 configurations were discarded in order to avoid dependence on initial conditions.

For searching equilibrium solution, the Metropolis algorithm is used [105]: the difference of energy ΔW between two consequent configurations is calculated, and if this difference is negative, then the configuration is included with the weight factor equal to 1, and if it is positive then with the weight factor equal to $\exp[-\Delta W/T]$. This allows to avoid the system trapping in local random minima. Evidently, during approaching the equilibrium, $\Delta W \to 0$. All equilibrium values of microfield are calculated after reaching the equilibrium. For example, in the widely used by experts results of MC modeling [35–39], the number of particles in the cell was 700–800, while the number of configurations after reaching the equilibrium 10^7. It should be noted that unlike the initial version of method [110], the later results [35–39] are obtained after an average of total potential over the angles of radius vector of test particle, which accelerates the convergence and secure the fulfilment of conditions of isotropy.

In a recent paper [39], the rather simple approximate functions of reduced microfield and coupling parameters for various regions of plasma parameters were proposed during fitting procedure to results of MC calculations of plasma microfield distributions.

In regions of very small and very large reduced microfield values, β MC has very large fluctuations and could not provide prescribed accuracy. For description of distribution functions in this regions, the matching with known asymptotic results is applied [21].

2.6. Adjustable Parameter Exponential Approximation. The Hooper's ideas gave rise to another approach in the theory of microfield distribution that is called Adjustable Parameter Exponential Approximation (APEX) developed in series of papers by Iglesias et al. (for current version, see [43, 184–189]). This method was aimed to describe first of all the microfield distribution at highly charged test ions in strongly coupled plasmas, where other theoretical approaches as Baranger-Mozer one fail, while MC at that time was considered as inconvenient and expensive for large-scale calculations together with magneto-hydrodynamic and radiation transfer codes in the laser inertial confinement fusion (LICF) studies [40–42]. Hence, the main motivation for APEX derivation [40–44] was an attempt to give alternative with respect to MC description of microfield distributions at test ions in strongly coupled plasmas. However, APEX from the beginning was formulated as *ad hoc* approach.

APEX also singles out the high frequency-electron and low frequency-ion components of plasma microfield. The constructions of microfield distributions for those components are rather different. The APEX model for high-frequency component could be considered in our classification as a mixed one, because it uses the notion of point separate electrons and the notion of uniform continuous positive background due to ions. In this APEX derivation, the results of the so-called one component plasma model (OCP) were applied [7–12]. Here, the narration mostly concerns the APEX results for ionic low-frequency part [42–44].

The key point in the APEX construction is the assumption of the Yukawa-type effective interaction potential between ions with the screening length, which is proportional to the adjustable parameter "α" to be determined later. Also, APEX utilizes the exact relation that have to be fulfilled at the test particle with charge equal to Z_0 [43]. At the same time if to remember that in the strongly coupled plasma the Debye radius as a rule is less than the mean interparticle distance, the validity and applicability of the Debye potential start to be doubtful for these conditions.

According to the APEX ideology, the introduction of the APEX effective field should account for high-order correlations and thus should make it possible to consider effectively noninteracting quasiparticles [43]. Thus, the initial APEX starting formulation and idea was using transformations of cluster expansion for $\ln A(k)$, like used by Hooper [27–29], to obtain single-term representation of cluster series with the help of more accurate methods for constructing the correlation functions than those provided by Debye approximation [7–12].

For transformation of cluster series to one term it was proposed to substitute in $\ln A(k)$ not a real, but some effective electric field and corresponding distribution of quasiparticles, equating the products of local probability density on the value of local field, namely:

$$\begin{aligned} eC_\sigma Z_\sigma G_\sigma(x) f_\sigma(x) &= eC_\sigma Z_\sigma g_\sigma(x) f(x), \\ G_\sigma(x) &= g_\sigma(x) \frac{f(x)}{f_\sigma(x)}, \\ f_\sigma(x) &= \frac{\exp[-\alpha_\sigma\, x]}{x^2}\,(1+\alpha_\sigma x), \\ f(x) &= \frac{\exp[-a\, x]}{x^2}(1+ax), \end{aligned} \tag{23}$$

where $a = R_0/R_{D_e}$; σ designates the field ions species; $C_\sigma = N_\sigma/N$, Z_σ are partial concentration and the charge of field ions species σ correspondingly; $g_\sigma(x)$ is the correlation function of the field and test ions; $f_\sigma(x)$ is the APEX effective field, depending on fitting parameter α_σ; $G_\sigma(x)$ is the effective distribution function of the field particles density with the charge Z_σ around the test ion with the charge Z_0; $f(x)$ is the reduced initial, screened by electrons according to Debye, this "so-called" elementary electric field is the adopted dependence for the electric field of single plasma ion.

Thus, the Hooper ideas of implementation of additional fitting parameter under optimization of distribution functions got in APEX alike, but another realization.

The set of fitting parameter $\{\alpha_\sigma\}$ according to [42] has to be found from the exact relation for mean square of microfield at test ion

$$\begin{aligned} \langle E^2 \rangle &= 4\pi NT \sum_\sigma \frac{C_\sigma\, Z_\sigma}{Z_0}\, \psi_\sigma(a), \\ \psi_\sigma(a) &= a^2 \int_0^\infty dx\; x g_\sigma(x) \exp[-ax], \end{aligned} \tag{24}$$

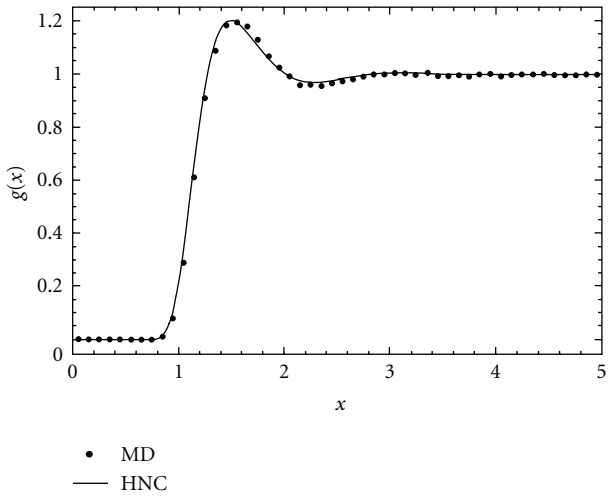

Figure 4: Comparison of pairwise radial distribution functions (RDF) for $Z_0 = Z_s = 25$, $T_e = 50$ eV, plasma coupling parameter $\Gamma = 50$ and $N_e = 10^{24}$ cm^{-3} calculated by Molecular Dynamics and in HCN approximation in [43].

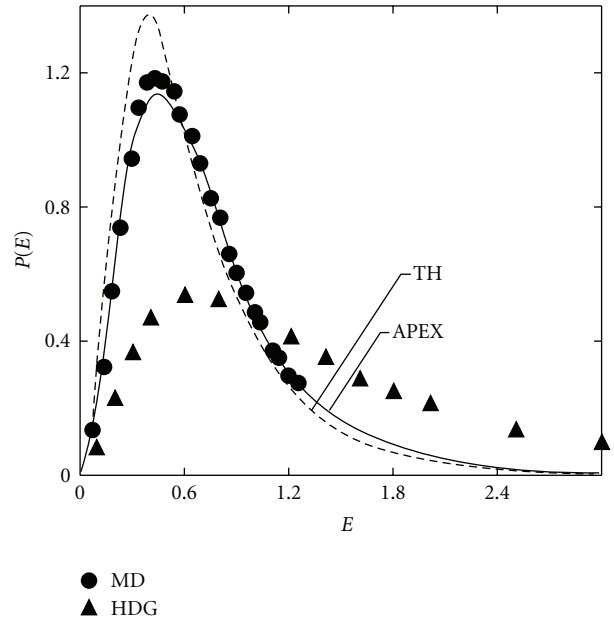

Figure 5: Microfield distribution function $P(E)$ in charged point $Z_0 = 9$ in mixture of field ions with charges $Z_1 = 9$ and $Z_2 = 1$, with equal partial concentrations, ($\Gamma_e = 0.21$) according to [42]: MC designates Monte-Carlo results, TH are results from [34], HDG are the results of [72, 73] (designations $E \equiv \beta$, $W(\beta) \equiv P(E)$ are the same as in the original paper [42]).

where Z_0 is the test ion charge.

The left-hand side of this equation in APEX takes the form [42]

$$\sum_{\sigma} Z_{\sigma}^2 \, C_{\sigma} \int_0^{\infty} dx \; x^2 g_{\sigma}(x) f_{\sigma}(x) f(x) = \frac{1}{Z_0 \; \Gamma_i} \sum_{\sigma} Z_{\sigma} C_{\sigma} \psi_{\sigma}(a). \tag{25}$$

It is assumed in [42] that the solution could be found for each species separately, which gives the set of equations for all σ:

$$Z_{\sigma}^2 \int_0^{\infty} dx \; x^2 g_{\sigma}(x) f_{\sigma}(x) f(x) = \frac{Z_{\sigma}}{Z_0 \; \Gamma_i} \; \psi_{\sigma}(a). \tag{26}$$

The correlation functions could not be determined within APEX. To close APEX scheme, the correlation functions are calculated separately within the hypernetted chain approximation (HCN) [7–12], when the so-called "bridge function" is put to zero [43]. The HCN correlation functions are considered as very precise and remarkably differ from Debye ones for large plasma coupling parameters and reproduce rather well MC and MD correlation functions [7–12, 40–43]. The illustration of correlation function behavior for strongly coupled plasma is shown in Figure 4 from [43]. Utilizing HCN correlation functions is one of the APEX significant advantages that gives possibility to describe microfield distributions in strongly coupled plasmas (SCP) [43]. At the same time as could be judged by laconic APEX papers, the starting potential in HCN is again Debye potential [42], which could be invalid for very large plasma coupling parameters.

The APEX results very well reproduce the MC simulations, considered by the APEX authors as more time consuming than APEX. However, recently MC programs were substantially improved and could compete with APEX speed of computations [37–39]. As shown in APEX publications, the value of fitting parameter α^{-1} can exceed unity several times [68, 69]. In Figure 5, the example of APEX distribution in the mixture of field ions with equal concentrations and its comparison with the results of other authors is presented [43]. It is seen that the APEX better reproduces MC calculations than it cold be done in the frames of TH [34] or HDG [72, 73] approaches, which were not designed to describe strongly coupled plasmas. In Figure 6, the calculated in APEX [68, 69] variation of the reduced fitting parameter α in the reciprocal Debye length units k_{DH} for the hydrogen-like Ar ions at temperature $T_e = 800$ eV is shown versus density. These results demonstrate that the effective APEX potential has all the time the radius of shielding $(2 \div 4)$ times less the Debye radius in the interval of density variation of 4 orders of magnitude. So, the effective interaction is more short-ranged in comparison with Debye potential.

The recently improved APEX version [43] can address to nonequilibrium plasma parameter-non-equality of ion T_i and electron T_e temperatures. The example in Figure 7 shows the case when the ion temperature by an order of magnitude less than the electron one could lead to two times difference of the quasistatic Stark line profile halfwidth [43]. The improved APEX scheme allows to consider the degeneracy of electronic component [43]. Although the significance of the degeneracy effects evidently signalize about an uprise of the quantum effects, it has almost no consequences on the derivation of the practically classical microfield distribution function beside changing the screening length of the interaction potential [43]. However, the APEX microfield distribution function itself could be

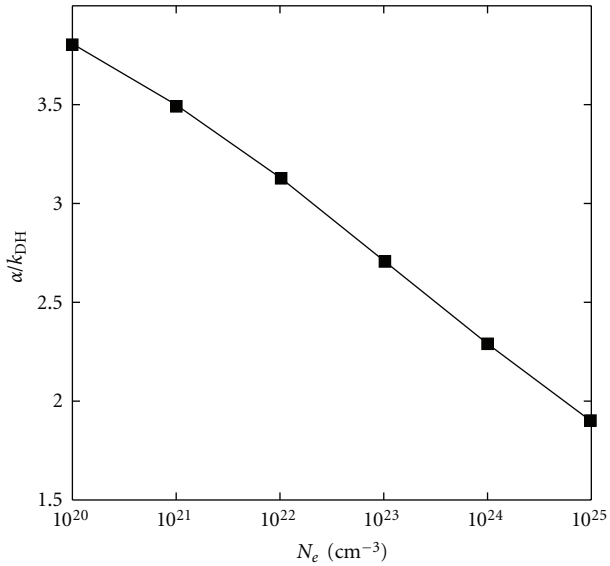

FIGURE 6: APEX α parameter in units of reciprocal Debye length of shielding k_{DH} versus density for hydrogen-like Ar ions at temperature 800 eV according to [68, 69].

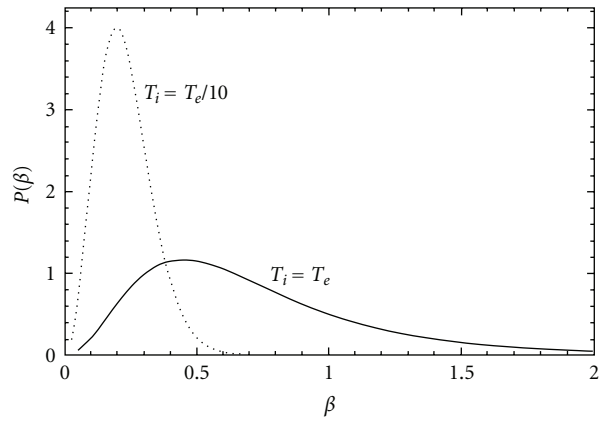

FIGURE 7: The comparison of APEX microfield distributions $P(\beta)$ for $Z_0 = Z_s = 12$, $N_e = 5 \cdot 10^{23}$ cm^{-3} at Ar^{+17} ion charged point for $T_e = 100$ eV and two values of ion temperature $T_i = T_e$ and $T_i = T_e/10$ from [43] (the reduced field is given in the electron units).

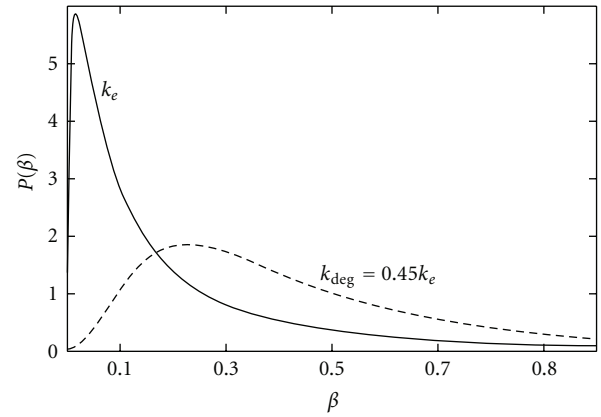

FIGURE 8: Microfield distribution functions $P(\beta)$ in charged point $Z_0 = Z_1 = 1$ with (dashed line) and without (solid line) account of electron degeneracy effects according to APEX [43] ($N_e = 10^{24}$ m^{-3}, $T_e = 5$ eV, $k_e \equiv r_{de}^{-1}$, k_{deg} is the reciprocal shielding length of electrons with account of degeneracy).

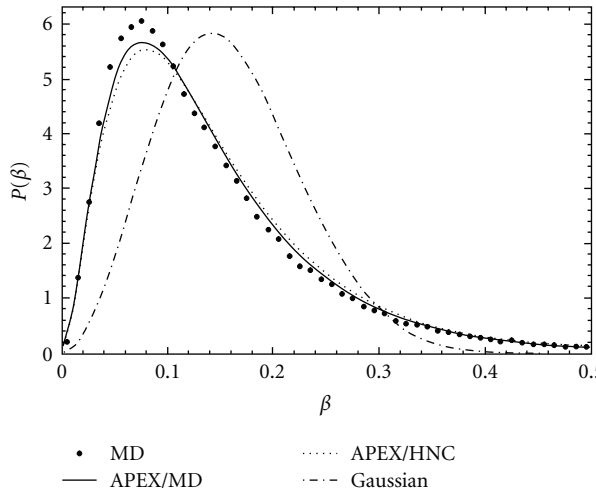

FIGURE 9: Microfield distributions for $Z_0 = Z_s = 25$, $N_e = 10^{24}$ cm^{-3}, $T_e = 50$ eV, giving $\Gamma = 50$ from [43]; dashed line: APEX with HCN RDF; solid line: APEX with MD RDF; • : MD; dot-dash line: Gaussian approximation.

changed quite considerably, which is well illustrated in [43, Figure 8]. It is worthy to discuss the $W(\beta)$ behavior at large Γ_i. In this limit, the pairwise Radial Distribution Function should acquire additional maxima on the scales, corresponding to short-range and long-range ordering. Moreover, it should be escorted by an uprise of pronounced anisotropy. From physical point of view [45] in this case, the distribution function should be alike Gaussian, describing small deviations from equilibrium particles positions in the vicinity of crystallization $\Gamma_i \sim 150$, which was really observed in modeling of strongly coupled plasmas. Hence, the asymptotic of distribution function could not be the nearest neighbor NN distribution [21, 39]. Although it is stated in APEX that at $\Gamma \to \infty$ the APEX is approaching Gaussian, this transition was not followed in detail, whereas it is doubtful how so qualitatively different asymptotic laws would replace each other. The available results do not allow to clear this question yet.

In Figure 9 from [43], the microfield distributions for $Z_0 = Z_s = 25$, $N_e = 10^{24}$ cm^{-3}, $T_e = 50$ eV, giving $\Gamma = 50$ from [43] are presented, where it is seen that at these conditions the APEX is approaching already Gaussian in some regions of β variation. However, APEX asymptotic at $\Gamma = 50$ is still more alike nearest neighbor (NN) [43]. Also, one can see the comparison of APEX distributions constructed with HCN and MD Radial Distribution Functions (RDFs) [43]. The current methods of simulations *ab initio*, the molecular dynamics (MD) [68, 69, 96, 101–109, 135–139] and MC [35–39], provide rather large noise with increasing of reduced microfield values, as was illustrated recently in [43].

For description of microfield distributions in neutral point, the APEX approach was reformulated [44]. In this case, the relations (24)–(26) do not take place. For the case of neutral point, it is suggested to determine α from the condition of equality of the second order derivative over Fourier-variable k to zero at $k = 0$ of any term beside the first one of specially renormalized cluster expansion [44]. If to return to the charged point, then it was stated that the new relation could be reduced to the form introduced for the charged point [44].

The APEX model was recently interestingly combined in works of Nersisyan et al. [184–186] for the classical two component plasmas (TCP) with the "potential-of-mean-force" (PMF) approximation very similar to the earlier work of Yan and Ichimaru [187]. Here the basic APEX ingredients like the expressions for the elementary electric fields are changed and modeled by the Coulomb fields modified in the case of attractive interactions by diffraction corrections [184–186]. The fitting parameter "α" is not introduced at all since the second moment relation is satisfied exactly [184–186]. The new model called PMFEX [184–186] preserves the APEX way for generating the correlation functions-HCN approximation and demonstrates rather good coincidence with MD simulations and admirable stability in providing data in the region of large reduced microfield values. Astonishingly, PMFEX has more natural generalization to obtain microfield distribution functions (MDF) in neutral point than APEX itself.

At last, the APEX procedure was generalized to extend it for modeling liquid domain in [189], where additional parameter of scaling is introduced

$$\kappa = \frac{r_{\mathrm{WS}}}{\lambda_e}, \tag{27}$$

where r_{WS} is the Wigner-Seitz radius, λ_e is the electron screening length. In this work, the set of analytical formulas are proposed for acceleration of computations depending beside reduced field β on κ and the coupling plasma ion parameter Γ_i, defined as

$$\Gamma_i = \frac{(Z^* \cdot e)^2}{k_B \cdot T \cdot r_{\mathrm{WS}}}, \tag{28}$$

alike it was done in [39], where obtained by Dr. Dominique Gilles, data in MC simulations were fitted by multiparametric approximate expressions. In [189] and the aforementioned expression, the thermodynamic equilibrium is assumed $T = T_i = T_e$, Z^* is the residual ion charge. However, to our opinion, an extension of microfield ideas on liquids with Yukawa type of interaction potential between particles is complicated and disputable subject.

In conclusion of this section, it should be resumed that in spite of evident success of APEX applications, the APEX itself is essentially *ad hoc* semiempirical method, whose reproduction is almost impossible without the help of its authors. At the same time the new APEX modifications evidently expand the range of successful implementation of these ideas.

2.7. Density Functional Theory. The most close to conventional thermodynamic notions method of construction of plasma microfield distribution functions was proposed in the work of Dharma-Wardana and Perrot [46, 47]. This method is based on generalization of local density functional theory of Kohn and Sham (LDFT) [116, 117] to finite temperatures. The outstanding research of these coauthors, who performed a row of fundamental studies, made possible the regular application of LDFT methods in plasmas (see, e.g., [118–123]).

The physical idea of this approach is the implementation of the self-consistent description of dense plasmas, which can reflect the influence of its properties on the quantum characteristics of free electrons with the arbitrary extent of degeneracy and partially ionized core of field ions and actually the states of emitter, determined simultaneously and self-consistently with correlation functions.

The request for self-consistency to some extent corresponds to the solution of kinetic problem, giving the answer on a question what partial concentration, temperature, and effective charge would have that or another plasma component at given temperature and density of free plasma electrons. Namely, relying on this initial information, the distribution functions are constructed in the other nonself-consistent approaches. It is evident that self-consistent approach would be by far more complicated due to necessity to find simultaneously with a distribution function the distribution of electron density, effective charges of ions cores, and various correlation functions.

The range of plasma parameters on which such a description is pretended corresponds to large values of electron plasma-coupling parameter $\Gamma_e \gg 1$ and strong ion-electron correlation due to influence of bounded electron states of emitter and field ions, but at the same time to values of ion plasma coupling parameter mainly less than unity $\Gamma_i < 1$.

The proper *variational* methods of local density functional is finding self-consistent distribution of electron density with simultaneous solution of the Schödinger equation for determining the wave functions and energy levels in potential, which in its turn is a functional of the electron density distribution [46, 116, 117].

The computational realization of approach is accomplished in the so-called correlation sphere of finite radius. This recalls the principles of mean ion plasma model (MIP), assuming finite size of ion sphere, in which the quasineutrality condition is fulfilled. It is common to refer on this procedure as on solution of DFT-Schrödinger equation [116].

In [46], this distribution of electron density is used further on in solution of Ornstein-Zernike equation in HCN approximation [7–12] for calculations of ion-ion correlation functions $g_{ii'}(r)$.

These functions are substituted then in two terms cluster expansion of Baranger-Mozer type [24, 25] for calculations of the logarithm of characteristic function with some amending modifications, connected with possibilities of partial summation of chain terms of higher orders in the so-called "weighted-chain-sum" (WCS) approximation [46].

This amendment functionally is expressed in appearance of majorizing factor for the second-order density term in the Baranger-Mozer expression for the characteristic function logarithm [46].

The principal moments of this approach [46] are (i) the choice of Baranger-Mozer scheme of cluster expansion, that allows generalization on quantum case in distinction from, for example, limited by classical approximation Hooper model; (ii) the criticism of a choice of the Yukawa type potentials for describing pairwise interactions in plasma; (iii) the determination of $g_{ii'}(r)$ with the help of special self-consistent procedure within HCN approximation; (iv) the way of calculation of the electric field value at the origin of reference frame due to field ion with the effective charge Z_B according to the exact result of pseudopotential theory of the second order:

$$E(r) = \frac{Z_B}{r^2} + \frac{1}{r^2}\int_0^r \overline{n}\,[g_{ei}(x) - 1]\,4\pi x^2 dx. \tag{29}$$

The expression for $E(r)$ is convenient to represent in the form

$$\begin{aligned} E(r) &= Z_B\,\frac{\overline{q}(r)}{r^2}, \\ \overline{q}(r) &= 1 - \frac{1}{Z_B}\int_0^r dx\; 4\pi x^2 \Delta n(x), \\ \Delta n(x) &= \overline{n}\,[g_{ei}(x) - 1]. \end{aligned} \tag{30}$$

The last equation determines the total nonlinear excess of electron density around ion "B," including exchange and correlations effects, which is found from the solution of DFT-Schrödinger equation in [46, 116, 117]. This pileup of electron density around ion is defined with respect to the level of uniform neutralizing background of free plasma electrons.

It should be noted that ionization equilibrium in DFT [46, 47, 116, 117] does not obey Saha equation because the correct condition of thermodynamic equilibrium is the free energy minimization. To the same resume, Hammer and Michalas arrived at one year later during analysis of the microfields influence on the equation of state [154–156].

At the same time, one drawback of this approach could be hidden here. Indeed, the emitter or field ion of "finite" size is inserted in the uniform electron background, but the plasma effects like lowering of ionization potential and kinetics of establishing of equilibrium with continuous spectra are not included in the description of levels population and realization of the bound electron states of the upper levels, as tried to formulate Hammer and Michalas [154–156].

As could be judged by original formulation [46, 47, 116, 117], it seems that DFT capability to describe nonequilibrium plasma conditions with complex chemical and ionization composition and different temperatures of electron and ion subsystems appears to be doubtful.

In the equation for electric field, the shielding of only one ion (field ion or emitter) is included. Due to the authors statement [46], the accounting for analogous terms for the second ion is beyond the accuracy of the used second-order pseudopotential theory.

It is important to underline that the electric field defined by the aforementioned equations in the quantum case could not be equalled as in the classical limit to the gradient (with opposite sign) of pairwise potential of ion-ion interaction. This is because in these conditions, this gradient will include nonelectrostatic terms connected with exchange and other purely quantum effects. Thereupon in [46] it is demonstrated that the usage of the effective pairwise potential of Yukawa type provides inadequate results.

The discussed approach operates with the following quantities: the effective charge of field ions $\overline{Z}$ and their mean density $\overline{\rho}$, and the mean density of free electrons $\overline{n}$, associated with quasineutrality condition:

$$\overline{n} = \overline{Z}\,\overline{\rho}, \qquad \frac{4}{3}\pi r_s^3 \overline{n} = 1, \tag{31}$$

where r_s has the sense of the electron sphere radius. The reduced and normal fields are determined by expressions

$$\begin{aligned} \overline{E} &= \frac{E}{E_0}, \\ E_0 &= \frac{Z}{r_0^2}, \\ \frac{4}{15}\,(2\pi)^{3/2}\, r_0^3\, \overline{n} &= 1, \\ r_0 &= 0.9991178\; r_s, \end{aligned} \tag{32}$$

where Z represents itself the charge of field ions. (This choice of the normal field, although admissible in principle, could be misleading. More adequate to our opinion would be $E_{0i} = \overline{Z}/r_{0i}^2$, $(4/15)(2\pi)^{3/2}\, r_{0i}^3\, \overline{\rho} = 1$.) The distribution functions depend on parameter

$$\begin{aligned} a \equiv r_{\mathrm{mf}} &= \frac{r_0}{r_{\mathrm{De}}} = 0.99912\;(3\Gamma_e)^{1/2}, \\ \Gamma_e &= \frac{e^2}{T r_s} \equiv \frac{r_c}{r_s}, \end{aligned} \tag{33}$$

where the electron Debye radius r_{De} is determined also on the basis of the mean free electrons density $\overline{n}$, the electron plasma coupling parameter Γ_e is defined in the same way as Hooper did, and r_c is the Coulomb radius.

The classical ion plasma coupling parameter is determined from the expression

$$\Gamma = \frac{Z^2 r_c}{r_{\mathrm{WS}}}, \qquad r_{\mathrm{WS}} = \left(\frac{3}{4\pi\overline{\rho}}\right)^{1/3}, \tag{34}$$

where r_{WS} is the radius of Wigner-Seitz cell. In this model, Z and $\overline{Z}$ are related to each other by

$$\overline{Z} = Z - \overline{n}_b, \tag{35}$$

where $\overline{n}_b$ is the number of bounded electrons per ion, calculated on the basis of DFT approach.

The DFT microfield distribution functions in distinction from the distribution functions in classical plasmas

depending not only on the parameter a but also on the parameter $\widetilde{T} = T/T_F$ at least, where T_F is the electron Fermi temperature, defined by the equation

$$kT_F = E_F = \frac{1}{2}\left(3\pi^2\overline{n}\right)^{2/3}, \quad \text{a.u.} \tag{36}$$

Moreover, according to authors [46, 47] opinion, the extent of plasma coupling in quantum case is characterized more correctly by parameter $\overline{\Gamma}$, which is determined by the basis of notion about the mean ion radius $\overline{R}$ assigned to each ion, so that the mean number of free electrons per ion $\overline{n}_f^i$ is equal to

$$\overline{n}_f^i = \frac{4}{3}\pi\overline{R}^3\overline{n}_f, \tag{37}$$

where $\overline{n}_f$ $(= \overline{n})$ is the density of plasma free electrons. On the other hand,

$$\begin{gathered} Z = \overline{n}_b + n_f^i, \\ \overline{n}_b = 2\int_0^{\overline{R}} 4\pi r^2 n_b(r) f_s(r) dr, \\ \overline{\Gamma} = \frac{\overline{Z}^2 r_c}{\overline{R}}, \end{gathered} \tag{38}$$

where $\overline{\Gamma}$ could be considered as the effective ionic plasma coupling parameter, corresponding to "equivalent" classical plasma, $f_s(r)$ is the Fermi factor, describing the character of electron states filling and depending on temperature and chemical potential. Thereby, the value $\overline{Z}$ or $\overline{n}_b$ are also the results of self-consistent solution of DFT-Schrödinger equations.

In the first article [46] of the authors of this approach, devoted to constructing microfield distribution functions, the Kirkwood approximation [7–12] was applied for disentanglement of the three particle correlations. This procedure was supplemented by separation of the central and noncentral parts of interactions in [47] on the basis of methods, elaborated in papers for description of quantum Hall effect. In particular, this improvement was connected with the APEX authors criticism of the DFT results for strongly coupled plasmas, where noticeable discrepancy was observed between the predictions of APEX and the first version of DFT-approach [46].

To illustrate this, the results of DFT-approach in comparison with APEX [40, 41] for Al plasma are presented in Figure 10 according to [46]. It is necessary to note that data of [40, 41] correspond to the so-called the high-frequency component of microfield, which describes the distribution of Coulomb electric fields of particles with the charge Z_e [40] or with arbitrary composition of ions of different species [41], inserted in the uniform neutralizing electron background. However, the authors of [46] did not point out for which values of Z or $\overline{Z}$ they took the data from [40, 41]. However, curiously enough, the most open for criticism moment of this approach is its complete self-consistency, which leads to the loss of possibility of the conventional identification of observed spectral transitions. In other words, in this

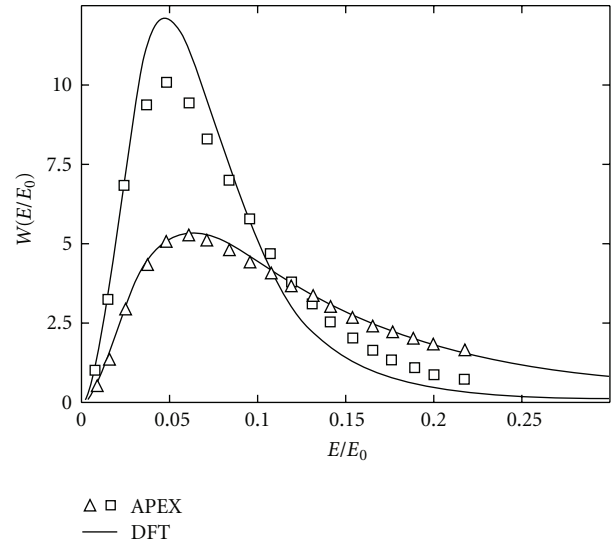

Figure 10: DFT-function of microfield distribution $W(E/E_0)$ in neutral (Δ- triangles, lower curves) and charged points (□ squares, upper curves) $Z = 0$ and $Z = 1$ in Al plasma in comparison with APEX results without account of electron degeneracy effects [40, 41] from [46] ($\overline{\Gamma} = 3.47$, $\Gamma = 3.31$, $\widetilde{T} \equiv T/T_F = 7.624$, $\overline{Z}_{\mathrm{Al}} = 5.178$, $r_s = 3a_0$, $r_{\mathrm{mf}} = a = 0.8$, T_F is the electron Fermi temperature see (36)).

DFT version, the self-consistent wave functions and the energy structure of emitters in plasma do not remember the corresponding characteristics of free emitters, which, generally speaking, are tools for decoding of observations.

Probably the cause of that is the insufficient accuracy in the description of the bounded excited states within DFT [46, 47]. The DFT version under discussion, however, could be successfully applied for calculations of the thermodynamic characteristics, when the affixment of results to observed properties of radiation in spectral lines is not important.

Moreover, it is not quite clear how to track the time scales of microfield variations in this approach, and the character of averages, applied in its derivation, more corresponds to purely thermodynamic notions. That is why the doubt arises in possibility to construct with the help of this approach *instantaneous* ion microfield distribution functions. Partially, it is connected with the very orientation of this method on description of quantum effects in the microfield distributions and necessity of possible reexamination of the "instantaneous distribution functions" notion in this case. However, this criticism concerns equally and Monte-Carlo method, and so forth.

In comparison with the other theoretical approaches to the microfield distribution functions construction, touched here, this method is perhaps the most laborious and complicated for realization, as the procedure of finding solution is very complicated and cumbersome, and requires preliminary complex calculations of additional auxiliary functions.

Beside, this method essentially does not give universal results for actually the microfield distribution functions, as the distribution from the very beginning depends on the

specific quantum properties of field ions and the emitter. At the same time, the doubt arises on how adequate and ample the developed notions about the character and the speed of establishing equilibrium between the emitter (test particle) and plasmas. Apparently DFT approach, of course, could not pretend on all completeness of plasma kinetic description, which is necessary for determination of plasma parameters. The latter are necessary as initial (input) data for the calculations of microfield distribution functions. Thus, the self-consistency of DFT approach in certain sense is limited.

Up to now, the DFT calculations of microfield distribution functions are performed only for several concrete cases and did not get wide-spread implementation. It is also unknown if there are any accessible for applied usage DFT codes for calculation of microfield distribution functions that are similar, for example, to APEX, although during the past years after the paper [47], the DFT approach as a method for description of atomic properties was considerably improved [120–123].

At the same time, no essential progress was achieved in the extent of adequateness of description with the help of DFT the excited atomic states, and consequently the radiative processes with their participation [122]. However, the DFT application to calculations of atomic, molecular, and chemical properties are all over considered currently as quite effective from point of view of universality, simplicity, and also due to the high speed of performing corresponding calculations on contemporary computers [123].

However, in spite of pointed out drawbacks the studies, performed within DFT approach, provided very interesting and instructive physical results, which without any doubt are very valuable for the further development in this field.

2.8. Plasma Collective Oscillations.

2.8.1. Microfield Separation on "Individual" and "Collective" Components. As it is evident, the "individual" and "collective" components of microfield are consequences of the same Hamiltonian of plasma charged particles [48]. Thus, many papers, dealing with the problem of microfield distributions of plasma collective oscillations, followed Bohm and Pines [30, 31], attempting to split the system of Coulomb particles with the help of canonical transformations of variables into the two weakly interacting subsystems, which could be considered independently [17, Section 2], [48, 49]. In addition, plasma could usually be considered as uniform and isotropic.

Then, the total distribution function $W(\vec{F})$ of summary microfield $\vec{F}$ under the condition that its components are additive, and the characteristic time scales of their variation are of the same order could be expressed as a convolution [48–50]:

$$W\left(\vec{F}\right) = \int d\vec{F}_c \; d\vec{F}_i W_c\left(\vec{F} - \vec{F}_i\right) W_i\left(\vec{F}_i\right), \quad \vec{F} = \vec{F}_c + \vec{F}_i, \tag{39}$$

where $W_c(\vec{F})$, $W_i(\vec{F})$ are distribution functions of the collective $\vec{F}_c$ and individual $\vec{F}_i$ microfield components correspondingly. The microfield distribution function of individual component more or less approaches the Baranger-Mozer-type function, whereas the distribution function of collective component is practically Gaussian [48].

However, the final result of such approach happens to depend on the choice of phenomenological parameter, which controls the separation of subsystems, while the satisfactory methods for its exact determination was not ever found [30, 31, 48, 49].

The determination of this parameter invoked certain difficulties already in Bohm and Pines [30, 31] papers. Firstly, it is rather not a parameter but a function in the space of oscillations wave vectors $\vec{k}$, and secondly the possibility of such separation is valid only in a quite narrow range of plasma parameters [30, 31]. Thereby, this procedure of collective variables extraction is not regular and universal.

In spite of that, it was declared in two publications (see [17, Section 2]), [49] about the realization of such separation after two canonical transformations although no explicit and proving demonstration of this statement was provided. These difficulties, of course, are due to strong interaction between subsystems, when, for example, the usage of the formal technique like the Zwanzig method of projection operators could not be rigorously justified, while the corresponding subsystems of quasiparticles, "dressed by interaction with each other", could not be managed reasonably in order to separate them by transformations of initial Hamiltonian (see, e.g., [14, 79, 96]).

Basing on sound sense, the separation on "collective" and "individual" subsystems should be possible when the resonance interaction of plasma waves with plasma particles is not essential [6, 50, 82].

So, for these specially stipulated conditions in fact *without proof*, it was conventionally accepted to consider that the two practically independent and noninteracting subsystems of plasma waves and quasiparticles exist, for which it is possible to introduce independent distributions of microfields.

Per se it means the construction of distribution function of collective oscillations on the basis of independent models. Evidently, this question has sense only if the conditions of quasistatics or large modulation depth are fulfilled:

$$\frac{dE_0}{\hbar} \gg \omega_c, \tag{40}$$

where d is the dipole moment of the emitter (test particle), E_0, ω_c are the amplitude and characteristic frequency of collective plasma electric microfield component.

2.8.2. Rayleigh Distribution. In the assumption of isotropy, multimode property, additivity and randomness of phases of collective oscillations, the distribution of collective microfields is described by Rayleigh function [50]:

$$W_c\left(\vec{F}\right) = 3\left(\frac{6}{\pi}\right)^{1/2} \frac{F^2}{\langle F^2\rangle^{3/2}} \exp\left[-\frac{3F^2}{2\langle F^2\rangle}\right],$$
$$\langle F^2\rangle = \int_0^\infty dF \; F^2 \; W_c(F). \tag{41}$$

This function is known also under the name of "distribution of random vector," and by definition, it corresponds to nonpolarized summary field of oscillations.

In one-dimensional case, this distribution has the form

$$W_c(F) = \left(\frac{2}{\pi}\right)^{1/2} \frac{1}{\langle F^2\rangle^{1/2}} \exp\left[-\frac{F^2}{2\langle F^2\rangle}\right], \tag{42}$$

and then the electric field of oscillations has definite polarization.

2.8.3. Regular Oscillations. For linearly polarized, one mode, and sinusoidal field, it is possible to introduce instantaneous distribution function [51, 52] in the so-called dynamic case, when the atomic state dipole precession frequency in the electric field is much larger than the frequency of oscillations Ω and the reciprocal life time of atomic state τ_{eff}^{-1}:

$$\frac{dE_0}{\hbar} \gg \Omega \gg \tau_{\text{eff}}^{-1}. \tag{43}$$

This distribution function has the form [48–50]

$$W_c(F) = \frac{1}{\pi} \frac{1}{\sqrt{E_0^2 - F^2}}, \tag{44}$$

where E_0 is the amplitude of sinusoidal oscillations.

2.9. Joint Distributions. In many problems, the information about distribution of the electrical field strength vector only is insufficient, and it is necessary to consider much more complex joint distribution functions of several scalar, vector, or tensor random variables at once [19–21, 53–70, 74–81]. These variables could have some limitations on the intervals of their variation, as, for example, it happens in APEX. Seemingly, the first works, where the joint distributions in ideal gas of Coulomb (gravitating) particles were considered in application to problems of stellar dynamics, belong to Chandrasekhar and von Neuman [19–21].

2.9.1. Distribution of Microfield and Its Space Derivatives. Let us consider the low-frequency ion joint distribution function $W(\vec{F}; \{\partial F_\alpha/\partial x_\beta\})$ of the ion electric microfield vector $\vec{F}$ and its spacial derivatives $\partial F_i/\partial x_k$, forming the symmetric second rank tensor, following [53–62] (compare [63, 64]). The "Spur" of this tensor is not equal to zero for the shielded ions, but is nullified in the case of Coulomb field. The values of arguments are sums of corresponding values of separate field ions, that is, the additivity condition is fulfilled:

$$\vec{F} = \sum_j \vec{F}_j, \qquad \frac{\partial F_\alpha}{\partial x_\beta} = \sum_j \frac{\partial\left(\vec{F}_j\right)_\alpha}{\partial x_\beta}. \tag{45}$$

In general form, it is rather complex function in 9-dimensional space of variables: the 3 components of electric field vector and the 6 independent components of symmetric tensor of the second rank.

For arbitrary plasma ionization composition, the quasineutrality condition could be expressed as

$$N = N_e = \sum_s Z_s N_s, \tag{46}$$

where Z_s, N_s are the charge and partial concentration of field ions of s species correspondingly.

The general expression for the joint distribution function then could be presented in the form

$$\begin{aligned} W\left(\vec{F}; \left\{\frac{\partial F_\alpha}{\partial x_\beta}\right\}\right) &= \frac{1}{(2\pi)^9} \int d^3\vec{\rho} \prod_{m=1}^{6} \int_{-\infty}^{+\infty} d\sigma_m \\ &\quad \cdot \exp\left[-i\vec{\rho}\vec{F} - i\sum_{m=1}^{6} \sigma_m \left(\frac{\partial F_\alpha}{\partial x_\beta}\right)_m\right] \\ &\quad \cdot A(\vec{\rho}; \{\sigma_m\}). \end{aligned} \tag{47}$$

For the distribution characteristic function $A(\vec{k})$, the following general exponential representation is valid:

$$A(\vec{\rho}; \{\sigma_m\}) = \exp[-N \cdot C(\vec{\rho}; \{\sigma_m\})]. \tag{48}$$

Using the generalization of Baranger-Mozer cluster expansion [53–58] (compare [63, 64]) on the case of arbitrary plasma composition, the index of exponent of characteristic function could be presented with the accuracy of up to the second-order terms over density in the following recording:

$$\begin{aligned} C(\vec{\rho}; \{\sigma_m\}) &= C^{(o)}(\vec{\rho}; \{\sigma_m\}) - \frac{N}{2!} \cdot C^{(1)}(\vec{\rho}; \{\sigma_m\}), \\ C^{(o)}(\vec{\rho}; \{\sigma_m\}) &= \sum_s C_s \int d^3\vec{r} \cdot g_{sr}(\vec{r}) \cdot \varphi_s(\vec{\rho}; \vec{r}; \{\sigma_m\}), \\ C^{(1)}(\vec{\rho}; \{\sigma_m\}) &= \sum_{s,s'} C_s C_{s'} \int d^3\vec{r}_1 \int d^3\vec{r}_2 \cdot \varphi_s(\vec{\rho}; \vec{r}_1; \{\sigma_m\}) \\ &\quad \cdot \varphi_{s'}(\vec{\rho}; \vec{r}_2; \{\sigma_m\}) \\ &\quad \cdot [g_{ss'}(\vec{r}_1; \vec{r}_2) - g_{sr}(\vec{r}_1) \cdot g_{s'r}(\vec{r}_2)], \\ \varphi_s(\vec{\rho}; \vec{r}; \{\sigma_m\}) &= 1 - \exp[i\Phi_s(\vec{\rho}; \vec{r}; \{\sigma_m\})], \\ \Phi_s(\vec{\rho}; \vec{r}; \{\sigma_m\}) &= \vec{\rho}\vec{E}_s(\vec{r}) + \sum_{m=1}^{6} \sigma_m \left(\frac{\partial(\vec{E}_s)_\alpha}{\partial r_\beta}\right)_m. \end{aligned} \tag{49}$$

Here, $C_s \equiv N_s/N$, $g_{sr}(\vec{r})$ is the pair correlation function of field ion from s species with charge Z_s and the test ion with charge Z_0, immersed in the origin of reference frame, $g_{ss'}(\vec{r}_1; \vec{r}_2)$ is the pair correlation function of field ions between each other with charges Z_s and $Z_{s'}$ *in the field of the test ion with charge* Z_0, $\vec{E}_s(\vec{r})$ is the elementary electric field, produced by any field ion (quasiparticle) of "s" species in the origin of the reference frame.

This field is determined by the effective interaction potential for such species in plasmas and could be described by the following equations:

$$\vec{E}_s(\vec{r}) = -eZ_s\frac{\vec{r}}{r^3}\cdot[1-\kappa_s(r)],$$
$$\operatorname{div}\vec{E}_s(\vec{r}) = \frac{eZ_s}{r^2}\cdot\frac{\partial\kappa_s(r)}{\partial r} - 4\pi eZ_s\delta(\vec{r}), \quad (50)$$
$$\oint_{\mathcal{V}\to\infty} d^3\vec{r}\cdot\operatorname{div}\vec{E}_s(\vec{r}) = 0.$$

The latter equations are followed from the properties of screening function $\kappa_s(r)$, connected with its definition: $\kappa_s(0) = 0$, $\kappa_s(\infty) = 1$, so that the excess charge of free electrons around the ion Z_s is determined by the expression

$$\delta n_e^{(s)}(r) = \frac{1}{4\pi}\frac{Z_s}{r^2}\cdot\frac{\partial\kappa_s(r)}{\partial r}. \quad (51)$$

Then the nonuniformity tensor components of elementary electric field are determined from

$$G_{ki}^{(s)}(\vec{r}) \equiv \frac{\partial\left(\vec{E}_s\right)_k}{\partial x_i} = \frac{eZ_s}{r^5}\cdot[3x_ix_k-\delta_{ik}r^2]\cdot\left[1-\kappa_s(r)+\frac{r}{3}\ \frac{\partial\kappa_s(r)}{\partial r}\right] + \frac{\delta_{ik}}{3}\frac{eZ_s}{r^2}\ \frac{\partial\kappa_s(r)}{\partial r}. \quad (52)$$

Hence, it follows that the screening function $\kappa_s(r) \geq 0$ could be found, for example, on the basis of the recent DFT approach receipts [46, 47], and $G_{ki}^{(s)}(\vec{r}) \equiv G_{ik}^{(s)}(\vec{r})$. In assumption that the field ions are bare nuclei here, the equations that determine the bound electrons distributions are not considered. It is assumed that quantum effects [14–17, 46, 47, 71] are not essential in microfield distribution.

The joint distribution obtained earlier provides the instantaneous distribution function of the low-frequency individual ion component of plasma microfield and its spacial derivatives, which per se are defined on time scales τ of the order $\omega_{\mathrm{pe}}^{-1} \ll \tau \ll (v_iN_i^{1/3})^{-1}$, where ω_{pe} is the plasma electron frequency, v_i is the relative thermal ion velocity with respect to the test particle, and N_i is the total ion density.

The basic ideas of this derivation were proposed by Baranger and Mozer and did not undergo any essential changes since that time, in spite of certain differences in posterior papers [27–29, 34–81, 96, 97], as they are inherent in microfield formalism.

It is important to underline that plasma polarization effects [46, 47, 53–62] (or in other words appearance of nonuniformity in distribution of plasma electron density) are included in general form in this consideration from the very beginning via screening function and its derivatives. The integration over $\vec{F}$ or over $\partial F_i/\partial x_k$ components leads to separate distributions of microfield or its tensor of nonuniformity, and after implementation of appropriate approximations recovers known earlier results.

One of the most interesting properties of the joint distributions follows from the analysis of its moments $\langle\partial F_i/\partial x_k\rangle_{\vec{F}}$ for a given value of $\vec{F}$ that represent itself the averages of $\partial F_i/\partial x_k$ over the joint distributions for the fixed vector value of $\vec{F}$:

$$\begin{aligned}
W\left(\vec{F}\right)\left\langle\frac{\partial F_i}{\partial x_k}\right\rangle_{\vec{F}} &= \frac{N}{(2\pi)^3}\int d^3\vec{\rho}\cdot\exp\left[-i\vec{\rho}\vec{F}\right]\\
&\quad\cdot A(\vec{\rho})\cdot\langle G_{ik}(\vec{\rho})\rangle,\\
\langle G_{ik}(\vec{\rho})\rangle &= \left\langle G_{ik}^{(o)}(\vec{\rho})\right\rangle + \left\langle G_{ik}^{(1)}(\vec{\rho})\right\rangle,\\
\left\langle G_{ik}^{(o)}(\vec{\rho})\right\rangle &= \sum_s C_s\left\langle G_{ik}^{(s)}(\vec{\rho})\right\rangle,\\
\left\langle G_{ik}^{(1)}(\vec{\rho})\right\rangle &= -\frac{N}{2}\sum_{s,s'}C_sC_{s'}\left\langle G_{ik}^{(ss')}(\vec{\rho})\right\rangle,\\
\left\langle G_{ik}^{(s)}(\vec{\rho})\right\rangle &= \int d^3\vec{r}\cdot g_{sr}(\vec{r})\cdot\exp[i\Phi_s(\vec{\rho};\vec{r})]\\
&\quad\cdot G_{ik}^{(s)}(\vec{r}),\\
\left\langle G_{ik}^{(ss')}(\vec{\rho})\right\rangle &= \int d^3\vec{r}_1\int d^3\vec{r}_2\\
&\quad\cdot[g_{ss'}(\vec{r}_1;\vec{r}_2) - g_{sr}(\vec{r}_1)\cdot g_{s'r}(\vec{r}_2)]\\
&\quad\cdot\left\{G_{ik}^{(s)}(\vec{r}_1)\cdot\exp[i\Phi_s(\vec{\rho};\vec{r}_1)]\right.\\
&\quad\cdot(1-\exp[i\Phi_{s'}(\vec{\rho};\vec{r}_2)])+G_{ik}^{(s')}(\vec{r}_2)\\
&\quad\cdot\exp[i\Phi_{s'}(\vec{\rho};\vec{r}_2)]\\
&\quad\cdot\left.(1-\exp[i\Phi_s(\vec{\rho};\vec{r}_1)])\right\}.
\end{aligned} \quad (53)$$

It was found that the expressions for the first moments of the nonuniformity tensor could be presented via microfield distribution functions in general form [52–55, 59]

$$\begin{aligned}
&W\left(\vec{F}\right)\left\langle\frac{\partial F_i}{\partial x_k}\right\rangle_{\vec{F}}\\
&= N\left[\sum_s C_s\int d^3\vec{r}\cdot g_{sr}(\vec{r})\cdot G_{ik}^{(s)}(\vec{r})\right.\\
&\quad\cdot W\left(\vec{F}-\vec{E}_s(\vec{r})\right) - \frac{N}{2}\sum_{ss'}C_sC_{s'}\int d^3\vec{r}_1\int d^3\vec{r}_2\\
&\quad\cdot[g_{ss'}(\vec{r}_1;\vec{r}_2) - g_{sr}(\vec{r}_1)\cdot g_{s'r}(\vec{r}_2)]\\
&\quad\cdot\left\{G_{ik}^{(s)}(\vec{r}_1)\cdot\left[W\left(\vec{F}-\vec{E}_s(\vec{r}_1)\right)\right.\right.\\
&\qquad\left.-W\left(\vec{F}-\vec{E}_s(\vec{r}_1)-\vec{E}_{s'}(\vec{r}_2)\right)\right]+G_{ik}^{(s')}(\vec{r}_2)\\
&\quad\left.\cdot\left[W\left(\vec{F}-\vec{E}_{s'}(\vec{r}_2)\right)-W\left(\vec{F}-\vec{E}_s(\vec{r}_1)-\vec{E}_{s'}(\vec{r}_2)\right)\right]\right\}\Bigg].
\end{aligned} \quad (54)$$

To carry out expressions that could be processed in numerical calculations, it is necessary to apply additional

simplifications and approximations for correlation functions in the aforedescribed general formulas. For this it is presumed that the pair correlation function depends only on the module of particles radii-vectors difference and the Kirkwood approximation is used for disentanglement [7–10] of the three-particle correlations. This yields [55–58, 80, 81]

$$g_{sr}(\vec{r}) \equiv g_{sr}(r),$$
$$g_{ss'}(\vec{r}_1;\vec{r}_2) \simeq g_{ss'}(|\vec{r}_1-\vec{r}_2|)\cdot g_{sr}(r_1)\cdot g_{s'r}(r_2), \tag{55}$$
$$h_{ss'}(|\vec{r}_1-\vec{r}_2|) \equiv g_{ss'}(|\vec{r}_1-\vec{r}_2|)-1.$$

Then, it is possible to obtain the following general representations of correlation functions in the form of series over harmonics:

$$h_{ss'}(|\vec{r}_1-\vec{r}_2|) = \sum_{n=0}^{\infty}(2n+1)\cdot P_n\left(\cos\left[\widehat{\vec{r}_1\vec{r}_2}\right]\right)\cdot h_{ss'}(n;r_1;r_2),$$
$$h_{ss'}(n;r_1;r_2) = \int_0^{\infty} dk\cdot k^2\cdot j_n(kr_1)\cdot j_n(kr_2)\cdot h_{ss'}(k),$$
$$h_{ss'}(k) = \frac{1}{(2\pi)^3}\int d^3\vec{r}\cdot\exp\left(i\vec{k}\vec{r}\right)\cdot h_{ss'}(r). \tag{56}$$

Here, $P_n(z)$ are the Legendre polynomials depending on cosine of the angle between vectors $\vec{r}_1$ and $\vec{r}_2$, where $j_n(y)$-is the spherical Bessel function.

This allows to simplify general results, mentioned earlier, and obtain, for example, the distribution function of reduced microfield values $\beta \equiv F/F_0$ (where F_0 is the value of normal microfield [18]), more general expression than those known before [24, 25] (compare [72, 73, 164]):

$$W\left(\vec{F}\right) = 4\pi F^2\cdot W(F), \qquad A(\vec{\rho}) = A(\rho),$$
$$F_0 = \Lambda e N^{2/3}, \qquad \Lambda \equiv 2\pi(4/15)^{2/3}, \tag{57}$$
$$W(\beta) = \frac{2\beta}{\pi}\int_0^{\infty} dk\cdot k\cdot\sin k\beta\cdot A(k), \tag{58}$$
$$A(k) = \exp\{-[\Psi_0(k)+\Psi_1(k)]\},$$
$$\Psi_0(k) = \frac{4\pi}{\Lambda^{3/2}}\sum_s C_s I_s(k), \tag{59}$$
$$\Psi_1(k) = -\frac{8\pi^2}{\Lambda^3}\sum_{ss'} C_s C_{s'} I_{ss'}(k), \qquad r_0 \equiv \left(\frac{e}{F_0}\right)^{1/2},$$
$$I_s(k) = \int_0^{\infty} dx\cdot x^2\cdot g_{sr}(r_0x)\cdot\left\{1-\frac{\sin k\epsilon_s(x)}{k\epsilon_s(x)}\right\}, \tag{60}$$
$$\epsilon_s(x) = \frac{Z_s}{x^2}[1-\kappa_s(r_0x)],$$
$$I_{ss'}(k) = \int_0^{\infty} dx_1\cdot x_1^2\int_0^{x_1} dx_2\cdot x_2^2\cdot g_{sr}(r_0x_1)\cdot g_{s'r}(r_0x_2)$$
$$\cdot\sum_{n=0}^{\infty}(-1)^n(2n+1)\cdot\{j_n[\epsilon_s(x_1)]-\delta_{on}\}$$
$$\cdot\{j_n[\epsilon_{s'}(x_2)]-\delta_{on}\}h_{ss'}(n;r_0x_1;r_0x_2). \tag{61}$$

Here, the function $\Psi_1(k)$ describes ion-ion correlations.

The explicit representation for distribution function allows to obtain analytical expressions for the first moments of nonuniformity tensor, describing its fundamental properties for the fixed value of the ion electric microfield vector:

$$\left\langle\frac{\partial F_X}{\partial X}\right\rangle_{\vec{F}} = -\frac{2\pi Ne}{3}\left\{B_D(\beta)\left[P_2(\cos\theta)-P_2^{|2|}(\cos\theta)\frac{\cos 2\phi}{2}\right]\right.$$
$$\left.-\,2B_{DO}(\beta)\right\}, \tag{62}$$

$$\left\langle\frac{\partial F_Y}{\partial Y}\right\rangle_{\vec{F}} = -\frac{2\pi Ne}{3}\left\{B_D(\beta)\left[P_2(\cos\theta)+P_2^{|2|}(\cos\theta)\frac{\cos 2\phi}{2}\right]\right.$$
$$\left.-\,2B_{DO}(\beta)\right\}, \tag{63}$$

$$\left\langle\frac{\partial F_Z}{\partial Z}\right\rangle_{\vec{F}} = \frac{4\pi Ne}{3}\{B_D(\beta)\cdot P_2(\cos\theta)+B_{DO}(\beta)\}, \tag{64}$$

$$\left\langle\frac{\partial F_Y}{\partial X}\right\rangle_{\vec{F}} = \frac{\pi Ne}{3}\cdot B_D(\beta)\cdot P_2^{|2|}(\cos\theta)\cdot\frac{\sin 2\phi}{2}, \tag{65}$$

$$\left\langle\frac{\partial F_Z}{\partial X}\right\rangle_{\vec{F}} = \frac{2\pi Ne}{3}\cdot B_D(\beta)\cdot P_2^{|1|}(\cos\theta)\cdot\cos\phi, \tag{66}$$

$$\left\langle\frac{\partial F_Z}{\partial Y}\right\rangle_{\vec{F}} = \frac{2\pi Ne}{3}\cdot B_D(\beta)\cdot P_2^{|1|}(\cos\theta)\cdot\sin\phi, \tag{67}$$

where θ and ϕ are the polar and azimuthal angles of vector $\vec{F}$ in the laboratory Cartesian reference frame XYZ, $P_n^{|m|}(x)$ is the generalized Legendre polynomial.

The universal function $B_{DO}(\beta)$ is due to plasma polarization effects [55–59].

The *universal functions* $B_D(\beta)$ and $B_{DO}(\beta)$ with an account of ion-ion correlations are determined by the expressions, where the terms with upper subindex (1) are connected with ion-ion correlations:

$$B_D(\beta) = B_D^{(o)}(\beta)+B_D^{(1)}(\beta),$$
$$B_{DO}(\beta) = B_{DO}^{(o)}(\beta)+B_{DO}^{(1)}(\beta),$$
$$B_D^{(o)}(\beta) = \frac{12}{\pi}\frac{\beta^2}{W(\beta)}\sum_s C_s Z_s b_s(\beta),$$
$$B_D^{(1)}(\beta) = -\frac{12}{\pi}\frac{\beta^2}{W(\beta)}\sum_{ss'} C_s C_{s'} b_{ss'}(\beta), \tag{68}$$
$$B_{DO}^{(o)}(\beta) = \frac{2}{\pi}\frac{\beta^2}{W(\beta)}\sum_s C_s Z_s b_s^{(o)}(\beta),$$
$$B_{DO}^{(1)}(\beta) = -\frac{2}{\pi}\frac{\beta^2}{W(\beta)}\sum_{ss'} C_s C_{s'} b_{ss'}^{(o)}(\beta),$$

The functions, describing the first terms of expansion and connected with quadrupolar tensor $b_s(\beta)$ and scalar $b_s^{(o)}(\beta)$ correspondingly, could be transformed to

the following form:

$$b_s(\beta) = \int_0^\infty dk \cdot k^2 \cdot A(k) \cdot j_2(k\beta) \cdot \Phi_s(k),$$
$$b_s^{(o)}(\beta) = \int_0^\infty dk \cdot k^2 \cdot A(k) \cdot j_0(k\beta) \cdot \Phi_s^{(o)}(k), \quad (69)$$

where the Fourier-components of nonuniformity tensor $\Phi_s(k)$ and its trace $\Phi_s^{(o)}(k)$ of the field ion for "s" species enters the integrands:

$$\Phi_s(k) = \int_0^\infty dx \cdot x^2 \cdot g_{sr}(r_0 x) \cdot j_2[k\epsilon_s(x)] \cdot \Phi_s(x),$$
$$\Phi_s^{(o)}(k) = 4\pi \int_0^\infty dx \cdot x^2 \cdot g_{sr}(r_0 x) \cdot j_0[k\epsilon_s(x)] \cdot \left\{ \frac{r_0^3 \delta n_e^{(s)}(r_0 x)}{Z_s} \right\},$$
$$\Phi_s(x) \equiv \frac{1}{x^3}\left[1 - \kappa_s(r_0 x) + \frac{x}{3}\frac{\partial \kappa_s(r_0 x)}{\partial x}\right]. \quad (70)$$

It is convenient to represent the next-order functions $b_{ss'}(\beta)$ and $b_{ss'}^{(o)}(\beta)$ due to ion-ion correlations in the following form using the same designations:

$$b_{ss'}(\beta) = \int_0^\infty dk \cdot k^2 \cdot A(k) \cdot j_2(k\beta) \cdot b_{ss'}(k),$$
$$b_{ss'}^{(o)}(\beta) = \int_0^\infty dk \cdot k^2 \cdot A(k) \cdot j_0(k\beta) \cdot b_{ss'}^{(o)}(k), \quad (71)$$

where the corresponding Fourier components of correlation contributions are represented in the series

$$b_{ss'}(k) = \int_0^\infty dx_1 \cdot x_1^2 \int_0^{x_1} dx_2 \cdot x_2^2 \cdot g_{sr}(r_0 x_1) \cdot g_{s'r}(r_0 x_2) \cdot b_{ss'}(k; x_1; x_2),$$
$$b_{ss'}(k; x_1; x_2) = Z_s \cdot \Phi_s(x_1) \cdot \left\{ j_2[k\epsilon_s(x_1)] \cdot h_{ss'}(0; r_0 x_1; r_0 x_2) - \sum_{n=0}^{\infty} (-1)^n (2n+1) \cdot \left[\left(\frac{3n(n-1)}{2k^2 \epsilon_s^2(x_1)} - 1 \right) j_n[k\epsilon_s(x_1)] + \frac{3}{k\epsilon_s(x_1)} j_{n+1}[k\epsilon_s(x_1)] \right] \cdot j_n[k\epsilon_{s'}(x_2)] \cdot h_{ss'}(n; r_0 x_1; r_0 x_2) \right\},$$
$$b_{ss'}^{(o)}(k) = \int_0^\infty dx_1 \cdot x_1^2 \int_0^{x_1} dx_2 \cdot x_2^2 \cdot g_{sr}(r_0 x_1) \cdot g_{s'r}(r_0 x_2) \cdot b_{ss'}^{(o)}(k; x_1; x_2),$$
$$b_{ss'}^{(o)}(k; x_1; x_2) = 4\pi \cdot r_0^3 \delta n_e(r_0 x_1) \cdot \left\{ j_0[k\epsilon_s(x_1)] \cdot h_{ss'}(0; r_0 x_1; r_0 x_2) - \sum_{n=0}^{\infty} (-1)^n (2n+1) \cdot j_n[k\epsilon_s(x_1)] \cdot j_n[k\epsilon_{s'}(x_2)] h_{ss'}(n; r_0 x_1; r_0 x_2) \right\}. \quad (72)$$

Now, it is useful to present substitutions for obtaining previous results [24, 25] in the linearized Debye-Hückel approximation for correlation functions of field particles from expressions, derived earlier:

$$\kappa_s(r_0 x) \longrightarrow \kappa_s^D(x) \equiv 1 - \exp[-ax] \cdot (1 + ax),$$
$$a \equiv \frac{r_0}{r_D}, \qquad r_D \equiv \sqrt{\frac{T_e}{4\pi e^2 N_e}},$$
$$g_{sr}(r_0 x) \longrightarrow \exp\left[-Z_0 Z_S \cdot \Theta \cdot a^2 \cdot \frac{\Lambda^{3/2}}{4\pi} \cdot \frac{\exp[-ax]}{x} \right],$$
$$\Theta \equiv \frac{T_e}{T_i},$$
$$h(n; x_1; x_2) \longrightarrow -\Theta \cdot a^3 \cdot \frac{\Lambda^{3/2}}{4\pi} \cdot f_n^{>}(ax_1) \cdot f_n^{<}(ax_2),$$
$$f_n^{>}(z) \equiv (-1)^n \cdot z^n \cdot \left(\frac{d}{zdz} \right)^n \frac{e^{-z}}{z},$$
$$f_n^{<}(z) \equiv z^n \cdot \left(\frac{d}{zdz} \right)^n \frac{\sinh(z)}{z}. \quad (73)$$

In these formulas, the conventional designations from original works [24–26, 72, 73, 164] are used, while T_i, T_e are the electron and ion temperatures correspondingly.

After performing the pointed out simplifications for one sort of field ions, the equations (57)–(61) reproduce the Baranger-Mozer results for low-frequency ion component of plasma microfield distribution function.

In Figure 11 the Baranger-Mozer (BM) functions $W(\beta)$ for several a values, calculated along with this section derivation in the charged point, and the results of corresponding MC calculations are presented. The comparison has shown that within the accuracy of the figure drawing BM and MC data are indistinguishable from each other. It should be noted that the direct calculations of general joint distribution functions is very complicated task even for the current powerful supercomputers. Moreover, sometimes even a definition of such functions is difficult to accomplish. That is why the most accessible approximation is characterizing these functions with the help of its moments of various ranks over different variables.

In practical application, it is important to keep in mind that even in the case of calculations the simplest distribution functions, depending only on the module of reduced field, the known difficulties exist with arising oscillations in results at small and especially at large β due to Fourier transform. That is why the most accepted method of introduction of various distribution functions in calculations is connected with the use of their tables. As a rule under calculations of the sum of terms with ion-ion correlations, the convergence is rather rapid, and it is quite enough to include only 3-4 first terms of the sum [22–26].

In Figure 12, the universal function $B_D(\beta)$ in the charged point $Z_r = Z_1 = 1$ for different values of parameter a is presented [58]. The dashed lines show the results of calculations using only the first two terms of cluster expansion and three terms of expansion over l. The nearest neighbor result is also shown as $2\beta^{3/2}$. Solid lines represent MC results. In

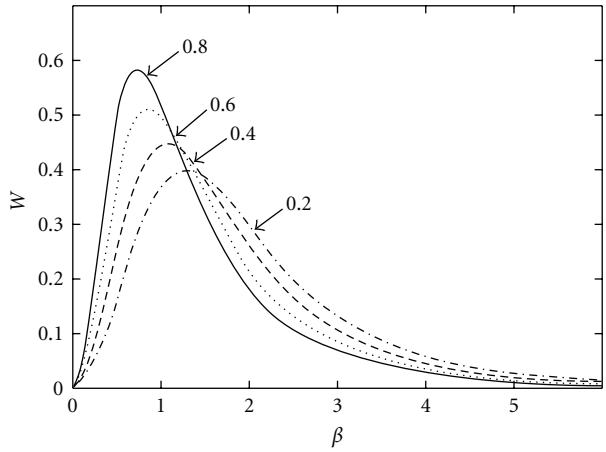

Figure 11: Microfield distribution function $W(\beta)$ in charged point $Z_r = 1$ in mixture of field ions with charge $Z = 1$ from [58] calculated within Baranger-Mozer and MC approaches (results of MC and Baranger-Mozer calculations are practically indistinguishable, numbers near arrows label a values).

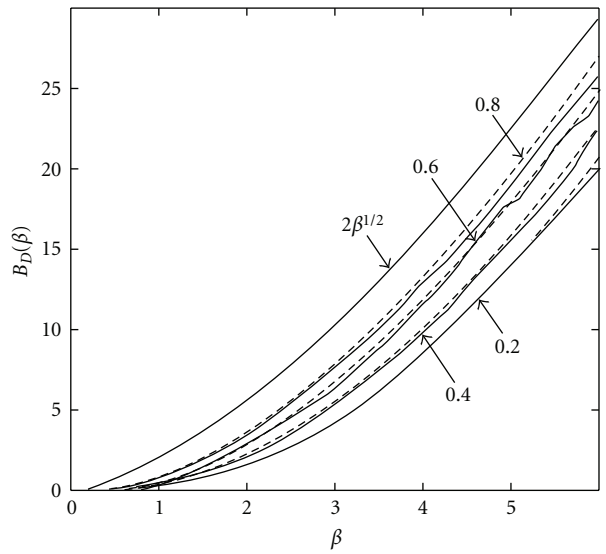

Figure 12: Universal functions $B_D(\beta)$ in charged point $Z_r = 1$ for various **a** values and charge of field ions equal to 1 [58].

Figure 13, the illustration of the universal function $B_{DO}(\beta)$ for different values of parameter a in the charged point $Z_r = Z_1 = 1$, according to [58] similarly to $B_D(\beta)$ is presented. Only the two first terms of cluster expansion and three terms of expansion over l are used. Solid lines show MC results (see [58]). The analysis of $B_{DO}(\beta)$ asymptotic for small β discovers that this function stems to constant at $\beta \to 0$. Moreover, from graphs, generally speaking, the presence of another constant is evident in asymptotic for large β. These properties have principal significance and signalize on the necessity of simultaneous correct account for electron contribution under consideration of quadrupole interaction, for example, in the spectral lines broadening [59, 60, 62].

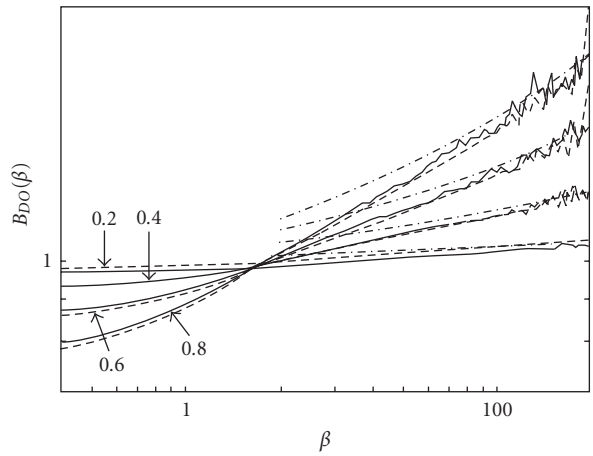

Figure 13: Universal functions $B_{DO}(\beta)$ in charged point $Z_r = 1$ for various **a** values and charge of field ions equal to 1 [58].

The described-here Baranger-Mozer cluster expansion approach for joint distribution function of ion microfield and its nonuniformity tensor with Debye-Hückel correlation functions was firstly proposed by the author of this review in [54] and completely realized in [55, 56], where the functions $B_D(\beta)$ and $B_{DO}(\beta)$ were defined and its asymptotics was described. Two years later and with much less generality, similar results appeared in [64]. Interestingly, the designations in [64] coincide with the corresponding from [55].

In order to obtain results for strongly coupled plasmas, it is necessary to apply MC [57–62], molecular dynamics or APEX approaches. However, the APEX scheme allows only some reformulation of general expression on the basis of (54) relations, and then derivation from it the expressions for the first moments [65, 68, 69]. However, it is not possible to construct with APEX namely the joint distributions and then to derive the first moment from such a function, if it would exist in APEX.

Indeed, within the APEX these operations do not commute (see [58, 65, 68, 69]), and APEX authors avoid the attempts of construction joint distribution functions [165]. Resultantly, they attempt to generalize the relation for the first moment, basing on [165] (where the correlation function in the given electric field $\vec{\epsilon}$ was introduced $g(\vec{r};\vec{\epsilon})$) and miss the partial derivative from $C(\rho;\sigma_m)$ over one of σ_m components, that during reduction of microfield function to APEX form provides the effective density distribution $g_{\text{eff.APEX}}(r)$ [59, 60], diverging at large values of argument.

For the APEX distribution function itself and the "quadrupole" part of the first moment of nonuniformity tensor, this increase is damped by corresponding decrease of function in (60) (see [57, 58, 80, 81]):

$$\left\{1 - \frac{\sin k\epsilon_s(x)}{k\epsilon_s(x)}\right\}, \quad \epsilon_s(x) = \frac{Z_s}{x^2}[1 - \kappa_s(r_0 x)] \tag{74}$$

and function in (70):

$$j_2[k\epsilon_s(x)], \tag{75}$$

but in the scalar part of first moment, this invokes divergence [68, 69, 80, 81].

Thus, pointed out noncommutativity is connected on one hand with the behavior of effective screening α in APEX, which is stronger than the Debye one (see Figure 14), and on the other hand with the outcome to constant for small reduced field values of the polarization (scalar) part of the first moment of nonuniformity tensor (see Figures 12 and 13), which was not taken into account in the first APEX work on the first moment of nonuniformity tensor calculation [65]. These factors both lead to divergence at upper limit in the polarization part of the first moment of nonuniformity tensor if to derive it from expression for the joint distribution function of microfield and its spacial derivatives within APEX (see [57, 58, 65, 68, 69, 76, 80, 81]).

In order to obtain the finite result, APEX authors in fact calculate field derivative, averaged over the APEX distribution function. This way means that such an average could be performed over any microfield distribution, and consequently, the given microfield is associated with the derivative as "if of quite other microfield". So, the presence of unequivocal connection between the field and its derivative is not requested, which does not correspond to the setting of a problem under consideration, and from the logic point of view is absurd.

Nevertheless, the general derivation in [65] contains several new interesting formal results. Indeed, in [65], the constrained distributions of the nonuniformity tensor components at the fixed value of microfield are introduced instead of joint distribution functions, which formally allows to avoid the approximation of preaveraged Hamiltonian over components of microfield nonuniformity tensor. However, to our opinion, the numerical calculation of such functions is not simpler than the full-joint distribution itself and avoiding the approximation of averaged Hamiltonian has only an illusive character.

The described difficulties are due to the fact that the APEX distribution itself already is derived under certain limitations, imposed by fulfillment of the (24) condition for the second moment of microfield in the charged point. So, trying to preserve the natural asymptotic for large field values on one hand, and on the other hand comprehending well that $g_{\text{eff.APEX}}(r)$ is divergent al large r, the authors of [65, 165] decided not to use the first moment of the joint distribution function, but to use the mean value of derivative over APEX distribution. (The presence of divergence and non-normalization of $g_{\text{eff.APEX}}(r)$ and the information on real values of screening parameter α in comparison with the Debye reciprocal length was not mentioned in previous APEX papers till [68, 69].) Per se introduced in [165], the definitions of averaged values deviate from the conventional approach of Chandrasekhar-von Neuman [19–21] and represent itself some additional approximation that is not connected with formalism of joint distribution functions, and which region of validity is at least unclear.

Besides the fact that APEX in this case does not allow to construct namely *joint* distribution function of the electric field strength vector and its nonuniformity tensor in the conventional "Chandrasekhar" sense [19–21], this problem seemingly is connected with inadmissibility of separate consideration of the electron and ion contributions to polarization interaction. Indeed, simultaneous consideration in real physical problems of the ion and electron contributions to polarization interaction lead to conversion to zero, at infinite distances, the constant in summary polarization interaction, and in this way remove the problem of pointed out divergence (see [59, 60]). The physical sense of this is that the distribution of ion charge also becomes nonuniform in response to the nonuniform distribution of electron density (see [59, 60]), and both effects compensate each other at sufficient distances from test charge according to general plasma quasineutrality condition. The alike outlook is presented in the interesting paper of Ortner, Valuev, and Ebeling, where such model is called as OCP on polarizable background (POCP).

On the other hand, it is obvious that up to now, not all variants of joint distribution function construction, using APEX, were analyzed.

The comparison of results for the moments of total nonuniformity tensor (without separation of contributions on tensor and scalar parts) for fixed value of the field ϵ using MD method, APEX (on the basis of relation (54)), and MC (from [58]) for $T = 800$ eV and $N = 10^{24}$ cm^{-3} is presented according to [68, 69] in Figure 14 versus the reduced field values. The designations are taken from original work [68,

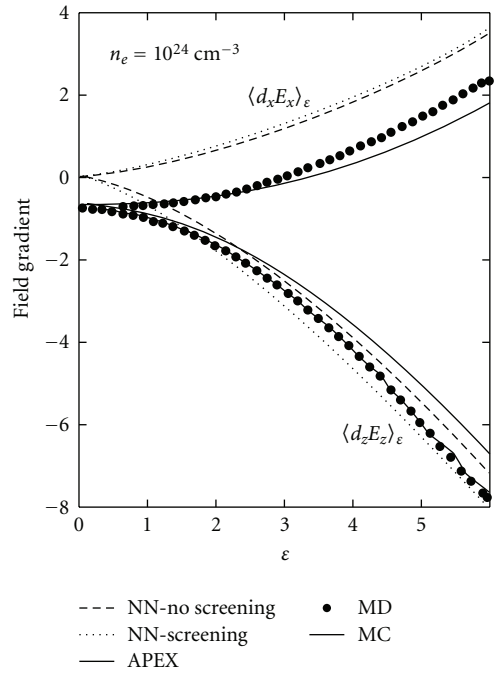

Figure 14: First moment components of ion microfield nonuniformity tensor for given value of microfield strength (without separation of quadrupole and scalar parts for MD, MC, and APEX) and nearest neighbor distribution NN (without scalar part) versus microfield-reduced values ϵ according to [68, 69] (MC from [58], MD from [68, 69]).

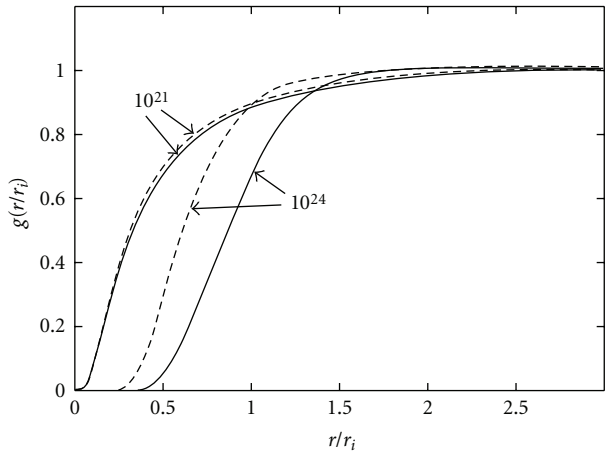

Figure 15: Pair radial correlation functions $g(r/r_i)$, calculated within *HCN* by Rogers code [124] (solid lines) and in Debye approximation (dotted lines) for $N_e = 10^{21}\,\mathrm{cm}^{-3}$ and $N_e = 10^{24}\,\mathrm{cm}^{-3}$ at $T = 800\,\mathrm{eV}$ according to [58].

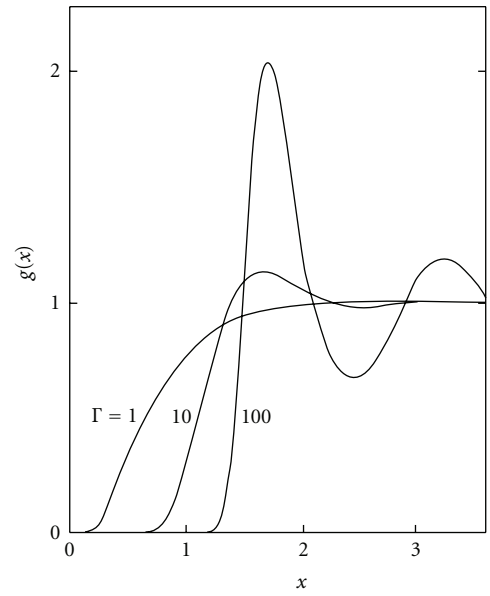

Figure 16: Pair radial distribution function $g(r/r_i)$, obtained by MC in OCP model according to [166] (numbers near curves provide corresponding values of plasma coupling parameter Γ).

69]. The designations in the figure are connected with the conventional ones in the present paper in the following way:

$$\langle d_x E_x \rangle_\epsilon \equiv \left\langle \frac{\partial F_x}{\partial x} \right\rangle_\beta, \qquad \langle d_z E_z \rangle_\epsilon \equiv \left\langle \frac{\partial F_z}{\partial z} \right\rangle_\beta, \qquad (76)$$

and the results are obtained after average over angles of microfield vector in the expressions (62)–(67).

In Figure 14, the dependencies presented are obtained specially for distribution of nearest neighbor (NN) with screening by plasma electrons and without it, but neglecting the scalar part of nonuniformity tensor. It is seen that the APEX version for *average* values of nonuniformity tensor [68, 69] noticeably deviates at large reduced microfield values from the results of the nearest neighbor distribution. The MD results practically coincide with MC ones, while APEX curves are located inside MC curves in Figure 14. The presence of constant at small values of reduced microfield is confirmed. This comparison shows that the APEX calculation of *averaged* components of nonuniformity tensor in principle gives sound results in the context of coincidence with values of the first moments of nonuniformity tensor, although its derivation within APEX could not be recognized as completely correct and justified.

It seems instructive to demonstrate how with the increase of plasma coupling the differences of radial distribution functions within Debye and *HCN* approximations become ever more pronounced, which is illustrated in Figure 15. Partially, namely, the implementation of *HCN* correlation functions provides the APEX success in description of microfield distribution functions for strongly coupled plasmas. As was already mentioned with the increase of plasma coupling, the considerable changes of pair correlation function $g(r)$ occur, which acquires oscillations versus r for large values of Γ, which are due to the formation of the short-range ordering [166, 167]. This is explicitly demonstrated in Figures 16 and 17 within one component plasma model (OCP) for the different values of plasma coupling Γ. The

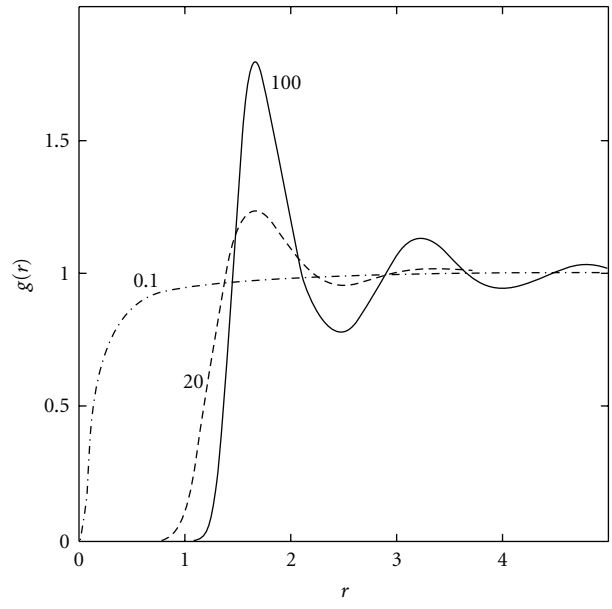

Figure 17: Pair radial correlation function $g(r/r_i)$, obtained by MC in OCP model according to [167] (numbers near curves provide corresponding values of plasma coupling parameter Γ).

presented results are obtained by the different authors with ten years interval [166, 167]. These data demonstrate visually qualitative changes of $g(r)$ versus variation of plasma coupling in the range $\Gamma = 0.1 - 1$, $\Gamma = 10 - 20$, $\Gamma \approx 100$. At the same time, the special study, done in [58], showed that using in the Baranger-Mozer scheme *HCN* correlation functions and MC correlation functions does not eliminate completely the noticeable discrepancies between

APEX and Baranger-Mozer microfield distribution functions for strongly coupled plasmas.

It should be taken into account that the linearization approximation for Debye-Hückel correlation functions is not inalienable part of Baranger-Mozer scheme, which allows the usage of any arbitrary accurate correlation function, including of the nonlinearized Debye-Hückel ones as well.

2.9.2. Distribution of Microfield and Its Time Derivatives. In the most general form, the joint distribution functions of microfield and its time derivatives could be written as Fourier-transform of its characteristic functions analogously to the previous section [19–21, 74–81], if following Chandrasekhar to consider the values of derivatives at initial time $t = 0$. These functions [74–81] describe microfield evolution in time on sufficiently small time intervals.

Without loss of generality, as an example, we present the function $W(\vec{F};\dot{\vec{F}};\ddot{\vec{F}})$ [54–56, 80, 81] (compare with [19–21]):

$$W\left(\vec{F};\dot{\vec{F}};\ddot{\vec{F}}\right) = \frac{1}{(2\pi)^9}\int d^3\vec{\rho}\int d^3\vec{\sigma}\int d^3\vec{\xi} \cdot \exp\left[-i\left(\vec{\rho}\cdot\vec{F}+\vec{\sigma}\cdot\dot{\vec{F}}+\vec{\xi}\cdot\ddot{\vec{F}}\right)\right]\cdot A\left(\vec{\rho};\vec{\sigma};\vec{\xi}\right),$$
$$A\left(\vec{\rho};\vec{\sigma};\vec{\xi}\right) = \exp\left[-NC\left(\vec{\rho};\vec{\sigma};\vec{\xi}\right)\right]. \tag{77}$$

It is worthy to underline that in spite of the presence of the first and the second derivatives of microfield over time, this is per se the instantaneous static distribution function. At the same time, of course, it is very complex function in 9-dimensional space of its variables. Using the same designations and plasma composition, we express $\ln A(\vec{\rho};\vec{\sigma};\vec{\xi})$ as in the previous section:

$$\begin{aligned}
C\left(\vec{\rho};\vec{\sigma};\vec{\xi}\right) &= C^{(o)}\left(\vec{\rho};\vec{\sigma};\vec{\xi}\right) - \frac{N}{2!}\ C^{(1)}\left(\vec{\rho};\vec{\sigma};\vec{\xi}\right),\\
C^{(o)}\left(\vec{\rho};\vec{\sigma};\vec{\xi}\right) &= \sum_s C_s\int d^3\vec{u}_s w_s(\vec{u}_s)\int d^3\vec{r}\, g_{sr}(\vec{r}) \cdot \varphi_s\left(\vec{\rho};\vec{r};\vec{\sigma};\vec{\xi}\right),\\
C^{(1)}\left(\vec{\rho};\vec{\sigma};\vec{\xi}\right) &= \sum_{s,s'} C_s C_{s'}\int d^3\vec{u}_s\, w_s(\vec{u}_s)\int d^3\vec{u}_{s'} \cdot w_{s'}(\vec{u}_{s'})\int d^3\vec{r}_1\int d^3\vec{r}_2 \\
&\quad\cdot \varphi_s\left(\vec{\rho};\vec{r}_1;\vec{\sigma};\vec{\xi}\right)\varphi_{s'}\left(\vec{\rho};\vec{r}_2;\vec{\sigma};\vec{\xi}\right) \\
&\quad\cdot \left[g_{ss'}(\vec{r}_1;\vec{r}_2) - g_{sr}(\vec{r}_1)\ \ g_{s'r}(\vec{r}_2)\right],\\
\varphi_s\left(\vec{\rho};\vec{r};\vec{\sigma};\vec{\xi}\right) &= 1-\exp\left[i\Phi_s\left(\vec{\rho};\vec{r};\vec{\sigma};\vec{\xi}\right)\right],\\
\Phi_s\left(\vec{\rho};\vec{r};\vec{\sigma};\vec{\xi}\right) &= \vec{\rho}\cdot\vec{E}_s(\vec{r}) + \vec{\sigma}\cdot\dot{\vec{E}}_s(\vec{r}) + \vec{\xi}\cdot\ddot{\vec{E}}_s(\vec{r}).
\end{aligned} \tag{78}$$

In distinction from the previous section, these expressions contain the additional integration over thermal velocities $\vec{u}_s$ of field ions with the velocity distribution function $w_s(\vec{u}_s)$.

Moreover, $\dot{\vec{E}}_s(\vec{r})$ and $\ddot{\vec{E}}_s(\vec{r})$ determine the first and the second time derivatives of elementary electric field, produced by arbitrary field ion of s species in the origin of reference frame and having the same value of relative velocity at $t = 0$:

$$\begin{aligned}
\dot{\vec{E}}_s(\vec{r}) &= \frac{eZ_s}{r^3}\left[3\vec{n}(\vec{n}\cdot\vec{v}_s) - \vec{v}_s\right] \cdot\left[1-\kappa_s(r)+\frac{r}{3}\frac{\partial\kappa_s(r)}{\partial r}\right] + \frac{\vec{v}_s}{3}\frac{eZ_s}{r^2}\frac{\partial\kappa_s(r)}{\partial r},\\
\ddot{\vec{E}}_s\left(\vec{r};\vec{v}_s;\dot{\vec{v}}_s\right) &= \ddot{\vec{E}}_s^{(1)}\left(\vec{r};\dot{\vec{v}}_s\right) + \ddot{\vec{E}}_s(\vec{r};\vec{v}_s),\\
\ddot{\vec{E}}_s^{(1)}\left(\vec{r};\dot{\vec{v}}_s\right) &= \frac{eZ_s}{r^3}\left[3\vec{n}\left(\vec{n}\cdot\dot{\vec{v}}_s\right) - \dot{\vec{v}}_s\right] \cdot\left[1-\kappa_s(r)+\frac{r}{3}\ \frac{\partial\kappa_s(r)}{\partial r}\right] + \frac{eZ_s}{3\,r^2}\ \frac{\partial\kappa_s(r)}{\partial r}\dot{\vec{v}}_s,\\
\ddot{\vec{E}}_s(\vec{r};\vec{v}_s) &= \frac{3eZ_s}{r^4}\left\{\left[2\vec{v}_s(\vec{n}\cdot\vec{v}_s) + \vec{n}v_s^2\right] \cdot\left[1-\kappa_s(r)+\frac{r}{3}\frac{\partial\kappa_s(r)}{\partial r}\right] - 5\vec{n}(\vec{n}\cdot\vec{v}_s)^2 \right.\\
&\quad\cdot\left[1-\kappa_s(r)+\frac{7}{15}\ r\frac{\partial\kappa_s(r)}{\partial r} \left.-\frac{r^2}{15}\ \frac{\partial^2\kappa_s(r)}{\partial^2 r}\right]\right\},
\end{aligned} \tag{79}$$

where $\vec{n}\equiv\vec{r}/r$, and $\vec{v}_s = \vec{u}_s - \vec{u}_r$ is the relative thermal velocity of field ion of "s" species with respect to the test particle with velocity $\vec{u}_r$. It is seen that there are summands, containing $\dot{\vec{u}}_s$, that is,

$$\dot{\vec{v}}_s = \dot{\vec{u}}_s\ -\ \dot{\vec{u}}_r = \frac{eZ_s}{m_s}\vec{F}(\vec{r}) - \frac{eZ_r}{m_r}\vec{F}(0), \tag{80}$$

where $\vec{F}(\vec{r})$ is the microfield in the location point of field ion of "s" species, and m_s, m_r are masses of the field ion and test particle correspondingly. These terms cause nonlinearity and loss of locality of joint distribution, if to include them into the expression for the second derivative.

Indeed, the microfield distribution at the origin of reference frame becomes dependent on microfield values in the total space. This controversy could be removed, assuming that the thermal velocities of field ions are constant due to stationarity conditions, as it was done in Chandrasekhar papers [19, 20], namely, $\dot{\vec{u}}_s = 0$ for all s. In the opposite case, the back reaction of field ions requests special study, which is beyond the frames of the present work.

On the other hand, there are terms due to polarization effects as well. That is why the results of Chandrasekhar and von Neuman could be reproduced only after discarding the neutralization background of electrons by setting $N_e = 0$. Here, it is supposed as before that all field ions are bare nuclei.

This joint distribution provide instantaneous low-frequency distribution function of individual (but many-body) ion component of plasma microfield and its time derivatives, which are defined on time scales τ of the order of $\omega_{\mathrm{pe}}^{-1} \ll \tau \ll (v_i N_i^{1/3})^{-1}$, where ω_{pe} is the electron plasma frequency, v_i is the relative thermal velocity of field ions with respect to the test particle.

We note that this distribution in distinction from Chandrasekhar results includes effects of neutralizing background of plasma electrons and its polarization (or in the other words the appearance of nonuniformity in distribution of free electrons). The convolution over components $\vec{F}$ or $\dot{\vec{F}}$ leads to separate distributions of the field and its derivatives, and after corresponding simplifications reproduces known results.

As it was already pointed out, the computation of joint distributions is very complex problem and it is possible now to present only some unique examples of such calculations [58, 70, 76], which contain as a rule many additional approximations and simplifications (only the projections of such functions are calculated with fixed values of a part of variables).

So, one of few methods to characterize these distributions is the calculations of their moments. This is achieved by the convolution over $d^3\ddot{\vec{F}}$. After that, it is possible to obtain the following expressions for the first moment of $\dot{\vec{F}}$ for a given value of $\vec{F}$:

$$
\begin{aligned}
W\left(\vec{F}\right)\left\langle\dot{\vec{F}}\right\rangle_{\vec{F}} &= \frac{N}{(2\pi)^3}\int d^3\vec{\rho}\exp\left[-i\vec{\rho}\cdot\vec{F}\right]\cdot A(\rho)\vec{D}(\vec{\rho}),\\
\vec{D}(\vec{\rho}) &= \vec{D}^{(o)}(\vec{\rho}) + \vec{D}^{(1)}(\vec{\rho}),\\
\vec{D}^{(o)}(\vec{\rho}) &= \sum_s C_s \vec{D}_o^{(s)}(\vec{\rho}),\\
\vec{D}^{(1)}(\vec{\rho}) &= -\frac{N}{2}\sum_{s,s'} C_s C_{s'}\vec{D}^{(ss')}(\vec{\rho}),\\
\vec{D}^{(s)}(\vec{\rho}) &= \int d^3\vec{u}_s \;\; w_s(\vec{u}_s)\int d^3\vec{r}\, g_{sr}(\vec{r})\\
&\quad\cdot\exp[i\Phi_s(\vec{\rho};\vec{r})]\dot{\vec{E}}_s(\vec{r}),\\
\vec{D}^{(ss')}(\vec{\rho}) &= \int d^3\vec{u}_s\, w_s(\vec{u}_s)\int d^3\vec{u}_{s'} \;\; w_{s'}(\vec{u}_{s'})\\
&\quad\cdot\int d^3\vec{r}_1\int d^3\vec{r}_2\\
&\quad\cdot\left[g_{ss'}(\vec{r}_1;\vec{r}_2) - g_{sr}(\vec{r}_1)\cdot g_{s'r}(\vec{r}_2)\right]\\
&\quad\cdot\left\{\dot{\vec{E}}_s(\vec{r}_1)\exp[i\Phi_s(\vec{\rho};\vec{r}_1)]\right.\\
&\qquad\cdot\left(1-\exp[i\Phi_{s'}(\vec{\rho};\vec{r}_2)]\right) + \dot{\vec{E}}_{s'}(\vec{r}_2)\\
&\qquad\cdot\left.\exp[i\Phi_{s'}(\vec{\rho},\vec{r}_2)]\left(1-\exp[i\Phi_s(\vec{\rho},\vec{r}_1)]\right)\right\}.
\end{aligned}
\tag{81}
$$

These formulas [80, 81] could be rewritten in terms of microfield distribution function similar to previous section:

$$
\begin{aligned}
&W\left(\vec{F}\right)\left\langle\dot{\vec{F}}\right\rangle_{\vec{F}}\\
&\quad= N\left[\sum_s C_s\int d^3\vec{u}_s\, w_s(\vec{u}_s)\int d^3\vec{r}\right.\\
&\qquad\cdot g_{sr}(\vec{r})\dot{\vec{E}}_s(\vec{r})\,W\left(\vec{F}-\vec{E}_s(\vec{r})\right)\\
&\qquad-\frac{N}{2}\sum_{ss'} C_s C_{s'}\int d^3\vec{u}_s\, w_s(\vec{u}_s)\int d^3\vec{u}_{s'}\; w_{s'}(\vec{u}_{s'})\\
&\qquad\cdot\int d^3\vec{r}_1\int d^3\vec{r}_2\left[g_{ss'}(\vec{r}_1;\vec{r}_2) - g_{sr}(\vec{r}_1)\cdot g_{s'r}(\vec{r}_2)\right]\\
&\qquad\cdot\left\{\dot{\vec{E}}_s(\vec{r}_1)\left[W\left(\vec{F}-\vec{E}_s(\vec{r}_1)\right)\right.\right.\\
&\qquad\qquad\left.-\;W\left(\vec{F}-\vec{E}_s(\vec{r}_1)-\vec{E}_{s'}(\vec{r}_2)\right)\right]\\
&\qquad+\dot{\vec{E}}_{s'}(\vec{r}_2)\left[W\left(\vec{F}-\vec{E}_{s'}(\vec{r}_2)\right)\right.\\
&\qquad\qquad\left.\left.-W\left(\vec{F}-\vec{E}_s(\vec{r}_1)-\vec{E}_{s'}(\vec{r}_2)\right)\right]\right\}\Bigg].
\end{aligned}
\tag{82}
$$

The expressions for $\ddot{\vec{F}}$ could be obtained in a similar manner by substitution $\ddot{\vec{E}}_s(\vec{r})$ instead of $\dot{\vec{E}}_s(\vec{r})$ in the right part of corresponding equations, if to put $\dot{\vec{u}}_s = 0$ for all $\{s\}$ as was pointed out earlier.

To obtain results in more detail, the approach, presented in the previous section, and the connection of spatial and time derivatives of the field, produced at test particle with the velocity $\vec{v}$ in the origin of reference frame, are used (compare with [19–21]):

$$
\left\langle\dot{\vec{F}}_i\right\rangle_{\vec{F}} = \left\langle\frac{\partial F_i}{\partial x_k}\right\rangle_{\vec{F}}\;\langle\dot{x}_k\rangle_{\vec{v}}\;\vec{e}_i,
\tag{83}
$$

where $\vec{e}_i$ are unit vectors of Cartesian reference frame, and the symbol $\langle\cdots\rangle_{\vec{v}}$ designates the average over thermal velocities of field ions. Substituting then in these expressions, the first moments of nonuniformity tensor, obtained in the previous section, we come to the next compact formulae (compare with [19–21]):

$$
\left\langle\frac{\partial F_i}{\partial x_k}\right\rangle_{\vec{F}} = \frac{2\pi e N}{3}\left\{B_D(\beta)\left(\frac{3F_iF_k}{F^2}-\delta_{ik}\right) + 2\;\delta_{ik}\;B_{DO}(\beta)\right\},
\tag{84}
$$

where the universal functions $B_D(\beta)$ and $B_{DO}(\beta)$ are determined in the previous section.

After substitution and convolution over indexes of components of $\vec{F}$ and $\vec{u}_r$ the sought result is

$$
\begin{aligned}
\left\langle\dot{\vec{F}}\right\rangle_{\vec{F}} = -\frac{2\pi e N}{3}\{&B_D(\beta)\left(3\;(\vec{n}_F\cdot\vec{u}_r)\vec{n}_F - \vec{u}_r\right)\\
&+2\;B_{DO}(\beta)\vec{u}_r\},\quad n_F \equiv \frac{\vec{F}}{F}.
\end{aligned}
\tag{85}
$$

The contribution from microfield variation disappears due to assumed isotropy of velocity distribution function of field ions.

It is seen that contributions of polarization effects, included in $B_D(\beta)$ and $B_{DO}(\beta)$, have different signs in the expression for vector oriented along $\vec{u}_r$, but, as it is possible to assure, they do not compensate each other due to the different symmetry of interactions (quadrupolar and scalar). This does happen in the coefficient in front of $\vec{F}$. Using the relation

$$\dot{\vec{u}}_r = \frac{eZ_r}{m_r}\vec{F}(0), \tag{86}$$

where m_r is the mass of test particle, it is possible to write down the part of the moment over the second field derivative, assuming $\dot{\vec{u}}_s = 0$ for all $\{s\}$due to the independence of ensemble of field particles on time:

$$\left\langle \ddot{\vec{F}}^{(1)} \right\rangle_{\vec{F}} = -\frac{4\pi e^2 Z_r N}{3}\left[B_D(\beta) + B_{DO}(\beta)\right]\frac{\vec{F}(0)}{m_r}. \tag{87}$$

This expression with the opposite sign is proportional to "zz" component of microfield nonuniformity tensor in the reference frame, in which $\vec{F}$ is directed along $\vec{OZ}$:

$$\left\langle \ddot{\vec{F}}^{(1)} \right\rangle_{\vec{F}} = -\,eZ_r\left\langle \frac{\partial F_z}{\partial Z}\right\rangle_{\vec{F}\,\|\vec{OZ}}\frac{\vec{F}(0)}{m_r}. \tag{88}$$

This result describes the influence of neutralizing background on dynamical friction [80, 81], that is, the consequence of plasma polarization effects. These terms do not disappear in the (OCP) limit for ions, when the neutralizing background has the constant density. So, the complete recover of the Chandrasekhar and von Neuman results [19–21] is possible only if to equal artificially this density to zero. The other results on this issue could be found in [76–79], where for advancing in the region of strongly coupled plasmas, the MD methods and models, used in theory of liquids, are applied.

It should be noted that in a row of problems on ion dynamics, the joint distribution functions of microfield and its time derivatives were also introduced in the case, when the total field is simultaneously defined by its individual and collective components. This question was considered in detail in [80, 81, 168]. In particular, the derivation of the expression for the second moment of the first derivative of total microfield was analyzed:

$$\left\langle \frac{\dot{\vec{F}}_{\perp}^{\,2}}{F^2}\right\rangle_{\vec{F}}, \tag{89}$$

which plays dominating role in the consideration of fluctuating microfield time evolution (ion dynamics) on small in comparison with $\omega_{pi}^{-1} \gg (N_i^{1/3}\, v_{Ti})^{-1}$ (or $R_{Di}\, N_i^{1/3} \gg 1$) time scales [80, 81]. The principal result of [80, 81] is that the asymptotic of this moment for small values of reduced summary field does not change in comparison with the results of Chandrasekhar and von Neuman (see [17, 19–21, 80, 81, 168]) in the case of three-dimensional isotropic distribution of collective fields and with account of the electron Debye screening and ion-ion correlations in individual component. Thereby, it was shown that Griem result [169–171] about the finiteness of the second moment values in the limit of small values of summary field is incorrect, but is the consequence of inconsistent performing of averaging and violation of the additivity condition in [169–171]. As these incorrect results [169–171] look like graphically. the finiteness of the second moment (89) in the limit of small values of summary microfield is shown in Figure 18 from [170].

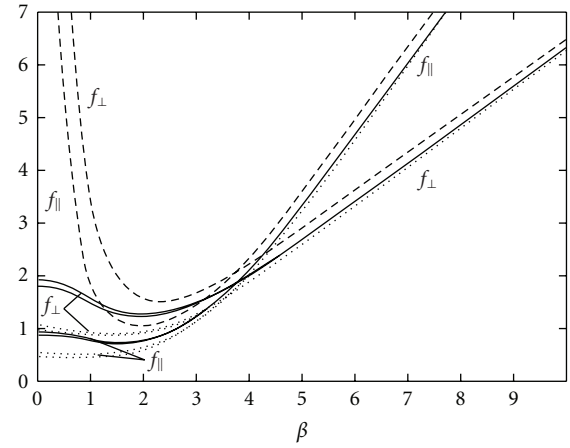

Figure 18: Reduced values of longitudinal and perpendicular second moments according to [170, 171]: dashed curves correspond to Chandrasekhar and von Neuman results [19–21] for fixed velocity values of test particle; solid curves are erroneous results [170, 171] with account of Doppler broadening (see [170]); the upper curves according to [170, 171] correspond to $N = 10^{17}$ cm^{-3}, $T = 12\,700$ K, and lower curves to $N = 3\ 10^{17}$ cm^{-3}, $T = 14\,800$ K; dotted curves the results that account for Debye screening due to authors [170] statements; the axis of abscisses shows the reduced microfield values.

Alas it is worthy to note that the results presented in this figure, as if corresponding to the account of Debye screening, are obtained with the help of rather unfounded and unreliable procedure (see [80, 81, 172, 173]). It must be noted that in Griem papers [169–171], the derivation of results from [168] was repeated word to word, except absent in [168] incorrect resume on finiteness of the second moment (89) in the limit of small values of summary microfield. It follows from this analysis that the collective component becomes more rapid than individual one with increase of plasma coupling, and at $\Gamma \sim 1$, the characteristic scales of their time variation are of the same order of magnitude.

In conclusion of this section, it is necessary to mention that the first attempt to generalize Chandrasekhar and von Neuman results [19–21] for the first and the second moments of the first time derivative of microfield accounting for Debye screening but without ion-ion correlations in the middle of seventieth was made by Hey and Griem [172, 173]. They used expansion over parameter a. In this

respect, it is similar to Margenau approach, who attempted by expansion over parameter R_c/R_0 (R_c is the Coulomb radius, R_0 is the mean interparticle distance) to account for the influence of ion-ion repulsion on distribution functions [174]. Regrettably, such types of expansions are poor even for establishing asymptotic limits and in fact integrally are inapplicable for these functions due the absence of a real small expansion parameter. Related to these approaches is the method of the characteristic functions (or thermodynamic potentials) expansion over Fourier variable in the absence of any parameter of infinitesimality, which very often resort to in theory of liquids, where it appears under term of "λ" expansion [8]. The similar mathematical problems arise in the method of collective variables of Bohm and Pines [30, 31] also. The development of microfield theory has shown that there is no proof of convergence of such a type of expansions, and thereby their application is unjustified [80, 81].

2.10. Asymptotic Expansions. As was already noted, in fact, all distribution functions and connected with them universal functions have universal form of asymptotic at large and small values of reduced field, but at the same time, the procedure of those asymptotic derivation from general expressions as a rule is rather complicated and laborious. In the case of not so large plasma coupling, at large values of reduced microfield asymptotic should approach the distribution of nearest neighbor NN. For ions of the same species with the charge Z, the following relations are valid [53–62, 72, 73, 80, 81]:

$$\begin{aligned}
W_{\mathrm{NN}}(\beta) &= \frac{15}{4(2\pi)^{1/2}Z^2}\frac{y^5 g(y)}{1+ay+a^2y^2/2}\\
&\quad\cdot\exp\left[ay-\frac{1}{Z}\,\frac{15}{2\sqrt{2\pi}}\int_0^y dx\, x^2 g(x)\right],\\
B_{\mathrm{NN},D}(\beta) &= \frac{3}{Z\,W_{\mathrm{NN}}(\beta)}\frac{y^2(1+ay+a^2y^2/3)g(y)}{1+ay+a^2y^2/2}\\
&\quad\cdot\exp\left[-\frac{1}{Z}\frac{15}{2\sqrt{2\pi}}\int_0^y dx\, x^2 g(x)\right]\\
&\simeq \frac{4\sqrt{2\,\pi}\,Z}{5\,y^3}\left(1+ay+\frac{a^2y^2}{3}\right)\exp(-ay),\\
B_{\mathrm{NN},D0}(\beta) &= C_\infty+\frac{1}{2\,ZW_{NN}(\beta)}\frac{a^2y^4 g(y)}{1+ay+a^2y^2/2}\\
&\quad\cdot\exp\left[-\frac{1}{Z}\frac{15}{2\sqrt{2\pi}}\int_0^y dx\, x^2 g(x)\right]\\
&\simeq C_\infty+\frac{2(2\pi)^{1/2}a^2Z\,\exp(-ay)}{15y},
\end{aligned}\tag{90}$$

where the quantity y is expressed in units of r_0 and is determined by

$$\beta = Z\frac{\exp(-ay)}{y^2}(1+ay),\tag{91}$$

and C_∞ is determined from the other relation (see [57–62]). When ay is small enough, $\beta \simeq Z/y^2$, then

$$\begin{aligned}
B_{\mathrm{NN},D}(\beta) &\simeq \frac{4\sqrt{2\,\pi}}{5}\,\frac{\beta^{3/2}}{Z^{1/2}},\\
B_{\mathrm{NN},DO}(\beta)-C_\infty &\simeq \frac{2(2\pi)^{1/2}a^2}{15}\,(Z\beta)^{1/2}\exp\left(-a\left(\frac{Z}{\beta}\right)^{1/2}\right).
\end{aligned}\tag{92}$$

3. Fluctuating Microfields in Plasmas

As was already mentioned several times, the thermodynamic formalism not always happens to be adequate for problems, where the dynamics of time evolution of dipole interactions and actually plasma microfields is essential. Especially, this became critical for the sufficiently large effective time scales of evolution. However, in these cases, the statistical methods of modeling were developed, including as a rule two stages: (i) statistical modeling of system time dynamics, (ii) statistical average over random sampling from results of previous stage. The systems that require such an approach conventionally are called the systems "with partial memory loss" [7], when in spite of stochastic character of the process, the result often depends on prehistory of system evolutional dynamics.

3.1. Correlation Function Expansion over Time. In a row of problems and approaches, it is sufficient to follow only the very initial stage of microfield time evolution. Then it is possible to use the expansion over time of the state evolution operator, and reduce the problem solution to finding various moments of joint distribution functions of microfield over the microfield time derivatives at the starting moment of evolution ($t = 0$) [17, 19–21, 54–56, 74–81]. Chandrasekhar and von Neuman [19–21] and V. I. Kogan were the first who used this. This method could be applied to characterize the evolution of microfield distributions [19–21, 74–81, 104, 105] itself. In particular, this method allows to separate the ion dynamics contributions due to the different physical effects like the amplitude (rotation of microfield vector) and phase modulations (variation of microfield module) and the finite life time of Stark substates due to electronic collisions [168].

3.2. Method of Model Microfield. The method of model microfield (MMM) is known for providing the closed analytical expression for the spectrum of evolution operator $U(t)$ [86–94, 146], reducing the time dependent problem to the statistical average of static evolution operators $U_{\mathrm{St}}(t)$ over quasistatic distributions of microfield:

$$\begin{aligned}
\langle U(\omega)\rangle_{\mathrm{MMM}} &= \langle U_{\mathrm{St}}(\omega+i\nu)\rangle+\langle \nu U_{\mathrm{St}}(\omega+i\nu)\rangle\\
&\quad\cdot\left\langle \nu I-\nu^2 U_{\mathrm{St}}(\omega+i\nu)\right\rangle^{-1}\langle \nu U_{\mathrm{St}}(\omega+i\nu)\rangle,
\end{aligned}\tag{93}$$

where ν designates $\nu(\vec{F})$ (the frequency of jumps in the MMM Kangaroo-process), $U_{St}(\omega + i\nu)$ is the Laplace transform at $z = -i\omega + \nu$ of the static evolution operator, the symbol $\langle \cdots \rangle$ designates the average over the static microfield distribution function $W(F)$, I is the unit operator. This expression is valid if the evolution operator is the function of only the difference between final and initial moments of time. Hence, MMM is applicable only in the absence of the $U(t)$ explicit time dependence. There is essential assumption in the derivation of this general result that microfield changes in time by jumps and only by their amplitude. The frequency of jumps $\nu(F)$ depends on the microfield value F at the given time moment. This character of changes was called Kangaroo-process [86–94, 146]. To close the procedure, it is necessary to know $\nu(F)$. The most wide-spread way to close the MMM system of equations and definition of $\nu(F)$ is based on equating the microfield correlator $C(t)$ to the mean square of microfield with the weight function equal to the the product of the static microfield distribution function $W(F)$ and the factor $\exp[-|\nu(F)| \cdot t]$ with the exponential decay in time with the rate $|\nu(F)|$ [86–94]:

$$C(t) = \left\langle \vec{F}(t) \cdot \vec{F}(0) \right\rangle = \int_0^\infty dF \; W(F) F^2 \exp[-\nu(F)t]. \tag{94}$$

This significant correlation function $\langle \vec{F}(t)\, \vec{F}(0) \rangle$ was considered in many works: in the absence of Debye screening implicitly by Cohen, Spitzer and Routly [128]; for the gas of Coulomb particles by Kogan [129]; in the general form on the basis of kinetic plasma theory by Rosenbluth and Rostocker [130, 131]; by Taylor [132]; with account to Debye screening by Lewis [133]. This correlation function could be expressed via integral from the plasma structure factor $S(k, \omega)$ [4, 5, 7–10] and has direct connections with the problems of collisional transport and determination of plasma conductivity. (In recent work of Gordienko [134] an attempt was made to reconsider the canonical results that the microfield correlator effectively acquires binary form in the process of average [129]. In [134], on the basis of quite unclear and entangled computations, the statement is made about the existence of nonbinary, many-body and essential contribution to the microfield correlator. However, augmentations and derivations in [134] are based on a row of rather strong, unreliable, and difficult to test assumptions of statistical and mathematical character, which does not allow to consider the results of [134] as correct.) Thus, in MMM, the known analytical expression is substituted in the left-hand side of (94), derived in [89, 90] for classical plasmas in assumption of rectilinear trajectories and static Debye screening in the neutral point:

$$C(t) = \frac{4\pi N\, e^2}{D} \left\langle \left(\frac{D}{\nu t} - \frac{1}{2} \right) \exp\left(-\frac{\nu t}{D} \right) \right\rangle_\nu, \tag{95}$$

where $\langle \cdots \rangle_\nu$ designates the average over velocities of field particles and

$$\begin{aligned} C(t) &= \frac{4\pi N\, e^2}{t} \left\langle \frac{1}{\nu} \right\rangle_\nu \left[1 + x^2 - \pi^{1/2} x \left(x^2 + \frac{3}{2} \right) \right. \\ &\qquad \left. \cdot \exp(x^2) \operatorname{erfc}(x) \right], \\ \operatorname{erfc}(y) &= \frac{2}{\sqrt{\pi}} \int_y^\infty \exp(-s^2)\, ds, \qquad x \equiv \frac{\omega_p t}{\sqrt{2}}, \\ \left\langle \frac{1}{\nu} \right\rangle_\nu &= \left(\frac{2\, m}{\pi k_B T} \right)^{1/2}. \end{aligned} \tag{96}$$

Often the paper of Rosenbluth and Rostocker [130, 131] is unreasonably connected with this result.

In MMM additionally the μ- ion model (or the ion of reduced mass, corresponding to the masses of perturbing and test particles) is used. The result for $C(t)$ is applied to the same extent as for electrons and as for ions, because the values of Debye radius, density, velocity, and reduced mass of the pair of test and perturbing particles D, N, v, m correspondingly are not specified.

The account of trajectory curvature in the case of calculations of $\langle \vec{F}(t)\, \vec{F}(0) \rangle$ in the charged point was performed numerically in [94]. However, it is not sufficient especially for strongly coupled plasmas.

The application of these methods [86–94, 128–134] to ions suffers from essential defect in determining $\nu(F)$. The thing is that the correlator of the fields at test-charged particle could be expressed as the correlator of accelerations, the integral of which over time should be equal to zero [8, 9]. At the same time, the analytical result for such a correlator is unknown, and that is why often the correlator in neutral point is used, which does not satisfy this condition.

It is worthy to note that MMM practical realization requests usage of rather tedious and complex procedure for the reduction of multiple products of irreducible spherical operators, that is not published yet.

For the case of charged test particle, Boercker et al. proposed the kinetic model [95], analogous to used in theory of liquids [8–12]. In this model, the frequency of microfield changes is constant $\nu(F) = \text{const}$, and does not depend on microfield value. By special selection of parameters, based on the introduction of the dependence on frequency detunings $\Delta\omega$, and using the relation with diffusion coefficient, the authors were able to satisfy the condition of conversion to zero of the integral of $\langle \vec{F}(t)\vec{F}(0) \rangle$ over time in the charged point [95]. At the same moment, this model contains a good few of other assumptions, which could not allow to give unequivocally the preference to that or another method in the case of the electric field description at test ion.

For calculations of this correlator, the MD methods are applied also, but each concrete case corresponds to the fixed plasma parameters, and it is difficult to detect scaling. The study of this correlator in strongly coupled plasmas using methods from the theory of liquids and Molecular Dynamics (MD) simulations was performed in the series of papers by Dufty et al. [79, 96, 104–107]. In [79, 96], certain criticism

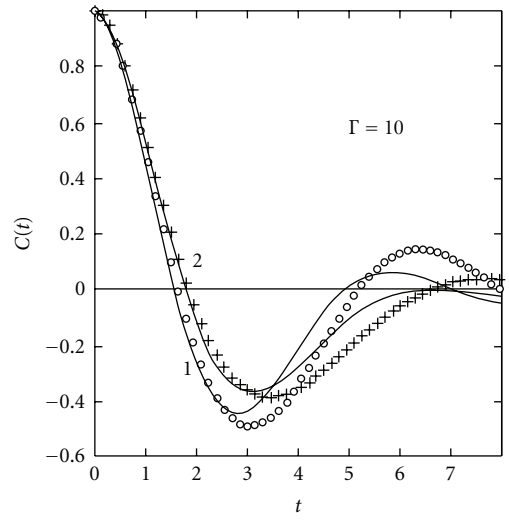

FIGURE 19: Model microfield correlation function $C(t)$ according to [96] in charged point for $\Gamma = 10$: 1 Coulomb interaction; 2 with account to Debye screening for $k = r_{De}/R_i = 1$; points-results of MD simultions.

on MMM is expressed in the case of its application for description of microfield fluctuations at charged test particle. This nevertheless seems rather strange, since MMM could allow any closing in the sense of $\nu(F)$ calculations. For example, the corresponding results for $C(t) \equiv \langle \vec{F}(t)\, \vec{F}(0) \rangle$ for small values of electron plasma-coupling parameter (when $R_{De} = R_i$, R_i is the ion sphere radius in OCP) from [96] are presented in Figure 19. It should be pointed out that the parameter of screening k in this model is uniquely related to plasma coupling parameter Γ, which in this example is about 10. As could be seen in Figure 19, $C(t)$ is alternating-sign function that assures the conversion to zero of $\int_0^\infty dt C(t) = 0$. There were also attempts to derive the expression for correlator in the neutral point on the basis of cluster expansion formalism [97] (see also [79]), however, the application of these results in MMM itself led to appearance of strange, nonphysical consequences [98].

In this respect, it is necessary to take caution to progress in the construction of $\nu(F)$ and $C(t)$ because insignificant peculiarities in the behavior of this quantities could lead to unforeseen nonphysical spectrum singularities. This is the reflection of the fact that per se here there is situation of the so-called "ill-posed inverse problem."

Currently, there is also another significantly developed method of Frequency Fluctuation Model (FFM) [99, 100], ideologically adjoining to MMM. However, its principal difference is that this model to the more extent than MMM is a way to describe the spectra in the fluctuating microfield than the method to describe microfield characteristics itself. It is based on the assumption of the microfield fluctuation frequency independence from the value of the electric microfield strength, and in total, the statistical problem settings correspond more to Kubo resolvent (see [88, 146]). On the other hand, there is a possibility to model this frequency using the methods from theory of liquids. Due to application of the latter effectively the fluctuation frequency starts to depend on frequency detunings from the line center [95, 99, 100]. Then, the limits of small and large frequency detunings could be expressed via "fundamental" parameters (see [79, 95, 99, 100]). It was already mentioned that for some time, the used $\nu(F)$ was obtained also in the process of special MD simulations for corresponding parameters, which up to now is rather laborious procedure. Regretfully, the details of published FFM formulation do not allow to use it freely for practical calculations.

3.3. Method of Molecular Dynamics. The method of molecular dynamics is the simultaneous self-consistent solution of equations of motion for the finite number of particles $\mathcal{N}$ in the finite cell and allows to determine the time evolution of summary electric microfield, acting on the test particle [101–109].

The cell size is defined from the similar considerations as in the Monte-Carlo method [34–39]. However, the simultaneous modeling of electrons and ions was not managed to succeed even on the current supercomputers not only due to the large difference of characteristic time scales but also due to the complexity of sound accounting for the effects of attraction between particles with the opposite signs of charge.

As a rule, the quasiparticles are used with Debye screening by plasma electrons. The numerical calculations could be performed, for example, in cubic cell with periodic boundary conditions, or elastic, or isotropic scattering on its borders [108, 109]. If to use in calculations ensembles from 50 and 120 particles, the accuracy of results makes up about ~10%. The trajectories in the system are evaluated on time scales much larger than the correlation time $\tau_c \sim r_0/v_i$, where $r_0 \sim (N_e/Z)^{-1/3}$ is the mean distance between ions, v_i the mean ion velocity with respect to the emitter at rest. During integration, the conservation of the total energy of the system is controlled. Also, the test calculations on reproduction of results for the static distribution functions are performed [104–106], and on their basis, the additional subsidiary algorithms for convergence acceleration are introduced [104–107]. The other methods for acceleration of convergence and reduction of fluctuations in the results of computations with regard to the concrete mathematical setting of that or another physical problem are used as well.

In the majority of performed MD calculations, the μ-ion model was used. Nevertheless, the separate modeling of the test particle motion is possible as well. The final result is obtained by an average over the large number of "histories" of time evolution. Following large effective time intervals, MD had rather large fluctuations that, for example, made difficult to recover impact limit in broadening by ions [101–109].

The MD was used to study the dependencies of microfield time evolution [105, 106, 135–137], the characteristic time and spacial scales of screening setting during simulations of microfield distribution functions [135–137] (compare [84, 85, 125–127]). However, in [135–137] the particles with negative sign had the same mass as positive

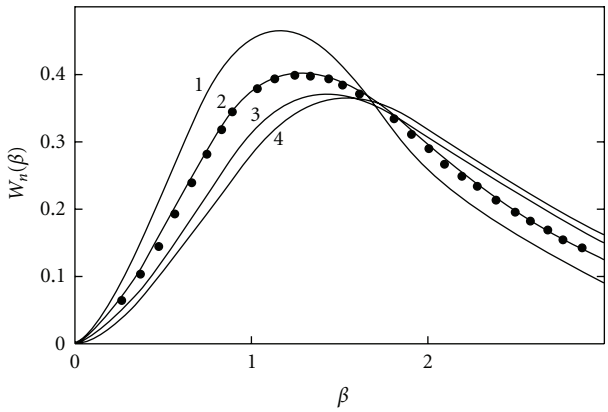

Figure 20: Distribution of static ion microfield [135], produced by finite number $\mathcal{N}$ of noninteracting particles, placed in cube: 1 $\mathcal{N} = 4$; 2 $\mathcal{N} = 27$; 3 $\mathcal{N} = 1000$; 4 Holtsmark distribution; points-microfield distribution for 27 particles, placed in sphere.

ions, which did not allow to model the real plasma screening of ions by electrons. In series of papers of these authors, the attention was payed to the effect of finiteness of particles number in the effective sphere of interaction, which formally did not permit to switch to thermodynamic limit:

$$N = \lim_{\mathcal{N}\to\infty, \mathcal{V}\to\infty} \frac{\mathcal{N}}{V}, \tag{97}$$

being the key condition during conducting of thermodynamic averages. Here, $\mathcal{N}$ is the total number of particles, V is the total volume, N is the particles density. The display of the finiteness of particles number effects could be followed by results of modeling [135], presented in Figure 20. On the other hand, it is seemed that, particularly, the damping of this influence is achieved by operation with the large number of tracked microfield time evolutions (configurations) during the statistical average and the reduction of results dispersion [101–109]. It follows from results of modeling [135–137], presented in Figure 21, that Coulomb interaction shifts somehow the maximum of distribution in the direction of small fields with respect to the case of ideal plasma with noninteracting quasiparticles. However, this shift is much smaller than the shift, arisen due to hypothetic Debye screening [135–137]. In other words, according to [135–137], the distribution of instantaneous microfields does not coincide with Debye field, which is evidently the result of average over sufficiently large time interval. At the same time the distribution of summary field experience more essential shift [135–137] than the distribution of ion field, as far as the correlation of like sign charges is less essential than the correlation of charges with opposite signs.

At the same moment in cited works [135–137], the question of applicability of static Debye shielding to the modeling of the electric fields of plasma ions was considered. However, as was assumed from intuitive notions, the Debye shielding is settled for rather large time intervals in comparison with characteristic time scales of the plasma electrons electric fields variation. That is why the MD instantaneous microfield distribution for this case becomes more similar to the

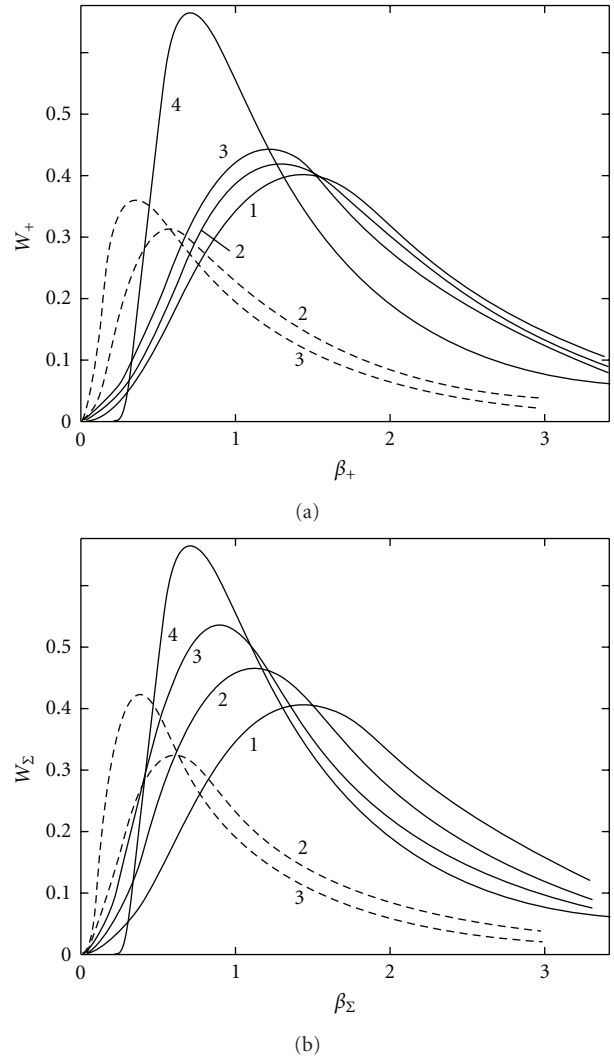

Figure 21: Distribution of static ion microfield [135], produced by positive charges (a) and by charges of both signs (b) (solid lines correspond to Coulomb interaction, dashed lines to hypothetic microfield distribution with Debye screening): 1: $T \to \infty$ modified Holtsmark distribution accounting to finite number of particles in modeling; 2: $T = 1$ eV, plasma coupling parameter $d \equiv (r_c/R_0)^3 = 0.006$; 3: $T = 0.5$ eV, $d = 0.05$; 4 is nearest neighbor distribution $W(\beta) = (3/2)\,\beta^{-5/2}\exp[-\beta^{-3/2}]$ (solid lines are normalized by condition $\int d\beta W(\beta) = 1$, dashed ones by-$\int d\beta W(\beta) = 1/2$; density of like-sign charges $N = \mathcal{N}/R^3 = 10^{18}\,\mathrm{cm}^{-3}$, $\mathcal{N} = 27$, $R = 0.03\mu$; total density of particles $2N$, $2\mathcal{N} = 54$; $\beta_+ = F_+/F_{+,0}$, $\beta_\Sigma = F_\Sigma/F_{\Sigma,0}$, $F_{+,0} = (4\pi\,\mathcal{N}/3)^{2/3}\,e$, $F_{\Sigma,0} = 2^{2/3}F_{+,0}$).

Holtsmark distribution [135–137] than to the Ecker-Müller one. At the time when the works of Yakovlenko et al. were performed, it was not yet possible to judge on the validity of conventional results for the microfield distribution functions (MDFs) of the low-frequency ion component of plasma microfield with static Debye screening, since they could manage joint simulations with only heavy negative particles, not electrons. However, after several decades, the power of computers allowed to consider and realize such task. Professor Sergey Yakovlenko spoke against implementation

of the term "molecular dynamics" in the case of plasma proposing instead the term "method of dynamics of many particles."

Indeed, recently within the certain assumptions on interaction potentials, MD modeling of plasma electrons and ions electric fields action on the emitter was realized simultaneously on the same footing with account of correlations between them [138, 139, 182, 183]. The principal moment, which allows to perform such modeling, is the replacing of attracting ion-electron Coulomb potential at the small distances either by finite potential or by potential of "impermeable sphere." Moreover, of course, this becomes possible also due to the evident significant progress in recent MD programming, that allowed to consider now the very tiny time steps and huge numbers of evolution histories [182].

In [138, 139], the results of these rather detailed and interesting studies were related only to consideration of evolution of plasma electrons microfield simultaneously with the evolution of ion field with switched off and switched on interaction between electrons and ions. Firstly, this program was realized in [182]. These results were further developed in [182, 183] that we follow in what follows. In [182, 183], the interaction potential of particles with the same sign is taken in the form

$$V_{ee,ii}(r) = \frac{e^2}{r}\ \exp\left(-\frac{r}{\lambda}\right), \tag{98}$$

where λ is taken to be about a half of the size of simulation cubic cell $\sim \mathbf{s}/2$. The electron-ion potential is approximated with the function

$$V_{ei}(r) = -\frac{e^2}{r}\ \left[1 - \exp\left(-\frac{r}{\delta}\right)\right] \exp\left(-\frac{r}{\lambda}\right), \tag{99}$$

where the short-range regularization parameter δ is chosen to satisfy in the limit of small $\mathbf{r}$ the value of ionization potential of hydrogen atom. The total electric microfield is evidently represented as the sum of summary plasma ions and electrons fields, which is subdivided into slow $\mathcal{S}$ and fast $\mathcal{F}$ microfield components:

$$\vec{E}(t) = \vec{E}_i(t) + \vec{E}_e(t) = \vec{E}_{\mathcal{S}}(t) + \vec{E}_{\mathcal{F}}(t). \tag{100}$$

Introducing in [182] the average of the electron summary field $\overline{\vec{E}_e(t)}_{\Delta t}$ over variable time interval Δt provides the tool for analysis of stochastic fluctuations:

$$\overline{\vec{E}_e(t)}_{\Delta t} = -\frac{1}{\Delta t}\ \int_{-\Delta t/2}^{\Delta t/2} dt'\ \vec{E}_e(t - t'). \tag{101}$$

After that, the slow $\mathcal{S}$ and fast $\mathcal{F}$ components are defined as

$$\begin{aligned} \vec{E}_{\mathcal{S}}(t) &= \vec{E}_i(t) + \overline{\vec{E}_e(t)}_{\Delta t}, \\ \vec{E}_{\mathcal{F}}(t) &= \vec{E}(t) - \vec{E}_{\mathcal{S}}(t) = \vec{E}_e(t) - \overline{\vec{E}_e(t)}_{\Delta t}. \end{aligned} \tag{102}$$

At the same time, due to ergodicity [182],

$$\lim_{\Delta t \to \infty} \overline{\vec{E}_e(t)}_{\Delta t} = \left\langle \vec{E}_e(t) \right\rangle = 0. \tag{103}$$

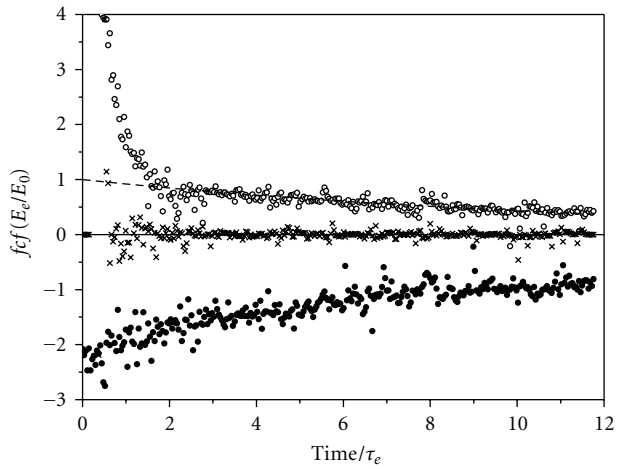

FIGURE 22: MD correlation functions of electric fields for **a = 0.8** from [182] at neutral point: black circles is correlation of summary ion and summary electron fields $\langle \vec{E}_{\text{ion}}(0) \cdot \vec{E}_e(t) \rangle$; open circles $\langle \vec{E}_e(0) \cdot \vec{E}_e(t) \rangle$; crosses is a correlation function of fast component of total microfield $\langle \vec{E}_{F,\Delta t}(0) \cdot \vec{E}_{F,\Delta t}(t) \rangle$ for $\Delta t = 0.4 \cdot \tau_e$; dashes-exponential fit.

The conventional parameters of simulations are the electron-electron and ion-ion mean distance $r_0 = (3/4\pi N_e)^{1/3}$, the mean electric field modulus $E_0 = e^2/{r_0}^2$, the electron thermal velocity $v_e = (k_B T_e/m_e)^{1/2}$, the electron and proton coupling constants $\Gamma = e^2/(r_0 k_B T_e)$, and Debye length $r_D = (k_B T_e/4\pi N_e e^2)^{1/2}$, $\tau_e \sim r_0/v_e$. The conditions were considered with **a = 0.4** and **a = 0.8**, $N_e = 10^{18}\,\text{cm}^{-3}$, $T_e \sim 1$ eV. During simulations, the cell is taken about $\mathbf{s} \sim 3r_D$, and the number of particles in the cell is $\mathcal{N} \sim 1000$. The introduction of λ screening ensures the more rapid convergence of results but has no deal with much more stronger Debye screening [182]. As usual, the periodic boundary conditions allow to address the infinite homogeneous system. During simulations, the total energy is preserved with accuracy about 1%. The authors of [182] correctly noticed that the fast component could not represent the electron fields due to correlations between ion and electrons, while all definitions are the functions of the average time interval Δt that have to be determined from physical peculiarities of the problem, which are beyond the model. To our opinion in the case of line broadening, the detuning from the line center could be such a parameter to require $\Delta\omega\Delta t \sim 1$.

The results for correlation functions presented in Figure 22 along with [182] are very instructive and physically reasonable. The symbol $\langle \cdots \rangle$ means as usual the average over ensemble of microfield evolution histories. The correlation functions itself are common and valuable additional tool for study of fluctuations. In Figure 22, the fast component looses correlation very soon, and the strong anticorrelation of ionic and electron fields is pronounced. The statistical independence of introduction slow and fast microfield components is clearly demonstrated in Figure 22 too.

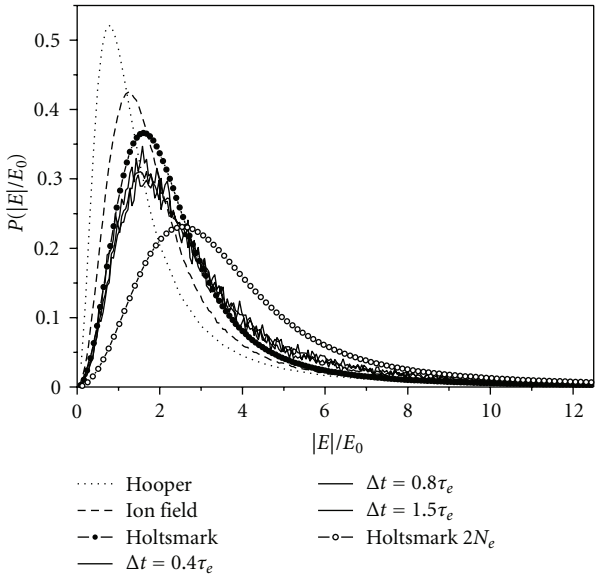

Figure 23: MD distributions at neutral emitters for slow component of total plasma microfield $\mathcal{S}$ from [182] for **a = 0.8** monotonously shifted to smaller reduced microfield values versus increasing intervals of time average Δt.

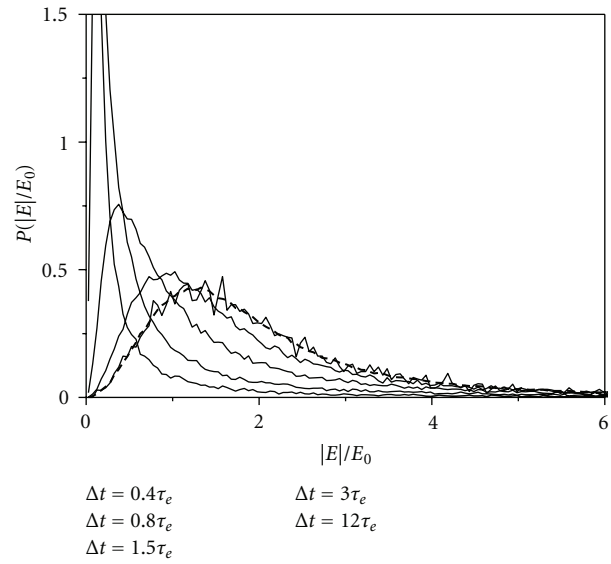

Figure 24: MD distribution functions at neutral emitters for fast component of total plasma microfield $\mathcal{F}$ and for electron distribution function (dashes) from [182] for **a = 0.8**, monotonously shifted to larger reduced microfield values versus increasing intervals of time average Δt.

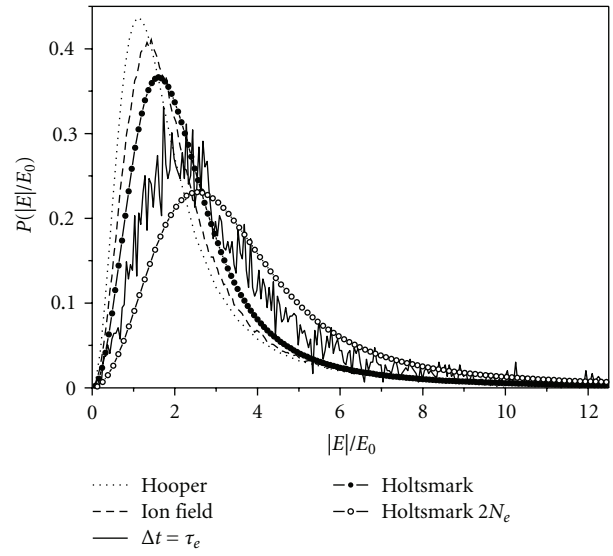

Figure 25: MD distribution function at neutral emitters for slow component of total plasma microfield from [182] for **a = 0.4.**

Astonishingly, the results of simulations in Figures 23 and 25 for slow component qualitatively coincide with previously obtained results [135–137] for heavy negatively charged particles in Figures 20 and 21. So, the main resume is that for instantaneous microfields, the Debye shielding is not realized, while the correlation between electrons and ions shifts the realistic distribution for slow component somewhere in between two Holtsmakians corresponding to densities N_e and $2N_e$ in opposite direction from Hooper or Baranger results, corresponding to the static Debye screening model. However, additionally, it is seen that the ion field distribution function obtained from the slow component in the limit $\Delta t \to \infty$ interestingly differs from the Hooper result, thus showing that in this case the screening effect is not static either.

This shift also detects the electron contribution into the ionic distribution function. In Figure 24, the fast component distribution functions are shifted more far from the ordinate axis as the Δt increases. This is opposite to the behavior of the slow microfield component in Figure 23, which is shifted toward smaller fields while the Δt increases. The authors of [182] thus reasonably state that due to symmetry relations for $\Delta t \to \infty$, both the slow and fast MDF should converge to the same limit—common MDF. It should be noted that the authors of [182] soundly outline the characteristic time scales τ of processes for which the definitions of the fast and slow components are introduced. Of course, like in the works of BM, τ is related to inequality $\tau_e < \tau < \tau_i$ [182]. Resuming discussion of MD simulations in [182], it is worthy to remind earlier attempts of separation of slow and fast microfield components on the basis of rather vague consideration in [180], where no constructive instruments that could allow to realize this general idea were proposed. In contrast, in [182], the logically clear *ab initio* MD simulation method enabling to perform this separation and study physical characteristics of slow and fast components of microfield is created.

The obtained in [182, 183] results put under doubt practically all ones, which were previously obtained on the subject, and bid their reconsideration and confirmation.

Due to its complexity the MD method is computationally time-consuming, and that is why more simple approach of modeling using the motion of particles along the prescribed

type of trajectories becomes sometimes more appropriate. This latter approach could assure the achievement of the same accuracy of calculations as MD using at least the quasi-particle models with the lesser expenditure of computational resources.

3.4. Modeling along Trajectories. The methods of computer simulations using prescribed type of trajectories for particles motion for modeling the microfield time evolution were developed in works of Voslamber and Stamm [101–103], Seidel and Stamm [101–103], Stamm-Smith-Talin and Cooper [104, 105], Gigosos and Cardenoso [140, 141], Hegerfeldt and Kesting [142], Gigosos et al. [143, 144], Kesting [145], and Stambulchik [190].

The method of modeling along the straight or hyperbolic trajectories also uses the finite number of particles $\mathcal{N}$ in the spherical cell of the finite radius "R" [140, 141], which is determined by given plasma density. The trajectory characteristics and localization of the particles inlet are sampled randomly [140, 141], and the particle velocity is sampled with the Maxwell distribution [140, 141]. The interval of velocities is split into $\mathcal{N}$ equal regions, having equal probability of sampling. To preserve isotropy, the orientation of collision plane is spread over angles evenly, and the range of impact parameters b is divided into $\mathcal{N}$ identical regions, having the equal sampling probability, in which the impact parameter value is generated using the following distribution:

$$P(b)db = \frac{3}{R^3} b\sqrt{R^2 - b^2}db. \tag{104}$$

The trajectory of collision is described in terms of the μ-ion model. After the particle leaves the cell, another particle instead of it is injected randomly for conserving the total number of particles in the cell [140, 141]. During this, the module of particle impulse is attributed to the new particle for the fulfillment of the conservation law of system energy. Moreover, the impact parameter of the new particle had to correspond to the same range of impact parameters, to which belonged the impact parameter of a particle that left the cell.

Simultaneously, the evolution of summary electric field of all particles produced at the place of test particle localization is followed. The final result was determined by the average over set of generated time histories, the number of which could approach up to 20000 for the achievement of appropriate accuracy not lower than ~10%. In order to decrease the number of those histories, the average over the initial configurations is performed with special discretization, which is the request to reproduce with the help of this average the statistical microfield distribution functions. This method allowed to perform simultaneously the *joint* modeling of electric fields of ions and electrons [143, 144], which provides valuable tool for implementation in plasma spectroscopy, for example. The electric elementary ion field is approximated using Debye potential for the approximate account of electron-ion correlations.

Kesting managed to go beyond the frames of μ-ion model, and elaborated more complex procedure for modeling the motion of test particle [145] as well.

4. Kinetic Plasma Theory

4.1. Microfield Distribution Functions Accounting to Dynamical Electron Screening. As was mentioned, the construction of the distribution function and its properties depend on those time scales, during which the average over ensemble is performed [24, 25].

The application of microfield distribution, for example, in theory of spectral line broadening brings forward rather tough requests. For small values of detunings from the line center, the effective time of average are large, and the screening of ions by electrons could be considered static. However, with the extent of advancing into the line wings, the effective average times become shorter, and static screening does not have enough time to be settled [24, 25]. That is why the approaches are necessary in which the screening changes would be adequately accounted for in construction of microfield distribution functions. To some extent, this could be said about insufficiency of thermodynamic approach for this row of problems, as far as in thermodynamics two procedures of average could not exist at the same time.

One of the ways to this could be the representation of elementary electric field of separate field ion via the dielectric plasma permeability [3–6]:

$$\vec{E}_{\text{eff}}(\vec{r};t) = \frac{Ze}{2\pi^3 i}\int d^3k \left\{\frac{\vec{k}}{k^2\epsilon_l(k,\omega)} + \frac{\vec{v} - \left(\vec{k}\left(\vec{k}\vec{v}\right)/k^2\right)}{\omega[\epsilon_t(k,\omega) - (k^2c^2/\omega^2)]}\right\} \cdot \exp\left[i\left(\vec{k}\vec{r} - \omega t\right)\right]. \tag{105}$$

The study of this expression had showed that the extent of screening of the potential of field particle in collisionless plasma is the complex function of its velocity value and the distance to the point, where its electric field is detected, as well as the angle between the velocity direction and the radius-vector of observation point [125–127]. Meanwhile, the extent of potential screening decreases with the increase of velocity value and the radius-vector module. So, the Debye screening could be possible only for particles at rest [3–6, 125–127].

However, the straightforward implementation of this expression for derivation of the instantaneous microfield distribution function of low-frequency plasma microfield component is difficult, as this field depends on time and contains nonelectrostatic summand—the second term in the curly brackets, describing the transversal electric field. Moreover, the question arises what effects of interaction are included in dielectric permeability? Presently, the methods of account of plasma coupling effects (electron-electron or ion-ion correlations) to dielectric permeability still are not elaborated, and it is calculated in assumption of straight trajectories of free particles. One more general objection stems from the fact that per se the notion of dielectric permeability is related to macroscopic method of description, that is, it

is valid at scales $L \gg r_{D_{e,i}}$ and thereby unable in principle to describe processes on lesser scales, on which actually the microfield notion is introduced.

Nevertheless, the formal substitution of this expression in characteristic function is possible. As the notions and, moreover, the methods of calculations of correlations functions, depending on time, were not elaborated, in this case, one could speak about the calculations of microfield distribution functions only for noninteracting quasiparticles. However, it is known that this procedure reproduces the Debye screening of electric field [3–6].

For the separation of low-frequency component, the dielectric permeability should be represented as the sum of ion and electron contributions, and then the contribution of the poles residuals of ion summand should be taken. As the dynamical screening depends on the direction of particle velocity with respect to its radius vector to the test particle, as well as on the value of particle velocity [3–6, 125–127], this considerably complicates not only the calculations but also the interpretation of results.

The attempts of realization of this approach firstly are based on discarding the nonelectrostatic terms in the expression for the electric field of moving field particle in terms of dielectric permeability [82, 83]. In the paper of Ecker and Schumacher [82], it is shown that the contribution of nonelectrostatic terms converges to zero on time scale $t_{\min} \gg 1/\omega_{pi}$ that in truth exceeds the characteristic time scale of forming the distribution function of instantaneous low-frequency microfield component $1/\omega_{pi} \gg 1/(v_{T_i} N_i^{1/3}) \gg t_{\text{eff}} \gg 1/\omega_{\text{pe}}$ at least for ideal or weakly coupled plasmas. According to the authors' statement, it is equivalent to condition $N_i {r_{D_e}}^3 \gg 1$ that by now does not allow to consider the region of parameters $a \sim 1$ reasonably. Moreover, from the previous sections, it is evident that the distribution function corresponding to time scales $\tau_{\text{eff}} \gg 1/(v_{T_i} N_i^{1/3})$ no longer could describe the instantaneous distribution of individual component of ion microfield.

As one of their main results, the authors presume the demonstration of factorization of the total distribution function into two independent distributions of high-frequency and low-frequency microfield components. In assumption of straight path trajectories firstly the substitution $\omega = \vec{k}\vec{v}_{oi}$, corresponding to the major contribution, which is provided by the function $\epsilon_l^{-1}(\vec{k};\omega)$, and then the change of variables $\vec{r}_{0i} + \vec{v}_{0i}t = \vec{r}$, which removes the explicit dependence on time [62] and means the transition to the intrinsic reference frame of the given particle, are performed. Then similar to Hooper [27–29] and later to APEX [40–44], the fitting parameter ξ is inserted inside the value of the Debye screening radius of separate statically screened ion. After that, it is assumed that the main term in the expansion of natural logarithm of characteristic function describes the microfield distribution with the elementary ion field in the form of statically screened according to Debye $\vec{E}^0(\vec{r};\xi)$. The second term of expansion is chosen in the form $i\vec{q}[\vec{E}_{\text{eff}}(\vec{r};\vec{v}) - \vec{E}^0(\vec{r};\xi)]\exp[-i\vec{q}\,\vec{E}^0(\vec{r};\xi)]$, defining some corrective function similar to the Baranger-Mozer papers. However, the corrective function does not contain in the integrand any correlation functions in distinction from the Baranger-Mozer approach. The fitting parameter value ξ was determined from the condition of the optimal convergence of computations and turned out to be equal $\sqrt{3/2}$. The resulting distribution shifted with respect to the Baranger-Mozer distribution sideways small field values, but did not reach the Ecker-Müller distribution, which is localized still more nearer to the ordinate axis.

The other result, using this representation, was derived within implementation of some version of Green function formalism [83]. The distribution function in [83] depends not only on the reduced field value but also on the value of detuning from the line center with regard to problems of spectral lines broadening [1, 2]. In this work, the second nonelectrostatic summand in the expression for the field of single charge in terms of plasma dielectric permeability was discarded without any discussion or comments [83]. Regrettably, although the idea of the paper is physically sound, the derivation itself is not quite clear, and alas did not get confirmation in other papers.

In total, the results of this approach were not further developed and were not carried to the form that is necessary for practical calculations, and, moreover, there are certain doubts about the range of its validity.

The questions about time and spacial scales for fixing Debye screening in plasmas [125–127] again became the subject of detailed analytical and computational studies in the recent instructive works of Trofimovich and Krainov [84, 85]. However, alas up to now it is not clear how it would be possible to use these results in the theory of distribution functions. Nevertheless, it is evident that they are related to the functional choice of interaction potential and its dependence on space and time variables.

4.2. Microfields due to Plasma Fluctuations. The theory of plasma fluctuations has the whole row of interesting and useful general relations for the correlation functions of the current density, the charge density, the strengths of electrical and magnetic fields [3–6, 147]. Nevertheless, the physical settings that would allow within the fluctuations theory notions and formalism to construct the microfield distribution functions are unknown yet.

For the case of electrical fields in most general assumptions from the theory of fluctuations in plasma, it is possible to obtain the following expressions for the Fourier components of correlation functions of fluctuating electrical fields in isotropic plasmas $\langle E_j\, E_i\rangle_{\vec{k},\omega}$ [4, 5]:

$$\left\langle E_j\, E_i\right\rangle_{\vec{k},\omega} = 8\pi \frac{\hbar}{\exp[(\hbar\,\omega)/T] - 1} \cdot \left\{ \frac{k_i k_j}{k^2} \frac{\operatorname{Im}\epsilon_l}{|\epsilon_l|^2} + \left(\delta_{ij} - \frac{k_i k_j}{k^2}\right) \frac{\operatorname{Im}\epsilon_t}{|\epsilon_t - \eta^2|^2} \right\}, \tag{106}$$

where l, t are the indecies of longitudinal and transverse electrical fields correspondingly; $\epsilon(\omega, \vec{k})$ is the dielectric

permeability; $\eta = k\,c/\omega$ is the index of refraction of the plasma wave with the cyclic frequency ω and the wave vector $\vec{k}$ in the isotropic case.

Up to the moment the dielectric function is known practically only for weakly coupled plasmas. Although for strongly coupled plasmas recently a row of model representations was developed for the dielectric function, this problem in total is not studied quite enough first of all due to the variety of physical conditions realizable in strongly coupled plasma [3–12, 148–159].

In the case of isothermal ideal isotropic classical plasmas $T \gg \hbar\omega$, this expression for $\langle E_j\ E_i\rangle_{\vec{k},\omega}$ might be reduced for the Maxwell distributions over electrons and ions velocities to the form [4, 5]

$$\begin{aligned}\left\langle E_j\ E_i\right\rangle_{\vec{k},\omega} &= \frac{32\pi^2}{\omega}\left\{\frac{k_i k_j}{k^2}\ \frac{1}{|\epsilon_l|^2}\ \left(T_e\ \mathrm{Im}\ \kappa_l^e + T_i\ \mathrm{Im}\ \kappa_l^i\right)\right.\\ &\quad + \left(\delta_{ij} - \frac{k_i k_j}{k^2}\right)\frac{1}{|\epsilon_t - \eta^2|^2}\\ &\quad \left.\cdot\ \left(T_e\ \mathrm{Im}\ \kappa_t^e + T_i\ \mathrm{Im}\ \kappa_t^i\right)\right\},\end{aligned} \tag{107}$$

where $T_{i,e}$ are ion and electron temperatures correspondingly; $\kappa^{e,i}(\omega,\vec{k})$ are the electron and ion electrical susceptibilities correspondingly.

The dielectric permeability of ideal collisionless plasma is determined by the expressions (compare with [4, 5])

$$\begin{aligned}\epsilon_l(k,\omega) &= 1 + \frac{1}{r_{\mathrm{De}}^2\ k^2}\{1 - \phi(z) + t\ [1 - \pi(\mu z)] + i\sqrt{\pi}z\\ &\quad \cdot\ (\exp[-z^2] + t\mu\ \exp[-\mu^2\ z^2])\},\\ \epsilon_t(k,\omega) &= 1 - \frac{\omega_{\mathrm{pe}}^2}{\omega^2}\left\{\phi(z) + \frac{t}{\mu}\ \phi(\mu\ z) - i\ \sqrt{\pi}\ z\right.\\ &\quad \left.\cdot\ \left(\exp[-z^2] + \frac{t}{\mu}\ \exp[-\mu^2\ z^2]\right)\right\},\\ \phi(z) &= 2z\ \exp[-z^2]\int_0^z dz\ \exp[z^2],\\ \omega_{\mathrm{pe}} &= \sqrt{\frac{4\pi e^2\ n_e}{m}},\\ z &= \sqrt{\frac{3}{2}}\ \frac{\omega}{k v_e}, \qquad t = \frac{T_e}{T_i}, \qquad \mu^2 = \frac{M}{m}\ \frac{T_e}{T_i},\\ v_e^2 &= \frac{3T_e}{m}, \qquad r_{\mathrm{De}}^2 = \frac{T_e}{4\pi e^2\ n_e}.\end{aligned} \tag{108}$$

The expressions for $\kappa^{e,i}(\omega,\vec{k})$ in the case of ideal collisionless plasma have the forms (compare with [4, 5])

$$\begin{aligned}\kappa_l^e\left(\omega,\vec{k}\right) &= \frac{1}{4\pi r_{\mathrm{De}}^2\ k^2}\ \{1 - \phi(z) + i\ \sqrt{\pi}\ z\ \exp(-z^2)\},\\ \kappa_l^i\left(\omega,\vec{k}\right) &= \frac{t}{4\pi r_{\mathrm{De}}^2\ k^2}\ \{1 - \phi(\mu\ z) + i\ \sqrt{\pi}\mu z\ \exp(-\mu^2\ z^2)\},\\ \kappa_t^e\left(\omega,\vec{k}\right) &= -\frac{1}{4\pi}\ \frac{\omega_{\mathrm{pe}}^2}{\omega^2}\ \{\ \phi(z) - i\ \sqrt{\pi}z\ \exp(-z^2)\},\\ \kappa_t^i\left(\omega,\vec{k}\right) &= -\frac{t}{4\pi\mu}\ \frac{\omega_{\mathrm{pe}}^2}{\omega^2}\ \{\phi(\mu\ z) - i\ \sqrt{\pi}z\ \exp(-\mu^2 z^2)\}.\end{aligned} \tag{109}$$

As it is known, all these expressions could be reproduced starting from the notions of elementary currents, produced by non-interacting between each other charged plasma particles moving randomly along straight line trajectories [3]. The generalization of these formulas and their asymptotic under account of collisions could be found in the kinetic approach for description of fluctuations in [6]. In spite of absence of interactions, these particles, nevertheless, create the Debye screening of the electric field in plasmas. Indeed, integrating over cyclic frequencies the expression for the correlation functions of microfields in the simplest case $T_i = T_e$ and converging it over indexes $i = j$, after the inverse Fourier transform, we obtain the expression [4, 5]

$$\langle E^2\rangle_{\vec{r}} = 8\pi T\ \left\{\ \delta(\vec{r}) + \frac{1}{8\pi r_{\mathrm{De}}^2}\ \frac{\exp(-r/r_{\mathrm{De}})}{r}\right\}. \tag{110}$$

The first summand in $\langle E^2\rangle_{\vec{r}}$ contains the divergence at zero which is interpreted as being due to the absence of spacial correlations [6], whereas the integral from $\langle E^2\rangle_{\vec{r}}$ over volume is finite and equal, being divided on 8π, to the energy content W per one structureless particle:

$$W = \oint_{\mathcal{V}} d^3r\ \frac{1}{8\pi}\langle E^2\rangle_{\vec{r}} = \frac{3}{2}T. \tag{111}$$

This result again raises the question about proportions of contributions into the obtained density of plasma energy content $\langle E^2\rangle_{\vec{r}}$ by plasma collective oscillations, which are forming the plasma dielectric permeability, and by the electrical fields from the individual particles that rapidly decrease on the scales larger than Debye radius.

As the plasma dielectric permeability is a macroscopic characteristic, the collective oscillations have macroscopic origin either. This means that the characteristic spacial scale of their variations at least for weakly coupled plasmas is much larger than the Debye radius. At less scales, these fields decay rapidly and thereby do not provide the essential contribution into the individual microfield component, whose scale of variation is less than the Debye radius in ideal plasmas.

As all derivations of these results were based on collective plasma oscillations, it would seem that it would be possible to state that there is no contribution from the individual component of the electric field, which in principle has

nonthermodynamic origin. However, on the other hand, these results could be derived just from simple notions about the straight line trajectories of particles, having the Maxwell distribution over velocities, and thus should correspond to the individual plasma microfield component. However, both statements are not quite correct as the energy is drawn from the same fixed source $(3/2)\mathcal{N}T$.

In truth, in order to make conclusion about the ratio of energy density between the collective and individual microfield components to $\langle E^2\rangle_{\vec{r}}$, it is necessary to study the contributions from resonance regions under integration of $\langle E_j\ E_i\rangle_{\vec{k},\omega}$ in the space $(\omega, \vec{k})$, which actually are responsible for collective plasma oscillations. Few examples of such studies could be found in textbooks on plasma physics [191, 192].

Nevertheless, still the certain difficulties with the notions about separation of individual and collective variables for Hamiltonian of Coulomb particles do exist even for the switched off interaction between them.

4.3. Dissolution Effect and Statistical Sums. One of the known problems in thermodynamics of plasma and gas is the divergence of statistical sums for bound states of partially ionized atoms and ions at arbitrary finite temperatures [7, 10].

However, in the external electric field, the upper excited atomic states are ionized due to the distortion of potential and nonequal to zero probability of penetration under the barrier so-called tunnel effect [146]. In plasma, the microfield plays the role of such external electric field, devastating the upper levels. This effect leads to the finite number of really existing excited states and ensures the convergence of statistical sums. The other physical consequence is the lowering of ionization potential, which influences on relation of equilibrium concentrations of atoms and ions, and thereby on the degree of plasma ionization [146, 148–159]. These tendencies both are visualized in observations by decreasing of spectral line intensities, originating from the upper levels to the extent of advancing to the continuum. This phenomenon conventionally is called as the dissolution effect of spectral lines.

The pointed out effects turn out to be very important for plasma equation of state. Ones of the first Hammer, Michalas [154–159] and Dappen [154–157] payed attention on the microfield influence on plasma equation of state. In recent works, the sensitivity of seismological Sun data treatment to the choice of microfield distribution functions was demonstrated [157], and the comparison of implementation of microfield distributions due to Hooper, APEX, and Holtsmark was performed.

Not all the questions in this complex problem are completely clear and actively disputed up to now (see, e.g., [158, 159, 161, 162]).

4.4. Microfield Influence on Rate Coefficients. The influence of microfield on probabilities of elementary processes in plasma leads to variation of the rate coefficients [146, 162], entering in the balance equations for populations of atomic levels. This influence is known for processes of excitation and ionization (due to the lowering of ionization potential), charge exchange, photoionization, autoionization and dielectronic recombination (due to the levels structure change) [146], and so forth. The electrical field influences also on the absorption processes, the localization of continuum edge, bremsstrahlung, and other processes, which could in its turn determine the plasma thermodynamic characteristics, and, in particular, the equation of state. However, this subject, due to its extensiveness, complexity, and diversity, needs the special analysis that is beyond the frames of the present work (see, e.g., [146–159, 161, 162]).

5. Discussion

(i) It should be noted that convergence of cluster expansion series of Baranger-Mozer and Hooper, and so forth, for plasma microfield could not be recognized as rigourously proved. In fact, these methods are based on practical convergence of the terms of the first and second order of density for the logarithm of characteristic function. The next terms of expansion after the second cluster expansion term, corresponding to more higher orders over density is difficult to estimate strictly due to the lack of reliable data about correlation functions of the third order and more higher ones. Nevertheless, the results of these papers are physically obvious and do not contradict to existing experimental data.

(ii) Numerous works, in which the cluster expansion is built up with the help of diagrammatic technique, were not considered. In series of papers, there were attempts to renormalize electron-ion interaction, especially in the range of noticeable plasma nonideality.

However, due to the long-range character of Coulomb interaction in plasma, the convergence of renown Bogolubov-Born-Green-Kirkwood-Yvon (BBGKY) chain of equations [6–12] in this case is not rigourously proved [11, 12, 160] at least within the classic theory domain for point particles. The convergence of BBGKY chain in plasmas is possible only for modified Coulomb potential at small distances with the help of the introduction of strong repulsion or various forms of pseudopotentials [7–12, 160] or, in particular, for particles with finite sizes.

On the other hand, it is well known that the sum of only ring diagrams is quite sufficient to reproduce static Debye potential [7–12, 160]. However, in literature, devoted to derivations of cluster expansions of characteristic functions of plasma microfield distributions functions within diagrammatic technique, the results depend on what type of diagrams could be summed and calculated at least partially. The substantial analysis of these questions is a very complex problem and is beyond the scope of present consideration.

(iii) Remind, that the necessity to consider, namely, the conception of instantaneous distribution functions, which we adhere to in the present review, generally speaking, is also under debate. In this discussion, it is stated that test particle is a merely microprobe, detecting the state of a medium, which had enough time to be set long ago before the measurement process. Hence, from this point of view, the implementation

of methods of conventional thermodynamics is sufficient to perform averages. At the same time, the process of the test particle equilibration with the medium and its dynamics represent the separate problem, which has as thermodynamic as statistical aspects.

(iv) We have to recognize that rather complicated theory of joint distribution functions has a number of unresolved questions up to now, connected, for example, with treatment of the shifts of the microfield tensor of nonuniformity distributions [19–21, 35, 66, 67], which appear also during numerical modeling by Monte-Carlo method [37, 38]. These results hold even for the gas of Coulomb particles, and seemingly contradict to initial conditions of plasma isotropy [66, 67]. Meanwhile, these results also depend on the sequence of integration in the corresponding multidimensional integrals. All this did not get clear understanding so far.

(v) The recent results [182, 183] of *ab initio* MD joint simulations of plasma ion and electron fields, and the proposed procedure of their separation into slow and fast microfield components together with the study of its behavior versus the value of average time interval (see [182, 183] and Section 3.3) opens the new era in the investigations of plasma microfield properties and their applications. This will cause obviously serious reanalysis and reconsideration of many questions and notions. For example, it could have drastic impact on the possible magnitude of the aforementioned inhomogeneity effects due cancelation of contributions from ions and electrons, the extent of which could not be predicted from general consideration.

(vi) Thus we see that the whole row of calculations performed in quasistatic approximation and in MD simulations [135–137, 182, 184–189] demonstrate the significance of correlations between subsystems with opposite signs of charges and the necessity to develop and apply TCP models. The more realistic distributions are localized between Holtsmark for N_e and Holtsmark $2N_e$ distributions [182, 187, 188]. In TCP again, we face the divergence of the second microfield moment, which was made convergent in the Debye screened OCP model after divergence for the Holtsmark distribution of noninteracting field particles.

(vii) In consideration of thermodynamic properties as already was discussed earlier, the implementation of static screening notions within conventional thermodynamic ideas is quite sufficient. However, the model of Debye screening was criticized for many inconsistencies [46, 47, 154–156]. The discussion and search of more consistent models of screening and more realistic potentials in plasmas is still continuing (see, e.g., [193, 194] and references therein) as for static and for dynamic conditions [182].

(viii) In some cases, as the attentive reader could see, we preserved the title of articles in the reference list in attempt to underline its significance for the development of the subject and draw attention to their original results.

It should be noted that beside the covered in this review problems, there are also many other interesting ones (see recent reviews [195–198]) or other connected with microfield notion, regrettably not touched here. For example, these are an idea of "mean ion" [158], the so-called NNN distribution [161], the distribution of microfields due to third particle, peculiarities of microfield distributions in dusty plasmas [163], and so on. At the same time, the choice of works in the reference list was based on some balanced merits: firstly, physical significance of ideas; secondly, adequately chosen formalism that does not reduce the work mainly to its study; thirdly, the final results available for applications. However, of course, the reader must know that this review is focused mainly on conceptual aspects of the problem and only a highly condensed sketch of original scientific papers, which contain much more detailed and ample information on particular studies.

Acknowledgments

The author thanks G. V. Sholin, V. S. Lisitsa, V. I. Kogan, A. N. Starostin, Yu. K. Zemtsov, E. A. Oks, M. D. Ginzburg, D. A. Shapiro, A. E. Bulyshev and A. E. Suvorov, D. Voslamber, D. Kelleher, H. R. Griem, J. Hey, J. Seidel, Nguyen Hoe, C. Stehlé, D. Gilles, Ch. Hooper, R. Stamm, V. Kesting, B. Jancovici, F. Perrot, G. Massacrier, B. Talin, A. Calisti, S. Ferri, G. Kalman, J. Dufty, D. Boercker, C. A. Iglesias, F. J. Rogers, R. W. Lee, R. Mancini, M. Zoppi, M.-M. Gombert, J. L. Lebowitz, D. P. Kilcrease, M. W. C. Dharma-wardana, M. A. Gigosos, M. A. Gonzalez, S. I. Yakovlenko, A. A. Knizhnik, I. L. Iosilevski, and F. Rosmej for cooperation, correspondence, explanations, and discussions on the subject during the last four decades. At the same time, the author's point of view could differ from expertise of thanked above renown scientists. The author is grateful to Dr. Bernard Talin for permission to use the data from [182] before publication. It is a pleasure to thank V. Khudjakov, D. Nikolić, S. Djurović for generous valuable help in collecting literature, resolving LaTeX problems, and improving figures, and referees of IJS for valuable comments.

References

[1] H. R. Griem, *Spectral Line Broadening by Plasmas*, Academic Press, New York, NY, USA, 1974.

[2] I. I. Sobelman, *Introduction to Atomic Spectra*, Pergamon Press, Oxford, UK, 1972.

[3] V. D. Shafranov, "Electromagnetic waves in plasmas," in *Reviews on Plasma Physics*, M. Gosatomizdat, Ed., vol. 3, pp. 3–140, 1963.

[4] N. Rostoker, "Fluctuations of a plasma," *Nuclear Fusion*, vol. 1, pp. 101–120, 1961.

[5] A. G. Sitenko, *Electromagnetic Fluctuations in Plasmas*, KhGU, Khar'kov, Ukraine, 1965.

[6] A. I. Akhiezer, *Plasma Electrodynamics*, Nauka, Moscow, Russia, 1974.

[7] A. Isihara, Ed., *Statistical Physics*, Academic Press, New York, NY, USA, 1971.

[8] J.-P. Hansen and I. R. McDonald, *Theory of Simple Liquids*, Academic Press, New York, NY, USA, 1976.

[9] M. Baus and J.-P. Hansen, "Statistical mechanics of simple coulomb systems," *Physics Reports*, vol. 59, no. 1, pp. 1–94, 1980.

[10] Ph. A. Martin, "Sum rules in charged fluids," *Reviews of Modern Physics*, vol. 60, no. 4, pp. 1075–1127, 1988.

[11] A. B. Schmidt, *Statistical Thermodynamics of Classical Plasmas*, Energoizdat, Moscow, Russia, 1991.
[12] G. A. Martynov, *Fundamental Theory of Liquids*, Adam Hilger, New York, NY, USA, 1992.
[13] E. Oks, "Advance in diagnostics for high-temperature plasmas based on the analytical result for the ion dynamical broadening of hydrogen spectral lines," *Physical Review E*, vol. 60, no. 3, pp. R2480–R2483, 1999.
[14] J. W. Dufty, "The microfield formulation of spectral line broadening," in *Spectral Line Shapes*, B. Wende, Ed., vol. 1, pp. 41–61, W. de Grüyter, Berlin, Germany, 1981.
[15] C. F. Hooper, "Electric microfield distribution functions: past and present," in *Spectral Line Shapes*, R. J. Exton, Ed., vol. 4, p. 161, Deepak, Hampton, UK, 1987.
[16] J. W. Dufty, "Electric microfield distributions," in *Srongly Coupled Plasma Physics*, F. J. Rogers, Ed., p. 493, Plenum Press, New York, NY, USA, 1987.
[17] V. S. Lisitsa, V. I. Kogan, and G. V. Sholin, "Broadening of spectral lines in plasmas," in *Reviews on Plasma Physics*, B. B. Kadomtsev and M. Energoatomizdat, Eds., vol. 13, pp. 205–261, 1984.
[18] J. Holtsmark, "Uber die verbreiterung von spektrallinien," *Annalen der Physik*, vol. 58, no. 4, pp. 577–630, 1919.
[19] S. Chandrasekhar and J. von Neuman, "The statistics of the gravitational field arising from a random distribution of stars. I. The speed of fluctuations," *The Astrophysical Journal*, vol. 95, pp. 489–531, 1942.
[20] S. Chandrasekhar and J. von Neuman, "The statistics of the gravitational field arising from a random distribution of stars II," *The Astrophysical Journal*, vol. 97, pp. 1–27, 1943.
[21] S. Chandrasekhar, "Stochastic problems in physics and astronomy," *Reviews of Modern Physics*, vol. 15, no. 1, pp. 1–89, 1943.
[22] G. Ecker, "Das Mikrofeld in Gesamtheiten mit Coulombscher Wechselwirkung," *Zeitschrift für Physik*, vol. 148, no. 5, pp. 593–606, 1957.
[23] G. Ecker and K. G. Müller, "Plasmapolarisation und Trägerwechselwirkung," *Zeitschrift für Physik*, vol. 153, no. 3, pp. 317–330, 1958.
[24] M. Baranger and B. Mozer, "Electric field distributions in an ionized gas," *Physical Review*, vol. 115, no. 3, pp. 521–525, 1959.
[25] B. Mozer and M. Baranger, "Electric field distributions in an ionized gas. II," *Physical Review*, vol. 118, no. 3, pp. 626–631, 1960.
[26] H. Pfennig and E. Trefftz, "Die Druckverbreiterung der diffusen Heliumlinien, Vergleich zwischen messung und Theorie im quasistatischen Bereich," *Zeitschrift für Naturforschung A*, vol. 21, p. 697, 1966.
[27] C. F. Hooper Jr., "Electric microfield distributions in plasmas," *Physical Review*, vol. 149, no. 1, pp. 77–91, 1966.
[28] C. F. Hooper Jr., "Low-frequency component electric microfield distributions in plasmas," *Physical Review*, vol. 165, no. 1, pp. 215–222, 1968.
[29] C. F. Hooper Jr., "Asymptotic electric microfield distributions in low-frequency component plasmas," *Physical Review*, vol. 169, no. 1, pp. 193–195, 1968.
[30] D. Bohm and D. Pines, "A collective description of electron interactions: II. Collective vs individual particle aspects of the interactions," *Physical Review*, vol. 85, pp. 338–353, 1952.
[31] D. Bohm and D. Pines, "A collective description of electron interactions: III. Coulomb interactions in a degenerate electron gas," *Physical Review*, vol. 92, no. 3, pp. 609–625, 1953.
[32] A. A. Broyles, "Stark fields from ions in a plasma," *Physical Review*, vol. 100, no. 4, pp. 1181–1187, 1955.
[33] A. A. Broyles, "Calculation of fields on plasma ions by collective coordinates," *Zeitschrift für Physik*, vol. 151, pp. 187–201, 1958.
[34] R. J. Tighe and C. F. Hooper, "Low-frequency electric microfield distributions in a plasma containing multiply-charged ions: extended calculations," *Physical Review A*, vol. 15, no. 4, pp. 1773–1779, 1977.
[35] D. Gilles and A. Angelie, "Monte- Carlo distributions of electric microfield," *Annales de Physique*, vol. 11, no. 3, supplement 3, p. 157, 1986.
[36] J. M. Caillol and D. Gilles, "Monte Carlo simulations of the Yukawa one-component plasmas," *Journal of Statistical Physics*, vol. 100, no. 5-6, pp. 933–947, 2000.
[37] D. Gilles, "Calcul de la repartition statistique du microchamp electrique dans les plasmas," Internal CEA-Report, 1997.
[38] D. Gilles, *Méthode de Monte-Carlo en Mécanique Statistique Appliquée à la Physique des Plasmas*, Laboratoire de Physique des Gaz et des Plasmas, Université Paris XI, Lecture Notes, Orsay, France, 1997.
[39] A. Y. Potekhin, G. Chabrier, and D. Gilles, "Electric microfield distributions in electron-ion plasmas," *Physical Review E*, vol. 65, no. 3, Article ID 036412, 12 pages, 2002.
[40] C. A. Iglesias, J. L. Lebowitz, and D. MacGowan, "Electric microfield distributions in strongly coupled plasmas," *Physical Review A*, vol. 28, no. 3, pp. 1667–1672, 1983.
[41] C. A. Iglesias and J. L. Lebowitz, "Electric microfield distributions in multicomponent plasmas," *Physical Review A*, vol. 30, no. 4, pp. 2001–2004, 1984.
[42] C. A. Iglesias, H. E. DeWitt, J. L. Lebowitz, D. MacGowan, and W. B. Hubbard, "Low-frequency electric microfield distributions in plasmas," *Physical Review A*, vol. 31, no. 3, pp. 1698–1702, 1985.
[43] C. A. Iglesias, F. J. Rogers, R. Shepherd, et al., "Fast electric microfield distribution calculations in extreme matter conditions," *Journal of Quantitative Spectroscopy and Radiative Transfer*, vol. 65, no. 1–3, pp. 303–315, 2000.
[44] J. W. Dufty, D. B. Boercker, and C. A. Iglesias, "Electric field distributions in strongly coupled plasmas," *Physical Review A*, vol. 31, no. 3, pp. 1681–1686, 1985.
[45] H. Mayer, "Method of opacity calculations," Tech. Rep. LA-647, Los Alamos Scientific Laboratory, 1947.
[46] M. W. C. Dharma-Wardana and F. Perrot, "Electric microfield distributions in plasmas of arbitrary degeneracy and density," *Physical Review A*, vol. 33, no. 5, pp. 3303–3313, 1986.
[47] F. Perrot and M. W. C. Dharma-Wardana, "Ion correlations and ion microfields at impurities in dense plasmas," *Physical Review A*, vol. 41, no. 6, pp. 3281–3293, 1990.
[48] G. H. Ecker and K. G. Fisher, "Individual and collective aspects of microfield distribution," *Zeitschrift für Naturforschung*, vol. 26a, pp. 1360–1365, 1971.
[49] K.-H. Spatschek, "Collective contributions to the electric microfield distribution in a turbulent plasma," *Physics of Fluids*, vol. 17, no. 5, pp. 969–972, 1974.
[50] E. A. Oks and G. V. Sholin, "Stark profiles of hydrogen lines in a plasma with low-frequency turbulence," *Zhurnal Tekhnicheskoi Fiziki*, vol. 46, pp. 254–264, 1976 (Russian).
[51] H. H. Klein and N. A. Krall, "Probability distribution of electric fields in thermal and nonthermal plasmas," *Physical Review A*, vol. 8, no. 2, pp. 881–886, 1973.
[52] E. A. Oks, *Plasma Spectroscopy with Quasi-Monochromatic Electric Fields*, M. Energoatomizdat, 1990.

[53] A. V. Demura and G. B. Sholin, "Theory of asymmetry of hydrogen-line Stark profiles in dense plasma," *Journal of Quantitative Spectroscopy and Radiative Transfer*, vol. 15, no. 10, pp. 881–899, 1975.

[54] A. V. Demura, *Certain questions in theory of hydrogen spectral lines broadening in plasmas*, Ph.D. thesis, I.V. Kurchatov Institute of Atomic Energy, Moscow, Russia, 1976.

[55] A. V. Demura, "Theory of ion microfield distributions and its space and time derivatives in plasmas with complex ionization composition," preprint IAE-4632/6, TsNIIatominform, Moscow, Russia, pp. 1–17, 1988.

[56] A. V. Demura, "First moments of joint distribution function of electric Ion microfield and it's spatial and time derivatives in a plasma with weak nonideality," in *Proceedings of the 9th International Conference on Spectral Line Shapes (ICSLS '88)*, Nicolas Copernicus University Press, Torun, Poland, 1988, abstract no. A39.

[57] A. V. Demura and C. Stehlé, "Effects of microfield nonuniformity in dense plasmas," in *Spectral Line Shapes, Vol. 8*, D. May, J. Drummond, and E. Oks, Eds., vol. 328 of *AIP Conference Proceedings*, pp. 177–208, American Institute of Physics, New York, NY, USA, 1995.

[58] A. V. Demura, D. Gilles, and C. Stehlé, "Comparative study of microfield nonuniformity in plasmas," *Journal of Quantitative Spectroscopy and Radiative Transfer*, vol. 54, no. 1-2, pp. 123–136, 1995.

[59] C. Stehlé, D. Gilles, and A. V. Demura, "Asymmetry of Stark profiles. The microfield point of view," *The European Physical Journal D*, vol. 12, no. 2, pp. 355–367, 2000.

[60] A. V. Demura, D. Gilles, and C. Stehlé, "Asymmetry of stark profiles in nonuniform fluctuating microfield," in *Spectral Line Shapes, Vol. 11*, J. Seidel, Ed., vol. 559 of *AIP Conference Proceedings*, pp. 99–107, American Institute of Physics, New York, NY, USA, 2001.

[61] A. V. Demura and C. Stehlé, "Asymmetry in wings of stark profiles in dense plasmas," in *Spectral Line Shapes, Vol. 11*, J. Seidel, Ed., vol. 559 of *AIP Conference Proceedings*, pp. 111–113, American Institute of Physics, New York, NY, USA, 2001.

[62] A. V. Demura, D. Gilles, and C. Stehlé, "On plasma statistics of microfield gradients and line asymmetries," in *Strongly Coupled Coulomb Systems*, G. J. Kalman, J. M. Rommel, and K. Blagoev, Eds., pp. 377–380, Plenum Press, New York, NY, USA, 1998.

[63] R. F. Joyce, L. A. Woltz, and C. F. Hooper Jr., "Asymmetry of Stark-broadened Lyman lines from laser-produced plasmas," *Physical Review A*, vol. 35, no. 5, pp. 2228–2233, 1987.

[64] J. Halenka, "Asymmetry of hydrogen lines in plasmas utilizing a statistical description of ion-quadruple interaction in Mozer-Baranger limit," *Zeitschrift für Physik D*, vol. 16, no. 1, pp. 1–8, 1990.

[65] D. P. Kilcrease, R. C. Mancini, and C. F. Hooper Jr., "Ion broadening of dense-plasma spectral lines including field-dependent atomic physics and the ion quadrupole interaction," *Physical Review E*, vol. 48, no. 5, pp. 3901–3913, 1993.

[66] K. G. Müller, "Influence of field inhomogeneity on ionic line broadening," *Journal of Quantitative Spectroscopy and Radiative Transfer*, vol. 5, no. 2, pp. 403–423, 1965.

[67] V. S. Milliyanchuk, thesis doctor of science, L'vov State University, L'vov, Ukraine, 1956.

[68] M. S. Murillo, D. P. Kilcrease, and L. A. Collins, "Dense plasma microfield nonuniformity," *Physical Review E*, vol. 55, no. 5, pp. 6289–6292, 1997.

[69] D. P. Kilcrease, M. S. Murillo, and L. A. Collins, "Theoretical and molecular dynamics studies of dense plasma microfield nonuniformity," *Journal of Quantitative Spectroscopy and Radiative Transfer*, vol. 58, no. 4–6, pp. 677–686, 1997.

[70] D. P. Kilcrease and M. S. Murillo, "The ion electric microfield gradient joint probability distribution function for dense plasmas," *Journal of Quantitative Spectroscopy and Radiative Transfer*, vol. 65, no. 1–3, pp. 343–352, 2000.

[71] C. A. Iglesias and C. F. Hooper, "Quantum corrections to the low-frequency-component microfield distributions," *Physical Review A*, vol. 25, no. 3, pp. 1632–1635, 1982.

[72] B. Held, C. Deutsch, and M. M. Gombert, "Low-frequency electric microfield in dense and hot multicomponent plasmas," *Physical Review A*, vol. 29, no. 2, pp. 880–895, 1984.

[73] B. Held and P. Pignolet, "Low-frequency electric microfield calculations by iterative methods," *Journal de Physique*, vol. 48, no. 11, pp. 1951–1961, 1987.

[74] V. I. Kogan, "Broadening of spectral lines in high temperature plasmas," in *Plasma Physics and Problem of Controlled Thermonuclear Reactions*, M. A. Leontovich, Ed., vol. 4, pp. 258–304, AS USSR, 1958.

[75] L. J. Roszman and C. F. Hooper, "Distribution of the time-dependent microfield in a plasma," *Physical Review A*, vol. 7, no. 6, pp. 2121–2130, 1973.

[76] A. Alastuey, J. L. Lebowitz, and D. Levesque, "Time-dependent statistical properties of the electric microfield seen by a neutral radiator," *Physical Review A*, vol. 43, no. 6, pp. 2673–2693, 1991.

[77] J. W. Dufty and L. Zogaib, "Electric-field dynamics in plasmas: theory," *Physical Review A*, vol. 44, no. 4, pp. 2612–2624, 1991.

[78] J. W. Dufty and L. Zogaib, "Short-time electric-field dynamics at a neutral point in strongly coupled plasmas," *Physical Review E*, vol. 47, no. 4, pp. 2958–2961, 1993.

[79] M. Berkovsky, J. W. Dufty, A. Calisti, R. Stamm, and B. Talin, "Nonlinear response of electric fields at a neutral point," *Physical Review E*, vol. 51, no. 5, pp. 4917–4929, 1995.

[80] A. V. Demura, "Instantaneous joint distributions of ion microfield and its time derivatives and effects of dynamical friction in plasmas," *Journal of Experimental and Theoretical Physics*, vol. 83, pp. 60–72, 1996.

[81] A. V. Demura, "Microfield fluctuations in plasmas with low frequency ocsillations," in *Proceedings of the 19th International Conference on Phenomena in Ionized Gases (ICPIG '90)*, vol. 2, pp. 352–353, Beograd, Serbia, 1990.

[82] G. H. Ecker and A. Schumacher, "Dynamic screening model of the electric microfield distribution," *Zeitschrift für Naturforschung A*, vol. 30, p. 413, 1975.

[83] L. E. Pargamanik and M. D. Ginzburg, "Distribution function of ionic microfields in plasma," *Ukraine Physical Journal*, vol. 22, pp. 938–943, 1977.

[84] E. E. Trofimovich and V. P. Krainov, "Setting in of Debye screening in a Maxwellian plasma," *Zhurnal Eksperimentalnoi i Teoreticheskoi Fiziki*, vol. 102, pp. 71–77, 1992.

[85] E. E. Trofimovich and V. P. Krainov, "Shielding of a moving charge in a Maxwellian plasma," *Zhurnal Eksperimentalnoi i Teoreticheskoi Fiziki*, vol. 104, pp. 3971–2329, 1993.

[86] U. Frisch and A. Brissaud, "Theory of Stark broadening-I soluble scalar model as a test," *Journal of Quantitative Spectroscopy and Radiative Transfer*, vol. 11, no. 12, pp. 1753–1766, 1971.

[87] A. Brissaud and U. Frisch, "Theory of Stark broadening-II exact line profile with model microfield," *Journal of Quantitative Spectroscopy and Radiative Transfer*, vol. 11, no. 12, pp. 1767–1783, 1971.

[88] A. Brissaud and U. Frisch, "Solving linear stochastic differential equations," *Journal of Mathematical Physics*, vol. 15, no. 5, pp. 524–534, 1973.

[89] A. Brissaud, C. Goldbach, J. Leorat, A. Mazure, and G. Nollez, "On the validity of the model microfield method as applied to Stark broadening of neutral lines," *Journal of Physics B*, vol. 9, no. 7, pp. 1129–1146, 1976.

[90] A. Brissaud, C. Goldbach, J. Leorat, A. Mazure, and G. Nollez, "Application of the model microfield method to Stark profiles of overlapping and isolated neutral lines," *Journal of Physics B*, vol. 9, no. 7, pp. 1147–1162, 1976.

[91] J. Seidel, "Effects of ion motion on hydrogen stark profiles," *Zeitschrift für Naturforschung A*, vol. 32a, pp. 1207–1214, 1977.

[92] J. Seidel, "Hydrogen stark broadening by ion impacts on moving emitters," *Zeitschrift für Naturforschung A*, vol. 34a, pp. 1385–1397, 1979.

[93] J. Seidel, "Theory of hydrogen stark broadening," in *Spectral Line Shapes*, B. Wende, Ed., vol. 1, pp. 3–39, Walter de Gruyter, Berlin, Germany, 1981.

[94] C. Stehlé, "Stark Profiles of He^+," *Astronomy and Astrophysics*, vol. 292, p. 699, 1994.

[95] D. B. Boercker, C. A. Iglesias, and J. W. Dufty, "Radiative and transport properties of ions in strongly coupled plasmas," *Physical Review A*, vol. 36, no. 5, pp. 2254–2264, 1987.

[96] M. A. Berkovsky, J. W. Dufty, A. Calisti, R. Stamm, and B. Talin, "Electric field dynamics at a charged point," *Physical Review E*, vol. 54, no. 4, pp. 4087–4097, 1996.

[97] S. Sorge, S. Günter, and G. Röpke, "On the consequences of a realistic conditional covariance in MMM-calculations," *Journal of Physics B*, vol. 32, no. 3, pp. 675–681, 1999.

[98] A. Könes, S. Günter, and G. Röpke, "On the time evolution of the ionic microfield in plasmas," *Journal of Physics B*, vol. 29, p. 6091, 1999.

[99] B. Talin, A. Calisti, S. Ferri, et al., "Ground work supporting the codes based upon the frequency fluctuation model," *Journal of Quantitative Spectroscopy and Radiative Transfer*, vol. 58, no. 4–6, pp. 953–964, 1997.

[100] B. Talin, A. Calisti, S. Ferri, C. Mossé, and B. Talin, "Frequency fluctuation model survey," in *Spectral Line Shapes, Vol. 12*, C. Back, Ed., vol. 645 of *AIP Conference Proceedings*, pp. 247–251, American Institute of Physics, New York, NY, USA, 2002.

[101] R. Stamm and D. Voslamber, "On the role of ion dynamics in the stark broadening of hydrogen lines," *Journal of Quantitative Spectroscopy and Radiative Transfer*, vol. 22, no. 6, pp. 599–609, 1979.

[102] J. Seidel and R. Stamm, "Effects of radiator motion on plasma-broadened hydrogen Lyman-β," *Journal of Quantitative Spectroscopy and Radiative Transfer*, vol. 27, no. 5, pp. 499–503, 1982.

[103] R. Stamm, "Simulation studies of the dynamics of plasma microfields," in *Spectral Line Shapes*, K. Burnett, Ed., vol. 2, pp. 3–29, Walter de Gruyter, Berlin, Germany, 1983.

[104] E. W. Smith, R. Stamm, and J. Cooper, "Discussion of the conditional-probability function for electric fields in a plasma," *Physical Review A*, vol. 30, no. 1, pp. 454–467, 1984.

[105] R. Stamm, E. W. Smith, and B. Talin, "Study of hydrogen Stark profiles by means of computer simulation," *Physical Review A*, vol. 30, no. 4, pp. 2039–2046, 1984.

[106] E. L. Pollock and W. C. Weisheit, "Local fields in strongly coupled plasmas," in *Spectral Line Shapes*, F. Rostas, Ed., vol. 3, p. 181, W. de Grüyter, New York, NY, USA, 1985.

[107] R. Stamm, B. Talin, E. L. Pollock, and C. A. Iglesias, "Ion-dynamic effects on the line shapes of hydrogenic emitters in plasmas," *Physical Review A*, vol. 34, no. 5, pp. 4144–4152, 1986.

[108] A. V. Anufrienko, A. E. Bulyshev, A. L. Godunov, et al., "Nonlinear interference effects and ion dynamics in the kinetic theory of stark broadening of the spectral lines of multicharged ions in a dense plasma," *Journal of Experimental and Theoretical Physics* , vol. 78, pp. 219–227, 1993.

[109] A. E. Bulyshev, A. V. Demura, V. S. Lisitsa, A. N. Starostin, A. E. Suvorov, and I. I. Yakunin, "Redistribution function for resonance radiation in a hot dense plasma," *Journal of Experimental and Theoretical Physics*, vol. 81, pp. 113–121, 1995.

[110] S. G. Brush, H. L. Sahlin, and E. Teller, "Monte Carlo study of a one-component plasma. I," *The Journal of Chemical Physics*, vol. 45, no. 6, pp. 2102–2118, 1966.

[111] V. M. Zamalin, G. E. Norman, and V. S. Filinov, *Monte-Carlo Method in Statistical Thermodynamics*, Nauka, Moscow, Russia, 1977.

[112] P. H. Acioli, "Review of quantum Monte Carlo methods and their applications," *Journal of Molecular Structure*, vol. 394, no. 2-3, pp. 75–85, 1997.

[113] I. K. Kamilov, A. K. Murtazaev, and Kh. K. Aliev, "Monte Carlo studies of phase transitions and critical phenomena," *Uspekhi Fizicheskikh Nauk*, vol. 169, no. 7, p. 795, 1999 (Russian).

[114] P. P. Ewald, "Die berechnung optischer und eletrostatischer gitterpotentiale," *Annals of Physics*, vol. 64, pp. 253–287, 1921.

[115] C. Kittel, *Introduction to Solid State Physics*, John Wiley & Sons, New York, NY, USA, 1986.

[116] P. Hohenberg and W. Kohn, "Inhomogeneous electron gas," *Physical Review B*, vol. 136, no. 3, pp. B864–B871, 1964.

[117] W. Kohn and L. J. Sham, "Self-consistent equations including exchange and correlation effects," *Physical Review A*, vol. 140, no. 4, pp. A1133–A1138, 1965.

[118] F. Perrot and M. W. C. Dharma-Wardana, "Exchange and correlation potentials for electron-ion systems at finite temperatures," *Physical Review A*, vol. 30, no. 5, pp. 2619–2626, 1984.

[119] F. Perrot and M. W. C. Dharma-Wardana, "Embedding an iron atom in a plasma: influence of the host plasma on the photoeffect," *Physical Review A*, vol. 31, no. 2, pp. 970–979, 1985.

[120] J. Chihara, "Dharma-wardana Perrot theory and the quantal hypernetted-chain equation for strongly coupled plasmas," *Physical Review A*, vol. 44, no. 2, pp. 1247–1256, 1991.

[121] G. Massacrier, "Self-consistent schemes for the calculation of ionic structures and populations in dense plasmas," *Journal of Quantitative Spectroscopy and Radiative Transfer*, vol. 51, no. 1-2, pp. 221–228, 1994.

[122] R. Singh and B. M. Deb, "Developments in excited-state density functional theory," *Physics Report*, vol. 311, no. 2, pp. 47–94, 1999.

[123] W. Kohn, "Nobel lecture: electronic structure of matter—wave functions and density functional," *Reviews of Modern Physics*, vol. 71, no. 5, pp. 1253–1266, 1999.
[124] F. J. Rojers, "Integral-equation method for partially ionized plasmas," *Physical Review A*, vol. 29, no. 2, pp. 868–879, 1984.
[125] A. A. Vlasov, *Theory of Many Particles*, Gostekhizdat, Moscow, Russia, 1950.
[126] A. A. Vlasov, *Statistical Distribution Functions*, Nauka, Moscow, Russia, 1966.
[127] A. A. Vlasov, *Nonlocal Statistical Mechanics*, Nauka, Moscow, Russia, 1978.
[128] R. S. Cohen, L. Spitzer Jr., and P. McR. Routly, "The electrical conductivity of an ionized gas," *Physical Review A*, vol. 80, no. 2, pp. 230–238, 1950.
[129] V. I. Kogan, "Fluctuating microfield and multiple collisions in gas of charged (or gravitating) particles," *Doklady USSR*, vol. 135, p. 1374, 1960.
[130] M. Rosenbluth and N. Rostoker, "Test particles in a completely ionized plasma," *Physics of Fluids*, vol. 3, no. 1, pp. 1–14, 1960.
[131] M. N. Rosenbluth and N. Rostoker, "Scattering of electromagnetic waves by a nonequilibrium plasma," *Physics of Fluids*, vol. 5, no. 7, pp. 776–788, 1962.
[132] J. B. Taylor, "Electric field correlation and plasma dynamics," *Physics of Fluids*, vol. 3, no. 5, pp. 792–796, 1960.
[133] M. Lewis, "Stark broadening of spectral lines by high-velocity charged particles," *Physical Review A*, vol. 121, no. 2, pp. 501–505, 1961.
[134] S. N. Gordienko, "Multiparticle nature of collisions in plasma and a unique feature of Coulomb interaction," *Fizika Plazmy*, vol. 26, no. 6, pp. 519–528, 2000 (Russian).
[135] S. A. Majorov, A. N. Tkachev, and S. I. Yakovlenko, "Thermodynamic parameters and distributions of instantaneous microfield values in nonideal plasmas," *Doklady USSR*, vol. 290, no. 1, pp. 106–109, 1988.
[136] S. A. Majorov, A. N. Tkachev, and S. I. Yakovlenko, "Thermodynamic parameters and debye screening in coulomb gas with small numbers of particles in debye sphere," *Pis'ma v ZhTF*, vol. 14, no. 4, pp. 354–359, 1988.
[137] S. A. Majorov, A. N. Tkachev, and S. I. Yakovlenko, "Modeling of fundamental Coulomb plasmas properties by method of dynamics of many particles," in *Nonequilibrium Plasma of Multiply Charged Ions*, vol. 40 of *Proceedings of General Physics Institute of Russian Academy of Science*, pp. 4–43, Nauka, Moscow, Russia, 1992.
[138] B. Talin, A. Calisti, and J. Dufty, "Classical description of electron structure near a positive ion," *Physical Review E*, vol. 65, no. 5, Article ID 056406, 11 pages, 2002.
[139] B. Talin, E. Dufour, A. Calisti, et al., "Molecular dynamics simulation for modelling plasma spectroscopy," *Journal of Physics A*, vol. 36, no. 22, pp. 6049–6056, 2003.
[140] M. A. Gigosos and V. Cardenoso, "Study of the effects of ion dynamics on Stark profiles of Balmer-α and -β lines using simulation techniques," *Journal of Physics B*, vol. 20, no. 22, pp. 6005–6019, 1987.
[141] M. A. Gigosos and V. Cardenoso, "New plasma diagnosis tables of hydrogen Stark broadening including ion dynamics," *Journal of Physics B*, vol. 29, no. 20, pp. 4795–4838, 1996.
[142] G. C. Hegerfeldt and V. Kesting, "Collision-time simulation technique for pressure-broadened spectral lines with applications to Ly-α," *Physical Review A*, vol. 37, no. 5, pp. 1488–1496, 1988.
[143] A. Barbés, M. A. Gigosos, and M. Á. González, "Analysis of the coupling between impact and quasistatic field mechanisms in Stark broadening," *Journal of Quantitative Spectroscopy and Radiative Transfer*, vol. 68, no. 6, pp. 679–688, 2001.
[144] M. A. Gigosos, M. Á. González, and V. Cardeñoso, "Computer simulated Balmer-α, -β and -γ Stark line profiles for non-equilibrium plasmas diagnostics," *Spectrochimica Acta*, vol. 58, no. 8, pp. 1489–1504, 2003.
[145] V. Kesting, "Joint stark-doppler broadening of hydrogen lines in plasma," in *Spectral Line Shapes*, R. Stamm and B. Talin, Eds., vol. 7, pp. 103–117, Science Nova, New York, NY, USA, 1993.
[146] L. A. Bureeva and V. S. Lisitsa, *Perturbed Atom*, Izdat, Moscow, Russia, 1997.
[147] M. L. Levin and S. M. Rytov, *Theory of Equilibrium Thermal Fluctuations in Electrodynamics*, Nauka, Moscow, Russia, 1967.
[148] L. M. Biberman, V. S. Vorob'ev, and I. T. Yakubov, *Kinetics of Non-Equilibrium Low Temperature Plasmas*, Nauka, Moscow, Russia, 1982.
[149] G. E. Norman and A. N. Starostin, "Thermodynamics of a strongly nonideal plasma," *Teplofizika Visokikh Temperatur*, vol. 8, no. 2, pp. 381–408, 1970.
[150] V. S. Vorob'ev and A. A. Likal'ter, "Physical properties of strongly coupled plasmas," in *Plasma Chemistry*, B. M. Smirnov, Ed., vol. 15, pp. 163–208, Energoatomizdat, Moscow, Russia, 1989.
[151] V. E. Fortov, I. T. Yakubov, and A. G. Khrapak, *Physics of Strongly Coupled Plasma*, Clarendon Press, Oxford, UK, 2006.
[152] L. P. Kudrin, *Statistical Plasma Physics*, Atomizdat, Moscow, Russia, 1974.
[153] W. Ebeling, W. D. Kraeft, and D. Kremp, *Theory of Bound States and Ionization Equilibrium in Plasmas and Solids*, Academie, Berlin, Germany, 1976.
[154] D. G. Hummer and D. Mihalas, "The equation of state for stellar envelopes. I. An occupation probability formalism for the truncation of internal partition functions," *Astrophysical Journal*, vol. 331, pp. 794–814, 1988.
[155] D. Mihalas, W. Däppen, and D. G. Hummer, "The equation of state for stellar envelopes. II. Algorithm and selected results," *Astrophysical Journal*, vol. 331, pp. 815–825, 1988.
[156] W. Däppen, D. Mihalas, D. G. Hummer, and B. W. Mihalas, "The equation of state for stellar envelopes. III. Thermodynamic quantities," *Astrophysical Journal*, vol. 332, pp. 261–270, 1988.
[157] A. Nayfonov, W. Däppen, D. G. Hummer, and D. Mihalas, "The MHD equation of state with post-Holtsmark microfield distributions," *Astrophysical Journal*, vol. 526, no. 1, pp. 451–464, 1999.
[158] D. V. Fisher and Y. Maron, "Effective statistical weights of bound states in plasmas," *European Physical Journal D*, vol. 18, no. 1, pp. 93–111, 2002.
[159] W. Ebeling and S. Hilbert, "On Saha's equation for partially ionised plasmas and Onsager's bookkeeping rule," *European Physical Journal D*, vol. 20, no. 1, pp. 93–101, 2002.
[160] K. P. Gurov, *Basics of Kinetic Theory*, Mir, Moscow, Russia, 1966.
[161] D. V. Fisher and Y. Maron, "Statistics of inter-particle distances and angles in plasmas," *European Physical Journal D*, vol. 14, no. 3, pp. 349–359, 2001.
[162] M.-Y. Song and Y.-D. Jung, "Screening and collective effects on electron-impact excitation of hydrogen-like ions in nonideal plasmas," *Journal of Physics B*, vol. 36, no. 10, pp. 2119–2128, 2003.

[163] A. Bouchoule, Ed., *Dusty Plasmas Physics, Chemistry and Technological Impacts in Plasma Processing*, John Wiley & Sons, New York, NY, USA, 1999.

[164] G. Peach, "Theory of the pressure broadening and shift of spectral lines," *Advances in Physics*, vol. 30, no. 3, pp. 367–474, 1981.

[165] F. Lado and J. W. Dufty, "Charge distribution in plasmas with field constraint," *Physical Review A*, vol. 36, no. 5, pp. 2333–2337, 1987.

[166] J. P. Hansen, "Statistical mechanics of dense ionized matter. I. Equilibrium properties of the classical one-component plasma," *Physical Review A*, vol. 8, no. 6, pp. 3096–3109, 1973.

[167] F. J. Rogers, D. A. Young, H. E. Dewitt, and M. Ross, "One-component plasma structure factor in tabular form," *Physical Review A*, vol. 28, no. 5, pp. 2990–2992, 1983.

[168] A. V. Demura, V. S. Lisitsa, and G. V. Sholin, "Effect of reduced mass in stark broadening of hydrogen lines," *Journal of Experimental and Theoretical Physics* , vol. 46, pp. 209–215, 1977.

[169] H. R. Griem, "Broadening of the Lyman-α line of hydrogen by low-frequency electric fields in dense plasma," *Physical Review A*, vol. 20, no. 2, pp. 606–615, 1979.

[170] H. R. Griem and G. D. Tsakiris, "Broadening of the Lyman-β line of hydrogen by low-frequency electric fields in dense plasma," *Physical Review A*, vol. 25, no. 2, pp. 1199–1202, 1982.

[171] R. Cauble and H. R. Griem, "Broadening of Lyman lines of hydrogen and hydrogenic ions by low-frequency fields in dense plasmas," *Physical Review A*, vol. 27, no. 6, pp. 3187–3199, 1983.

[172] J. D. Hey and H. R. Griem, "Central structure of low-n Balmer lines in dense plasmas," *Physical Review A*, vol. 12, no. 1, pp. 169–185, 1975.

[173] J. D. Hey, "Ion dynamical corrections to the Holtsmark theory of spectral line broadening," *Transactions of the Royal Society of South Africa*, vol. 42, part 1, pp. 81–101, 1976.

[174] H. Margenau and M. Lewis, "Structure of spectral lines from plasmas," *Reviews of Modern Physics*, vol. 31, p. 56, 1983.

[175] G. J. Dalenoort, "The Holtsmark-continuum model for the statistical description of a plasma," *Zeitschrift für Physik*, vol. 248, no. 1, pp. 22–40, 1971.

[176] R. Gans, "Das elelektrische molekularfeld," *Annalen der Physik*, vol. 66, p. 396, 1921.

[177] K. Weise, "The probability distributions of the electric and magnetic microfield in a relativistic plasma," *Zeitschrift für Physik*, vol. 212, no. 5, pp. 458–466, 1968.

[178] K. Hunger and R. W. Larenz, "Das mikrofeld im plasma," *Zeitschrift für Physik*, vol. 163, no. 3, pp. 245–261, 1961.

[179] V. I. Kogan and A. D. Selidovkin, "About fluctuating microfield in system of charged particles," *Beiträge aus der Plasma Physik*, vol. 9, no. 3, pp. 199–216, 1969.

[180] S. Alexiou, "Collective coordinates for ion dynamics," *Journal of Quantitative Spectroscopy and Radiative Transfer*, vol. 54, no. 1-2, pp. 1–26, 1995.

[181] S. Alexiou, A. Calisti, P. Gauthier, et al., "Aspects of plasma spectroscopy: recent advances," *Journal of Quantitative Spectroscopy and Radiative Transfer*, vol. 58, no. 4–6, pp. 399–412, 1997.

[182] A. Calisti, S. Ferri, C. Mossé, et al., "Slow and fast microfield components in warm and dense hydrogen plasmas," http://arxiv1.library.cornell.edu/abs/0710.2091v1.

[183] A. Calisti, S. Ferri, C. Mossé, et al., "Electric microfield in simulated two component plasmas," in *Spectral Line Shapes, Vol. 15*, M. A. Gigosos and M. Á. González, Eds., vol. 1058 of *AIP Conference Proceedings*, pp. 27–33, Science Nova, New York, NY, USA, 2008.

[184] H. B. Nersisyan, C. Toepffer, and G. Zwicknagel, "Microfield distributions in strongly coupled two-component plasmas," *Physical Review E*, vol. 72, no. 3, Article ID 036403, 14 pages, 2005.

[185] H. B. Nersisyan and G. Zwicknagel, "Microfield distributions in a classical two-component plasma," *Journal of Physics A*, vol. 39, no. 17, pp. 4677–4681, 2006.

[186] H. B. Nersisyan, D. A. Osipyan, and G. Zwicknagel, "Renormalized cluster expansion of the microfield distribution in strongly coupled two-component plasmas," *Physical Review E*, vol. 77, no. 5, Article ID 056409, 2008.

[187] X.-Z. Yan and S. Ichimaru, "Theory of interparticle correlations in dense, high-temperature plasmas. VI. Probability densities of the electric microfields," *Physical Review A*, vol. 34, no. 3, pp. 2167–2172, 1986.

[188] J. Ortner, I. Valuev, and W. Ebeling, "Electric microfield distribution in two-component plasmas. Theory and simulations," *Contributions to Plasma Physics*, vol. 40, no. 5-6, pp. 555–568, 2000.

[189] S. Laulan, C. Blancard, and G. Faussurier, "Fast electric microfield distribution calculations in strongly coupled Yukawa plasmas," *High Energy Density Physics*, vol. 4, no. 3-4, pp. 131–141, 2008.

[190] E. Stambulchik and Y. Maron, "A study of ion-dynamics and correlation effects for spectral line broadening in plasma: K-shell lines," *Journal of Quantitative Spectroscopy and Radiative Transfer*, vol. 99, pp. 730–749, 2006.

[191] N. A. Krall and A. W. Trivelpiece, *Principles of Plasma Physics*, McGraw-Hill, New York, NY, USA, 1973.

[192] S. Ichimaru, *Basic Principles of Plasma Physics*, Benjamin, Reading, Mass, USA, 1973.

[193] A. A. Mihajlov, Y. Vitel, and Lj. M. Ignjatović, "The new screening characteristics of strongly non-ideal and dusty plasmas—part 1: single-component systems," *High Temperature*, vol. 46, no. 6, pp. 737–745, 2008.

[194] A. A. Mihajlov, Y. Vitel, and Lj. M. Ignjatović, "The new screening characteristics of strongly non-ideal and dusty plasmas—part 2: two-component systems," *High Temperature*, vol. 47, no. 1, pp. 1–12, 2009.

[195] A. V. Demura, "Statistical and thermodynamical aspects of microfield conception in plasmas," in *Encyclopedia of Low Temperature Plasmas: Volume II, Thermodynamics of Plasma*, I. Iosilevski and A. Starostin, Eds., pp. 163–202, Fizmatlit, Moscow, Russia, 2004.

[196] A. V. Demura and D. Gilles, "Overview of plasma microfield in Stark broadening of spectral lines," in *Proceedings of the 17th International Conference on Spectral Line Shapes*, E. Dalimier, Ed., pp. 121–128, Frontier Group, Paris, France, 2004.

[197] A. V. Demura, "Evolution of plasma microfield notion," in *Proceedings of the 22nd Summer School and International Symposium on Physics of Ionized Gases (SPIG '04)*, L. Hadzievski, T. Grozdanov, and N. Bibic, Eds., vol. 740 of *AIP Conference Proceedings*, pp. 297–308, AIP, Bajina Basta, Serbia and Montenegro, August 2004.

[198] C. Stehle, D. Gilles, M. Busquet, and A. Demura, "On Stark broadening as a tool for diagnostics of high density plasmas," *Laser and Particle Beams*, vol. 23, no. 3, pp. 357–363, 2005.

Hindawi Publishing Corporation
International Journal of Spectroscopy
Volume 2010, Article ID 983578, 7 pages
doi:10.1155/2010/983578

Review Article

Pressure Broadening of Some He I Lines

Banaz Omar

Physics Department, Research Center OPTIMAS, Technical University of Kaiserslautern, Erwin Schroedinger Str. 46, 67663 Kaiserslautern, Germany

Correspondence should be addressed to Banaz Omar, omar@rhrk.uni-kl.de

Received 29 April 2009; Accepted 12 July 2009

Academic Editor: Roland Stamm

Quantum statistical approach is adopted for calculating the spectral line shapes of neutral helium in dense plasmas. Stark broadening of isolated He I lines 5048 Å ($2^1P - 4^1S$), 3889 Å ($2^3S - 3^3P$), and 3188Å ($2^3S - 4^3P$) is presented. Based on thermodynamic Green's function, the electronic contribution to the shift and width is considered. The participation of ions to the line broadening is treated in a quasistatic approximation, by taking both quadratic Stark effect and quadrupole interaction into account. The calculated shifts and widths are compared with existing data.

1. Introduction

Plasma spectroscopy deals with the characteristics of radiation emitted from a plasma. In dense plasmas, damping of the emitted radiation occurs by means of several mechanisms; the most effective one is pressure broadening (Stark broadening). The interaction between a radiating atom and surrounding perturbing particles leads to Stark broadening. High-speed electrons perturb the emitter by collisions, causing the interruption of the spontaneous emission and altering the emitter energy levels [1–4].

Line profile calculation is an interesting tool for both laboratory and astrophysical plasma diagnostics, for example, to determine the internal parameters, to understand the microscopic processes within the plasma, and to check the quality of the predicted experimental and theoretical parameters [1, 2].

The emission spectra of helium and He-like ions with their simple atomic structures are interesting for plasma diagnostics such as in shock wave tube or pulsed arc plasmas [5, 6] and in the astrophysical context, for example, stellar atmospheres of hot stars and white dwarfs [7–9]. Helium is used as a carrier gas in many laboratories and is weekly interacting with materials and less harmful for plasma facing components than hydrogen and its isotopes [5]. The He-like ions may exist even at extremely high temperatures and densities. Even ITER is started with helium discharge, also He can be observed in discharge of JET. Spectroscopic measurements of tokamak plasmas are not free from helium [10].

Various approaches have been investigated to calculate spectral line shapes in plasmas [9, 11–24]. In a semiclassical approach helium lines were calculated by Griem et al. [22, 23], using an impact approximation for electrons with a cutoff procedure, while almost stationary heavy ions are treated in a quasistatic ion approximation due to the static microfield. Also, molecular dynamics (MD) simulations have been performed by Calisti et al. [25] and Gigosos et al. [26] to include the influence of time-dependent microfield by introducing two kinds of simulations for calculating He I Stark line profiles.

Thermodynamic Green's function approach is a powerful tool to describe the Stark broadening [27–30]. In the last two decades, a quantum statistical approach has been developed, taking into account the medium effects by using Green's function [31–36]. In principle, this approach is able to describe dynamical screening and strong collisions by electrons, as well as the dynamic ion microfield, in a systematic way. This quantum statistical approach has been successfully applied to calculate the spectral line shapes of hydrogen, helium, H-, and He-like ions in dense plasmas [37–42].

In this paper thermodynamic Green's function approach is considered to calculate the pressure broadening of some selected neutral helium lines. In Section 2 the definitions and spectral properties of Green's function approach to spectral

line shapes of nonideal plasmas are presented. A review of the basic formalism is introduced and extended to helium lines. Section 3 provides the calculated shifts and full widths at half maximum (FWHM) for nonoverlapping, isolated (nondegenerate) He I lines 5048 Å (2^1P-4^1S), 3889 Å (2^3S-3^3P), and 3188 Å (2^3S-4^3P) in dense plasmas. Finally, conclusions are given in Section 4.

2. Theoretical Calculations

Microscopic formation of the spectral line shapes in dense plasmas arises from perturbation of the radiative atom by collective and many-body effects [1, 4]. Thus, the interaction with the surrounding particles must be taken into account. For example, screening is considered as an important collective effect in plasmas. The influence of electrons and ions may be treated separately due to the difference in mass and mobility. Green's function methods provide a perturbative approach to correlation functions and quantum effects of many-body systems. Two-particle Green's function is used to calculate the line shape and electron broadening from the self-energy and the vertex function. From statistical properties of the system, the current-current correlations determine the absorption spectrum, which is utilized by Ross [27]. Recently, further improvements of this approach have been made by Röpke et al. [32], Hitzschke et al. [33], Günter et al. [34], and Omar et al. [41].

Optical properties of many-particle systems are specified by the dielectric function $\varepsilon(\mathbf{q},\omega)$ based on Green's function theory, which is the response of the medium to an external electromagnetic field. The longitudinal dielectric function is related to the polarization function $\Pi(\mathbf{q},\omega)$

$$\varepsilon_{\mathrm{l}}(\mathbf{q},\omega) = 1 - V(q)\Pi(\mathbf{q},\omega), \tag{1}$$

where $V(q) = e^2/(\epsilon_0 q^2)$ is the Fourier transformed Coulomb potential. In terms of the absorption coefficient $\alpha(\omega)$ and the index of refraction $n(\omega)$, the transverse dielectric function $\varepsilon_t(\mathbf{q},\omega)$ in the long wavelength limit $q \to 0$ reads

$$\lim_{\mathbf{q}\to 0} \varepsilon_t(\mathbf{q},\omega) = \left[n(\omega) + \frac{ic}{2\omega}\alpha(\omega) \right]^2. \tag{2}$$

In the visible region where the wavelength λ is large compared with the atomic dimension a_{B}, the transverse and the longitudinal part of dielectric function coincide. The absorption coefficient is proportional to the imaginary part of the dielectric function

$$\alpha(\omega) = \frac{\omega}{cn(\omega)} \lim_{\mathbf{q}\to 0} \mathrm{Im}\,\varepsilon(\mathbf{q},\omega),$$

$$n(\omega) = \frac{1}{\sqrt{2}} \lim_{\mathbf{q}\to 0} \left\{ \mathrm{Re}\,\varepsilon(\mathbf{q},\omega) + \left[\left(\mathrm{Re}\,\varepsilon(\mathbf{q},\omega)\right)^2 + \mathfrak{A} \right]^{1/2} \right\}^{1/2}, \tag{3}$$

where $\mathfrak{A}$ denotes $(\mathrm{Im}\varepsilon(\mathbf{q},\omega))^2$. In thermal equilibrium, the absorption coefficient is related to the emission coefficient by Kirchoff's law [43]. In optically thin plasma, the emission coefficient is proportional to the line emission. As mentioned above, the dielectric function is related to the polarization function $\Pi(\mathbf{q},\omega)$. Then the medium modifications of spectral line shapes can be addressed to the bound-bound two-particle polarization function, which concerns to dipole-dipole autocorrelation function [36].

The perturber-radiator interaction leads to pressure broadening, which contains electronic and ionic contributions. Describing the ionic contribution in the quasistatic approximation by averaging over the ionic microfield at radiating atom [31, 36, 44], we get

$$I^{\mathrm{pr}}(\omega) \sim \sum_{i,i',f,f'} I_{i,i'}^{f,f'}(\omega) \int_0^\infty d\beta P(\beta) \times \mathrm{Im} \left\langle i \left| \left\langle f \left| \left[\hbar\omega - \hbar\omega_{if} - \Sigma_{if}(\omega,\beta) + \mathrm{i}\Gamma_{if}^{\mathrm{V}} \right]^{-1} \right| f' \right\rangle \right| i' \right\rangle. \tag{4}$$

Here, the ionic microfield distribution function $P(\beta)$ is taken according to the Hooper field distribution, and $\beta = E/E_0$ is the normalized field strength [45]. So $\hbar\omega_{if} = E_i - E_f$ is the unperturbed transition energy between the initial i and the final f states; i' and f' are the corresponding intermediate states

$$I_{i,i'}^{f,f'}(\omega) = \langle i|\mathbf{r}|f\rangle \langle f'|\mathbf{r}|i'\rangle \frac{\omega^4}{8\pi^3 c^3} \mathrm{e}^{-\hbar\omega/k_{\mathrm{B}}T}, \tag{5}$$

where $\langle i|\mathbf{r}|f\rangle$ is identified as a dipole matrix-element for the transition between i and f states. The line profile itself is determined by the vertex correction Γ_{if}^{V} for the overlapping lines and by the self-energy corrections Σ of the initial and final states

$$\Sigma_{if}(\omega,\beta) = \mathrm{Re}\left[\Sigma_i(\omega,\beta) - \Sigma_f(\omega,\beta) \right] + \mathrm{i}\,\mathrm{Im}\left[\Sigma_i(\omega,\beta) + \Sigma_f(\omega,\beta) \right]. \tag{6}$$

Both electronic and ionic contributions occur in the self-energy $\Sigma_n(\omega,\beta)$, which is assumed to be diagonal in the atomic state n;

$$\Sigma_n(\omega,\beta) = \Sigma_n^{\mathrm{ion}}(\beta) + \Sigma_n^{\mathrm{el}}(\omega,\beta). \tag{7}$$

The electronic self-energy is obtained by performing a Born approximation with respect to the perturber-radiator interaction [36]

$$\Delta_n^{\mathrm{SE}} + \mathrm{i}\Gamma_n^{\mathrm{SE}} = \left\langle n \left| \Sigma^{\mathrm{el}}(E_n,\beta) \right| n \right\rangle = -\frac{1}{e^2} \int \frac{d^3q}{(2\pi)^3} V(q) \sum_\alpha |M_{n\alpha}(\mathbf{q})|^2 \times \int_{-\infty}^{\infty} \frac{d\omega}{\pi} [1 + n_{\mathrm{B}}(\omega)] \frac{\mathrm{Im}\,\varepsilon^{-1}(\mathbf{q},\omega+\mathrm{i}0)}{E_n - E_\alpha(\beta) - \hbar(\omega+\mathrm{i}0)}. \tag{8}$$

Here, the sum over α runs from $n-2$ to $n+2$ discrete bound states for virtual transitions, and the level splitting due to the

ion microfield $E_\alpha(\beta)$ has been neglected [35]. So $n_B(\omega) = [\exp(\hbar\omega/k_BT) - 1]^{-1}$ is the Bose distribution function, and $M_{n\alpha}(\mathbf{q})$ are the transition matrix-elements, given below. The inverse dielectric function $\varepsilon^{-1}(\mathbf{q},\omega)$ contains many particle effects which account for the dynamical screening of the interaction in the plasma:

$$\operatorname{Im}\varepsilon^{-1}(\mathbf{q},\omega) = -\frac{\operatorname{Im}\varepsilon(\mathbf{q},\omega)}{[\operatorname{Re}\varepsilon(\mathbf{q},\omega)]^2 + [\operatorname{Im}\varepsilon(\mathbf{q},\omega)]^2}. \quad (9)$$

The random phase approximation (RPA) for the dielectric function is used:

$$\varepsilon^{\mathrm{RPA}}(\mathbf{q},\omega) = 1 - 2V(q)\int \frac{d^3p}{(2\pi)^3}\frac{f_e\left(E_{\mathbf{p}}\right) - f_e\left(E_{\mathbf{p}+\mathbf{q}}\right)}{E_{\mathbf{p}} - E_{\mathbf{p}+\mathbf{q}} - \hbar(\omega + \mathrm{i}0)}. \quad (10)$$

where $E_{\mathbf{p}} = \hbar^2\mathbf{p}^2/2m_e$ is the kinetic energy of electrons, and $f_e(E_{\mathbf{p}})$ is the Fermi distribution function of the electrons, approximated to the Boltzmann distribution function in the degenerate limit

$$f_e\left(E_{\mathbf{p}}\right) \simeq \frac{1}{2}n_e\left(\frac{2\pi\hbar^2}{m_ek_BT}\right)^{3/2}\exp\left(-\frac{\hbar^2p^2}{2m_ek_BT}\right). \quad (11)$$

The full expression of the inverse dielectric function has to be used if the transition frequency $\omega_{n\alpha}$ becomes comparable to the electron plasma frequency $\omega_{\mathrm{pl}} = (n_e e^2/\epsilon_0 m_e)^{1/2}$. However, in the high-frequency limit $\omega_{n\alpha} \gg \omega_{\mathrm{pl}}$, the inverse dielectric function can be approximated by

$$\operatorname{Im}\varepsilon^{-1}(\mathbf{q},\omega) = \frac{-\operatorname{Im}\varepsilon(\mathbf{q},\omega)}{|\varepsilon(\mathbf{q},\omega)|^2} \approx -\operatorname{Im}\varepsilon(\mathbf{q},\omega). \quad (12)$$

This binary collision approximation leads to a linear behavior of the electronic shift contribution with respect to the electron density, whereas a nonlinear dependence of the electronic shift with increasing electron density is expected if the full expression of the inverse dielectric function is used [33, 35].

The vertex function for the coupling between the upper and the lower state is given by

$$\Gamma_{if}^V = \frac{2\pi}{e^2}\int\frac{d^3q}{(2\pi)^3}\,\frac{d^3p}{(2\pi)^3}\,f_e\left(E_{\mathbf{p}}\right)V^2 \times (q)M_{ii}(\mathbf{q})M_{ff}(-\mathbf{q})\,\delta\left(\frac{\hbar^2\mathbf{p}\cdot\mathbf{q}}{m_e}\right). \quad (13)$$

The transition matrix-elements $M_{n\alpha}(\mathbf{q})$ describe the coupling between free charges and bound states. In lowest order, they are determined by the atomic eigenfunctions $\psi_n(\mathbf{p})$ of the radiating electron and depend on the momentum transfer $\hbar\mathbf{q}$ [34, 46]

$$M_{n\alpha}(\mathbf{q}) = \int\frac{d^3p}{(2\pi)^3}\,\psi_n^*(\mathbf{p}) \times\left[Ze\psi_\alpha\left(\mathbf{p} - \frac{me}{m_i+m_e}\mathbf{q}\right) - e\psi_\alpha\left(\mathbf{p} + \frac{mi}{m_i+m_e}\mathbf{q}\right)\right], \quad (14)$$

assuming that the ion with charge Z is much heavier than the electron $m_i \gg m_e$:

$$M_{n\alpha}(\mathbf{q}) = \int\frac{d^3p}{(2\pi)^3}\,\psi_n^*(\mathbf{p})[Ze\,\psi_\alpha(\mathbf{p}) - e\psi_\alpha(\mathbf{p}+\mathbf{q})] = \mathrm{i}e\left(Z\delta_{n\alpha} - \int d^3r\,\psi_n^*(\mathbf{r})\,\exp(\mathrm{i}\mathbf{q}\cdot r)\psi_\alpha(\mathbf{r})\right). \quad (15)$$

Expanding the plane wave into spherical harmonics

$$\exp(\mathrm{i}\mathbf{q}\cdot r) = 4\pi\sum_{l=0}^{\infty}\sum_{m=-l}^{l}\mathrm{i}^l j_l(qr)Y_{lm}^*\left(\Omega_q\right)Y_{lm}(\Omega_r), \quad (16)$$

where $j_l(qr)$ is the Bessel function, a multipole expansion can be derived; for example, $l = 0, 1, 2$ gives the monopole, dipole, and quadrupole contribution of the radiator-electron interaction, respectively. The radial part of helium wave function is calculated based on Coulomb approximation method of Bates and Damgaard [47–49]. For more detail see [41].

By using the Born approximation, the electronic self-energy is overestimated. To avoid this we apply a cutoff procedure and add the strong collision term in contrast to partial summation of the three-particle T-matrix, which is quite suitable for treating short-range interactions between particles [50], where the result might be slightly modified. According to Griem, the cutoff parameter for the q-integration is the inverse of the minimum limiting impact parameter ($q_{\max} = 1/\rho_{\min}$) [22, 36, 49, 51].

To determine the ionic self-energy, we approximate the time-dependent microfield fluctuation by its static value. In general, dynamic ionic microfield is important for overlapping lines and at low electron density in the line center [52, 53]. Due to the slow movement of heavy ions, the ion microfield is assumed to be constant during the time of interest for the radiation process. The static ionic contribution to the ionic self-energy is treated by means of the microfield concept including both quadratic Stark effect and quadrupole effects. The first-order perturbation term vanishes for nonhydrogenic like atoms because of nondegeneracy with respect to the orbital quantum number l. According to second-order perturbation theory, the quadratic Stark effect is proportional to the square of the microfield [54]

$$\Sigma_{nlm}^2(E) = e^2|E|^2\sum_{n',l',m'}\frac{|\langle n,l,m|z|n',l',m'\rangle|^2}{E_{nlm} - E_{n'l'm'}}, \quad (17)$$

where E is the microfield strength; n, l, and m are the well-known principal, orbital, and magnetic atomic quantum numbers, respectively. The quadrupole Stark effect is due to the inhomogeneity of the ionic microfield. We use the expression derived by Halenka [55]:

$$\Sigma_{nn'}^3(E) = -\frac{5}{2\sqrt{32\pi}}\frac{eE_0}{r_0}B_\rho(\beta)\langle n|3z^2 - r^2|n'\rangle. \quad (18)$$

Here, $B_\rho(\beta)$ is the mean field gradient at a given field strength, and the screening parameter $\rho = r_0/r_D$ is taken as the ratio between the mean particles distance r_0 and the Debye radius r_D.

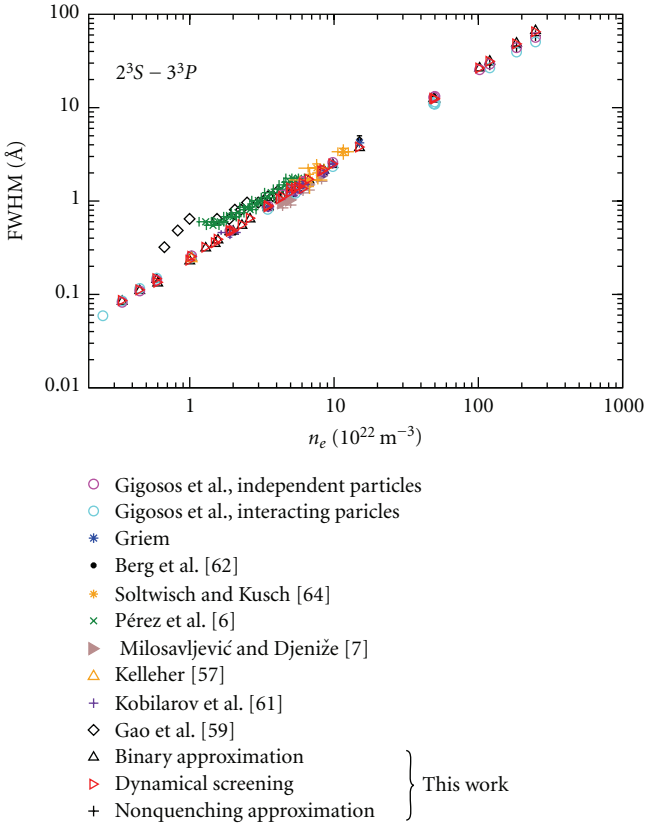

Figure 1: Stark FWHM for the He I line 3889 Å as a function of electron density. A comparison is made with the measured [6, 56–61] and other theoretical data [22, 62].

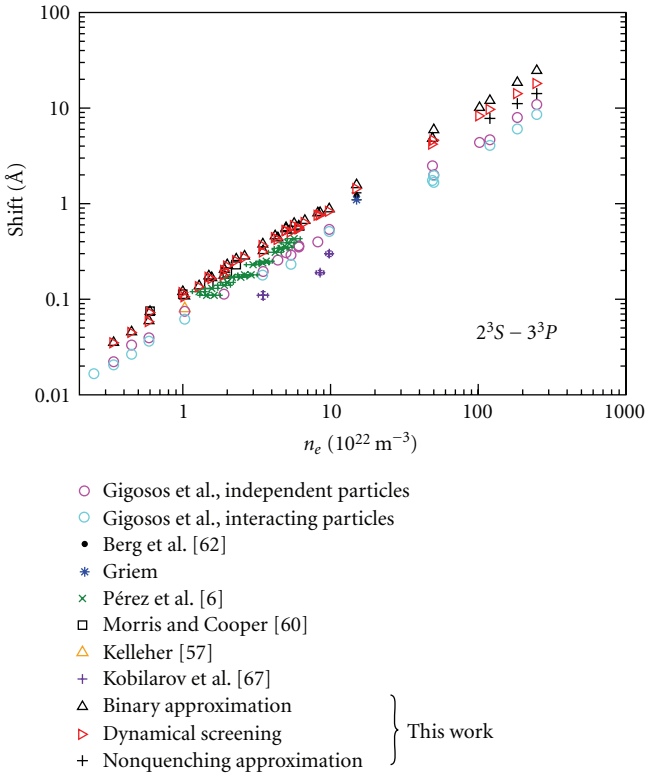

Figure 2: Stark shift for the He I line 3889 Å as a function of electron density. A comparison is made with the measured [6, 56–58, 63] and other theoretical data [22, 62].

3. Results and Discussions

The Stark broadening parameters for the transition ($2^1P - 4^1S$) 5048 Å are given in Table 1. Our width wth and shift dth results are compared to calculated values of Bassalo et al. (BCW) [66], measurements of Kelleher [56], and measurements of Diatta [67]. Our calculations agree better with the measured value by Kelleher [56] in contrast to the results given by Bassalo et al. [66]. The measured shift by Diatta [67] is obviously smaller than the calculated shifts given in Table 1.

The Stark width and shift of the line ($2^3S - 3^3P$) 3889 Å are measured by Pérez et al. [6]. The measured values were in the plasma density range of $(1 - 6) \times 10^{22}$ m^{-3} and temperature interval of $(0.8 - 3) \times 10^4$ K with a mean value of 2×10^4 K. The error bar in the case of n_e was ±10%, and the uncertainty in the temperature evaluation was about 20%. Recently, the FWHM of this line is measured by Gao et al. [61] for a helium arc for density range $(0.5 - 4) \times 10^{22}$ m^{-3}. Figures 1 and 2 include other available experimental [56–60, 63] and theoretical results [22, 62]. The MD simulation results of Gigosos et al. [62] have been performed for independent as well as interacting particles in nonquenching approximation. Our calculations are also presented, the width shows a good agreement especially with the MD simulations data of Gigosos et al. [62], where no Doppler broadening is included. Nonlinearity can be seen at very high electron density. The discrepancy between the measured and calculated line broadening may be related to self absorption [61]. However, our results for the shift are overestimated, on the other hand better agreement can be seen by comparing our results in non-quenching approximation with the results of Gigosos et al. [62], which give lower values of shift at high electron density.

The Stark parameters of the line ($2^3S - 4^3P$) 3188 Å are measured by Peláez et al. [64]. They made a spectroscopic and interferometric analysis of a pulsed plasma. The electron temperature (from 1900 K to 2300 K) was obtained from the intensity ratio of He II lines. Electron density was determined by interferometry, ranging from 1.25×10^{22} m^{-3} to 6.22×10^{22} m^{-3}. From these experimental results an empirical calibration for the Stark parameters was obtained in a broad range of electron densities [64]. The experimental and various theoretical Stark parameters are reported by Peláez et al. [64], and our results are included in Figures 3 and 4 for Stark width and shift as a function of electron density, respectively, at the given plasma temperatures. Theoretical predictions of Bassalo et al. (BCW) [24] can also be seen in Figures 3 and 4. Further experimental results are presented, carried out by Kelleher [56], Mijatovic′ et al. [65], Berg et al. [58], and Soltwisch and Kusch [60]. The measured value of Berg et al. [58] was compared with Griem's theory [58]

Table 1: The calculated FWHM and shift (without/with screening) for the line 5048 Å are given; w_{th} and d_{th} this work; w_B and d_B Bassalo et al. [66]. The experimental w_{exp} and d_{exp} are included [56, 67].

n_e (10^{22} m^{-3})	T_e (10^3 K)	w_B (Å)	w_{th} (Å)	w_{exp} (Å)	d_B (Å)	d_{th} (Å)	d_{exp} (Å)
3.2	30.0	5.22/5.22	5.385/5.378	—	2.19/2.05	2.56/2.397	—
2.0	18.0	3.10/3.10	3.183/3.179	3.4	1.43/1.35	1.783/1.677	0.9 [67]
1.03±12%	20.9±20%	1.58/1.58	1.623/1.622	1.68	0.75/0.68	0.862/0.82	0.89 [56]

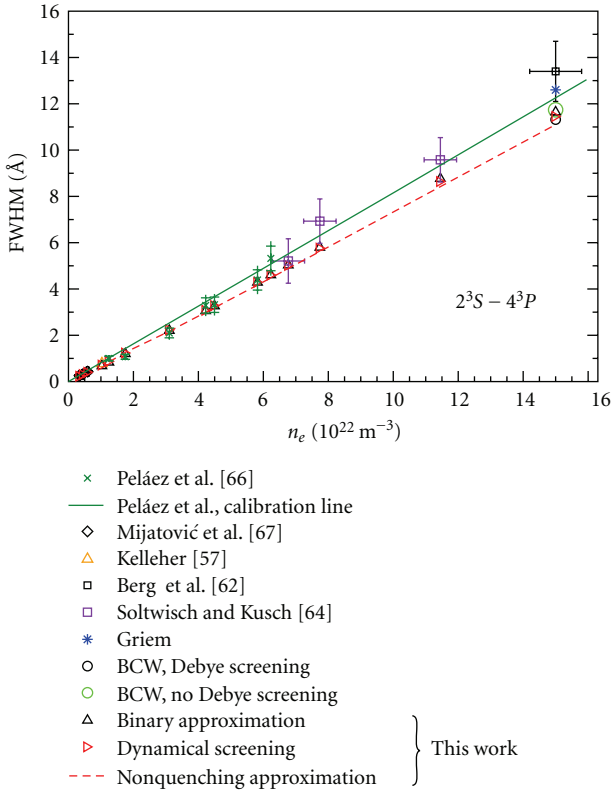

Figure 3: The measured Stark FWHM and calculated values for He I 3188 Å line versus electron density. The calculated Stark widths are included from different approaches [22, 24, 56, 58, 60, 64, 65].

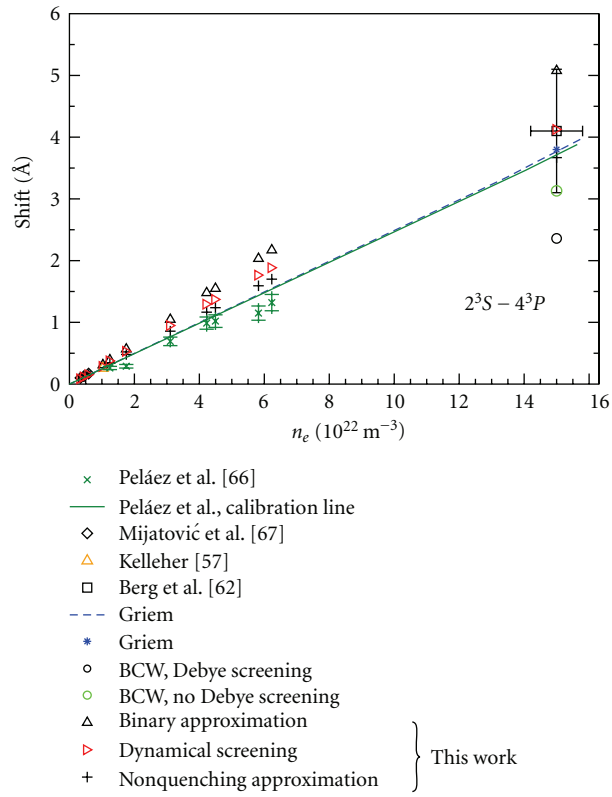

Figure 4: The measured Stark shift and calculated values for He I 3188 Å line versus electron density. The calculated Stark shifts are included from different theoretical approaches [22, 24, 56, 58, 64, 65].

at electron density $(1.5 \pm 0.08) \times 10^{23}$ m^{-3} and temperature $(2.9 \pm 0.2) \times 10^4$ K.

4. Conclusions

The quantum statistical approach has been developed to calculate spectral line shapes in dense plasmas. By using thermodynamic Green's function, a systematic perturbative treatment of the polarization function has been performed [33, 34, 46]. In contrast to the molecular dynamics (MD) simulations, consistent quantum description is applied here to calculate the Stark parameters by using the formalism presented above. The calculated Stark shift and full width at half maximum (FWHM) of He I lines 5048 Å ($2^1P - 4^1S$), 3889 Å ($2^3S - 3^3P$), and 3188 Å ($2^3S - 4^3P$) have been calculated in the density range $(10^{21} - 10^{24})$ m^{-3} and for temperatures between $(0.5 - 6) \times 10^4$ K. In dense plasmas the *binary (few-particle) collision approximation* is not appropriate to describe the collective interactions; therefore at high densities the *dynamical screening effect* will be more important seen (12), which reduces the linearity of Stark parameters with increasing electron density. This affects mostly the shift than the width, and it can be seen in Figures 2 and 4. The Hooper microfield distribution function is applicable for plasmas in the regime $\Gamma \leq 1$, in which the correlations between plasma particles are considered as small perturbations. This distribution is not applicable in strongly coupling regime, where the correlation effect is important at high density, and therefore a new distribution function should be adopted. Generally, our calculated line widths show good agreement by comparing with other results, while the shift is slightly overestimated for the lines 3889 Å and 3188 Å. However, by performing *nonquenching approximation* better agreement can be seen.

Moreover, our quantum statistical approaches can be applied not only to investigate the line shapes of two-electron atom but also to complex atoms. Furthermore, the deformation of spectral line profiles can be investigated in a strong magnetic field for stellar diagnostic.

Acknowledgments

This project is supported by Emmy Noether-Program of the Deutsche Forschungsgemeinschaft, RE1141/11-1. The author would like to thank A. Wierling, G. Röpke, and M. A. Gonzalez for helpful discussions.

References

[1] H. R. Griem, *Principles of Plasma Spectroscopy*, Cambridge University Press, Cambridge, UK, 1997.

[2] W. Lochte-Holtgreven, *Plasma Diagnostics*, American Institute of Physics, New York, NY, USA, 1995.

[3] T. Fujimoto, *Plasma Spectroscopy*, Claredon Press, Oxford, UK, 2004.

[4] G. W. Collins, *The Fundamentals of Stellar Astrophysics*, W. H. Freeman, New York, NY, USA, 1989.

[5] C. Pérez, I. de la Rosa, A. M. de Frutos, and S. Mar, "Calibration of the Stark-broadening parameters for some He i lines," *Physical Review A*, vol. 44, no. 10, pp. 6785–6790, 1991.

[6] C. Pérez, R. Santamarta, M. I. de la Rosa, and S. Mar, "Stark broadening of neutral helium lines and spectroscopic diagnostics of pulsed helium plasma," *European Physical Journal D*, vol. 27, no. 1, pp. 73–75, 2003.

[7] V. Milosavljević and S. Djeniže, "Ion contribution to the astrophysical important 447.15, 587.56 and 667.82 nm He I spectral lines broadening," *Astronomy and Astrophysics*, vol. 393, no. 2, pp. 721–726, 2002.

[8] A. Beauchamp, F. Wesemael, and P. Bergeron, "Spectroscopic studies of DB white dwarfs: improved stark profiles for optical transitions of neutral helium," *Astrophysical Journal, Supplement Series*, vol. 108, no. 2, pp. 559–573, 1997.

[9] M. S. Dimitrijević and S. Sahal-Bréchot, "Stark broadening of neutral helium lines," *Journal of Quantitative Spectroscopy and Radiative Transfer*, vol. 31, no. 4, pp. 301–313, 1984.

[10] M. Koubiti, H. Capes, L. Mouret, et al., "Density diagnostic using Stark broadening of HeI spectral line emission from Rydberg levels," in *Proceedings of the Workshop on Privacy Enhancing Technologies (PET '05)*, Forschungszentrum Jülich GmbH, Cavtat, Croatia, October 2005.

[11] A. C. Kolb and H. Griem, "Theory of line broadening in multiplet spectra," *Physical Review*, vol. 111, no. 2, pp. 514–521, 1958.

[12] M. Baranger, in *Atomic and Molecular Processes*, D. R. Bates, Ed., chapter 13, Academic Press, New York, USA, 1962.

[13] H. Margenau and M. Lewis, "Structure of spectral lines from plasmas," *Reviews of Modern Physics*, vol. 31, no. 3, pp. 569–615, 1959.

[14] E. W. Smith, J. Cooper, and C. R. Vidal, "Unified classical-path treatment of stark broadening in plasmas," *Physical Review*, vol. 185, no. 1, pp. 140–151, 1969.

[15] R. W. Lee, "Plasma line shapes for selected transitions in hydrogen-, helium- and lithium-like ions," *Journal of Quantitative Spectroscopy and Radiative Transfer*, vol. 40, no. 5, pp. 561–568, 1988.

[16] M. Baranger, "General impact theory of pressure broadening," *Physical Review*, vol. 112, no. 3, pp. 855–865, 1958.

[17] D. Voslamber, "Unified quantum statistical formulation of pressure broadening," *Physics Letters A*, vol. 40, no. 3, pp. 266–268, 1972.

[18] T. Hussey, J. W. Dufty, and C. F. Hooper Jr., "Kinetic theory of spectral line broadening," *Physical Review A*, vol. 12, no. 3, pp. 1084–1093, 1975.

[19] D. B. Boercker and J. W. Dufty, "Quantum kinetic theory of time-correlation functions," *Physical Review A*, vol. 23, no. 4, pp. 1952–1968, 1981.

[20] H. Nguyen, M. König, D. Benredjem, M. Caby, and G. Coulaud, "Atomic structure and polarization line shift in dense and hot plasmas," *Physical Review A*, vol. 33, no. 2, pp. 1279–1290, 1986.

[21] S. Günter, "Stark Shift and Broadening of Hydrogen Spectral Lines," *Contributions to Plasma Physics*, vol. 29, p. 479, 1989.

[22] H. R. Griem, *Spectral Line Broadening by Plasmas*, Academic Press, New York, NY, USA, 1974.

[23] H. R. Griem, M. Baranger, A. C. Kolb, and G. Oertel, "Stark broadening of neutral helium lines in a plasma," *Physical Review*, vol. 125, no. 1, pp. 177–195, 1962.

[24] J. M. Bassalo, M. Cattani, and V. S. Walder, "Convergent calculations for electron impact broadening and shift of neutral helium lines," *Journal of Quantitative Spectroscopy and Radiative Transfer*, vol. 28, no. 2, pp. 75–80, 1982.

[25] A. Calisti, R. Stamm, and B. Talin, "Simulation calculation of the ion-dynamic effect on overlapping neutral helium lines," *Physical Review A*, vol. 38, no. 9, pp. 4883–4886, 1988.

[26] M. A. Gigosos, M. A. Gonzalez, B. Talin, and A. Calisiti, "Molecular Dynamics Simulations of He I Stark broadened Line Profiles," in *Proceedings of the 17th International Conference on Spectral Line Shapes*, E. Dalimier, Ed., p. 451, Frontier Group, Paris, France, 2004.

[27] D. W. Ross, "Pressure broadening as a many-body problem," *Annals of Physics*, vol. 36, no. 3, pp. 458–485, 1966.

[28] H. R. Zaidi, "Calculation of resonance broadening," *Physical Review*, vol. 173, no. 1, pp. 123–132, 1968.

[29] B. Bezzerides, "Radiation absorption phenomena in gases-I general theory of line broadening," *Journal of Quantitative Spectroscopy and Radiative Transfer*, vol. 7, no. 2, pp. 353–371, 1967.

[30] B. Bezzerides, "Resonance broadening of absorption lines," *Physical Review*, vol. 159, no. 1, pp. 3–10, 1967.

[31] G. Röpke and L. Hitzschke, "Shift and Broadening of Spectral Lines in Non-ideal Plasmas," in *Proceedings of the 9th International Conference on Spectral Line Shapes*, J. Szudy, Ed., p. 49, Ossolineum, Waroclaw, Poland, 1989.

[32] G. Röpke, T. Seifert, and K. Kilimann, "A Green'n Function Approach to the Shift of Spectral lines in Dense Plasmas," *Annalen der Physik (Leipzig)*, vol. 38, p. 381, 1981.

[33] L. Hitzchke, G. Röpke, T. Seifert, and R. Zimmermann, "Green's function approach to the electron shift and broadening of spectral lines in non-ideal plasmas," *Journal of Physics B*, vol. 19, no. 16, pp. 2443–2456, 1986.

[34] S. Günter, L. Hitzschke, and G. Röpke, "Hydrogen spectral lines with the inclusion of dense-plasma effects," *Physical Review A*, vol. 44, no. 10, pp. 6834–6844, 1991.

[35] S. Günter and A. Könies, "Quantum mechanical electronic width and shift of spectral lines over the full line profile-Electronic asymmetry," *Journal of Quantitative Spectroscopy and Radiative Transfer*, vol. 52, no. 6, pp. 819–824, 1994.

[36] S. Günter, "Optische Eigenschaften dichter Plasmen," Habilitation thesis, Rostock University, Rostock, Germany, 1996, IPP MPI no. 5/67.

[37] St. Böddeker, S. Guünter, A. Könies, L. Hitzschke, and H.-J. Kunze, "Shift and width of the H_α line of hydrogen in dense plasmas," *Physical Review E*, vol. 47, no. 4, pp. 2785–2791, 1993.

[38] A. Döhrn, P. Nowack, A. Könies, S. Günter, and V. Helbig, "Stark broadening and shift of the first two Paschen lines of hydrogen," *Physical Review E*, vol. 53, no. 6, pp. 6389–6395, 1996.

[39] S. Günter and A. Könies, "Shifts and asymmetry parameters of hydrogen Balmer lines in dense plasmas," *Physical Review E*, vol. 55, no. 1, pp. 907–911, 1997.

[40] B. Omar, A. Wierling, S. Günter, and G. Röpke, "Hydrogen Balmer spectrum from a high-pressure arc discharge: revisited," *Contributions to Plasma Physics*, vol. 47, no. 4-5, pp. 315–323, 2007.

[41] B. Omar, S. Günter, A. Wierling, and G. Röpke, "Neutral helium spectral lines in dense plasmas," *Physical Review E*, vol. 73, no. 5, Article ID 056405, 2006.

[42] B. Omar, A. Wierling, S. Günter, and G. Röpke, "Analysing brilliance spectra of a laser-induced carbon plasma," *Journal of Physics A*, vol. 39, no. 17, pp. 4731–4737, 2006.

[43] G. A. Kobzev, I. T. Iakubov, and M. M. Popovich, Eds., *Transport and Optical Properties of Nonideal Plasmas*, Plenum Press, New York, NY, USA, 1995.

[44] S. Sorge, A. Wierling, G. Röpke, W. Theobald, R. Sauerbrey, and T. Wilhein, "Diagnostics of a laser-induced dense plasma by hydrogen-like carbon spectra," *Journal of Physics B*, vol. 33, no. 16, pp. 2983–3000, 2000.

[45] C. F. Hooper Jr., "Low-frequency component electric microfield distributions in plasmas," *Physical Review*, vol. 165, no. 1, pp. 215–222, 1968.

[46] W.-D. Kraeft, D. Kremp, W. Ebeling, and G. Röpke, *Quantum Statistics of Charged Particle Systems*, Akademie, Berlin, Germany, 1986.

[47] D. R. Bates and A. Damgaard, "The Calculation of the Absolute Strengths of Spectral Lines," *Philosophical Transactions of the Royal Society A*, vol. 242, p. 101, 1949.

[48] I. I. Sobel'mann, *Atomic Spectra and Radiative Transitions*, Springer, Berlin, Germany, 1992.

[49] H. R. Griem, "Stark broadening of isolated spectral lines from heavy elements in a plasma," *Physical Review*, vol. 128, no. 2, pp. 515–523, 1962.

[50] V. G. Morozov and G. Röpke, "The "Mixed" Green's Function Approach to Quantum Kinetics with Initial Correlations," *Annals of Physics*, vol. 278, p. 127, 1999.

[51] H. R. Griem and C. S. Shen, "Application of a dispersion relation to the electron impact widths and shifts of isolated spectral lines from neutral atoms," *Physical Review*, vol. 125, no. 1, pp. 196–199, 1962.

[52] G. Röpke, S. Sorge, and A. Wierling, "Line profiles in dense plasmas: dynamical microfield, radiation transport," *Contributions to Plasma Physics*, vol. 41, no. 2-3, pp. 187–190, 2000.

[53] S. Sorge, S. Günter, and G. Röpke, "On the consequences of a realistic conditional covariance in MMM-calculations," *Journal of Physics B*, vol. 32, no. 3, pp. 675–681, 1999.

[54] H. A. Bethe and E. E. Salpeter, *Quantum Mechanics of One- and Two-Electron Atoms*, Plenum, New York, NY, USA, 1977.

[55] J. Halenka, "Asymmetry of hydrogen lines in plasmas utilizing a statistical description of ion-quadruple interaction in Mozer-Baranger limit," *Zeitschrift für Physik D*, vol. 16, no. 1, pp. 1–8, 1990.

[56] D. E. Kelleher, "Stark broadening of visible neutral helium lines in a plasma," *Journal of Quantitative Spectroscopy and Radiative Transfer*, vol. 25, no. 3, pp. 191–220, 1981.

[57] R. Kobilarov, N. Konjević, and M. V. Popović, "Influence of ion dynamics on the width and shift of isolated He i lines in plasmas," *Physical Review A*, vol. 40, no. 7, pp. 3871–3879, 1989.

[58] H. F. Berg, A. W. Ali, R. Lincke, and H. R. Griem, "Measurement of stark profiles of neutral and ionized helium and hydrogen lines from shock-heated plasmas in electromagnetic T tubes," *Physical Review*, vol. 125, no. 1, pp. 199–206, 1962.

[59] V. Milosavljević and S. Djeniže, "Ion contribution to the astrophysical important 388.86, 471.32 and 501.56 nm He I spectral lines broadening," *New Astronomy*, vol. 7, p. 543, 2002.

[60] H. Soltwisch and H. J. Kusch, "Experimental Stark profile Determination of some Plasma Broadened He I- and He II-Lines," *Zeitschrift für Naturforschung A*, vol. 34, p. 300, 1979.

[61] H. M. Gao, S. L. Ma, C. M. Xu, and L. Wu, "Measurements of electron density and Stark width of neutral helium lines in a helium arc plasma," *European Physical Journal D*, vol. 47, no. 2, pp. 191–196, 2008.

[62] M. A. Gigosos, M. A. Gonzalez, B. Talin, and A. Calisiti, private communications.

[63] R. N. Morris and J. Cooper, "Stark Shifts of He I 3889, He I 4713, and He I 5016," *Canadian Journal of Physics*, vol. 51, p. 1746, 1973.

[64] R. J. Peláez, V. R. Gonzalez, F. Rodriguez, J. A. Aparicio, and S. Mar, "Stark parameters of neutral helium 318.8 nm line," *Astronomy and Astrophysics*, vol. 453, no. 2, pp. 751–754, 2006.

[65] Z. Mijatović, N. Konjević, M. Ivković, and R. Kobilarov, "Influence of ion dynamics on the width and shift of isolated He i lines in plasmas. II," *Physical Review E*, vol. 51, no. 5, pp. 4891–4896, 1995.

[66] J. M. Bassalo, M. Cattani, and V. S. Walder, "Semiclassical convergent calculations for the electron-impact broadening and shift of some lines of neutral helium in a hot plasma," *Physical Review A*, vol. 22, no. 3, pp. 1194–1197, 1980.

[67] C. S. Diatta, Ph.D. thesis, University d'Orleans, Orleans, France, 1977.

Hindawi Publishing Corporation
International Journal of Spectroscopy
Volume 2010, Article ID 374372, 5 pages
doi:10.1155/2010/374372

Research Article

Time Ordering Effects on Hydrogen Zeeman-Stark Line Profiles in Low-Density Magnetized Plasmas

J. Rosato,[1] D. Boland,[2] M. Difallah,[2] Y. Marandet,[2] and R. Stamm[2]

[1] *Institut für Energieforschung (IEF) - Plasmaphysik, Forschungszentrum Jülich GmbH, Euratom Association, Trilateral Euregio Cluster, 52425 Jülich, Germany*
[2] *Physique des Interactions Ioniques et Moléculaires (PIIM), UMR 6633 Université de Provence - CNRS, Centre de St. Jérôme, Case 232, 13397 Marseille Cedex 20, France*

Correspondence should be addressed to J. Rosato, j.rosato@fz-juelich.de

Received 15 April 2009; Accepted 3 June 2009

Recommended by Manuel Á. González

Stark broadening of hydrogen lines is investigated in low-density magnetized plasmas, at typical conditions of magnetic fusion experiments. The role of time ordering is assessed numerically, by using a simulation code accounting for the evolution of the microscopic electric field generated by the charged particles moving at the vicinity of the atom. The Zeeman effect due to the magnetic field is also retained. Lyman lines with a low principal quantum number n are first investigated, for an application to opacity calculations; next Balmer lines with successively low and high principal quantum numbers are considered for diagnostic purposes. It is shown that neglecting time ordering results in a dramatic underestimation of the Stark effect on the low-n lines. Another conclusion is that time ordering becomes negligible only when ion dynamics effects vanish, as shown in the case of high-n lines.

1. Introduction

In magnetic fusion, detailed line shapes are of interest for accurate diagnostics or radiative transfer simulations. For plasma conditions and magnetic fields encountered in the divertor of present and future tokamaks, an accurate model for the line shape of the hydrogen isotopes should include Zeeman and Stark effects, and retain the dynamics of the ion-emitter interaction. Since we then have to solve a quantum time-dependent problem, understanding the role of time ordering becomes an important issue both from the fundamental and computational points of view (note, this problem is also investigated in other contexts, e.g., [1–3]). Time ordering has already been studied in the Stark broadening literature, but generally for the electron broadening [4–7]. Our aim here is to investigate the role of time ordering for the ion perturbation on hydrogen lines for plasmas with temperature in the eV range, and densities of about $10^{15}\,\mathrm{cm}^{-3}$, conditions which are expected in the divertor of the future ITER tokamak. We recall in Section 2 the basic formalism used for line shape calculations in the presence of Stark and Zeeman effects, and briefly introduce the issue of time ordering. Line shapes in the atom's frame of reference are considered, that is, in the Doppler free case. We present in Section 3 an ab initio simulation technique able to provide accurate line shapes including all the effects of time ordering. Calculations of hydrogen line shapes of Lyman and Balmer series are presented in Section 4, with and without the effect of time ordering, and compared to calculations performed in the static ion limit. The role of time ordering and the issue of retaining it in a line shape calculation are discussed in the conclusion for lines with low and high principal quantum number of the upper state.

2. Formalism

According to classical textbooks or review articles (e.g., [8–10]), a line shape in the atom's rest frame at a frequency ω, $I(\omega)$, is given by the Fourier transform of the dipole autocorrelation function $C(t)$:

$$I(\omega) = \frac{1}{\pi}\,\mathrm{Re}\int_0^\infty dt C(t)e^{i\omega t},$$
$$C(t) = \left\{\mathrm{Tr}\left(\rho_n \vec{d}_\perp \cdot U^+_{n'}(t)\,\vec{d}_\perp U_n(t)\right)\right\}. \quad (1)$$

Here, n and n' denote the principal quantum number with respect to the initial and final states, respectively; $\vec{d}_\perp$ is the dipole operator projected into the polarization plane; $U_n(t)$ (resp., $U_{n'}(t)$) is the evolution operator projected into the subspace related to the initial (resp., final) states; ρ_n is the density operator related to the initial states; the brackets $\{\cdots\}$ stand for a statistical average over the perturbers' states and the trace $\mathrm{Tr}(\cdots)$ is performed over the atomic states. The evolution operator obeys the time-dependent Schrödinger equation

$$i\hbar\frac{dU_n}{dt}(t) = \left(H_0 - \vec{d}_n \cdot \vec{E}(t)\right)U_n(t), \quad (2)$$

where $\vec{d}_n$ is the dipole projected into the subspace related to n; H_0 is the atomic Hamiltonian accounting for the Zeeman effect, that is, $H_0 = H_{\mathrm{at}} - \vec{\mu}\cdot\vec{B}$ with $\vec{\mu}$, $\vec{B}$ being, respectively, the magnetic moment and the magnetic field; and $\vec{E}(t) = \vec{E}_e(t) + \vec{E}_i(t)$ is the time-dependent electric field created at the atom's location by both electrons (e) and ions (i). In our conditions of interest the electron contribution can be safely described by an impact collision operator Φ_n. We will therefore formally replace $-\vec{d}_n \cdot \vec{E}_e(t)$ by $-i\hbar\Phi_n$. We will also use the interaction representation, that is, consider the evolution operator $\widetilde{U}_n(t) = \exp((iH_0/\hbar + \Phi_n)t)U_n(t)$ which obeys the following equation

$$i\hbar\frac{d\widetilde{U}_n}{dt}(t) = -\widetilde{\vec{d}}_n(t)\cdot\vec{E}_i(t)\widetilde{U}_n(t), \quad (3)$$

where $\widetilde{\vec{d}}_n(t) = \exp((iH_0/\hbar + \Phi_n)t)\,\vec{d}_n\exp((-iH_0/\hbar - \Phi_n)t)$ is the dipole operator in the interaction representation.

The Schrödinger equation in the interaction representation (3), associated with the initial condition $\widetilde{U}_n(0) = U_n(0) = 1$, admits as a formal solution the so-called Dyson series expansion

$$\widetilde{U}_n(t) = 1 + \sum_{p\geq 1}\frac{1}{(i\hbar)^p}\int_{0\leq\tau_1\leq\cdots\tau_p\leq t}\cdots \times\int d\tau_1\cdots d\tau_p\,\widetilde{V}_n(\tau_p)\cdots\widetilde{V}_n(\tau_1), \quad (4)$$

where $\widetilde{V}_n(\tau) = -\widetilde{\vec{d}}_n(\tau)\cdot\vec{E}(\tau)$. Following Baranger [11, 12], we write this solution a time-ordered exponential of a matrix

$$\widetilde{U}_n(t) = T\exp\left(\frac{1}{i\hbar}\int_0^t d\tau\widetilde{V}_n(\tau)\right). \quad (5)$$

Here, T is the time ordering operator, defined by its action on a product of time-dependent operators $A(t_1),\ldots,A(t_p)$ as follows:

$$T\left[A(t_p)\cdots A(t_1)\right] = \begin{cases} A(t_p)\cdots A(t_1), & \text{if } t_p \geq \cdots \geq t_1,\\ 0, & \text{otherwise.}\end{cases} \quad (6)$$

Because of the presence of the T-operator in (5), the evolution operator cannot in general be described by a pure exponential of a matrix since the $\widetilde{V}_n$-operator does not commute with itself at different times. The time ordering operator can only be dropped out in the limiting case where the electric field does not evolve significantly during the time of interest (quasistatic limit). In the following we will address the general case by using a simulation code.

3. Assessment of Time Ordering by Computer Simulations

3.1. The Numerical Simulation Method. The purpose of ab initio simulations is to numerically reproduce the motion of the charged particles in the plasma so as to obtain the time-dependent electric microfield $\vec{E}_i(t)$. Essentially, a numerical simulation consists of (i) the calculation of a set of realizations for the electric field; (ii) the numerical integration of the Schrödinger equation for each realization; (iii) the average of the evolution operators on a set of realizations and the Fourier transform of the autocorrelation function. In the simulations performed for this work, we use a code [13] developed according to the method reported in [14]. We consider that the ions move along straight line trajectories with constant velocities, sampled among the particles according to an equilibrium Maxwell distribution function. The electrons (whose contribution to line broadening is mostly negligible for our conditions of interest) are not simulated here, but are described with an impact collision operator (see previous section). The treatment of the correlations between ions and electrons is retained by using Debye screened fields. The largeness of the ratio $\rho_{\mathrm{Li}}/\lambda_{\mathrm{D}}$ between the ion Larmor radius and the Debye length (of about 40 at $N = 10^{14}\,\mathrm{cm}^{-3}$, $T = 1\,\mathrm{eV}$, $B = 5\,\mathrm{T}$, i.e., typical conditions expected in the ITER divertor) ensures the assumption of straight line trajectories. A cubic cell with periodic boundary conditions is considered. For each history of the electric field, the code solves the time-dependent Schrödinger equation for the evolution operator $\widetilde{U}_n(t)$ according to the algorithm $\widetilde{U}_n(t+\Delta t) = \widetilde{U}_n(t+\Delta t, t)\widetilde{U}_n(t)$, with $\widetilde{U}_n(t+\Delta t, t)$ being the infinitesimal evolution operator between times t and $t+\Delta t$. The latter operator is not affected by time ordering if the time step $\triangle$t is sufficiently small, and hence can be evaluated by a matrix exponential

$$\widetilde{U}_n(t+\Delta t, t) = \exp\left(\frac{1}{i\hbar}\Delta t\widetilde{V}_n(t)\right). \quad (7)$$

In the code, we use this property and calculate the exponential according to the scaling squaring method (e.g., [15]). This method is also used for the calculation of the expression of $\widetilde{U}_n(t)$ not accounting for time ordering, given by the exponential of $\int_0^t dt'\widetilde{V}_n(t')/i\hbar$.

3.2. Line Shape Calculations. Time ordering should play a role on lines which are affected by ion dynamics, that is, with a low upper principal quantum number n. To illustrate

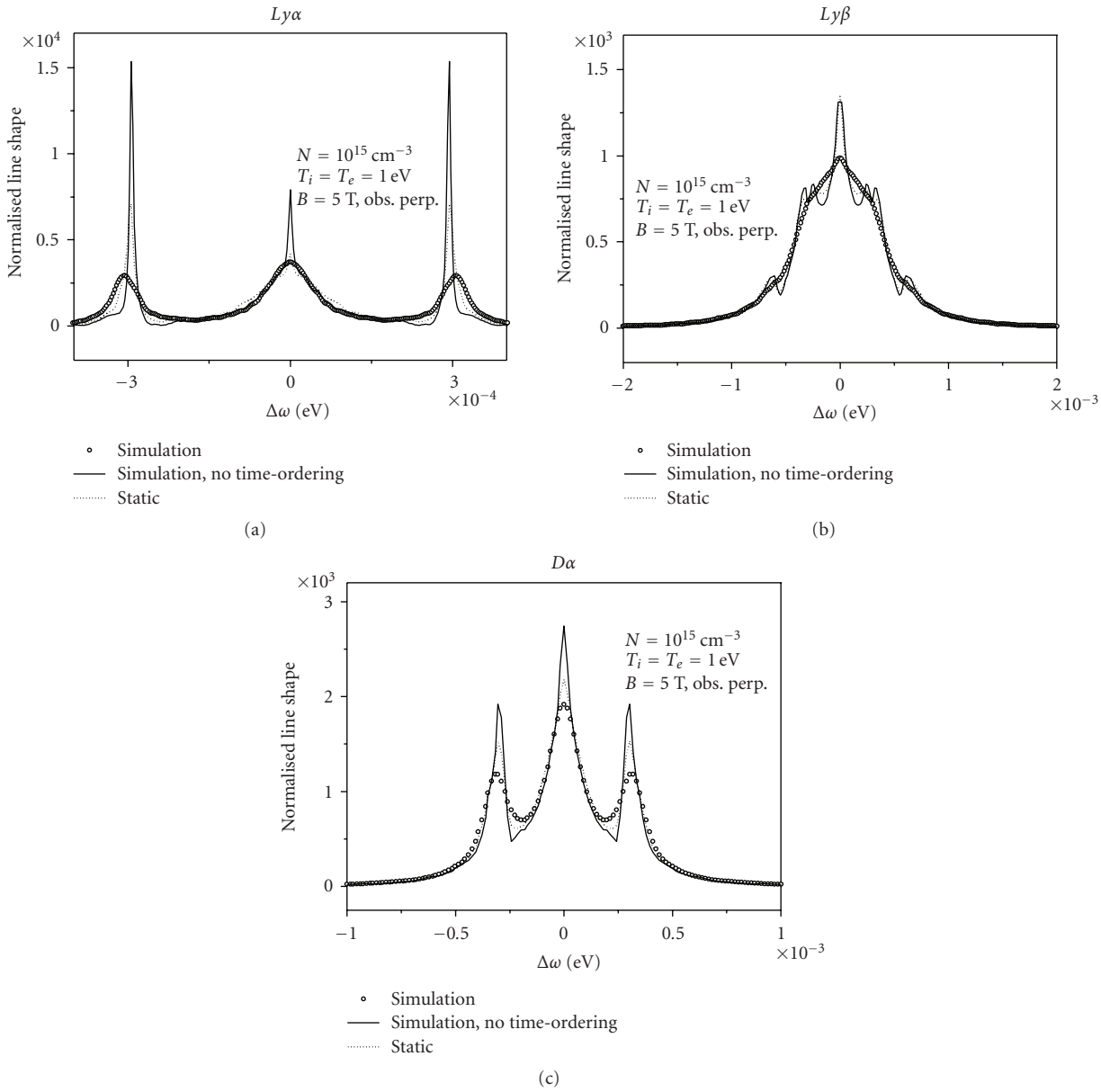

Figure 1: Zeeman-Stark profiles of (a) $Ly\alpha$, (b) $Ly\beta$, and (c) $D\alpha$, obtained at typical divertor conditions with the simulation method accounting for time ordering (circles) or not (full line), and with the quasistatic approximation (dots). In each case, neglecting time ordering leads to a dramatic underestimation of the line broadening, and provides more structure.

this point, we have successively calculated $Ly\alpha$, $Ly\beta$ (whose shapes are involved in the calculations of divertor plasma opacity), and $D\alpha$ (which is commonly observed in tokamak experiments and routinely used for diagnostic purposes). Figures 1(a), 1(b), and 1(c), show, for each line profile, the result obtained with simulations retaining time ordering or not, at $N = 10^{15}\,\mathrm{cm}^{-3}$, $T_e = T_i = 1\,\mathrm{eV}$, $B = 5\,\mathrm{T}$, and in perpendicular observation. The profiles resulting from the quasistatic approximation are also plotted. In each case, the Zeeman effect is important and leads either to a Lorentz triplet structure ($Ly\alpha$, $D\alpha$) or to an additional broadening ($Ly\beta$). As can be seen, neglecting time ordering leads to a dramatic underestimation of the Stark effect. The Zeeman components of $Ly\alpha$ and $D\alpha$ are much narrower than those obtained both with the exact solution and the quasistatic approximation (note, by a factor of ∼3-4 in the case of the lateral components of $Ly\alpha$), and the Zeeman-Stark pattern becomes visible on $Ly\beta$ when time ordering is neglected. Another gain of structure is provided by the apparition of Stark components, in particular on $Ly\beta$ where a splitting of the lateral Zeeman components due to Stark effect is clearly visible.

The underestimation of the Stark effect can be explained by noting that, in the solution of Schrödinger's equation neglecting time ordering, the matrix exponential essentially involves the time average of the electric field $(1/t)\int_0^t dt'\,\vec{E}_i(t')$.

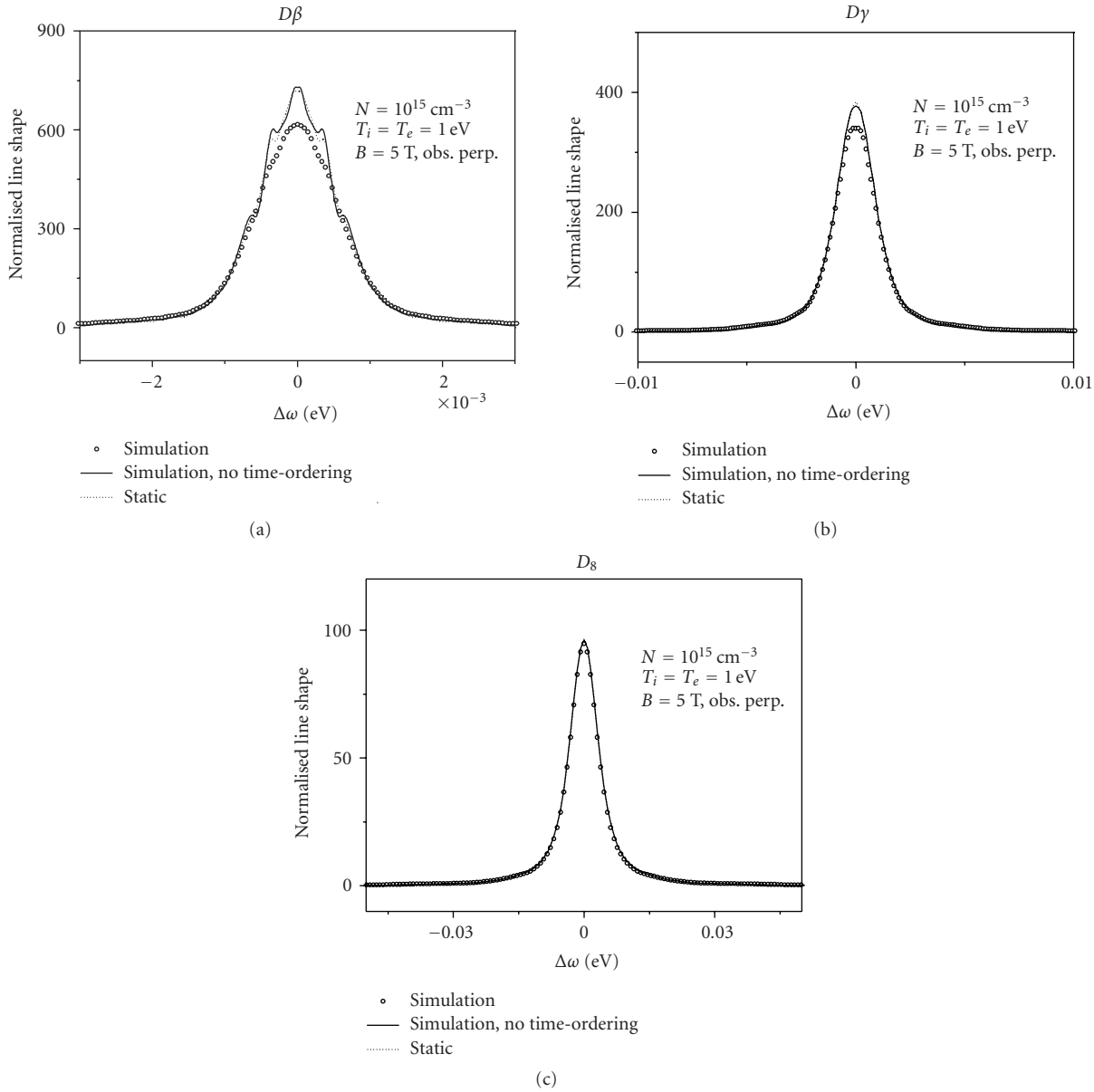

Figure 2: Profiles of (a) $D\beta$, (b) $D\gamma$, and (c) D_8. The effect of time ordering decreases as the upper principal quantum number increases, that is, as the quasistatic limit for ions is approached.

This quantity vanishes on a time scale smaller than the time of interest, a quantity usually defined as the inverse of the line width. Therefore, except for very large frequencies (which correspond to short times), the emitter-ion interaction potential is very small and the resulting line shape becomes very narrow. The line shape is even narrower than that obtained using the quasistatic approximation because the cancellation of the average electric field, equivalent to a cancellation of the evolution operator oscillations, leads to a slower decorrelation of the atomic dipole. The deviation should be smaller for lines with a higher upper principal quantum number n, because ion dynamics is less important in this case. This is indeed illustrated in Figure 2, where a plot of (a) $D\beta$, (b) $D\gamma$, and (c) D_8 are presented. For these lines, the ratio t_i/t_c between the time of interest at half maximum t_i and the collision time t_c is 14%, 9%, and 0.2%, respectively. As shown, the role of time ordering becomes less and less important as this ratio decreases, that is, as the ions become static.

4. Conclusion

We have addressed the role of time ordering on hydrogen Zeeman-Stark profiles in low-density plasmas, for typical conditions of tokamak divertors. With numerical simulations, we have shown that neglecting time ordering on lines with a low upper principal quantum number leads to

strong deviations, with a systematic underestimate of the Stark width of the Zeeman components. This is interpreted in terms of the time averaged electric field, namely, the latter rapidly vanishes during the decorrelation of the atomic dipole so that the resulting effective Stark effect is reduced. Conversely, we have shown that the deviations are weak on lines with a higher upper quantum number, merely because they are much less affected by ion dynamics. This result, of interest for spectroscopy of magnetic fusion experiments, shows that: (i) the development of line shape models including ion dynamics for Monte Carlo investigations of radiative transfer (e.g., [16]) requires to account for time ordering; (ii) in a similar way, time ordering must be accounted for in the Stark broadening models used for $D\alpha$ passive spectroscopy diagnostics; (iii) obviously, the effect of time ordering disappears as one approaches the validity conditions of the static ion approximation, and this is clearly the case for high-n lines in our divertor conditions. A possible extension of our work would consist of a parameterization of the role of time ordering on low-n lines, for diagnostic as well as for radiative transfer calculation purposes.

Acknowledgments

This work is supported by an EFDA Fellowship contract, by the French Federation on Magnetic Fusion Research (project "Radiation Absorption Effects"), by the French Research National Agency (Project "PHOTONITER", Contract ANR-07-BLAN-0187-01), and by the collaboration PIIM/CEA Cadarache (Contract LRC DSM 99-14).

References

[1] J. H. McGuire, A. L. Godunov, K. K. Shakov, et al., "Time ordering in multi-electron dynamics," *Journal of Physics B*, vol. 36, no. 2, pp. 209–216, 2003.

[2] L. Kaplan, K. K. Shakov, A. Chalastaras, M. Maggio, A. L. Burin, and J. H. McGuire, "Time ordering in kicked qubits," *Physical Review A*, vol. 70, no. 6, Article ID 063401, 2004.

[3] D. Lauvergnat, S. Blasco, X. Chapuisat, and A. Nauts, "A simple and efficient evolution operator for time-dependent Hamiltonians: the Taylor expansion," *Journal of Chemical Physics*, vol. 126, no. 20, Article ID 204103, 2007.

[4] C. R. Vidal, J. Cooper, and E. W. Smith, "Hydrogen Stark broadening calculations with the unified classical path theory," *Journal of Quantitative Spectroscopy and Radiative Transfer*, vol. 10, no. 9, pp. 1011–1063, 1970.

[5] J. T. Godfrey, C. R. Vidal, E. W. Smith, and J. Cooper, "Effect of time ordering in the unified theory," *Physical Review A*, vol. 3, no. 5, pp. 1543–1546, 1971.

[6] L. J. Roszman, "Effects of time ordering on plasma-broadened hydrogen profiles," *Physical Review Letters*, vol. 34, no. 13, pp. 785–788, 1975.

[7] M. A. Gunderson, G. C. Junkel-Vives, and C. F. Hooper Jr., "A comparison of a second-order quantum mechanical and an all-order semi-classical electron broadening model," *Journal of Quantitative Spectroscopy and Radiative Transfer*, vol. 71, no. 2–6, pp. 373–382, 2001.

[8] V. S. Lisitsa, "Stark broadening of hydrogen lines in plasmas," *Soviet Physics - Uspekhi*, vol. 20, p. 603, 1977.

[9] H. R. Griem, *Principles of Plasma Spectroscopy*, Cambridge University Press, New York, NY, USA, 1997.

[10] E. Oks, *Stark Broadening of Hydrogen and Hydrogenlike Spectral Lines in Plasmas*, Alpha Science, Oxford, UK, 2006.

[11] M. Baranger, "Problem of overlapping lines in the theory of pressure broadening," *Physical Review*, vol. 111, no. 2, pp. 494–504, 1958.

[12] M. Baranger, "General impact theory of pressure broadening," *Physical Review*, vol. 112, no. 3, pp. 855–865, 1958.

[13] J. Rosato, Y. Marandet, H. Capes, et al., "Stark broadening of hydrogen lines in low-density magnetized plasmas," *Physical Review E*, vol. 79, no. 4, Article ID 046408, 2009.

[14] R. Stamm, E. W. Smith, and B. Talin, "Study of hydrogen Stark profiles by means of computer simulation," *Physical Review A*, vol. 30, no. 4, pp. 2039–2046, 1984.

[15] C. Moler and C. Van Loan, "Nineteen dubious ways to compute the exponential of a matrix, twenty-five years later," *SIAM Review*, vol. 45, no. 1, pp. 3–49, 2003.

[16] D. Reiter, V. Kotov, P. Börner, K. Sawada, R. K. Janev, and B. Küppers, "Detailed atomic, molecular and radiation kinetics in current 2D and 3D edge plasma fluid codes," *Journal of Nuclear Materials*, vol. 363–365, no. 1–3, pp. 649–657, 2007.

Hindawi Publishing Corporation
International Journal of Spectroscopy
Volume 2010, Article ID 506346, 6 pages
doi:10.1155/2010/506346

Research Article

Hydrogen Stark Broadened Brackett lines

C. Stehlé and S. Fouquet

LERMA, UMR8112, Observatoire de Paris, CNRS et Université Pierre et Marie Curie, 5 place Jules Janssen, 92195 Meudon, France

Correspondence should be addressed to C. Stehlé, chantal.stehle@obspm.fr

Received 30 April 2009; Accepted 2 July 2009

Academic Editor: Manuel Á. González

Stark-broadened lines of the hydrogen Brackett series are computed for the conditions of stellar atmospheres and circumstellar envelopes. The computation is performed within the Model Microfield Method, which includes the ion dynamic effects and makes the bridge between the impact limit at low density and the static limit at high density and in the line wings. The computation gives the area normalized line shape, from the line core up to the static line wings.

1. Introduction

Hydrogen is the most abundant element in the universe. Its broad lines give noticeable features in the spectra of stellar atmospheres [1–4]. These lines are very sensitive to the interaction between hydrogen radiating atoms and the surrounding charges, electrons, and ions (mostly protons), which is connected to the random electric field generated by these charges. The electric field has two components, with different time scales: the rapidly varying electronic field and the slowly varying ionic electric field. The net field induces a strong mixing of the atomic states with the same principal quantum number, from which the Stark broadening originates. Astrophysical applications need to know the full line shape, from line centre up to the line wings, for a wide range of plasma conditions (i.e., electron density N_e and temperature T).

Whereas hydrogen line shapes have been widely used in stellar physics for the determination of gravity and/or temperature in the visible and UV ranges, the recent instrumental developments on various telescopes, such as AMBER [5] and CRIRES [6] on VLTI and VLT, require the availability of precise hydrogen lines in the infrared (i.e., between 1 and 5 μm). The latter are badly known [7].

This paper thus aims at providing a coherent description of the line shapes of Brackett α, β, γ, which connect the levels of principal quantum numbers n equal to 4, for the lower state of the transition, and n' equal to 5, 6, and 7, for the upper state, and have central wavelengths of 4.05, 2.63, and 2.12 μm. The chosen plasma conditions are relevant to stellar photospheres and circumstellar environments (electron densities between 10^{10} and 10^{19}cm^{-3} and temperatures between 10^3 and 10^7 K). The plasma charges are assumed to be electrons and protons. This is a standard approximation for this type of study, although some improvements may be possible by including the effect of ionization of He (which is, by number of atoms, only 10% as abundant as hydrogen) and traces of heavier elements.

We suppose that plasma collective effects are included in the Coulomb interactions between the hydrogen bound electron and the plasma charges by Debye screening. This requires that the Debye length λ_d is larger than the mean distance r_0 between the protons or that the parameter $a = r_0/\lambda_d$ is smaller than unity. Our tables will thus be limited to the values of temperatures and densities satisfying the following condition:

$$N_e < 2.6 \;\; 10^9 \; T^3 \quad (\mathrm{cm}^{-3},\ K), \tag{1}$$

which is fulfilled for standard stellar atmospheres.

We assume also that the proton/electron density is small enough to ensure that each line $4-n'(n' = 5, 6 \text{ or } 7)$ remains distinguishable from the subsequent line $4 - (n' + 1)$ of the Brackett series. Using the Inglis-Teller [8] criterium, the upper limit to the electron density N_e is thus

$$\log(N_{e,\max}) = 22 - 7.5\log(n') \quad (\mathrm{cm}^{-3}). \tag{2}$$

This, respectively, gives $\log(N_{e,\max}) = 16.75, 16.16$, and 15.66 for the n' (= 5, 6 and 7) values considered in this paper. However, in order to allow interpolation within the tables for astrophysical applications, the line shapes for higher values of N_e, up to a decade, have been computed.

Different methods can be used to generate high-quality spectral line shapes for hydrogen lines perturbed by protons and electrons: Molecular Dynamics for describing precisely the ion dynamics effects in the line center [9, 10], quantum theory for the electron contribution to the line wings [11], and short range H–H^+ molecular interactions also for the line wings, leading to the apparition of quasimolecular satellites, which are observed in the atmospheres of white dwarfs [12]. However, they are limited either to part of the profile, to restricted plasmas conditions, or to simple lines like Lyman or Balmer lines. Thus, as for astrophysical purposes, the tabulations go from the line centre up to the line wings, and it is necessary to find a compromise between accuracy and description of the whole profile.

In this context, the tabulations of Vidal et al. [13], using Unified Theory for the electrons and static approximation for the ions, have been used for stellar atmospheres, despite the intrinsic lack of accuracy in the line center due to the neglect of ion dynamics effects. The tabulations of Stehlé et al., for the Lyman, Balmer [14, 15], and Paschen lines [16], using Model Microfield Method, which was initially developed by Brissaud et Frisch [17, 18] brought an important improvement by taking into account the ion dynamics effects. They are now used for atmospheres and for the computation of radiative diffusion processes in the radiative stellar envelopes [19]. In the case of partly ionized plasmas, like for the atmospheres of cool stars, the contribution of neutral broadening by hydrogen has to be included in the line shape, especially in the line wings [20, 21]. This effect will be neglected in the following.

In this paper we will present the Stark broadened profiles of Brackett lines. They will be computed within the formalism of Model Microfield Method, hereafter denoted by MMM. We will neglect the fine structure effects, which play a role, at low density, in the core of the lines with low n quantum mumbers, like Lyα or Hα [22]).

For Brα, the profiles are computed at densities $\log_{10}(N_e(\mathrm{cm}^{-3}))$ ranging from 10 to 18.5, by step of 0.5. For each density, the profiles are computed at temperatures equal to 1000, 2500, 5000, 10000, 19550, 39810, 79810, 158500, 316200, 63100, and 1259000 K, assuming that condition 1 is satisfied. For Brβ , the computation stops at $\log_{10}(N_e(\mathrm{cm}^{-3})) = 18$ and for Brγ at 17.5, as explained previously.

2. Method

The broadening of spectral lines results from the interactions between the radiating hydrogen atom and the free ions and protons. These two contributions can be described in terms of interaction potentials, with the corresponding electronic and ionic plasma microfields $\mathbf{F}_{\mathrm{el}}$ and $\mathbf{F}_{\mathrm{ion}}$. Neglecting quadrupolar and other contributions that play a role at high densities [23], the dipolar potential of interaction between the bound electron and the microfields may be written as

$$V(t) = -\mathbf{d} \cdot (\mathbf{F}_{\mathrm{el}}(t) + \mathbf{F}_{\mathrm{ion}}(t)). \tag{3}$$

The spectral line profile $I(\omega)$ (with area normalized to unity) is thus defined in the Liouville space [24, 25], spanned by the states $| i, f \gg$ (which stands for $| n_i, l_i, m_i; n_f, l_f, m_f \gg$) as

$$I(\omega) = \frac{1}{\pi \sum_{i,f} \mathbf{d}_{i,f} \cdot \mathbf{d}^*_{i,f}} \mathrm{Re} \sum_{i,f,i',f'} \mathbf{d}_{i,f} \cdot \mathbf{d}^*_{i',f'} \times \langle \mathbf{U}(\omega) \rangle_{\mathrm{el,ion};\, if;i'f'}, \tag{4}$$

where $\langle \mathbf{U}(\omega) \rangle_{\mathrm{el,ion}}$ is the Fourier transform of the evolution operator of radiating Hydrogen atom in the Liouville space, averaged over the realizations of the stochastic dynamic electronic and ionic microfields $\mathbf{F}_{\mathrm{el}}$ and $\mathbf{F}_{\mathrm{ion}}$. The term $\mathbf{d}_{i,f} \cdot \mathbf{d}_{i',f'}$ is the product of dipole operator elements between initial low states (denoted by i, i') and final upper states (denoted by f, f'), of the hydrogen bound electron. As fine structure and inelastic effects are neglected, one has $E_f - E_i = E'_f - E'_i = \hbar\omega_0$.

The two microfields are stochastic processes. It is thus possible to define two distribution functions $P(\mathbf{F})$ [26, 27], respectively, associated to the slowly varying ionic and rapidly varying electronic microfields. In order to take into account the dynamic effects of these microfields, a model for the dynamical statistics of field fluctuations is necessary. In MMM, the microfield fluctuations are handled with a statistical process model, where the microfield (electronic or ionic) is assumed to be constant during a given time interval. The microfield then jumps instantaneously to another constant value for the next time interval. The jumping times are assumed to follow a Poisson law, with a field dependent frequency $\nu(F)$. The jumping frequency $\nu(F)$ is chosen to reproduce the true field autocorrelation function [17, 18, 28]. This method has been tested against asymptotic impact and quasistatic limits and has been proved to lead to very good results for hydrogen [29] and hydrogenic ion lines [28].

The method has been already described in Stehlé and Hutcheon [15], and we refer the reader to this paper for the details. An important point is that it is possible to disentangle the contributions of ions and fast electrons by introducing a frequency dependent electronic relaxation operator $\gamma_{\mathrm{el}}(\omega)$, which is independent from ionic fields and thus may be computed separately. The Fourier transform of the evolution operator, $\langle \mathbf{U}(\omega) \rangle_{\mathrm{el}}$, averaged over all the realisations of the electronic fields, may be written as

$$\langle \mathbf{U}(\omega) \rangle_{\mathrm{el}} = i \left[\Delta\omega \mathbf{I} + i\gamma_{\mathrm{el}}(\omega) \right]^{-1}, \tag{5}$$

where $\Delta\omega = \omega - \omega_0$ is the detuning from line center, and $\mathbf{I}$ is the identity operator in the Liouville space.

Thus, this electron damping is first computed to account for average effect of the electronic fields. Then, the static Fourier transform of the evolution operator, $\langle \mathbf{U}(\omega) \rangle_{\mathrm{el,ion}}$,

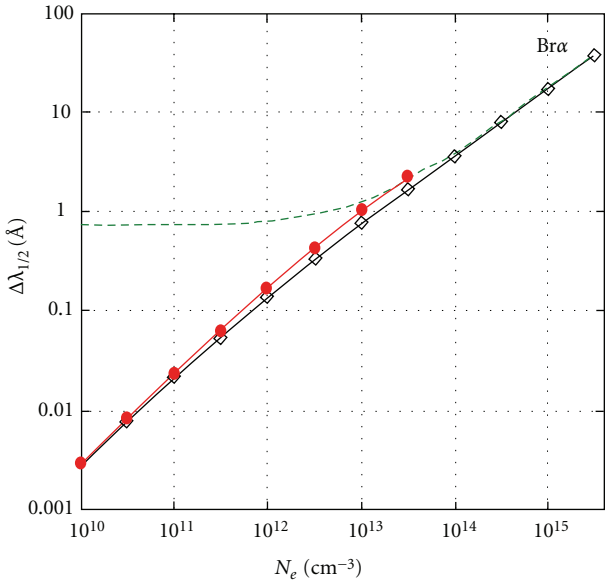

FIGURE 1: HWHM of Brα at 2500 K, in Å, versus electron density N_e in cm^{-3} (black and squares: MMM Stark only; red and circles: analytical impact formula; dashed green: MMM Stark profile with Doppler convolution).

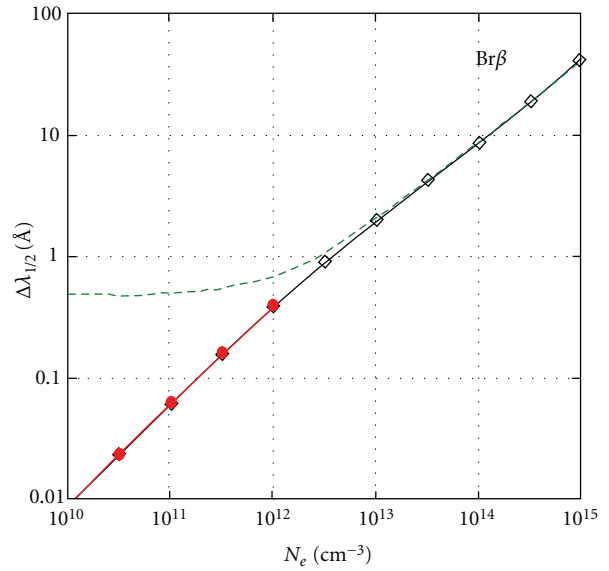

FIGURE 2: Same as Figure 1 for Brβ.

averaged over the realisations of the electronic and ionic fields, may be written as

$$\langle \mathbf{U}(\omega)\rangle_{\text{el,ion}} = i\int P(\mathbf{F}_{\text{ion}})d\mathbf{F}_{\text{ion}}\left[\Delta\omega\mathbf{I} + \mathbf{d}\cdot\mathbf{F}_{\text{ion}} + \gamma_{\text{el}}(\omega)\right]^{-1}. \tag{6}$$

The MMM expression is more complex [17, 18] than this one, which corresponds to the usual Unified Theory with static ionic fields.

In order to reduce the dimensions of the Liouville space, ($16 \times 25 = 400$ states for Brα, i.e.), we use the formalism of the reduced Liouville space, which takes advantage of the invariance of the different operators, like $\mathbf{d}\cdot\mathbf{d}$, by angular average over all the orientations of the electric fields and of the fact that the dipole tensor $\mathbf{d}$ in (4) is of rank 1 (see e.g. [28, 29]). However, the number of reduced states $|\ n_i, l_i; n_f, l_f\ \gg$ (with $|l_i - l_f| \leq 1$) remains important (i.e., 10 reduced Liouville states of rank 1 for Brα). Thus, we use another approximation, already called "isotropic" approximation in [15], which uses the diagonal form $\gamma_{\text{el}}^{\text{iso}}(\omega)$, with equal diagonal matrix elements, instead of $\gamma_{\text{el}}(\omega)$. This scalar tensor is deduced from the pure electronic profile $I(\omega)_{\text{el}}$ by the following relation:

$$I(\omega)_{\text{el}} = -\frac{1}{\pi}\, Im\left[\Delta\omega + i\gamma_{\text{el}}^{\text{iso}}(\omega)\right]^{-1}, \tag{7}$$

or

$$\gamma_{\text{el}}^{\text{iso}}(\omega) = \frac{\sum_{i,f;i',f'} \mathbf{d}_{i,f}\cdot\mathbf{d}^{*}_{i',f'}\gamma_{\text{el};\,if;i'f'}(\omega)}{\sum_{i,f}\mathbf{d}_{i,f}\cdot\mathbf{d}^{*}_{i,f}}\,. \tag{8}$$

The Stark profile is thus obtained after computing the average over electronic field values, which gives $\gamma_{\text{el}}^{\text{iso}}(\omega)$, and then the average over the ionic fields, both using the formalism of Model Microfield Method. The third step is then the Doppler convolution, which gives the final line shape.

3. Results

The three Brackett α, β, γ line shapes have been studied in a wide range of stellar conditions, but we report hereafter only a selection of results, relative to the line center and the line wings.

3.1. Line Center. We present in Figures 1, 2, and 3 the variations of the half-width (HWHM) of Brα, Brβ, and Brγ lines for different values of the electron density. This quantity is the detuning from the line center, at the point where the profile reaches half the maximum value of the line profile (which is not necessarily at the line center, as will be discussed below). The figures show the half width of the MMM profile with and without Doppler effect and also the value of the impact half-width in its own validity range.

Hence, impact limit has been proved to be valid, for both electron and ion contributions, in the line center and at low densities. Moreover, it has been proved that the value of the impact width is analytical and that the corresponding profile is Lorentzian in the line center [30]. The validity condition of the impact limit is that the half-width value is smaller than the ion plasma frequency. Let us take the example of Brα. At 10^{12} cm^{-3} and 2500 K the ion plasma frequency is equal to 2.6 10^9 rd $\cdot$ s^{-1}, whereas the ion impact contribution to the HWHM is equal to 1.8 10^9 rd $\cdot$ s^{-1}. At 10^{14}cm^{-3}, they are respectively, equal to 2.6 10^{10} and 3.9 10^{10}. The impact limit should thus be reached gradually as the density decreases below 10^{13}cm^{-3}.

Figure 1, relative to Brα, shows indeed that the half-width of the Stark profile (black) tends to converge towards the impact analytical limit (red) at these low densities.

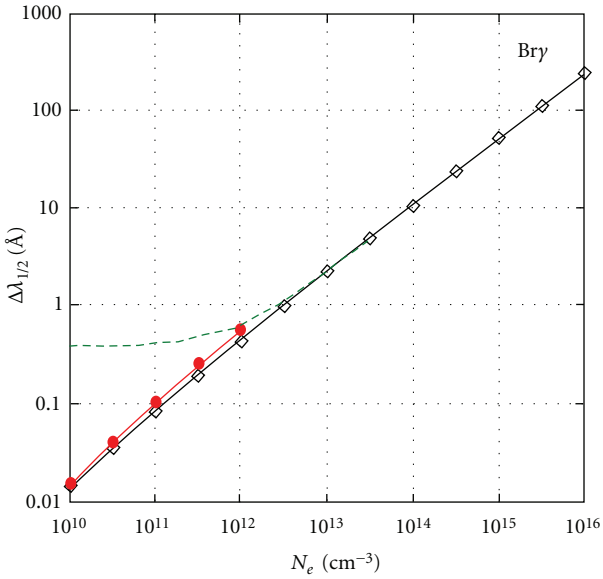

FIGURE 3: Same as Figure 1 for Brγ.

However, the convolution with the Doppler profile increases the half-width value. As a consequence, the half width is dominated by the Doppler broadening at low densities. Similar behaviour occurs for the other lines, as may be on Figures 2 and 3 for Brβ and Brγ.

At higher densities, the ion dynamic effects become smaller in the line center (they are negligible in the line wings, as will be seen below), and the line shape departs from the Lorentzian shape. We found that, depending on the temperature conditions, the Brackett β line may present a small dip in the line center at moderate densities of 10^{15} cm^{-3} and for the largest temperatures as seen in Figure 4. This effect was well known in earlier tabulations for the Lymanβ and Hβ lines. The dependence versus the temperature is a consequence of the the electron impact broadening, which varies in $T^{-1/2}$ and which may fill (at low T values) or not (at large T values) the central dip.

3.2. Line Shapes. Another typical behaviour of hydrogen lines is the convergence towards the (Holtsmark) static limit in the line wings, which scales as $|\Delta\omega|^{-5.2}$ when the line shape is expressed in angular frequency units (which is the appropriate unit for the line shape computations). However, traditionally, the line intensity was expressed in units of $\Delta\alpha = \Delta\lambda/F_0$, where F_0 (esu) = 1.25 $10^9(N_e)^{2/3}$ is the normal Holtsmark field. In these units, the Holtsmark limit is given by

$$I(\Delta\alpha) = \frac{K_\alpha}{|\Delta\alpha|^{5/2}}\left(\frac{\lambda_0/F_0 + \Delta\alpha}{\lambda_0/F_0}\right)^{1/2} \simeq \frac{K_\alpha}{|\Delta\alpha|^{5/2}} \quad \text{for } |\Delta\alpha| \ll \frac{\lambda_0}{F_0}, \tag{9}$$

where λ_0 is the central wavelength, and K_α a constant, which depends on the transition,

$$K_\alpha = 1.512 \text{ for Br}\alpha,\ 2.401 \text{ for Br}\beta, 2.926 \text{ for Br}\gamma. \tag{10}$$

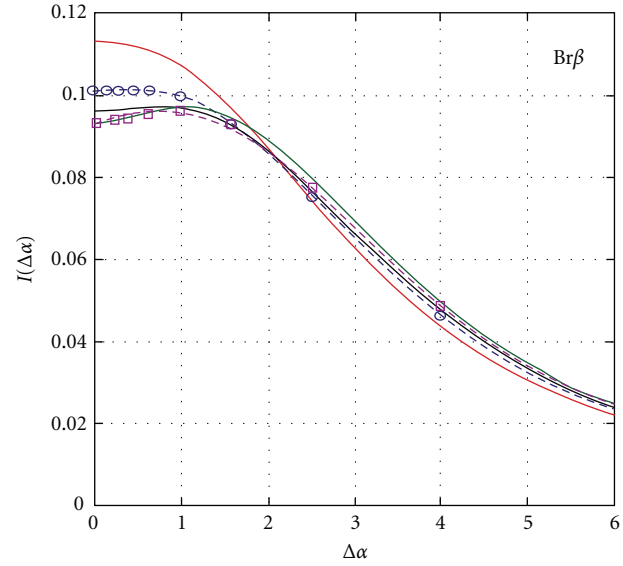

FIGURE 4: MMM Brβ line at 10^{15} cm^{-3} versus $\Delta\alpha = \Delta\lambda/F_0$ without Doppler convolution for different temperatures (red : 1000 K; blue with empty circles : 2500 K; violet with empty squares: 10000 K; green: 19950 K).

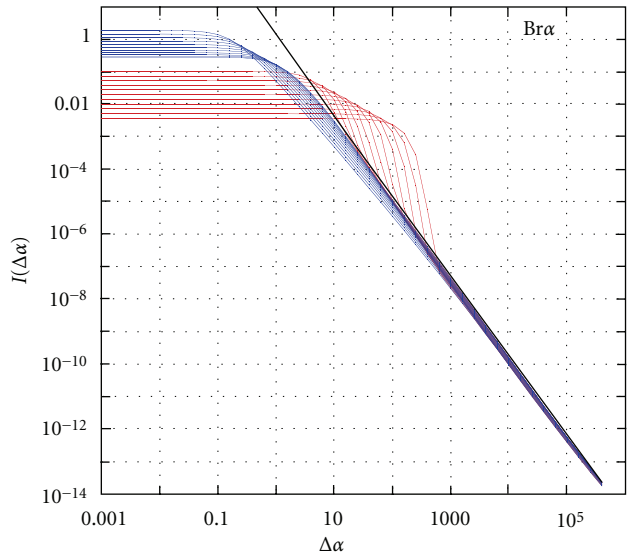

FIGURE 5: MMM Brα line at $N_e = 10^{12}$cm^{-3}, with (red) and without (blue) Doppler broadening, and the asymptotic Holstmark limit (black) in $|\Delta\alpha|^{-5/2}$ for 11 different temperatures in K (1000, 2500, 5000, 10^4, 2 10^4, 3.98 10^4, 7.94 10^4, 1.58 10^5, 3.16 10^5, 6.31 10^5, 1.26 10^6). The corresponding values of the profiles in the line center are, respectively, 0.28, 0.30, 0.34, 0.46, 0.56, 0.69, 0.88, 1.23, 1.45, 1.87, without Doppler effect (blue), and, 0.102, 0.071, 0.053, 0.039, 0.028, 0.020, 0.014, 0.010, 0.0072, 0.0051, 0.0036 including Doppler effect (red).

This variation in $\Delta\alpha$ of 9 introduces, at large detunings, a "trivial" asymmetry between $I(\Delta\alpha)$ and $I(-\Delta\alpha)$ (which does not exist between $I(\Delta\omega)$ and $I(-\Delta\omega)$). Figures 5, 6 and 7 show the profiles $I(\Delta\alpha)$ of Brα, Brβ, and Brγ lines at 10^{12} cm^{-3} and various temperatures. The profiles, including Doppler effects are reported in red color, and the pure Stark profiles in blue.

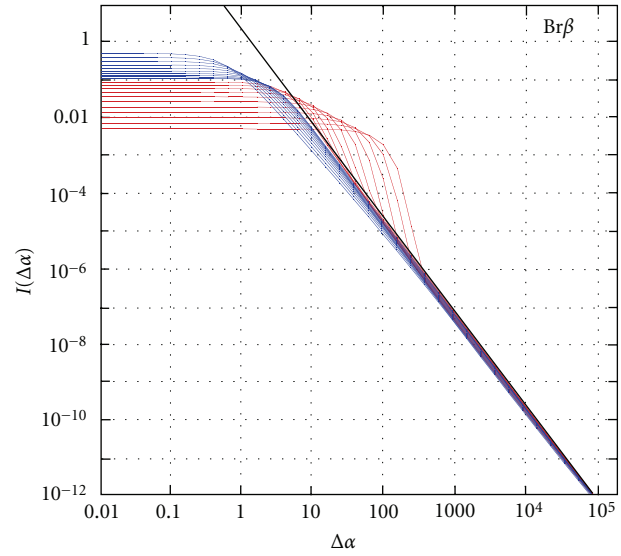

FIGURE 6: Same as Figure 5 but for Brβ, the values of the profiles in the line center are, for the 11 different temperatures of Figure 5, respectively, 0.124, 0.129, 0.136, 0.149, 0.168, 0.195, 0.233, 0.285, 0.355, 0.451, 0.579 without Doppler effect (blue), and 0.099, 0.082, 0.067, 0.053, 0.040, 0.030, 0.0215, 0.015, 0.011, 0.0078, 0.0056 including Doppler effect (red).

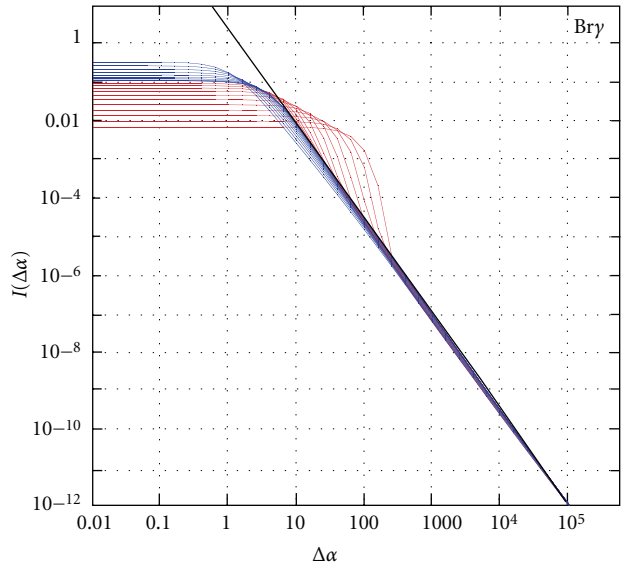

FIGURE 7: Same as Figure 5 but for Brγ, the values of the profiles in the line center are, f for the 11 different temperatures of Figure 5, respectively, 0.107, 0.107, 0.109, 0.113, 0.121, 0.132, 0.150, 0.175, 0.211, 0.260, 0.327 without Doppler effect (blue), and 0.091, 0.080, 0.069, 0.057, 0.0450, 0.034, 0.025, 0.018, 0.013, 0.0094, 0.0067 including Doppler effect (red).

The profiles are area normalized, that is,

$$\int_{-\infty}^{+\infty} I(\Delta\alpha) \times d(\Delta\alpha) = 1. \quad (11)$$

As a consequence, broad profiles have small values of $I(\Delta\alpha = 0)$. For the density considered in Figures 5–7, the Doppler profile dominates the Stark profile in the line center and becomes indistinguishable, as expected, in the line wings, where they follow the asymptotic limit of (9). At higher densities (not reported here), the Doppler width is smaller than the Stark width, and Doppler convolution is no longer necessary.

4. Conclusions

This study shows that Stark broadened infrared Brackett lines of hydrogen follow the same trends as the lines of lower series which are more known theoretically and experimentally. This study will allow missing absorption in the spectra of stellar atmospheres in the infrared due to the lack of data to be filled in a next future. Dedicated experiments and comparisons with other methods, for instance, FFM [31], would be helpful to test these theoretical results, which will be also constrained by observational data. The corresponding tables will be accessible at http://amrel.obspm.fr/stark-h.

Acknowledgments

The authors would like to thank Nicolas Moreau for his helpful technical support, and Pauline Béghin, Edrice Bouteldja, Aurélie de Paz and Cécile Turc, students at University of Pierre et Marie Curie, Paris, for their contribution in checking the data. The support of French INSU program PNPS is acknowledged.

References

[1] P. S. Barklem, "Hydrogen lines," *Physica Scripta*, vol. 133, Article ID 014023, 5 pages, 2008.

[2] I. Hubeny and T. Lanz, "Non-LTE line-blanketed model atmospheres of hot stars. I. Hybrid complete linearization/accelerated lambda iteration method," *Astrophysical Journal*, vol. 439, no. 2, pp. 875–904, 1995.

[3] N. F. Allard and D. Koester, "Theoretical profiles of Lyman-alpha satellites and application to synthetic spectra of DA white dwarfs," *Astronomy & Astrophysics*, vol. 258, no. 2, pp. 464–468, 1992.

[4] M. F. Nieva and N. Przybilla, "Hydrogen and helium line formation in OB dwarfs and giants: a hybrid non-LTE approach," *Astronomy & Astrophysics*, vol. 467, no. 1, pp. 295–309, 2007.

[5] R. G. Petrov, F. Malbet, G. Weigelt, et al., "AMBER, the near-infrared spectro-interferometric three-telescope VLTI instrument," *Astronomy & Astrophysics*, vol. 464, no. 1, pp. 1–12, 2007.

[6] H. U. Käufl, P. Amico, P. Ballester, et al., "CRIRES: commissioning and first science results," in *Ground-based and Airborne Instrumentation for Astronomy II*, vol. 7014 of *Proceedings of SPIE*, Marseille, France, June 2008.

[7] N. Przybilla and K. Butler, "Non-LTE line formation for hydrogen revisited," *Astrophysical Journal*, vol. 609, no. 2, pp. 1181–1191, 2004.

[8] D. R. Teller and E. Inglis, "Ionic depression of series limits in one-electron spectra," *Astrophysical Journal*, vol. 90, no. 3, pp. 439–448, 1968.

[9] M. A. Gigosos and V. Cardeñoso, "New plasma diagnosis tables of hydrogen Stark broadening including ion dynamics," *Journal of Physics B*, vol. 29, no. 20, pp. 4795–4838, 1996.

[10] R. Stamm, E. W. Smith, and B. Talin, "Study of hydrogen Stark profiles by means of computer simulation," *Physical Review A*, vol. 30, no. 4, pp. 2039–2046, 1984.

[11] C. Stehlé, "Stark broadening of the hydrogen Lyman-α line from the center to the near line wings for low-density plasmas," *Physical Review A*, vol. 34, no. 5, pp. 4153–4162, 1986.

[12] N. F. Allard, D. Koester, N. Feautrier, and A. Spielfiedel, "Free-free quasi-molecular absorption and satellites in Lyman-alpha due to collisions with H and H^+," *Astronomy & Astrophysics*, vol. 108, pp. 417–431, 1994.

[13] C. R. Vidal, J. Cooper, and E. W. Smith, "Hydrogen Stark-broadening tables," *The Astrophysical Journal Supplement*, vol. 25, no. 214, pp. 37–136, 1973.

[14] C. Stehlé, "Stark broadening of hydrogen Lyman and Balmer in the conditions of stellar envelopes," *Astronomy & Astrophysics*, vol. 104, pp. 509–527, 1994.

[15] C. Stehlé and R. Hutcheon, "Extensive tabulations of Stark broadened hydrogen line profiles," *Astronomy & Astrophysics*, vol. 140, pp. 93–97, 1999.

[16] C. Stehlé, "Paschen lines of hydrogen and He^+ ion," *Physica Scripta*, no. T65, pp. 183–187, 1996.

[17] U. Frisch and A. Brissaud, "Theory of Stark broadening—I soluble scalar model as a test," *Journal of Quantitative Spectroscopy & Radiative Transfer*, vol. 11, no. 12, pp. 1753–1766, 1971.

[18] A. Brissaud and U. Frisch, "Theory of Stark broadening—II exact line profile with model microfield," *Journal of Quantitative Spectroscopy & Radiative Transfer*, vol. 11, no. 12, pp. 1767–1783, 1971.

[19] F. Clausset, C. Stehlé, and M. C. Artru, "Parametrized Stark profiles of hydrogen lines in hot stellar plasmas," *Astronomy & Astrophysics*, vol. 287, no. 2, pp. 666–675, 1994.

[20] P. S. Barklem, H. C. Stempels, C. Allende Prieto, O. P. Kochukhov, N. Piskunov, and B. J. O'Mara, "Detailed analysis of Balmer lines in cool dwarf stars," *Astronomy & Astrophysics*, vol. 385, pp. 951–967, 2002.

[21] P. S. Barklem, N. Piskunov, and B. J. O'Mara, "Self-broadening in Balmer line wing formation in stellar atmospheres," *Astronomy & Astrophysics*, vol. 363, pp. 1091–1105, 2000.

[22] C. Stehlé and N. Feautrier, "Stark broadening of the hydrogen H_α line at low densities: fine structure and spontaneous emission effects," *Journal of Physics B*, vol. 18, no. 7, pp. 1297–1306, 1985.

[23] C. Stehlé, D. Gilles, and A. V. Demura, "Asymmetry of Stark profiles," *The European Physical Journal D*, vol. 12, no. 2, pp. 355–367, 2000.

[24] U. Fano, "Description of states in quantum mechanics by density operator techniques," *Reviews of Modern Physics*, vol. 29, no. 1, pp. 74–93, 1957.

[25] A. Ben-Reuven, "Symmetry considerations in pressure-broadening theory," *Physical Review*, vol. 141, no. 1, pp. 34–40, 1966.

[26] C. F. Hooper Jr., "Electric microfield distributions in plasmas," *Physical Review*, vol. 149, pp. 77–91, 1966.

[27] C. F. Hooper Jr., "Low-frequency component electric microfield distributions in plasmas," *Physical Review*, vol. 165, pp. 215–222, 1968.

[28] C. Stehlé, "Stark profiles of He^+," *Astronomy & Astrophysics*, vol. 292, no. 2, pp. 699–712, 1994.

[29] C. Stehlé, A. Mazure, G. Nollez, and N. Feautrier, "Stark broadening of hydrogen lines—new results for the Balmer lines and astrophysical consequences," *Astronomy & Astrophysics*, vol. 127, no. 2, pp. 263–266, 1983.

[30] C. Stehlé, "Analytical expressions for the lines of one-electron ions," *Astronomy & Astrophysics*, vol. 305, no. 2, pp. 677–686, 1996.

[31] B. Talin, A. Calisti, L. Godbert, R. Stamm, R. W. Lee, and L. Klein, "Frequency-fluctuation model for line-shape calculations in plasma spectroscopy," *Physical Review A*, vol. 51, no. 3, pp. 1918–1928, 1995.

Hindawi Publishing Corporation
International Journal of Spectroscopy
Volume 2010, Article ID 347080, 4 pages
doi:10.1155/2010/347080

Research Article

New Statistical Multiparticle Approach to the Acceleration of Electrons by the Ion Field in Plasmas

Eugene Oks

Department of Physics, Auburn University, 206 Allison Laboratory, Auburn, AL 36849, USA

Correspondence should be addressed to Eugene Oks, goks@physics.auburn.edu

Received 30 April 2009; Accepted 8 June 2009

Recommended by Elisabeth Dalimier

The phenomenon of the acceleration of the (perturbing) electrons by the ion field (AEIF) significantly reduces Stark widths and shifts in plasmas of relatively high densities and/or relatively low temperature. Our previous analytical calculations of the AEIF were based on the *dynamical* treatment: the starting point was the ion-microfield-caused changes of the trajectories and velocities of individual perturbing electrons. In the current paper, we employ a *statistical* approach: the starting point is the electron velocity distribution function modified by the ion microfield. The latter had been calculated by Romanovsky and Ebeling in the multiparticle description of the ion microfield. The result shows again the reduction of the electron Stark broadening. Thus two totally different analytical approaches (dynamical and statistical) agree with each other and therefore disprove the corresponding recent fully-numerical simulations by Stambulchik et al. that claimed an increase of the electron Stark broadening.

1. Introduction

The phenomenon of the acceleration of the (perturbing) electrons by the ion field (AEIF) significantly reduces Stark widths and shifts in plasmas of relatively high densities and/or relatively low temperature. This phenomenon was first described analytically in the binary approach in paper [1] with subsequent analytical improvements in paper [2]. Then it was also described analytically in the multiparticle approach in book [3] and paper [4]. The essence of this phenomenon is the following.

Due to the presence of the ion field, perturbing electrons are passing by the radiator at higher velocities than it would be at the absence of the ion field. The increase of the electron velocities translates into a decrease of the electron broadening (i.e., a decrease of Stark widths and shifts). The narrowing (and shift-reducing) phenomenon caused by the AEIF is the realization of a *direct* coupling between electrons and ions. It affects the spectral line shape in addition to the effect of the *indirect* coupling between the electron and ion broadenings (see, e.g., [3]). The latter coupling is indirect because it is carried out via the radiating atom which acts as an intermediary, this being manifested by the fact that the coupling parameter depends on the quantum numbers of the atomic states (as well as on the parameters of the electron and ion microfields). In distinction to this, the coupling parameter in the narrowing phenomenon does not depend on the atomic quantum numbers. It should be emphasized that in the conventional theory [5] there was no coupling of any kind between the electrons and ions.

The analytically described direct and indirect couplings of the electron and ion microfields combined with the analytical description of the ion dynamics constituted a highly advanced theory of the Stark broadening [3, 4]. A code based on this analytical theory eliminated significant discrepancies between variety of benchmark experiments and previous theories and/or simulations [3, 4].

However, there are two different schools of thought on what should be the ultimate test of various theories. One school of thought considers the comparison with benchmark experiments as the ultimate test of the theory. For spectral line shapes in plasmas, benchmark experiments are those, where plasma parameters are determined independently of the spectral line shape theory to be tested.

Another school of thought insists that the ultimate test of a particular theory is the comparison with results of a code based on fully-numerical simulations starting from the "scratch" rather than from some analytical advance.

Within this school of thought, there have been recently conducted fully numerical simulations trying to "mimic" the phenomenon of AEIF [6]. Based on their fully-numerical simulations conducted for the H_α line at just one value of the electron density N_e and just one value of the temperature T, the authors of [6] claimed that the AEIF leads to an increase of the electron-caused Stark width rather than to its decrease.

It should be emphasized that those simulations [6] had lots of limitations. The primary limitation was their employment of the binary version of the AEIF. Thus, their results have no bearing on the analytical results for the AEIF obtained in the multiparticle approach [3, 4]. Nevertheless, the controversial results of simulation from [6] for the binary version of the AEIF required a resolution.

In the current paper we resolve this issue as follows. Our previous analytical calculations of the AEIF [1–4] were based on the *dynamical* treatment of the perturbing electrons. In other words, in [1–4] we calculated analytically how the ion microfield changes the trajectories and velocities of the individual perturbing electrons and then averaged their contribution to the broadening over the ensemble of electrons. In the current paper, instead of the dynamical treatment we employ a *statistical* approach. Namely, we start from the electron velocity distribution function modified by the presence of the ion microfield—this modified electron velocity distribution function had been calculated (for a different purpose) by Romanovsky and Ebeling in the multiparticle description of the ion microfield [7]. With the help of the modified electron velocity distribution function from [7], we then calculate the Stark broadening by electrons within the framework of the conventional theory usually assigned to Griem [5] (who is one of the coauthors of [6]). The result shows that the electron Stark broadening decreases.

Thus two totally different analytical approaches (dynamical and statistical) agree with each other (by predicting a decrease of the electron Stark broadening) and therefore disprove the fully-numerical simulations from [6] (that claimed an increase of the electron Stark broadening). In conclusion we briefly discuss possible reasons for the failure of the fully-numerical simulations from [6].

2. Analytical Calculations

Romanovsky and Ebeling [7] considered the instantaneous state of a plasma as a set as "domains" (the size of the domains being of the order of the Debye radius) with different constant values of the ion microfield **F**. The latter was treated in the multiparticle description. The characteristic time of the domain structure changes is of the order of the inverse plasma frequency. By applying the statistical approach, Romanovsky and Ebeling derived the following (unnormalized) velocity distribution function of the plasma electrons affected by the ion microfield

$$f^{(u)}(v) = \left(\frac{2v}{\pi}\right)\int_0^\infty dt\,\sin(tv)\exp\left[-(v_E t)^{3/2} - \frac{(v_T t)^2}{4}\right], \tag{1}$$

where the superscript "u" stands for "un-normalized", $v_T = (2T_e/m)^{1/2}$ is the mean thermal velocity of the electrons, and v_F is the scaled (to the dimension of velocity) characteristic ion microfield defined as follows:

$$v_E = \left(\frac{eE_H}{m}\right)\left[\frac{m}{4\pi e^2 N_i}\right]^{1/2}(Ti/Te)^{1/2}. \tag{2}$$

Here e, m, and T_e are the electron charge, mass, and temperature, respectively; N_i and T_i are ion density and temperature, respectively; the quantity

$$E_H = 2\pi\left(\frac{4}{15}\right)^{2/3} eN_i^{2/3} \tag{3}$$

is the characteristic Holtsmark microfield. (The authors of [7] used F_H in the form $E_H = 2\pi(4/15)^{2/3}e(N_i^{2/3} + N_e^{2/3})$, where N_e was the electron density—because the focus of their study was the effect of the plasma microfield on the ionization by very rapid electrons having the kinetic energy much greater than T_e . Those electrons were affected by both the ion and electron microfields.) The distribution function $f(v)$ becomes the Maxwell distribution if $v_E = 0$, and it becomes the Holtsmark distribution if $v_T = 0$.

Let us first consider the most practically important case where $v_E \ll v_T$. In this case we can expand $\exp[-(v_F t)^{3/2}]$ in the integrand in (1):

$$f^{(u)}{}_{\text{small}}(\text{v}) = \left(\frac{2v}{\pi}\right)\int_0^\infty dt\,\sin(tv) \times \left[1 - (v_E t)^{3/2}\right]\exp\left[-\frac{(v_T t)^2}{4}\right]. \tag{4}$$

Here subscript "small" stands for a relatively small ion density/field. After calculating the integral in (4) analytically and then normalizing the corresponding distribution function (also analytically), we obtain the following normalized velocity distribution function:

$$f_{\text{small}}(v) = \left[\frac{4v^2}{\pi\, v_T^{9/2}}\right] \times \left[\pi^{1/2} v_T^{3/2}\exp\left(-\frac{v^2}{v_T^2}\right) - 2^{5/2}\Gamma\left(\frac{9}{4}\right)v_E^{3/2}\, F\left(\frac{9}{4}, \frac{3}{2};\, -\frac{v^2}{v_T^2}\right)\right]. \tag{5}$$

Here $\Gamma(z)$ is the gamma-function, $F(a, c;\, z)$ is the confluent hypergeometric function.

At the stage preceding the averaging over velocities, the electron impact broadening operator in the dipole approximation has the following form (in accordance to the conventional theory [5]):

$$\Phi(v) = \frac{K}{v^2}, \tag{6}$$

where K is a well-known operator that practically does not depend on velocity (see, e.g., [8])

$$K = -\left(\mathbf{r}_a\mathbf{r}_a - 2\mathbf{r}_a\mathbf{r}_b^* + \mathbf{r}_b^*\mathbf{r}_b^*\right)\left[\frac{4\pi e^4 N_e}{3\hbar^2}\right]\left[\ln\left(\frac{\rho_{\max}}{\rho_{\min}}\right) + \frac{1}{2}\right]. \tag{7}$$

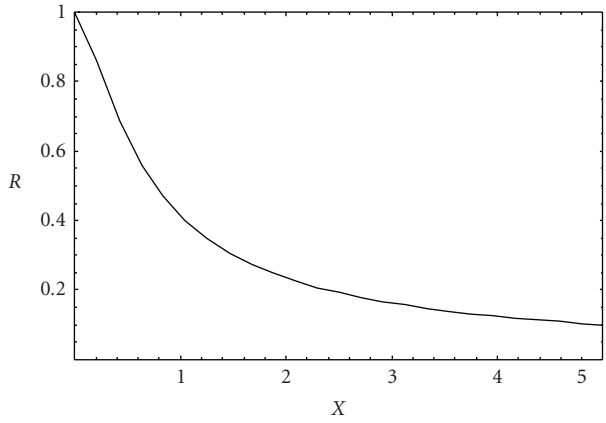

FIGURE 1: The electron broadening reducing factor R versus the parameter $X = \nu_E/\nu_T$ representing the scaled dimensionless ion density/field. Here $\nu_T = (2T_e/m)^{1/2}$, and ν_E is defined by (2), (3).

The next step is the usual averaging over velocities

$$\Phi_{\text{small}} = \int_0^\infty d\nu\ \nu\ f_{\text{small}}(\nu)\,\Phi(\nu) \tag{8}$$

By calculating the integral in (8) analytically, we obtained

$$\Phi_{\text{small}} = \left[\frac{2K}{\pi^{1/2}\nu_T}\right]\left[1 - \frac{2^{3/2}\,\Gamma(5/4)\nu_E^{3/2}}{\left(\pi^{1/2}\nu_T^{3/2}\right)}\right]. \tag{9}$$

From (9) it is clearly seen that as the parameter ν_E/ν_T (representing the scaled dimensionless ion density/field) increases from zero, the electron impact broadening *decreases*. Just this result alone disproves the claim by the authors of [6] that the AEIF leads to an increase of the electron-caused Stark width.

For completeness, let us now consider the opposite case: $\nu_E \gg \nu_T$. In this case we can expand $\exp[-(\nu_T t)^2/4]$ in the integrand in (1):

$$f^{(u)}{}_{\text{large}}(\text{v}) = \left(\frac{2\nu}{\pi}\right)\int_0^\infty dt\,\sin(t\nu) \times\left[1 - \frac{(\nu_T t)^2}{4}\right]\exp\left[-(\nu_E t)^{3/2}\right]. \tag{10}$$

Here subscript "large" stands for a relatively large ion density/field. After calculating the integral in (10) analytically and then normalizing the corresponding distribution function (also analytically), we obtain the normalized velocity distribution function $f_{\text{large}}(\nu)$. The expression for $f_{\text{large}}(\nu)$ is rather bulky, and we omit it (since it is only an intermediate result). Then by using $f_{\text{large}}(\nu)$, we perform the usual averaging over velocities

$$\Phi_{\text{large}} = \int_0^\infty d\nu\ \nu\ f_{\text{large}}(\nu)\Phi(\nu). \tag{11}$$

By calculating the integral in (11) analytically, we obtained the following relatively simple result:

$$\Phi_{\text{large}} = \left[\frac{9K\Gamma(11/3)}{20\pi\nu_E}\right]\left[1 - \frac{20\nu_T^2}{27\Gamma(11/3)\nu_E^2}\right]. \tag{12}$$

To better visualize our results, we define in a natural way the electron broadening reducing factor

$$R = \frac{\Phi(\nu_E/\nu_T)}{\Phi(0)}. \tag{13}$$

Figure 1 shows the dependence of the electron broadening reducing factor R on the parameter $X = \nu_E/\nu_T$ representing the scaled dimensionless ion density/field. It is seen that the new statistical approach used in this paper confirms that the effect of the ion microfield on the electron broadening is the *reduction* of the electron Stark widths and shifts.

3. Conclusions

We performed analytical calculations of the phenomenon of AEIF based on the new statistical multiparticle approach originating from Romanovsky-Ebeling's paper [7]. We showed that the results are in agreement with the previous analytical results obtained by a different (dynamical rather than statistical) approach employed in [1–4]. Both approaches demonstrated a decrease of the electron Stark broadening. This is a clear indication that the results of fully-numerical simulations [6] claiming an increase of the electron Stark broadening are incorrect.

The failure of the fully-numerical simulations from [6] could be due to quite general reasons. Complicated codes (such as the one from [6]) require *adequate verification* and *adequate validation* [9]. The verification is the determination that the code solves the chosen model correctly. Validation is the determination that the model itself captures the essential physical phenomena with adequate fidelity. Post and Votta [9] noted that without adequate verification and validation, computational results are not credible.

Complicated codes are a collection of individual blocks or components. Even if the individual blocks are relatively accurate, the entire code may be not. In another publication [10] Post and Votta emphasized that since a computational simulation is only a model of nature, not nature itself, there is no assurance that a collection of accurate individual components will capture the emergent effects.

There are numerous failures of complicated large-scale codes/simulations (see, e.g., [9]). In the area of plasma fusion—the area for which spectral line shapes serve as diagnostics—examples are the following [9]. By stretching boundary conditions far beyond what could be scientifically justified, computer simulations were able to "reproduce" the exciting but wrong experimental discovery of sonoluminescent fusion. With regard to the International Thermonuclear Experimental Reactor (ITER), preliminary computational predictions in 1996 of inadequate performance by the proposed facility were wrongly characterized as definitive. Those predictions contributed to the 1998 US withdrawal from that important and promising international undertaking.

So, the failure of the fully-numerical simulations from [6] probably resulted from *inadequate verification* and/or *inadequate validation*. By the way, the authors of [6] admit that their simulations failed to reproduce straightforward analytical calculations from [11] concerning the breakdown

of the so-called "line space concept," while they did not find any intrinsic deficiency of those analytical calculations. (The line space concept limits the lineshape calculations to the direct product of the two manifolds, corresponding to the upper and lower principal quantum numbers involved in the radiative transition.) This failure of the authors of [6] should have warned them about seemingly inadequate verification and/or inadequate validation of their code.

The last but not least: other codes (developed by Alexiou, who is one of the coauthors of [6]), that are similar in nature to the one from [6], fail to agree with the benchmark experiments by about 30%—as described in detail in [3]. This discrepancy with the benchmark experiments is by one order of magnitude higher than the estimate of the code inaccuracy provided in [6], so that the latter seems to be significantly underestimated.

References

[1] E. Oks, "A new spectroscopic effect resulting in a narrowing of hydrogen lines in dense plasmas," *Journal of Quantitative Spectroscopy and Radiative Transfer*, vol. 65, no. 1–3, pp. 405–414, 2000.

[2] E. Oks, "Reduction of spectral line shifts due to the acceleration of electrons by the ion field in plasmas," *Journal of Physics B*, vol. 35, no. 10, pp. 2251–2260, 2002.

[3] E. Oks, *Stark Broadening of Hydrogen and Hydrogenlike Spectral Lines in Plasmas: The Physical Insight*, Alpha Science International, Oxford, UK, 2006.

[4] E. Oks, "Stark Widths of Hydrogen Spectral Lines in Plasmas: a Highly-Advanced Non-Simulative Semiclassical Theory and Tables," in *Spectral Line Shapes*, E. Oks and M. Pindzola, Eds., vol. 18 of *AIP Conference Proceedings no. 874*, p. 19, AIP Press, New York, NY, USA, 2006.

[5] H. R. Griem, *Spectral Line Broadening by Plasmas*, Academic Press, New York, NY, USA, 1974.

[6] E. Stambulchik, D. V. Fisher, Y. Maron, H. R. Griem, and S. Alexiou, "Correlation effects and their influence on line broadening in plasmas: application to H_α," *High Energy Density Physics*, vol. 3, no. 1-2, pp. 272–277, 2007.

[7] M. Yu. Romanovsky and W. Ebeling, "Corrections of electron impact ionization rates by plasmas electric microfield," *Physics Letters A*, vol. 317, no. 1-2, pp. 150–155, 2003.

[8] V. S. Lisita, "Stark Broadening of Hydrogen Lines in Plasmas," *Soviet Physics Uspekhi*, vol. 122, p. 449, 1977.

[9] D. E. Post and L. G. Votta, "Computational science demands a new paradigm," *Physics Today*, vol. 58, no. 1, pp. 35–41, 2005.

[10] *Physics Today*, p. 14, August 2005.

[11] R. W. Lee and E. Oks, "Breakdown of the line-space concept in Stark broadening of spectral lines by plasmas," *Physical Review E*, vol. 58, no. 2, pp. 2441–2445, 1998.

Hindawi Publishing Corporation
International Journal of Spectroscopy
Volume 2010, Article ID 561697, 5 pages
doi:10.1155/2010/561697

Research Article

Elementary Statistical Models for Vector Collision-Sequence Interference Effects with Poisson-Distributed Collision Times

John Courtenay Lewis

Department of Physics and Physical Oceanography, Memorial University of Newfoundland, St. John's, NL, Canada A1B 3X7

Correspondence should be addressed to John Courtenay Lewis, court@physics.mun.ca

Received 22 April 2009; Accepted 22 May 2009

Recommended by Roland Stamm

In a recent paper (Lewis, 2008) a class of models suitable for application to collision-sequence interference was introduced. In these models velocities are assumed to be completely randomized in each collision. The distribution of velocities was assumed to be Gaussian. The integrated induced dipole moment μ_k, for vector interference, or the scalar modulation μ_k, for scalar interference, was assumed to be a function of the impulse (integrated force) $\mathbf{f}_k$, or its magnitude f_k, experienced by the molecule in a collision. For most of (Lewis, 2008) it was assumed that $\mu_k \propto \mathbf{f}_k$ and $\mu_k \propto f_k$, but it proved to be possible to extend the models, so that the magnitude of the induced dipole moment is equal to an arbitrary power or sum of powers of the intermolecular force. This allows estimates of the infilling of the interference dip by the disproportionality of the induced dipole moment and force. One particular such model, using data from (Herman and Lewis, 2006), leads to the most realistic estimate for the infilling of the vector interference dip yet obtained. In (Lewis, 2008) the drastic assumption was made that collision times occurred at equal intervals. In the present paper that assumption is removed: the collision times are taken to form a Poisson process. This is much more realistic than the equal-intervals assumption. The interference dip is found to be a Lorentzian in this model.

1. Introduction

Spectra resulting from dipole moments induced in molecular collisions typically have the form of broad bands with widths determined by the durations of those collisions [1]. However, these broad bands often exhibit narrow features, which result from the coherence or correlation of induced dipole moments extending over successive or sometimes many collisions. The most conspicuous such features are the vector intercollisional interference dips found in the fundamental bands of $H_2 - X$ spectra and in the pure translational bands of mixtures of rare gas atoms [2]. Also well known are scalar collisional interference features found in the R and P transitions in the fundamental bands of $HD - X$ spectra [3–5] and the corresponding R transitions in the pure rotational spectra [6, 7]. The terms "vector intercollisional interference" or "vector collision-sequence interference" refer to the fact that an internal H_2 scalar transition operator is modulated by a vector function of intermolecular displacement. Thus only a Q branch is observed, with the intercollisional dynamics being those which describe the vector property (intermolecular force, to a good approximation) of the external coordinates.

The present work is based on that of paper I, which will henceforth be referred to as paper I. In paper it was assumed that the collisions suffered by a molecule occur at equally spaced times. This drastic Ansatz allowed the use of the apparatus of discrete Fourier transforms. In this present work it is assumed that the collision times of a given molecule are distributed exactly as a Poisson process, which is in fact an excellent approximation to reality (see [9, 10]). A summary of this work has appeared in [11].

2. Poisson-Distributed Collision Times

At sufficiently low densities and for the study of interference phenomena collisions can be assumed to be instantaneous; the dipole moment induced in one atom or molecule by interaction with a bath of dissimilar atoms or molecules can be represented as

$$\boldsymbol{\mu}(t) = \sum_k \boldsymbol{\mu}_k \delta(t - t_k) e^{-\imath\omega_0 t}, \tag{1}$$

where binary collision k occurs at time t_k and the dipole moment induced in collision k is $\boldsymbol{\mu}_k$. For the vector interference dips in Q branches the quantity $\boldsymbol{\mu}_j$ is parallel to and approximately proportional in magnitude to the impulse (integrated force) $\mathbf{f}_k$ experienced by a molecule in the collision. Our models will be expressed in terms of these impulses $\mathbf{f}_k$. A second assumption is that the velocities before and after a collision are uncorrelated and are Gaussian:

$$P(\ldots,\mathbf{v}_k,\mathbf{v}_{k+1},\mathbf{v}_{k+2},\ldots) = \ldots P(\mathbf{v}_k)P(\mathbf{v}_{k+1})P(\mathbf{v}_{k+2})\ldots, \tag{2}$$

where

$$P(\mathbf{v}) = \begin{cases} \dfrac{1}{2\pi}\ e^{-(1/2)v^2} & \text{in two dimensions,} \\ \dfrac{1}{(2\pi)^{3/2}} e^{-(1/2)v^2} & \text{in three dimensions.} \end{cases} \tag{3}$$

Then the persistence of velocity is zero. This is a fair approximation in some useful cases, such as H_2-H_2, H_2-He, and $HD-He$, and a good approximation for systems such as H_2 in Ar. It is inappropriate for high-mass atoms or molecules dilute in a fluid of low-mass molecules, such as Ar in H_2. Equations (2) and (3) are exact for hard spheres of equal mass, as was first shown by Clerk Maxwell [12].

In general, as stated above, the collision times t_k approximate to a Poisson process, and in the present work it will be assumed that they are drawn from a true Poisson process, with frequency $\overline{\nu}$, whereas in paper I the collisions were assumed to occur at equal intervals.

Equation (1) describes the transition moment for a transition with frequency ω_0 in the absence of shifting and broadening mechanisms.

It will be assumed initially that N collisions lie in the finite-time time interval $[0,T)$ such that $0 \le t_1 \le \cdots \le t_{N-1} \le t_N \le T$. The time T is of course a random variable if N is fixed, but when N is large the record length T can be taken equal to its expectation value, which will be $N/\overline{\nu}$. The Fourier transform of $\boldsymbol{\mu}(t)$ is

$$\begin{aligned} \mathbf{a}(\omega) &= \int_{-\infty}^{\infty} e^{\imath\omega t}\boldsymbol{\mu}(t)\ dt \\ &= \sum_k \boldsymbol{\mu}_k e^{\imath\widetilde{\omega}t_k}, \end{aligned} \tag{4}$$

where $\widetilde{\omega} \equiv \omega - \omega_0$. The unaveraged periodogram is given by

$$\frac{1}{T}|\mathbf{a}(\omega)|^2 = \frac{1}{T}\sum_k\sum_{k'} \boldsymbol{\mu}_k \cdot \boldsymbol{\mu}_{k'}^* e^{\imath\widetilde{\omega}(t_k - t_{k'})}, \tag{5}$$

whence the spectrum itself is given by

$$\begin{aligned} S(\omega) &= \lim_{T\to\infty}\frac{1}{T}\langle|\mathbf{a}(\omega)|^2\rangle \\ &= \overline{\nu}\Big[\left\langle \boldsymbol{\mu}_k \cdot \boldsymbol{\mu}_k^* \right\rangle + 2\mathfrak{Re}\left\langle \boldsymbol{\mu}_k \cdot \boldsymbol{\mu}_{k+1}^* e^{\imath\widetilde{\omega}(t_k - t_{k+1})}\right\rangle \\ &\qquad + 2\mathfrak{Re}\langle \boldsymbol{\mu}_k \cdot \boldsymbol{\mu}_{k+2}^* e^{\imath\widetilde{\omega}(t_k - t_{k+2})}\rangle + \cdots\Big]. \end{aligned} \tag{6}$$

In the present class of models, as stated above, $\boldsymbol{\mu}_k$ is expressed in terms of the impulse $\mathbf{f}_k$. Hence, in full generality,

$$\boldsymbol{\mu}_k = \boldsymbol{\mu}_k(\mathbf{v}_k, \mathbf{v}_{k+1}) \tag{7}$$

whence, by (2) and (3),

$$\langle \boldsymbol{\mu}_k \cdot \boldsymbol{\mu}_{k+p}\rangle = \langle \boldsymbol{\mu}_k\rangle^2 = 0 \quad \text{for } p \ge 2. \tag{8}$$

Then (6) for the spectrum becomes

$$\frac{S(\omega)}{\overline{\nu}} = \left\langle \boldsymbol{\mu}_k \cdot \boldsymbol{\mu}_k^* \right\rangle + 2\mathfrak{Re}\left\langle \boldsymbol{\mu}_k \cdot \boldsymbol{\mu}_{k+1}^* e^{\imath\widetilde{\omega}(t_k - t_{k+1})}\right\rangle. \tag{9}$$

A principal assumption of the present model, and the feature in which it differs from the class of models discussed in paper I, is that the intervals $\Delta_k \equiv t_{k+1} - t_k$, $k = 1, 2, \ldots, N-1$ between collisions are independent of the velocities of the particle, that is, the collision times $t_k, \ldots, t_{k'}, \ldots$ are random variables which constitute a Poisson process. Poisson-distributed collision times are a good approximation for real gases [9], even at high densities [10], though not exact.

If the random variables $\ldots t_k, \ldots, t_{k'}, \ldots$ form a Poisson process, then the intervals Δ_i are exponentially distributed [13]:

$$P(\Delta_i) = \overline{\nu} e^{-\overline{\nu}\Delta_i}. \tag{10}$$

The intervals $[0, t_1)$ and $[t_N, T)$ of durations Δ_0 and Δ_N, respectively, also follow the distribution law (11), this constitutes a well-known "paradox" in the theory of Poisson processes.

From (10) it follows immediately that

$$\langle e^{\imath\widetilde{\omega}(t_k - t_{k+1})}\rangle = \langle e^{-\imath\widetilde{\omega}\Delta_i}\rangle = \overline{\nu}\int_0^{\infty} e^{-(\overline{\nu}+\imath\widetilde{\omega})\Delta}\ d\Delta = \frac{\overline{\nu}}{\overline{\nu}+\imath\widetilde{\omega}}. \tag{11}$$

Then the spectrum is, from (9), given by

$$\frac{S(\omega)}{\overline{\nu}} = \left\langle \boldsymbol{\mu}_k \cdot \boldsymbol{\mu}_k^* \right\rangle + 2\mathfrak{Re}\left\{\left\langle \boldsymbol{\mu}_k \cdot \boldsymbol{\mu}_{k+1}^*\right\rangle \frac{\overline{\nu}}{\overline{\nu}+\imath\widetilde{\omega}}\right\}. \tag{12}$$

The dipole moment or transition moment induced in a collision is roughly but not exactly proportional to the intermolecular force; the overlap parts differ in range by about 25%. For purposes of calculating the intercollisional interference the integrated induced dipole moment $\boldsymbol{\mu}_k$ can be taken parallel to the intermolecular force $\mathbf{f}_k$, but with magnitude proportional to some nonlinear function of the magnitude of the intermolecular force; specifically, we consider

$$\boldsymbol{\mu}_k = \mathbf{f}_k\left(1 + \alpha f_k^{\beta}\right) = \left(1 + \alpha|\mathbf{v}_{k+1} - \mathbf{v}_k|^{\beta}\right)(\mathbf{v}_{k+1} - \mathbf{v}_k), \tag{13}$$

where α and β are constants, which will not in general be integerial. With this model for $\boldsymbol{\mu}_k$, the calculation of

$$\begin{aligned} \max S &= \lim_{\omega\to\infty} S(\omega) = \left\langle \boldsymbol{\mu}_k \cdot \boldsymbol{\mu}_k \right\rangle, \\ \min S &= S(0) = \langle \boldsymbol{\mu}_k \cdot \boldsymbol{\mu}_k\rangle + 2\left\langle \boldsymbol{\mu}_k \cdot \boldsymbol{\mu}_{k+1}\right\rangle \end{aligned} \tag{14}$$

is exactly the same as in paper I.

2.1. Two Dimensions. For two dimensions it was found in paper I that

$$\begin{aligned}\left\langle \boldsymbol{\mu}_k \cdot \boldsymbol{\mu}_k \right\rangle &= 4 + \alpha 2^{\beta+3}\Gamma\left(\frac{\beta}{2}+2\right) + \alpha^2 2^{2\beta+2}\Gamma(\beta+2),\\ \left\langle \boldsymbol{\mu}_k \cdot \boldsymbol{\mu}_{k+1} \right\rangle &= -2 - 2\alpha\mathcal{J}(\beta+1,1) - \alpha^2\mathcal{J}(\beta+1,\beta+1),\end{aligned} \tag{15}$$

where

$$\begin{aligned}\mathcal{J}(\nu,\nu') &\equiv \left\langle (\mathbf{v}_k - \mathbf{v}_{k-1}) \cdot (\mathbf{v}_{k+1} - \mathbf{v}_k) |\mathbf{v}_k - \mathbf{v}_{k-1}|^{\nu-1} \right.\\ &\quad \left. \times |\mathbf{v}_{k+1} - \mathbf{v}_k|^{\nu'-1} \right\rangle\\ &= \frac{3^{(\nu+\nu')/2+1}\Gamma(\nu/2+3/2)\Gamma(\nu'/2+3/2)}{8}\\ &\quad \times {}_2F_1\left(\frac{\nu}{2}+\frac{3}{2}, \frac{\nu'}{2}+\frac{3}{2}; 2; \frac{1}{4}\right).\end{aligned} \tag{16}$$

Note that ν and ν' are exponents, typically fractional, and are not connected in any way with the mean collision frequency $\overline{\nu}$.

Because

$$\mathcal{J}(\beta+1,1) = 2^{\beta+1}\Gamma\left(\frac{\beta}{2}+2\right), \tag{17}$$

it follows that

$$\min S = 2\alpha^2\left(2^{2\beta+1}\Gamma(\beta+2) - \mathcal{J}(\beta+1,\beta+1)\right). \tag{18}$$

For the power-law model, which is a limiting case for $\alpha \gg 1$ of (13) such that

$$\boldsymbol{\mu}_k = \mathbf{f}_k f_k^{\beta} \tag{19}$$

with $\beta \approx -0.25$ (for which value see [14]), it can be shown that

$$\min S = 2\left(2^{2\beta+1}\Gamma(\beta+2) - \mathcal{J}(\beta+1,\beta+1)\right) = \mathcal{O}(\beta^2) \tag{20}$$

while

$$\max S = 2^{2\beta+2}\Gamma(\beta+2). \tag{21}$$

For the case $\beta = -0.25$, we obtain

$$\left.\frac{\min S}{\max S}\right|_{\beta=-0.25} = 0.0088399. \tag{22}$$

2.2. Three Dimensions. The necessary integrals to evaluate $\min S$ and $\max S$ in three dimensions are evaluated in Appendix A. It is found that

$$\begin{aligned}\left\langle \boldsymbol{\mu}_k \cdot \boldsymbol{\mu}_k \right\rangle &= 6 + 2\alpha\frac{2^{\beta+3}}{\sqrt{\pi}}\Gamma\left(\frac{\beta}{2}+\frac{5}{2}\right) + \alpha^2\frac{2^{2\beta+3}}{\sqrt{\pi}}\Gamma\left(\beta+\frac{5}{2}\right),\\ \left\langle \boldsymbol{\mu}_k \cdot \boldsymbol{\mu}_{k+1} \right\rangle &= -\mathcal{J}_{3D}(1,1) - 2\alpha\mathcal{J}_{3D}(\beta+1,1)\\ &\quad - \alpha^2\mathcal{J}_{3D}(\beta+1,\beta+1)\\ &= -3 - 2\alpha\frac{2^{\beta+2}}{\sqrt{\pi}}\Gamma\left(\frac{\beta}{2}+\frac{5}{2}\right)\\ &\quad - \alpha^2\frac{3^{\beta+3/2}}{2\pi}\Gamma\left(\frac{\beta}{2}+\frac{5}{2}\right)^2\\ &\quad \times {}_2F_1\left(\frac{\beta}{2}+\frac{5}{2}, \frac{\beta}{2}+\frac{5}{2}; \frac{5}{2}; \frac{1}{4}\right).\end{aligned} \tag{23}$$

Then from (14), it follows that

$$\begin{aligned}\min S = \alpha^2\left[\frac{2^{2\beta+3}}{\sqrt{\pi}}\Gamma\left(\beta+\frac{5}{2}\right) - \frac{3^{\beta+3/2}}{\pi}\Gamma\left(\frac{\beta}{2}+\frac{5}{2}\right)^2\right.\\ \left. \times {}_2F_1\left(\frac{\beta}{2}+\frac{5}{2}, \frac{\beta}{2}+\frac{5}{2}; \frac{5}{2}; \frac{1}{4}\right)\right],\end{aligned} \tag{24a}$$

$$\max S = 6 + \mathcal{O}(\alpha). \tag{24b}$$

The fact that

$$\frac{\min S}{\max S} \propto \alpha^2 \tag{25}$$

is in accord with discussions in [2, 15].

For the power-law model given in (19), we have

$$\min S = 0.58\beta^2 + \mathcal{O}(\beta^3), \tag{26a}$$

$$\max S = 6 + \mathcal{O}(\beta) \tag{26b}$$

and, for $\beta = -0.25$, we obtain

$$\left.\frac{\min S}{\max S}\right|_{\beta=-0.25} = 0.0064980 \tag{27}$$

which may be compared with the two-dimensional value given in (22).

3. Conclusions

In this paper, we have extended a class of model developed in paper I for the study of collision-sequence interference effects in collision-induced absorption, to include realistic distributions of collision times. In these models, a single particle is followed. Its collisions are supposed to

be instantaneous. In paper I the collisions were assumed to occur at equally spaced times, whereas in the present work the collision times are distributed according to a Poisson process. Velocities are supposed to be completely randomized at each collision. It is supposed that the dipole moment $\boldsymbol{\mu}_k$ or μ_k induced in a collision is proportional to the integrated intermolecular force $\mathbf{f}_k$ or f_k, respectively, or a power or sum of powers of the integrated intermolecular force.

It is important that the model spectra can be determined analytically, or at worst, reduced to straightforward numerical integrations. The models of paper I, of [11], and of the present work are among the few exactly soluble but nontrivial models found in spectral line-shape studies.

The extension of the induced dipole moment model to dipole moments which are proportional to an arbitrary power of the integrated intermolecular force shows that the interference dip is partially filled in for any disproportionality between induced dipole moment and integrated induced dipole moment. In this paper, the calculation is given for the three-dimensional case. For a realistic value of the power the infilling is slight, being about 0.6% of spectral maximum for the three-dimensional case.

Appendix

A. Evaluation of Certain Integrals

A.1. Evaluation of $\langle f^\nu \rangle$. In three dimensions, the Gaussian distribution of velocities is given by

$$P(\mathbf{v}) = \frac{1}{(2\pi)^{3/2}} e^{-(1/2)v^2} \tag{A.1}$$

whence

$$\langle f^\nu \rangle = \frac{1}{8\pi^3} \int d^3v d^3v' e^{-(1/2)(v^2+v'^2)} \left| \mathbf{v} - \mathbf{v}' \right|^\nu \tag{A.2}$$

which, setting $\mathbf{u} = \mathbf{v} - \mathbf{v}'$ and $\mathbf{U} = (1/2)(\mathbf{v} + \mathbf{v}')$, yields

$$\begin{aligned} \langle f^\nu \rangle &= \frac{1}{8\pi^3} \int d^3u d^3U e^{-(1/4)u^2 - U^2} u^\nu \\ &= \frac{2}{\pi} \left(\int_0^\infty dU U^2 e^{-U^2} \right) \left(\int_0^\infty du e^{-(1/4)u^2} u^{\nu+2} \right) \\ &= \frac{2^{\nu+1}}{\sqrt{\pi}} \Gamma\left(\frac{\nu+3}{2} \right). \end{aligned} \tag{A.3}$$

Then

$$\langle f \rangle = \frac{4}{\sqrt{\pi}} = 2.2567583, \qquad \langle f^2 \rangle = 6. \tag{A.4}$$

A.2. Evaluation of $\mathcal{J}_{3D}(\nu, \nu')$. For these vectorial cross terms we have

$$\begin{aligned} \mathcal{J}_{3D}(\nu, \nu') = -\frac{1}{(2\pi)^{9/2}} \int d^3v d^3v' d^3v'' e^{-(1/2)(v^2+v'^2+v''^2)} \\ \times \left| \mathbf{v} - \mathbf{v}' \right|^{\nu-1} \left| \mathbf{v}' - \mathbf{v}'' \right|^{\nu'-1} (\mathbf{v} - \mathbf{v}') \cdot (\mathbf{v}' - \mathbf{v}''). \end{aligned} \tag{A.5}$$

We set $\mathbf{u} = \mathbf{v} - \mathbf{v}'$ and $\mathbf{u}' = \mathbf{v}' - \mathbf{v}''$ and $\mathbf{U} = (1/2)(\mathbf{v} + \mathbf{v}' + \mathbf{v}'')$ so that

$$\begin{pmatrix} \mathbf{v} \\ \mathbf{v}' \\ \mathbf{v}'' \end{pmatrix} = \begin{pmatrix} \frac{2}{3}\mathbf{u} + \frac{1}{3}\mathbf{u}' + \frac{2}{3}\mathbf{U} \\ -\frac{1}{3}\mathbf{u} + \frac{1}{3}\mathbf{u}' + \frac{2}{3}\mathbf{U} \\ -\frac{1}{3}\mathbf{u} - \frac{2}{3}\mathbf{u}' + \frac{2}{3}\mathbf{U} \end{pmatrix}, \tag{A.6}$$

$$\frac{1}{2}(v^2 + v'^2 + v''^2) = \frac{1}{3}u^2 + \frac{1}{3}\mathbf{u} \cdot \mathbf{u}' + \frac{1}{3}u'^2 + \frac{2}{3}U^2.$$

The Jacobian of the transformation $u_x, u'_x, U_x \leftarrow v_x, v'_x, v''_x$ is

$$\begin{vmatrix} \frac{2}{3} & \frac{1}{3} & \frac{2}{3} \\ -\frac{1}{3} & \frac{1}{3} & \frac{2}{3} \\ -\frac{1}{3} & -\frac{2}{3} & \frac{2}{3} \end{vmatrix} = \frac{2}{3}. \tag{A.7}$$

Then

$$\begin{aligned} &\mathcal{J}_{3D}(\nu, \nu') \\ &= -\frac{1}{54\sqrt{2}\pi^{9/2}} \int d^3u d^3u' d^3U \\ &\qquad \times e^{-((1/3)u^2 + (1/3)\mathbf{u}\cdot\mathbf{u}' + (1/3)u'^2 + (2/3)U^2)} \\ &\qquad \times u^\nu (u')^{\nu'} \cos\vartheta \\ &= -\frac{3^{(3+\nu+\nu')/2}}{\pi} \int_0^\infty du \int_0^\infty du' \\ &\quad \times \int_0^\pi d\vartheta \sin\vartheta u^{\nu+2} (u')^{\nu'+2} e^{-\left(u^2 + uu' \cos\vartheta + u'^2\right)} \cos\vartheta \\ &= \frac{2 \times 3^{(3+\nu+\nu')/2}}{\pi} \int_0^\infty du \\ &\quad \times \int_0^\infty du' u^\nu (u')^{\nu'} e^{-u^2 - u'^2} (uu' \cosh uu' - \sinh uu'), \end{aligned} \tag{A.8}$$

where $\vartheta = \measuredangle \mathbf{u}, \mathbf{u}'$. This gives

$$\begin{aligned}
\mathcal{J}_{3D}(\nu,\nu') &= \frac{2\times 3^{(3+\nu+\nu')/2}}{\pi}\sum_{k=0}^{\infty}\frac{1}{(2k+1)!(2k+3)}\\
&\quad\times\int_0^\infty du\int_0^\infty du' u^{2k+3+\nu}(u')^{2k+3+\nu'}e^{-u^2-u'^2}\\
&= \frac{3^{(3+\nu+\nu')/2}}{2\pi}\Gamma\left(2+\frac{\nu}{2}\right)\Gamma\left(2+\frac{\nu'}{2}\right)\\
&\quad\times\sum_{k=0}^{\infty}\frac{(2+\nu/2)_k(2+\nu'/2)_k}{(2k+1)!(2k+3)}\\
&= \frac{3^{(1+\nu+\nu')/2}}{2\pi}\Gamma\left(2+\frac{\nu}{2}\right)\Gamma\left(2+\frac{\nu'}{2}\right)\\
&\quad\times\sum_{k=0}^{\infty}\frac{(2+\nu/2)_k(2+\nu'/2)_k}{(5/2)_k k!}\left(\frac{1}{4}\right)^k\\
&= \frac{3^{(1+\nu+\nu')/2}}{2\pi}\Gamma\left(2+\frac{\nu}{2}\right)\Gamma\left(2+\frac{\nu'}{2}\right)\\
&\quad\times {}_2F_1\left(2+\frac{\nu}{2},2+\frac{\nu'}{2};\frac{5}{2};\frac{1}{4}\right).
\end{aligned} \tag{A.9}$$

Then

$$\begin{aligned}
\mathcal{J}_{3D}(1,1) &= 3,\\
\mathcal{J}_{3D}(\beta+1,1) &= \frac{2^{\beta+2}}{\sqrt{\pi}}\Gamma\left(\frac{5+\beta}{2}\right),\\
\mathcal{J}_{3D}(\beta+1,\beta+1) &= \frac{3^{3/2+\beta}}{2\pi}\Gamma\left(\frac{5+\beta}{2}\right)^2\\
&\quad\times {}_2F_1\left(\frac{5+\beta}{2},\frac{5+\beta}{2};\frac{5}{2};\frac{1}{4}\right).
\end{aligned} \tag{A.10}$$

Acknowledgments

The author thanks the Department of Physics of the Pennsylvania State University for its hospitality in 1999, in 2000, in 2005, and in 2008; he gratefully acknowledges many useful discussions on collision-induced absorption with Roger Herman; and he thanks Eugene Oks for providing the opportunity to develop this paper. The support from the Natural Sciences and Engineering Research Council of Canada is acknowledged.

References

[1] L. Frommhold, *Collision-Induced Absorption in Gases*, Cambridge University Press, Cambridge, UK, 1993.

[2] J. C. Lewis, "Intercollisional interference—theory and experiment," in *Phenomena Induced by Intermolecular Interactions*, G. Birnbaum, Ed., pp. 215–257, Plenum Press, New York, NY, USA, 1985.

[3] R. M. Herman, "Analysis of the R1(J)- and P1(J)-branch absorption spectrum of HD-rare-gas mixtures: an example of positive intercollisional interference," *Physical Review Letters*, vol. 42, no. 18, pp. 1206–1209, 1979.

[4] R. M. Herman, R. H. Tipping, and J. D. Poll, "Shape of the R and P lines in the fundamental band of gaseous HD," *Physical Review A*, vol. 20, no. 5, pp. 2006–2012, 1979.

[5] R. M. Herman, in *Proceedings of the 14thConference on Spectral Line Shapes (ICSLS '99)*, R. M. Herman, Ed., AIP Conference Proceedings no. 467, pp. 552–555, American Institute of Physics, Melville, NY, USA, 1999.

[6] J. B. Nelson and G. C. Tabisz, "Intracollisional interference in the pure rotational spectrum of HD: determination of the permanent electric dipole moment," *Physical Review A*, vol. 28, no. 4, pp. 2157–2161, 1983.

[7] A. R. W. McKellar, J. W. C. Johns, W. Majewski, and N. H. Rich, "Interference effects in the spectrum of HD: III. The pure rotational band at 77 K for HD and HD-Ne mixtures," *Canadian Journal of Physics*, vol. 62, no. 12, pp. 1673–1679, 1984.

[8] J. C. Lewis, "Elementary statistical models for collision-sequence interference effects," *Physical Review A*, vol. 77, no. 6, Article ID 062702, 2008.

[9] S. Chapman and T. G. Cowling, *The Mathematical Theory of Non-Uniform Gases*, Cambridge University Press, Cambridge, UK, 2nd edition, 1964.

[10] J. C. Lewis, "Distributions of collision times for rough disks and for a two-dimensional lorentz gas with non-overlapping fixed scatterers," *Chemical Physics Letters*, vol. 76, no. 1, pp. 96–100, 1980.

[11] J. C. Lewis and R. M. Herman, "A statistical model for scalar collision—sequence interference," in *Proceedings of the 19th Conference on Spectral Line Shapes (ICSLS '08)*, M. A. Gigoros and M. Á. González, Eds., AIP Conference Proceedings no. 1058, pp. 122–124, American Institute of Physics, Melville, NY, USA, 2008.

[12] J. C. Maxwell, "Illustrations of the dynamical theory of gases," *Philosophical Magazine*, vol. 19, pp. 19–32, 1860.

[13] W. Feller, *An Introduction to Probability Theory and Its Applications*, John Wiley & Sons, New York, NY, USA, 3rd edition, 1968.

[14] R. M. Herman and J. C. Lewis, "Theory of the fundamental vibration-rotation-translation spectrum of H_2 in a C_{60} lattice," *Physical Review B*, vol. 73, no. 15, Article ID 155408, pp. 1–14, 2006.

[15] J. C. Lewis, "Theory of intercollisional interference effects—II: induced absorption in a real gas," *Canadian Journal of Physics*, vol. 50, no. 22, pp. 2881–2901, 1972.

Hindawi Publishing Corporation
International Journal of Spectroscopy
Volume 2010, Article ID 306392, 9 pages
doi:10.1155/2010/306392

Research Article

Unified Impact Theory for Velocity-Changing Effects and Speed Dependencies in Neutral Species Lineshapes

Roger M. Herman

Department of Physics, The Pennsylvania State University, 104 Davey Laboratory, University Park, PA 16802, USA

Correspondence should be addressed to Roger M. Herman, rmh@phys.psu.edu

Received 27 April 2009; Accepted 19 July 2009

Academic Editor: Roland Stamm

A dipole correlation function which incorporates velocity-changing (motional narrowing) effects and the effects of speed-dependent Lorentz relaxation rates into otherwise Voigt profile correlation functions is developed, based partly upon previous work by the author. For the first time simple closed expressions, which lend themselves to elementary calculation beginning only with the relevant parts of intermolecular interaction energies, are developed for the cubic time-dependent term within the exponent describing the decay of the correlation function. This term is of first order in perturber number density, as are the Lorentz parameters, and is complex, thereby allowing for narrowing, changing in shape and asymmetry in the line profile. "Soft" and "hard" collisions play no explicit role, though both are variously present for each line. Quartic time dependencies are also discussed, though they are thought to be negligible in nonhydrogen molecular spectroscopy. Finally, some comments are added about a relevant technique for hydrogen spectra.

1. Introduction

For several decades, now, neutral species coherence transport and relaxation has followed a number major thrusts, above and beyond the simplest convolution of the optical coherence interruption (Lorentz) and Gaussian (Doppler) contours, as embodied in the Voigt profile for isolated spectral lines. To mention a few, five such developments come immediately to mind: (1) the incorporation of the speed dependence of coherence destruction (with speed dependent Lorentz lineshape parameters) within the Voigt convolution (SDVP effect) [1–3]; (2) the incorporation of collisional reduction of free-streaming molecular motions, which had previously been assumed in the initial inclusion of Doppler broadening, known as Dicke (or motional) narrowing [4]; (3) finite duration of collision effects [5] as they influence narrow lines that otherwise are regarded as having been generated by effectively instantaneous collisions; (4) line-mixing effects, in which coherent collisional mixing of the transition of immediate interest with other nearby (frequency-wise) transitions leads to an effective blending of contours in which each becomes distorted into combination Lorentzian-anomalous dispersion (Fano) contour [5–7]; (5) nonlinear spectroscopies [8], where, in two-photon absorption, the Doppler broadening may be cancelled out, due to the opposite propagation direction (and therefore compensatory momentum uptake by the excited molecule) of the two photons involved in producing the absorption signals. Also, in saturation spectroscopies, a primary interaction causes a population "hole" to be produced at a selected frequency corresponding to a specific Doppler velocity group, which can then be broadened directly by velocity-changing collisions for detection by a secondary beam. These are what might be called "special effects" which lie outside of the scope of this article, although the methods described herein are sometimes useful in dealing with these phenomena [9]. Line mixing effects can be readily introduced into the formalism that will be described, though they will again be omitted from the present discussion, for simplicity. Finite duration effects fall into two categories, the first being that for a single spectroscopic line the correlation function for nearly zero time (equal to or less than the duration of typical collisions) will differ from the more typical decaying exponential time dependence seen in the longer time behavior. This gives rise to a short time correction to the correlation function which leads to the appearance of an additive (as opposed

to multiplicative as in some literature; see [10], e.g.) low intensity, broad frequency contribution that will ensure finite nth moments of the intensity distributions for all n, as must result for analytic forms of the correlation functions. [11–14] The second finite-duration effect would be described as true binary collisions throughout the collision sequences which give rise to Lorentzian shapes. These would primarily lead to slight quadratic (in density) Lorentzian width and shift dependences. The finite duration-of-collision effects are indeed important for the accurate description of narrow isolated spectral features. Nonetheless, for purposes of simplicity, they again will be omitted from further discussion in the present theoretical treatment.

Of special interest in the present paper are the highly detailed experimental studies of individual spectral lines, such as those carried out by Pine et al. [15–17], and Wehr [18, 19] for hydrogen halide spectra, by Rohart et al. [20, 21] for atmospheric ozone, by Lisak et al. [22] for water vapor and by Priem et al. [23] and Wehr et al. [24, 25] for CO. Self- and foreign gas-perturbed hydrogen Raman spectra [26, 27] show effects related to those cases mentioned above, though the analysis of the latter lies a bit outside of the present development. Most of the articles cited contain theoretical analyses and there exist many independent theoretical analyses, too numerous to cite here. In the related analysis, there have emerged two models that seem, in varying situations, to be applicable to an understanding of the experimental results: the "soft" collision model first introduced by Galatry [10] in which, in collisions leading to internal state coherence modification, collisions gently act to reduce the free-streaming motions of molecules as assumed in Doppler broadening, together with the introduction of diffusional translational motions, and the "hard" collision model first introduced by Rautian and Sobel'man [28], in which, in addition to internal state coherence modification, molecular motion is totally randomized to the extent allowed by dynamical constraints. To a large extent these models are still in use, though some efforts have been made to bridge the gaps between the two pictures through the introduction of an additional hardness parameter. In actuality, both pictures operate separately but simultaneously, to a greater or lesser extent in producing any given spectral line, in that the distant collisions, which traditionally do not substantially limit internal state coherence but are often the primary cause of line shifts would typically be characterized as being soft, only slightly altering translational motions in any of the numerous such encounters, while the hard collisions would accompany events in which the coherence is often nearly terminated. In the present paper, we will introduce a treatment which formally makes no delineation between the soft and hard collision cases, including both types in a "seamless" unified description of all of the above-mentioned processes. Also included in a natural way are all aspects of interference between internal state coherence limitation and velocity changes, which can give rise to slight asymmetries of the lines which have, on occasion, been observed.

One of the difficulties of the descriptions of Dicke narrowing is that there seem not to be any reasonably transparent first principles expressions, or series of expressions giving the relevant parameters associated with these phenomena. In the present paper we shall, for the first time, derive intuitively appealing closed expressions for the relevant quantities, in terms of relevant parts of intermolecular potential functions and intrinsic parameters such as number density and temperature. The present work follows a partial description which was first published in 2000 [29], which carried the capricious title utilizing the phrase "Theory for Everything…" henceforth referred to as paper *I*. However, the detailed expressions for relevant parameters occurring in the correlation functions are newly derived in the present paper. While the closely allied SDVP effects have been variously discussed, the first description in which it was systematically related to the time dependence of the correlation function was provided by Looney [30], and that treatment will be followed here, with modifications.

The dipole-dipole (or other optically active operators, depending upon the spectroscopy being described) correlation function for an isolated transition can be described as having an exponential behavior of type [30, 31]:

$$\exp\left[-\gamma t - \frac{k_B T}{2m} k^2 t^2 + \beta t^3 - \delta t^4 + \cdots\right], \quad t > 0. \tag{1}$$

In the first term $\gamma = \gamma_r + i\gamma_i$ represents the standard internal state coherence interruption effect, providing a Lorentz shape half-width at half maximum, γ_r, and line shift, $-\gamma_i$. The second term expresses the Doppler effect which, by itself, leads to the standard Gaussian lineshape with k being the optical wavevector magnitude. The cubic term depends upon the coefficient β, which we might call the first motional narrowing coefficient. It is intrinsically complex, due to correlations of internal phase perturbation and translational velocity changes. Then δ is the second motional narrowing coefficient, and so on. We will supply closed expressions for ready calculation of β, and indicate how one may approach the calculation of δ, in the unlikely event that it would be needed. Higher order terms are required to give a convergent expression for $C(t)$ at very large times, opposing the indefinite increase in the cubic term. But explicit calculation would only proceed to the point that $C(t)$ becomes essentially zero, even with only the cubic term, and the higher terms would remain as being negligible, at which point the Fourier transform integration would be truncated. Higher parameters are of unlikely practical significance in virtually all nonhydrogen spectroscopy. In hydrogen spectroscopy (through Raman, quadrupole or permanent and collisionally induced dipole sharp line spectra in HD) motional narrowing is extremely important [26, 27] at moderately low densities (corresponding to around one to ten atmospheres at room temperature). For these cases the above-mentioned higher terms become important. While the present theory surely applies (in a different limit) to these cases, detailed studies will not be carried out at this time. Nonetheless, an indication of how one might approach the molecular hydrogen problem is suggested.

We will assume that classical paths are sufficient for the description of collisional processes. As indicated, one can

presumably make the entire calculation quantum mechanically as has been done in the past for the calculation of Lorentz lineshape parameters [32]. But there are other possibilities: One might accept fully quantum computation for the Lorentz parameters, accept as true in quantum mechanics as well as classical mechanics the simple Doppler terms, and use classical methods for the description of motional narrowing. If ones interest is solely to understand motional narrowing, measured values of the Lorentz parameters can be accepted, while ensuring that the correct density dependences are strictly adhered to throughout.

A note of caution should be expressed at the present time. This is, that obtaining agreement between theory and experiment on a single molecular line at a single density can lead to deceptive satisfaction. One must strive to analyze all lines that have been observed at all possible pressures, while rigorously adhering to the correct pressure dependencies of the real and imaginary parts of γ and β throughout.

2. Theoretical Considerations

The development of a correlation function describing isolated spectral lines, omitting duration-of-collision effects, essentially follows that of paper I. Minor changes will be made, to more accurately reflect current notation. In particular, the subscripts "fi" will be dropped from expressions involving the correlation function, the choice of final and initial states in the transition being obvious. Moreover, τ and t will be replaced by t, t', and $\mathbf{v_o}$, $\mathbf{v}$ will be replaced by $\mathbf{v}$, $\mathbf{v}'$, respectively. Vectors will be denoted by boldface type.

The spectral line profile for absorption from a lower state i to upper state f (normalized to the relevant dipole moment matrix element squared) can be represented by the form

$$\mathcal{L}_{fi}(w) = \frac{|\mu_{fi}|^2}{\pi} \operatorname{Re} \int_0^\infty C_{fi}(t) \exp\Big[\Big(w_{fi} - w\Big)t\Big]dt, \quad (2)$$

where $C_{fi}(t)$, the correlation function, satisfies the ensemble average:

$$C_{fi}(t) \equiv C(t) = \Big\{U^*_{ff}(t)U_{ii}(t)\exp[i\mathbf{k}\cdot\mathbf{R}(t)]\Big\}_{\text{ens.avg.}}, \quad (3)$$

where $\mathbf{k}$ is the optical propagation vector, $\mathbf{R}$ is the molecular displacement following time t relative to the position at time $t = 0$, and U_{ff} and U_{ii} are diagonal time-development matrix elements for the respective internal molecular states resulting from whatever collisional events may occur in the time interval $0 \rightarrow t$. As indicated above, classical paths are envisioned in the present description, though quantum mechanical descriptions of the translational motion problem can be readily developed. For the internal states, U^*_{ff} and U_{ii} can be written as product matrix elements for noncorrelated random collisions. However, the same factorization cannot be made for the translational factor. And it is this nonMarkovian property that has possibly inhibited the development which now is presented here. Concentrating on the internal states, for a single collision it is well known [33, 34] that the product of U matrix elements can be put into the form

$$\begin{aligned} S(\mathbf{v};\mathbf{b},\mathbf{u}) = \exp\Big[-i\eta_{fi}(\mathbf{v};\mathbf{b},\mathbf{u})\Big] \\ \times \Big(1 - S^{*(2)}_f(\mathbf{v};\mathbf{b},\mathbf{u}) - S^{(2)}_i(\mathbf{v};\mathbf{b},\mathbf{u}) \\ + S^{*(4)}_f + S^{(4)}_i + \cdots\Big), \end{aligned} \quad (4)$$

where the superscripts (2), (4) indicate the order of collisional inelastic perturbation. The phase shift term can be represented quite exactly to all orders of perturbation [35] while the inelastic terms, $S^{(n)}_{f,i}$, often are subject to various mathematical approximations as the strength of the collisional interruption increases [36]. While the ATC treatment [33, 34] had envisioned the $S^{(n)}_{f,i}$ terms as being real, they are in general complex, at times contributing significantly to line shifts, otherwise given solely by the phase shifts [37–39].

In the present work, we will regard the calculation of the collisional interruption quantities $S(\mathbf{v};\mathbf{b},\mathbf{u})$ as being completely settled, along with the calculation of outgoing velocities following collisions. We will indicate such dynamical processes as leading to post-collisional velocities $\mathbf{v}'(\mathbf{v};\mathbf{b},\mathbf{u})$. Here $\mathbf{v}$ is the input velocity of the optically active molecule, $\mathbf{b}$ being the vector impact parameter lying in the plane perpendicular to $(\mathbf{v} - \mathbf{u})$, with $\mathbf{u}$ being the perturber initial velocity in any particular encounter.

Following the development of paper I, we now think in terms of a collision as being one in which $\mathbf{b}$ lies within a somewhat large radius of collision B, in an attempt to think about probabilities for zero collisions and a time distribution for a first collision. The actual value of B is unimportant, and it will be seen to fall away from the description as the theory is developed. For now, in the interest of simplicity, let us envision the perturbers as being motionless. According to Poisson statistics, for collisions within radius B the probability for there being no collisions in the interval $0 \rightarrow t$ is simply

$$\exp[-N\bar{v}\pi B^2 t], \quad (5)$$

while the probability per unit time of a first collision is

$$\frac{dP^{(t)}_1}{dt} = -\frac{dP^{(t)}_0}{dt} = N\bar{v}\pi B^2 \exp[-N\bar{v}\pi B^2 t], \quad (6)$$

with N being the perturber number density. Of course, following the first collision there can be a multitude of collisional events, though they will be included implicitly in the appearance of correlation functions for times following the first collision. For a specific initial velocity v, in the absence of any collision, the correlation function will simply be a translational (free-streaming) exponential $\exp[i\mathbf{k}\cdot\mathbf{v}t]$, so that $C(\mathbf{v};t)$ will have a no-collision contribution:

$$\exp[-N\bar{v}\pi B^2 t + i\mathbf{k}\cdot\mathbf{v}t]. \quad (7)$$

But now, in addition, we must include the first collision contribution, distributed throughout the interval $0 \rightarrow t$:

$$\int_0^t N\bar{v}\pi B^2 dt' \exp[-N\bar{v}\pi B^2 t']S(\mathbf{v})C(\mathbf{v}';(t-t')), \quad (8)$$

where S contains the collisional interruption effects, and $\mathbf{v}'$ represents the outgoing velocity in this first single collision. Of course one has to specify the actual impact parameter integration within B, and the integration on $\mathbf{u}$, utilizing the Maxwell distribution of perturber velocities $f(\mathbf{u})$, with the result

$$C(\mathbf{v};t) = \exp[-N\bar{v}\pi B^2 t + i\mathbf{k}\cdot\mathbf{v}t] + N\int_0^t dt' \exp[-N\bar{v}\pi B^2 t' + i\mathbf{k}\cdot\mathbf{v}t'] \times \int_0^B d\mathbf{b}\int d\mathbf{u} f(\mathbf{u})|\mathbf{v}-\mathbf{u}|S(\mathbf{v};\mathbf{b},\mathbf{u})C(\mathbf{v}';(t-t')). \tag{9}$$

The integrations over $\mathbf{b}$ and $\mathbf{u}$ are two- and three-dimensional, respectively. This equation contains the fundamental idea of this paper. As yet, however, this equation is somewhat difficult to utilize in a practical way, and the problem of how to specify B remains unsolved. These difficulties can be remedied through the transformations indicated in I and included in this paper, in the appendix. The final equation from the appendix, which has eliminated the troublesome feature of specifying B and which is capable of yielding fundamental expressions for the line shape parameters of current interest is repeated here:

$$C(\mathbf{v};t) = \exp\left[i\mathbf{k}\cdot\mathbf{v}t - N\int_0^t dt'\int_0^\infty d\mathbf{b}\int d\mathbf{u} \times f(\mathbf{u})|\mathbf{v}-\mathbf{u}|\left(1 - S(\mathbf{v};\mathbf{b},\mathbf{u})\frac{C(\mathbf{v}';t')}{C(\mathbf{v};t')}\right)\right] \tag{10}$$

keeping in mind that $\mathbf{v}' = \mathbf{v}'(\mathbf{v};\mathbf{b},\mathbf{u})$ in accordance with classical dynamics throughout. Note that this equation is equivalent to (10) of paper I.

Over the years, as mentioned above, the collision efficiency function $S(\mathbf{v};\mathbf{bu})$ has been the subject of traditional line shape studies within the classical path formalism. More recently quantum mechanical treatments of the translational motions have been included [32], with considerable success. Within the present theoretical development it is difficult to see how to include quantum translational motions because of the difficulty of computing differential cross-sections for internal state disruption.

3. Applications

The beauties of (10) are twofold. The first is purely conceptual, in that $C(\mathbf{v};t)$ follows all possible collisional histories, with many possible original and intermediate velocities, for ending at time t having velocity $\mathbf{v}$. But also, by redefining the various time intervals and utilizing the principle of detailed balance, by which the $(\mathbf{v},\mathbf{u}) \rightarrow (\mathbf{v}',\mathbf{u}')$ process is equally likely as its reverse process, one can see that $C(\mathbf{v};t)$ also can be viewed as applying to all histories such that one begins at $t = 0$ with velocity $\mathbf{v}$ and ends up with the reverse array of intermediate and final velocity $\mathbf{v}'$. The second is the more practical aspect of how to apply this equation to finding correlation functions that are useful in describing the wealth of spectra that can be illustrative of the effects of collisional narrowing. To accomplish this, we will explicitly find the complex t^3-dependent term in the correlation function in a closed form that represents such an expression for the first time. In addition, we will point the reader in a direction such as to be able to recover the t^4 terms, if the need should arise. We propose using an iterative technique, in which (10) will be solved in successive orders of refinement, such that the first nonVoigt term will be linear in number density of perturbers, the second will be quadratic, and so on. To begin with, let us rewrite (10) in the alternate form

$$C(\mathbf{v};t) = \exp[i\mathbf{k}\cdot\mathbf{v}t] \times \exp\left[-N\int_0^t dt' \iint d\mathbf{b}\, d\mathbf{u}|\mathbf{v}-\mathbf{u}| \times\left((1 - S(\mathbf{v};\mathbf{b},\mathbf{u})) + S(\mathbf{v};\mathbf{b},\mathbf{u})\left(1 - \frac{C(\mathbf{v}',t')}{C(\mathbf{v},t')}\right)\right)\right]. \tag{11}$$

But the $(1 - S(\mathbf{v};\mathbf{b},\mathbf{u}))$ term in this equation, by itself, is simply the ordinary pressure broadening, thus

$$C(\mathbf{v};t) = \exp\left[-\gamma t + i\mathbf{k}\cdot\mathbf{v}t - N\int_0^t dt' \iint d\mathbf{b}\, d\mathbf{u} \times |\mathbf{v}-\mathbf{u}|S(\mathbf{v};\mathbf{b},\mathbf{u})\left(1 - \frac{C(\mathbf{v}';t')}{C(\mathbf{v};t')}\right)\right]. \tag{12}$$

The third term in the exponent represents the complete effect of motional narrowing. Denoting $C^{(1)}(\mathbf{v};t)$ as a first iteration correlation function, we now use the collisionless form of the ratio of C's shown in (12) to be $\exp[-ik\cdot(\mathbf{v}-\mathbf{v}')\mathbf{t}']$ to obtain

$$-N\iint d\mathbf{b}d\mathbf{u}|\mathbf{v}-\mathbf{u}|S(\mathbf{v};\mathbf{b},\mathbf{u})t\left(1 + \frac{\exp[-i\mathbf{k}\cdot(\mathbf{v}-\mathbf{v}')t] - 1}{i\mathbf{k}\cdot(\mathbf{v}-\mathbf{v}')t}\right) \tag{13}$$

following integration on t', as the motional narrowing exponent. In Taylor expansion form, this is

$$-N\iint d\mathbf{b}\, d\mathbf{u}|\mathbf{v}-\mathbf{u}|S(\mathbf{v};\mathbf{b},\mathbf{u}) \times\left(\frac{i\mathbf{k}\cdot(\mathbf{v}-\mathbf{v}')t^2}{2} + \frac{k^2(v_z - v_z')^2 t^3}{6} + \cdots\right) \tag{14}$$

representing the lowest order motional narrowing terms which should, in all cases, be computer friendly and which, once computed, should allow one to find $C(t)$ through the t^3 motional narrowing. There are t^3 terms in $C(t)$ arising from speed dependent Voigt profile effects, however, as will be seen in the next section.

It is not so easy to proceed further from this point without (elementary) computer analysis. Nonetheless, we can make arguments which may indicate some of the basic properties. Beginning with the first Taylor term we note that integrating only over the angles for $\mathbf{b}$ and $\mathbf{u}$, the average velocity difference $(\mathbf{v}-\mathbf{v}')$ must take the direction of $\mathbf{v}$ itself.

Therefore, this part of the exponent can be written in the form $\exp[-i\mathbf{k}\cdot\mathbf{v}Xt^2]$, with

$$X = \left(\frac{N}{2}\right)\iint d\mathbf{b}\,d\mathbf{u}|\mathbf{v}-\mathbf{u}|S(\mathbf{v};\mathbf{b},\mathbf{u})\left(1-\frac{\mathbf{v}\cdot\mathbf{v}'}{v^2}\right) \quad (15)$$

which is first order in perturber number density N. Although X in the above expression probably varies with speed, in general this will be a small effect compared r.m.s. value of speed effect (and, indeed, with the speed dependence of γ itself, which will be addressed below).

At this stage, therefore,

$$C(\mathbf{v};t) \cong \exp[-\gamma t + i\mathbf{k}\cdot\mathbf{v}(t-Xt^2)]. \quad (16)$$

From (15) it is seen that X is complex, with the imaginary part of β in $C(t)$ ultimately arising from an interference between internal collisional phase shifts and velocity (z-component) changes.

The second term in (14), is less obvious in its effects, and the averaging over $\mathbf{b}$ and $\mathbf{v}$ angles is more subtle. The average will depend upon v_x and v_y, as well as v_z. As such, this term explicitly handles Doppler effects following collision arising from the production of v_z components generated from all velocity components present at $t = 0$. The overall effect of such terms might be quite small, however, as can be seen by reference to typical situations. For collisions between hydrogen halide and other molecules of somewhat similar mass, for the longer range encounters, $\mathbf{v}$ will hardly change, leaving $(\mathbf{v}-\mathbf{v}')$ as a very small quantity; for the closer collisions that can indeed change v through scattering more toward right angles, for which $(\mathbf{v}-\mathbf{v}')$ may be quite large, the collisional interruption given by $S(\mathbf{v};\mathbf{b},\mathbf{u})$ may be so large as to effectively screen the dipole moments from being sensitive to these velocity changes. Of course, for He being the foreign gas, large angle scattering of the optically active molecule will not be much of a factor, leaving $(\mathbf{v}-\mathbf{v}')$ as a very small term. Similar arguments might hold for the term linear in $(\mathbf{v}-\mathbf{v}')$ analyzed above, but in view of its first order appearance this term might remain the principal source of the t^3 term. To address this question for either case, let us imagine that the smaller angle scattering is most likely to survive the coherence loss dictated by $S(\mathbf{v};\mathbf{b},\mathbf{u})$. Thus, for polar and azimuthal scattering angles ψ, χ, measured form the incident velocity $\mathbf{v}$ direction, the term $(1/2)\mathbf{k}\cdot(\mathbf{v}-\mathbf{v}')t^2$ would be proportional to $(1/2)kv_z(1-\cos\psi)t^2$, and for small angles, $(1/4)kv_z\psi^2t^2$ prior to averaging over ψ. Relative to this, the term $(1/6)k^2(v_z-v_{z'})^2t^3$ is proportional to $(k^2/6)(v_z^2(1-\cos\psi)^2+(v_x^2+v_y^2)\sin^2\psi\cos^2\chi)$. One immediately averages over χ; the first term is quartic in the small scattering angle ψ, and can therefore be ignored. (This shows that the major effect in these terms comes from the v_x, v_y components of $\mathbf{v}$ being collisionally diverted toward the $\pm z$-directions.) Therefore this term is approximately equal to $(-k^2/6)((v_x^2+v_y^2)/2)\psi^2t^3$. This suggests that the entire exponent for this term can be written as

$$\frac{-N}{6}k^2t^3\iint d\mathbf{b}\,d\mathbf{u}f(\mathbf{u})|\mathbf{v}-\mathbf{u}|S(\mathbf{v};\mathbf{bu})(v_z-v_z')^2 = -k^2\left(\frac{\langle v_x^2+v_y^2\rangle}{2}\right)Yt^3 \quad (17)$$

with

$$Y = \frac{N}{6}\iint d\mathbf{b}\,d\mathbf{u}f(\mathbf{u})|\mathbf{v}-\mathbf{u}|S(\mathbf{v};\mathbf{bu})\frac{2(v_z-v_z')^2}{\langle v_x^2+v_y^2\rangle}; \quad (18)$$

the factor 2 somewhat compensates the $\cos^2\chi$ averaging. In this form, Y will tend to be insensitive to temperature, and is proportional to N.

The overall correlation function $C(t)$ is now found upon averaging over v_z, in the form

$$\begin{aligned} C(t) &= \sqrt{\frac{m}{2\pi k_BT}}\int dv_z \\ &\quad\times\exp\left[-\gamma t-\frac{mv_z^2}{2k_BT}+ikv_zt(1-Xt)-\frac{k^2\langle v_x^2+v_y^2\rangle}{2}Yt^3\right] \\ &= \exp\left[-\gamma t-\left(\frac{k_BT}{2m}\right)k^2t^2(1-Xt)^2-\left(\frac{k_BT}{m}\right)k^2Yt^3\right] \end{aligned} \quad (19)$$

noting that $\langle v_x^2+v_y^2\rangle = 2k_BT/m$. The t^4-term is quadratic in N. By itself it gives an incomplete accounting of the entire t^4 dependence so we will, for present purposes, work only to order t^3, for which

$$C(t) = \exp\left[-\gamma t-\left(\frac{k_BT}{2m}\right)k^2t^2+\frac{k_BT}{m}k^2(X-Y)t^3\right]. \quad (20)$$

Comparison of small angle approximations reveals that Y is about equal to $2X/3$, tending to diminish the motional narrowing. It actually represents a motional-broadening effect associated with collisional production of v_z velocity components (from previously v_y and v_y components), as noted. It is seen that both X and Y are complex quantities, the imaginary parts leading to asymmetries in line shapes; some of which have been observed.

For many spectra the fourth order, t^4 terms in the exponent of $C(t)$ are entirely negligible. If they are needed they will arise from the neglected t^4 terms as noted above, together with the second iteration $C^{(2)}$ in which the results of the first iteration for $C^{(1)}(\mathbf{v};t)$ are included. The calculation will follow the lines already set out, here, for $C^{(1)}(\mathbf{v};t)$, leading to further integrations, for pairs of collisions, in which not only $(\mathbf{v},\mathbf{u}) \rightarrow \mathbf{v}'$, but also $(\mathbf{v}',\mathbf{u}') \rightarrow \mathbf{v}''$. To work this out in detail is straightforward, though this lies beyond the scope of the present paper. In addition, there is a (neglected) t^4 term found in the next section.

Finally, as previously noted, hydrogen spectra are extremely collisionally narrowed, such that an expansion in terms of individually computed powers of t would seem pointless. In this case, it might be possible to use a model for the collisionally narrowed $C(\mathbf{v};t)$ for all $\mathbf{v}$, then for purposes of calculating a next iteration result, insert the model forms into (10) for use in the ratio $C(\mathbf{v}';t)/C(\mathbf{v};t)$. In this manner one can recover a once-refined result for $C(\mathbf{v};t)$ for all $\mathbf{v}$ and t. To the extent that the initial guess was reliable, the corrections within the first refinement result will indeed be small. This would then lead to correlation functions which can then be averaged over $\mathbf{v}$ leading to a refined expression for $C(t)$ which in turn can be used directly to obtain the line profile.

4. Speed Dependent Voigt Profile Effects

For some time now it has been known that the speed-dependence of internal coherence relaxation has had importance in determining the shape of spectral lines, shifting them away from the simple Voigt profile [1–3, 23]. Because this lies outside of the major thrust of the present paper we will only sketch the manner in which these effects can provide time-dependent terms in the correlation function $C(t)$. This, again, follows the development of Looney [30]. Beginning with the form of $C(\mathbf{v};t)$ leading to the voigt profile, one can make simple changes that will lead to the appropriate time dependences in the exponential decay rate for $C(\mathbf{v};t)$. Let us begin with the simple form of $C(\mathbf{v};t)$, modified so as to include velocity dependences of γ. Let $\gamma(v)$ depend upon the speed of the optically active molecule in the following manner:

$$\gamma(v) = \gamma_o + \left(\frac{d\gamma}{d(v^2)}\right)_N (v^2 - \langle v^2\rangle) + \cdots \tag{21}$$

as a general expression, $\langle v^2\rangle$ being the value for the mean squared speed, about which we will expand. Subscript N is used to remind us that this derivative is to be considered for constant number density. For present purposes we work within the quadratic approximation, for which we can write

$$\gamma(v) = \gamma_o + \gamma'(v_x^2 - \langle v_x^2\rangle + \cdots y, z) \tag{22}$$

with $\gamma' = (d\gamma/dv^2)_N$. The averages over velocity components are easily accomplished, ignoring, for the moment, the $\exp[-\gamma_o t]$ term. We begin with the average over v_x, using the Maxwell distribution, such that

$$C_x(t) = \sqrt{\frac{m}{2\pi k_B T}} \exp\left[-\frac{mv_x^2}{2k_B T} - \gamma'(v_x^2 - \langle v_x^2\rangle)t\right] \tag{23}$$

k_B being the Boltzmann constant and m the mass of the optically active molecule. We define the constant

$$Z = \frac{2\gamma' k_B T}{m} \tag{24}$$

for notational simplicity, so that $C_x(t)$ can be readily obtained, in the form

$$C_x(t) = (1 + Zt)^{-1/2} \exp[\gamma' \langle v_x^2\rangle t]. \tag{25}$$

By noting that $\langle v_x^2\rangle = k_B T/m$, one can find through expansion and subsequent identification of terms

$$\begin{aligned} C_x(t) &= \left(1 - \frac{1}{2}Zt + \frac{3}{8}Z^2t^2 - \frac{5}{16}Z^3t^3 + \cdots\right) \\ &\quad \times \left(1 + \frac{1}{2}Zt + \frac{1}{8}Z^2t^2 + \frac{1}{48}Z^3t^3 + \cdots\right) \\ &\cong \left(1 + \frac{1}{4}Z^2t^2 - \frac{1}{6}Z^3t^3\right) \end{aligned} \tag{26}$$

which is exact to terms in t^3, provided that mod $|Zt| < 1$. This will always be true for short enough times, and our assumption is that it will be possible to do this for any physically realistic times.

The same steps can be followed for the y-integration, as well. With the z integration, we begin with the same integral, but now with the Doppler (translational) phase factor, $\exp[ikv_z]$, leading directly to the result

$$\begin{aligned} C_z(t) &= \sqrt{\frac{m}{2\pi k_B T}} \exp\left[\frac{Zt}{2}\right] \\ &\quad \times \int dv_z \exp\left[-\frac{mv_z^2}{2k_B T}(1 + Zt) + ikv_z t\right] \\ &= (1 + Zt)^{-1/2} \exp\left[\frac{Zt}{2} - \frac{k_B T k^2 t^2}{2m(1 + Zt)}\right]. \end{aligned} \tag{27}$$

Within terms to order t^3, this is equivalent to the form

$$C_z(t) = \exp\left[-\left(\frac{k_B T k^2}{2m} - \frac{1}{4}Z^2\right)t^2 + \left(\frac{k_B T k^2 Z}{2m} - \frac{1}{2}Z^3\right)t^3\right]. \tag{28}$$

Note that Z is proportional to number density, so that the simple Doppler distribution will be altered (in width, e.g.) by terms quadratic in density, while the motional narrowing term will contain parts linear, and varying as the third power in density. While the change in the simple Doppler correlation function will probably be beyond detection, we will retain that term for reference, while dropping the Z^3 term. By now multiplying the x-, y- and z-results, and recovering the $\exp[-\gamma_o t]$ factor, we find

$$C_{\mathrm{SDVP}}(t) = \exp\left[-\gamma_o t - \left(\frac{k_B T k^2}{2m} - \frac{3Z^2}{4}\right)t^2 + \frac{k_B T k^2 Z}{2m}t^3\right]. \tag{29}$$

This represents the Voigt correlation function, whose width is supplemented the small (usually negligible) Z^2t^2 term and by a further exponential t^3 term. While γ', and therefore Z are presumably complex, the speed dependence of line shifts is thought to be minimal, because the increase in collision rate will be roughly matched by corresponding decreases in phase shifts, tending toward cancelation of the speed dependence. Therefore, we will assume Z to be real.

As described by Looney [30], the value of γ' can be inferred from the temperature dependence of γ, provided that it is known. To see this, note that

$$\gamma' = \left(\frac{d\gamma}{d(v^2)}\right)_N = \frac{dT}{d(v^2)}\left(\frac{d\gamma}{dT}\right)_N = \frac{m}{3k_B}\left(\frac{d\gamma}{dT}\right)_N. \tag{30}$$

This holds only if the perturbers are motionless (i.e., have infinite mass). For finite mass perturbers, however, the relative collision speeds will increase more rapidly with temperature, and m must be replaced by the reduced mass of the collision pair, with the result

$$\gamma' = \frac{mm_x}{3(m + m_x)k_B}\left(\frac{d\gamma}{dT}\right)_N, \tag{31}$$

with m_x being the mass of the perturbing molecule. This will obviously be most valuable if the temperature dependence of γ is known from separate measurements.

5. Conclusions

As a result of the above analysis the t^3 terms in the correlation function are given by the contributions coming from velocity-changing collisions (cf. (20)) together with the above SDVP effect, equation (29), giving as a final result

$$\beta = \frac{k_B T}{m} k^2 \left(X - Y + \frac{Z}{2} \right) \tag{32}$$

with X, Y, and Z being given by (15), (18), and (24). Each term is linear in perturber number density N.

To summarize, a formalism has been presented whereby one can find the relevant terms for the dipole-dipole correlation function needed to characterize the line shapes in the impact approximation for isolated (atomic or) molecular lines perturbed by foreign gases. Through standard techniques this formalism could be extended to a fully quantum description of the entirety of the collision problem treated here. In addition, one could treat the problem of line-mixing with neighboring transitions within the present formalism. For purposes of clarity, neither of these steps is presented here. The cubic time-dependent terms of the exponent describing the exponential decay of the correlation function have been explicitly found in terms of averages utilizing only equilibrium velocity distributions and the variously important terms of the perturber interaction with the optically active molecule. Although both "soft" and "hard" types of collisions occur for various impact parameters for almost every line, the present theory makes no fundamental distinction between these limits, and makes a seamless transition from one to the other type of behavior.

For the velocity changing t^3 effects there exist two competing influences: A line narrowing due to the fact that higher speed components tend to be reduced in collisions and a line broadening associated with collisional production of velocity components parallel to the optical propagation vector, derived from pre-collision components perpendicular to this direction. The two effects oppose one another, with the broadening being about two thirds of the narrowing. This means that the velocity-change broadening will not dominate the narrowing, but at the same time it is substantial. In addition, speed-dependent Voigt profile effects are active in giving rise to a further t^3 narrowing exponential term (presuming that the speed dependence of the ordinary Lorentz lineshape parameters shows an increase with increasing velocity, which is the standard case).

In hydrogen molecular spectra the coherence limiting effects are very small. Accordingly one can, at some pressures, see a pronounced line narrowing. One might approach the theoretical problem by using the best model form of $C(\mathbf{v}; t)$ (based upon a Dicke type approach), then compute $C(\mathbf{v}; t)$ using (10), with the ratio $C(\mathbf{v}; t')/C(\mathbf{v}'; t')$ replaced by the model result. $C(\mathbf{v}; t)$ will then show small correction terms, if the initial guess is close to being correct.

Appendix

In this development we wish to convert the expression

$$\begin{aligned} C(\mathbf{v}; t) = {} & \exp[-N\bar{v}\pi B^2 t + i\mathbf{k}\cdot\mathbf{v}t] \\ & + N\int_0^t dt' \exp[-N\bar{v}\pi B^2 t' + i\mathbf{k}\cdot\mathbf{v}t'] \\ & \times \int^B \int d\mathbf{b}\, d\mathbf{u} f(\mathbf{u})|\mathbf{v}-\mathbf{u}|S(\mathbf{v};\mathbf{b},\mathbf{u})C(\mathbf{v}';(t-t')) \end{aligned} \tag{A.1}$$

which was given as (9) into the form as shown in (10) of the text. We begin by defining a reduced correlation function:

$$D(\mathbf{v}; t) = C(\mathbf{v}; t)\exp[N\bar{v}\pi B^2 t - i\mathbf{k}\cdot\mathbf{v}t] \tag{A.2}$$

which satisfies

$$\begin{aligned} D(\mathbf{v}; t) = {} & 1 + N\int_0^t dt' \int^B \int d\mathbf{b}\, d\mathbf{u} f(\mathbf{u})|\mathbf{v}-\mathbf{u}|S(\mathbf{v};\mathbf{b},\mathbf{u}) \\ & \times \exp[-i\mathbf{k}\cdot(\mathbf{v}-\mathbf{v}')(t-t')]D(\mathbf{v}';(t-t')). \end{aligned} \tag{A.3}$$

It now simplifies things if one replaces $(t - t')$ by t' itself, for mathematical convenience, giving simply

$$\exp[-i\mathbf{k}\cdot(\mathbf{v}-\mathbf{v}')t']D(\mathbf{v}';t') \tag{A.4}$$

as the latter terms in (A.3). Now, differentiate $D(v; t)$ with respect to t, utilizing (A.3),

$$\begin{aligned} \frac{dD(\mathbf{v};t)}{dt} = {} & N\int^B \int d\mathbf{b}\, d\mathbf{u} f(\mathbf{u})|\mathbf{v}-\mathbf{u}|S(\mathbf{v};\mathbf{b},\mathbf{u}) \\ & \times \exp[-i\mathbf{k}\cdot(\mathbf{v}-\mathbf{v}')t]D(\mathbf{v}';t). \end{aligned} \tag{A.5}$$

Divide by $D(\mathbf{v}; t)$ itself, to obtain the logarithmic derivative, and noting the initial condition $D(\mathbf{v}; 0) = 1$, this can be integrated and exponentiated to the form

$$\begin{aligned} D(\mathbf{v}; t) = \exp\Bigg[& N\int_0^t dt' \int^B \int d\mathbf{b}\, d\mathbf{u} f(\mathbf{u})|\mathbf{v}-\mathbf{u}| \\ & \times S(\mathbf{v};\mathbf{b},\mathbf{u})\left(\frac{D(\mathbf{v}';t')}{D(\mathbf{v};t')}\right)\exp[-i\mathbf{k}\cdot(\mathbf{v}-\mathbf{v}')t']\Bigg]. \end{aligned} \tag{A.6}$$

Changing back to the corresponding equation in $C(v; t)$, we have

$$\begin{aligned} C(\mathbf{v}; t) = \exp\Bigg[& i\mathbf{k}\cdot\mathbf{v}t - N\bar{v}\pi B^2 t + N\int_0^t dt' \int^B \int d\mathbf{b}\, d\mathbf{u} \\ & \times f(\mathbf{u})|\mathbf{v}-\mathbf{u}|S(\mathbf{v};\mathbf{b},\mathbf{u})\left(\frac{C(\mathbf{v}';t')}{C(\mathbf{v};t')}\right)\Bigg]. \end{aligned} \tag{A.7}$$

It now looks as if the troublesome exponential $\exp[-N\bar{v}\pi B^2 t]$ still remains, but with $\bar{v}$ being the average relative speed of collision, we note that

$$\bar{v}\pi B^2 t = \int_0^t dt' \int_0^B \int d\mathbf{b}\, d\mathbf{u} f(\mathbf{u})|\mathbf{v}-\mathbf{u}| \tag{A.8}$$

itself, so that the final result

$$C(\mathbf{v};t) = \exp\left[i\mathbf{k}\cdot\mathbf{v}t - N\int_0^t dt' \iint d\mathbf{b}\, d\mathbf{u} f(\mathbf{u})|\mathbf{v}-\mathbf{u}| \times\left(1 - S(\mathbf{v};\mathbf{b},\mathbf{u})\left(\frac{C(\mathbf{v}';t')}{C(\mathbf{v};t')}\right)\right)\right] \tag{A.9}$$

is achieved, which is shown as (10) of the text. Importantly, the actual specification of B is no longer necessary with integration on all physically relevant $\mathbf{b}$ values being implied.

Acknowledgments

The author takes pleasure in acknowledging helpful conversations with R. Ciuryło, J. C. Lewis, J. P. Looney, and R. H. Tipping, and for help in manuscript preparation by A. Grugan.

References

[1] P. R. Berman, "Speed-dependent collisional width and shift parameters in spectral profiles," *Journal of Quantitative Spectroscopy and Radiative Transfer*, vol. 12, no. 9, pp. 1331–1342, 1972.

[2] J. Ward, J. Cooper, and E. W. Smith, "Correlation effects in the theory of combined doppler and pressure broadening-I. Classical theory," *Journal of Quantitative Spectroscopy and Radiative Transfer*, vol. 14, no. 7, pp. 555–590, 1974.

[3] I. Shannon, M. Harris, D. R. McHugh, and E. L. Lewis, "Low-pressure spectral line profiles: an analysis in terms of symmetric speed-dependent Voigt profiles," *Journal of Physics B*, vol. 19, no. 10, pp. 1409–1424, 1986.

[4] R. H. Dicke, "The effect of collisions upon the doppler width of spectral lines," *Physical Review*, vol. 89, no. 2, pp. 472–473, 1953.

[5] J.-M. Hartmann, C. Boulet, and D. Robert, *Collisional Effects on Molecular Spectra*, Elsevier, New York, NY, USA, 2008.

[6] M. Baranger, "Problem of overlapping lines in the theory of pressure broadening," *Physical Review*, vol. 111, no. 2, pp. 494–504, 1958.

[7] A. C. Kolb and H. Griem, "Theory of line broadening in multiplet spectra," *Physical Review*, vol. 111, no. 2, pp. 514–521, 1958.

[8] K. Shimoda, Ed., *High-Resolution Laser Spectroscopy*, Springer, Heidelberg, Germany, 1976.

[9] R. M. Herman and E. W. Weber, "Comprehensive theory for line broadening in high-resolution and nonlinear spectroscopies: application to the Na D lines," *Journal of Physics B*, vol. 16, no. 8, pp. 1323–1341, 1983.

[10] L. Galatry, "Simultaneous effect of doppler and foreign gas broadening on spectral lines," *Physical Review*, vol. 122, no. 4, pp. 1218–1223, 1961.

[11] P. W. Anderson and J. D. Talman, *Pressure Broadening of Spectral Lines at General Pressures*, Bell Telephone System Technical Publications, Monograph 3117, 1956.

[12] G. Traving, *Über die Theorie der Druckverbreiterung von Spectrallinien*, G. Braun, Karlsruhe, Germany, 1960.

[13] J. Szudy and W. E. Baylis, "Unified Franck-Condon treatment of pressure broadening of spectral lines," *Journal of Quantitative Spectroscopy and Radiative Transfer*, vol. 15, no. 7-8, pp. 641–668, 1975.

[14] J. Szudy and W. E. Baylis, "Asymmetry in pressure-broadened spectral lines," *Journal of Quantitative Spectroscopy and Radiative Transfer*, vol. 17, pp. 681–684, 1977.

[15] A. S. Pine, "Collisional narrowing of HF fundamental band spectral lines by Neon and Argon," *Journal of Molecular Spectroscopy*, vol. 82, pp. 435–448, 1980.

[16] A. S. Pine and J. P. Looney, "N_2 and air broadening in the fundamental bands of HF and HCl," *Journal of Molecular Spectroscopy*, vol. 122, no. 1, pp. 41–55, 1987.

[17] A. S. Pine and R. Ciurylo, "Multispectrum fits of Ar-broadened HF with a generalized asymmetric lineshape: effects of correlation, hardness, speed dependence, and collision duration," *Journal of Molecular Spectroscopy*, vol. 208, no. 2, pp. 180–187, 2001.

[18] R. Wehr, A. Vitcu, R. Ciuryło, F. Thibault, J. R. Drummond, and A. D. May, "Spectral line shape of the $P(2)$ transition in CO-Ar: uncorrelated ab initio calculation," *Physical Review A*, vol. 66, no. 6, Article ID 062502, 7 pages, 2002.

[19] R. Wehr, R. Ciuryło, A. Vitcu, F. Thibault, J. R. Drummond, and A. D. May, "Dicke-narrowed spectral line shapes of CO in Ar: experimental results and a revised interpretation," *Journal of Molecular Spectroscopy*, vol. 235, no. 1, pp. 54–68, 2006.

[20] J.-M. Colmont, B. Bakri, F. Rohart, et al., "Intercomparison between ozone-broadening parameters retrieved from millimetre-wave measurements by using different techniques," *Journal of Molecular Spectroscopy*, vol. 231, no. 2, pp. 171–187, 2005.

[21] F. Rohart, G. Włodarczak, J.-M. Colmont, G. Cazzoli, L. Dore, and C. Puzzarini, "Galatry versus speed-dependent Voigt profiles for millimeter lines of O_3 in collision with N_2 and O_2," *Journal of Molecular Spectroscopy*, vol. 251, no. 1-2, pp. 282–292, 2008.

[22] D. Lisak, J. T. Hodges, and R. Ciuryło, "Comparison of semiclassical line-shape models to rovibrational H_2O spectra measured by frequency-stabilized cavity ring-down spectroscopy," *Physical Review A*, vol. 73, no. 1, Article ID 012507, 13 pages, 2006.

[23] D. Priem, F. Rohart, J.-M. Colmont, G. Włodarczak, and J.-P. Bouanich, "Lineshape study of the $J = 3 \leftarrow 2$ rotational transition of CO perturbed by N_2 and O_2," *Journal of Molecular Structure*, vol. 517-518, pp. 435–454, 2000.

[24] R. Wehr, A. Vitcu, F. Thibault, J. R. Drummond, and A. D. May, "Collisional line shifting and broadening in the fundamental P-branch of CO in Ar between 214 and 324 K," *Journal of Molecular Spectroscopy*, vol. 235, no. 1, pp. 69–76, 2006.

[25] R. Wehr, A. Vitcu, F. Thibault, J. R. Drummond, and A. D. May, "Erratum to "Collisional line shifting and broadening in the fundamental P-branch of CO in Ar between 214 and 324 K" [J. Mol. Spectrosc. 235 (2006) 69–76]," *Journal of Molecular Spectroscopy*, vol. 237, no. 1, p. 126, 2006.

[26] R. L. Farrow, L. A. Rahn, G. O. Sitz, and G. J. Rosasco, "Observation of a speed-dependent collisional inhomogeneity in H_2 vibrational line profiles," *Physical Review Letters*, vol. 63, no. 7, pp. 746–749, 1989.

[27] F. Chaussard, R. Saint-Loup, H. Berger, et al., "Speed-dependent line profile: a test of a unified model from the Doppler to the collisional regime for molecule-molecule collisions," *Journal of Chemical Physics*, vol. 113, no. 12, pp. 4951–4956, 2000.

[28] S. G. Rautian and I. I. Sobel'man, "The effect of collisions on the Doppler broadening of spectral lines," *Soviet Physics Uspekhi*, vol. 9, pp. 701–716, 1967.

[29] R. M. Herman, "Toward a unified impact theory for everything concerning neutral species line shapes," in *CP559, Spectral Line Shapes: Volume 11, 15th ICSLS*, J. Seidel, Ed., pp. 237–243, American Institute of Physics, 2001.

[30] J. P. Looney, *Comprehensive theory for the broadening, shifting and narrowing of HF and HCl fundamental band absorption profiles*, Ph.D. thesis, The Pennsylvania State University, 1987.

[31] Priem, et al., loc. cit.

[32] S. Green and J. Hutson, "Spectral line shape parameters for HF in a bath of Ar are accurately predicted by a potential inferred from spectra of the van der Waals dimer," *The Journal of Chemical Physics*, vol. 100, no. 2, pp. 891–898, 1994.

[33] P. W. Anderson, "Pressure broadening in the microwave and infra-red regions," *Physical Review*, vol. 76, no. 5, pp. 647–661, 1949.

[34] C. J. Tsao and B. Curnutte, "Line-widths of pressure-broadened spectral lines," *Journal of Quantitative Spectroscopy and Radiative Transfer*, vol. 2, no. 1, pp. 41–91, 1962.

[35] J. Jarecki and R. M. Herman, "Widths and shifts of HF vibration-rotation absorption lines induced by pressure of rare gases," *Journal of Quantitative Spectroscopy and Radiative Transfer*, vol. 15, no. 9, pp. 707–726, 1975.

[36] J. S. Murphy and J. E. Boggs, "Collision broadening of rotational absorption lines. I. Theoretical formulation," *The Journal of Chemical Physics*, vol. 47, no. 2, pp. 691–702, 1967.

[37] R. M. Herman, "Impact theory of the noble-gas-broadened HCl vibration-rotation lines," *Journal of Quantitative Spectroscopy and Radiative Transfer*, vol. 3, p. 443, 1963.

[38] R. H. Tipping and R. M. Herman, "Impact theory for the noble gas pressure-induced HCl vibration-rotation and pure rotation line widths-I," *Journal of Quantitative Spectroscopy and Radiative Transfer*, vol. 10, no. 8, pp. 881–896, 1970.

[39] R. M. Herman and R. H. Tipping, "Impact theory for the noble gas pressure-induced HCl vibration-rotation and pure rotation line shifts-II," *Journal of Quantitative Spectroscopy and Radiative Transfer*, vol. 10, no. 8, pp. 897–908, 1970.

Hindawi Publishing Corporation
International Journal of Spectroscopy
Volume 2010, Article ID 705896, 5 pages
doi:10.1155/2010/705896

Research Article

Far Wing Asymmetry of Rotational Raman Lines in Hydrogen

Magnus Gustafsson

Department of Chemistry, University of Gothenburg, SE 412 96 Gothenburg, Sweden

Correspondence should be addressed to Magnus Gustafsson, magngu@chem.gu.se

Received 22 April 2009; Accepted 8 July 2009

Academic Editor: Chantal Stehle

Depolarized Raman spectra of compressed hydrogen gas have been computed rigorously previously for 36 K and 50 K (Gustafsson et al. (2009)). The far wings of the rotational lines show asymmetry that goes beyond that expected from the theory for intracollisional interference and Fano line shapes. Here we analyze the $S_0(0)$ line for pure hydrogen at 36 K in detail. The added asymmetry stems partly from a shape resonance which adds significant intensity to the higher frequency side of the line profile. The influence of the threshold energy for the rotational transition accounts for the remainder.

1. Introduction

The depolarized Raman spectrum of hydrogen shows a number of spectral lines corresponding to rotational transitions with $\Delta j_n = 0, \pm 2$ in hydrogen molecule number n [1]. These spectral features are broadened due to collisions between the molecules and the corresponding width is approximately inversely proportional to the time between the collisions. The transitions with $\Delta j_n = 2$ give rise to the so-called S-lines which are located on the Stokes side of the spectrum where the energy of the scattered photon is lower than that of the incident photon. The incident light may also scatter from pairs of hydrogen molecules in an *interaction-induced* Raman process [2, 3]. The pairs are transient complexes with a lifetime corresponding to the duration of the H_2–H_2 collisions. In gases under pressures of less than a few hundred atmospheres the time between collisions is typically much longer than the duration of the collisions. This implies that the spectral features due to interaction-induced light scattering are much broader than the pressure-broadened S-lines.

At high gas pressures, collisionally interacting triples of molecules will also scatter the light. In general the Raman intensity may be expressed as a virial expansion [4] in powers of the gas density, ρ, with the terms proportional to ρ, ρ^2, ρ^3, and so forth, where the second and third term correspond to binary and ternary collisions, respectively. The terms which is linear in the density will come into play if broadening mechanisms other than collisions dominate, such as Doppler or natural line broadening. Here, the temperature is low enough that Doppler broadening can be ignored as well as the natural line width which is extremely small for rotational states. Furthermore, in this work I consider the far wings of the S-lines with frequency shifts on the order of 20 cm^{-1} from the line centers. Small detunings, that is, frequencies approaching the line center, imply that a higher number of subsequent collisions have to be taken into account, and a higher number of terms in the virial expansion have to be included. Detunings of about 20 cm^{-1} are large enough so that single binary (H_2–H_2) collisions alone contribute to the Raman intensity. The density-squared component of the intensity is also what has been extracted in the experiments that are relevant for this work [5].

The impact approximation [6, 7] for collisional broadening considers single or several subsequent collisions and can thus describe spectral lines at arbitrarily small detuning. It does not, however, fully include the effects from mixing of molecular states, such as the H_2 rotational levels, j_n. The spectra in this work are computed with a close-coupling scheme [8, 9] for the diatom-diatom scattering including the angular momentum couplings exactly [10]. The method is an extension of the radiative close-coupling theory [11] and it is valid far from the line centers and for asymptotically forbidden transitions. Thus it provides a correct description of the wings of the monomer-allowed spectral lines, where only isolated two-body collisions need to be considered.

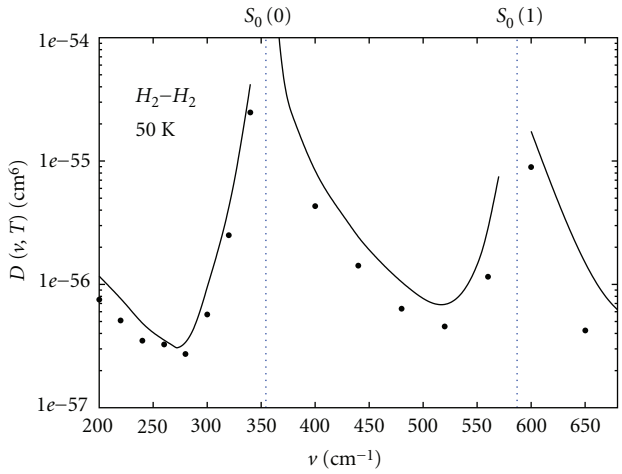

FIGURE 1: The $S_0(0)$ and $S_0(1)$ lines of the depolarized Raman spectrum of hydrogen (65% para-H_2, 35% ortho-H_2) at 50 K. The frequency of the rotational transitions are indicated with vertical blue dotted lines. The solid curves represent the computed data [10] and the filled circles a measurement [5].

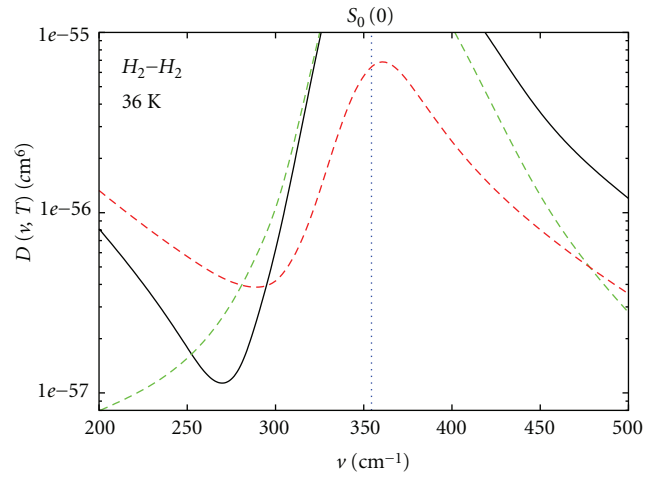

FIGURE 2: The $S_0(0)$ line of the depolarized Raman spectrum of pure hydrogen at 36 K. The frequency of the rotational transition is indicated with the vertical blue dotted line. The solid curve represents the computed data [10]. Computed data where only the permanent polarizability is included is indicated with a green dashed curve. Similarly, the spectrum due only to collision-induced polarizability is indicated with a red dashed curve.

Theory of far wings has been reviewed recently in chapter V of the book by Hartmann et al. [12]. A perturbative theoretical treatment which includes intracollisional interference was developed by [13] and applied to H_2–H_2 light scattering. Furthermore, a nonperturbative model based on the sudden description of the collisions [14, 15] has been applied to the depolarized Raman spectrum of nitrogen. The calculation in [10], which produced the theoretical data analysed in this work, does not rely on either of those approximations. It is an exact description of the collisional dynamics when vibrational and higher energy modes may be ignored and it represents the most accurate computation of the density-squared component of the hydrogen Raman spectrum.

2. Computed Spectra

The details of the calculation of the depolarized light scattering in compressed hydrogen gas may be found in [10]. Single binary collisions were taken into account, allowing for evaluation of the virial term of the Raman cross section which is proportional to the density squared. The close-coupling scattering calculations were carried out on the potential surface by Schäfer and Köhler [16] using the static collision-induced polarizability surface from [17]. It should be noted that the latter differs from the true dynamic polarizability by an amount which is thought to be several percent [2, 3].

The depolarized Raman intensity at a fixed temperature is evaluated through

$$D(\nu, T) = \lambda_0^3 \sum_{j_{1i} j_{2i}} P_{j_{1i}} P_{j_{2i}} \int_0^{E_{\max}} e^{-E/kT} D_{j_{1i} j_{2i}}(\nu, E) dE, \quad (1)$$

with the energy-dependent intensity defined by

$$D_{j_{1i} j_{2i}}(\nu, E) = \frac{2c\nu_s^2}{\phi_0 \phi_s h} \sum_{i^*} \sum_f \left| S_i^f(E) \right|^2, \quad (2)$$

where the scattering matrix element $S_i^f(E)$ for initial and final angular momentum states i and f, corresponding to incident and scattered photons with frequencies ν_0 and ν_s, respectively. λ_0 is the thermal de Broglie wave length, ϕ_0 and ϕ_s are the incident and scattered photon fluxes, respectively, in units s^{-1} cm^{-2} and $P_j(T)$ is the rotational population for H_2 at temperature T. The summation over i^* indicates all initial angular momenta except for j_{1i} and j_{2i}. It has been verified that an upper integration limit of $E_{\max} = 13\,kT$ provides convergence in (1).

Figure 1 shows the Raman spectrum at 50 K which is dominated by the wings of the $S(0)$ and $S(1)$ lines, except for at $\nu < 270$ cm^{-2} where the purely translational collision-induced band appears. The frequency shift $\nu = \nu_0 - \nu_s$ is positive for Stokes scattering. Experimental Raman intensities are also shown and the agreement of the line shapes is satisfactory. Considerable difficulty in the ab initio calculations of the potential and polarizability surfaces should be taken into account. Due to the low temperature only two S lines appear in the spectrum; all the para- and ortho-hydrogen molecules are in their lowest rotational states 0 and 1, respectively.

In Figure 2 the theoretical result for pure parahydrogen at 36 K is presented. The results when permanent and collision-induced polarizabilities (one at the time) are artificially turned off are also displayed to aid the analysis of the asymmetric broadening. There is strong destructive interference between the permanent and collision-induced components on the low frequency side of the $S_0(0)$ transition; inclusion

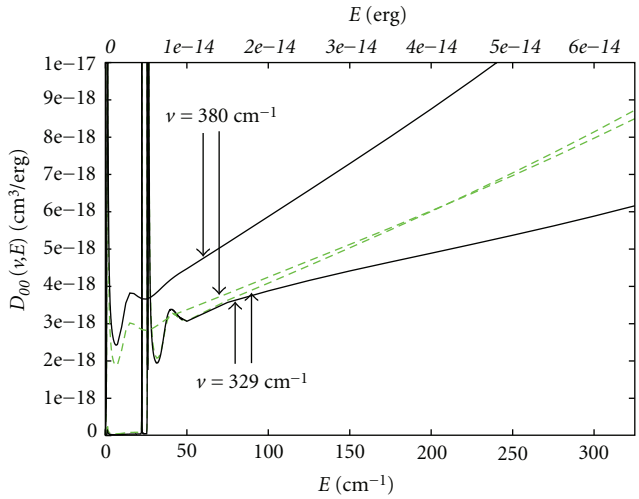

Figure 3: The light scattering intensity versus collision energy for frequency shifts of 329 cm^{-1} and 380 cm^{-1}. The result where the collision-induced part is excluded is shown with green dashed lines.

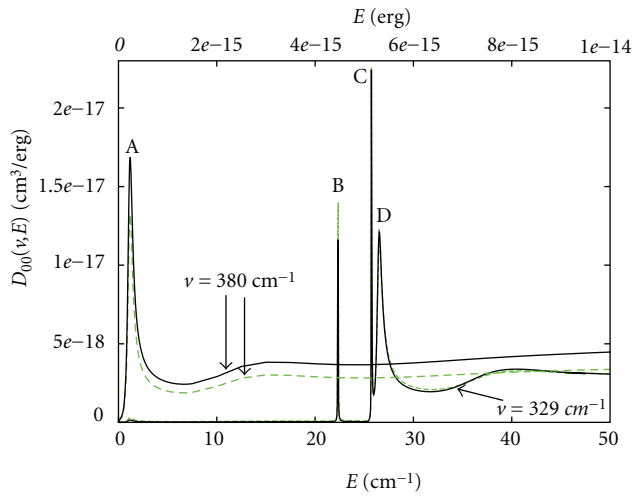

Figure 4: Same as in Figure 3 but for a smaller energy range. For 380 cm^{-1} there is a shape resonance due to $(j_1, j_2, l, J) = (0, 0, 2, 2)$ which is marked with an A. For 329 cm^{-1} there is structure due to a predissociating state $(j_1, j_2, l, J) = (0, 2, 0, 2)$ (B) and shape resonances on the $(j_1, j_2) = (0, 2)$ potential (C and D).

of both components gives a lower intensity than each of them alone around 280 cm^{-1}. The high frequency side, on the other hand, shows an equally strong constructive interference.

3. Rotational Line Shapes

It is helpful for the line shape analysis to briefly review the absorption spectroscopy analogue to the process at hand. The HD molecule has a tiny permanent dipole moment [18] and its infrared spectrum has been investigated in great detail both experimentally [19, 20] and theoretically [21–23]. For example, in the spectrum of HD molecules in a helium bath it has been established that an interference of the HD dipole with the interaction-induced HD–He dipole gives rise-to-so-called Fano line profiles for the R and P transitions. The low density limit of the Fano line shape has a symmetric Lorentzian term and an antisymmetric interference term [24]. It appears that the mechanism should be the same in a Raman spectrum when a permanent and an interaction-induced polarizability interfere.

In the pioneering theoretical work on the depolarized Raman line shapes in hydrogen Borysov and Moraldi [13, 25] assumed a three component contribution to the intensity: a pressure broadened allowed line described by a Lorentzian, a collision-induced quasicontinuum, and the interference of those two. For the first of those contributions the impact approximation predicts a pressure-broadened symmetric line shape described by a Lorentzian. If the collision-induced polarizability is removed from the calculation of the spectrum such a line shape is expected. The dashed (green) curve in Figure 2 shows our theoretical result for the allowed S-line which is clearly not symmetric. Intracollisional interference accounts for some of the added asymmetry when the collision-induced polarizability is included in the calculation, that is, when the solid black curve deviates from the sum of the dashed red and green curves. The asymmetry that is observed when only the permanent polarizability is included must, however, come about through a different mechanism.

4. Analysis of $D_{oo}(\nu, E)$

In the following analysis I will consider the case of pure parahydrogen with the spectrum presented in Figure 2. It should be noted that, due to the low temperature, all H_2-molecules are initially in their rotational ground state, j_n=0. The Raman intensity versus collision energy, D_{00}, which is given in (2) is shown for two frequency shifts in Figure 3 over the whole energy interval required for an accurate evaluation of the Boltzmann average in (1). The two frequency shifts, 329 and 380 cm^{-1}, were chosen so that they are positioned roughly symmetrically relative to the $S_0(0)$ transition at 354.4 cm^{-1}. The allowed contribution to the intensity is shown with dashed green curves and those virtually coincide for 329 and 380 cm^{-1} above $E \sim 50\ cm^{-1}$. One may thus conclude that it is the low energy behaviour that introduces the asymmetry that goes beyond the intracollisional interference effect, which is displayed as the difference between the solid black curves in Figure 3.

Figure 4 shows the same intensities for a low energy range. For the frequency shift $\nu = 380\ cm^{-1}$ a feature (A) around $E = 1.2\ cm^{-1}$ is now clearly visible. A computation of the cross section for different total angular momenta J (not reported here) shows that the partial wave with $J = l = 2$ alone gives rise to the feature. Thus it is consistent with a shape resonance on the $l = 2$ effective potential

$$V_{\text{eff}}(R) = V_{000}(R) + \frac{\hbar^2 l(l+1)}{2mR^2}, \tag{3}$$

Table 1: Raman intensity D at $\nu = 380\,\text{cm}^{-1}$ and $T = 36\,\text{K}$ evaluated with three different upper energy limits, $E_{\max}$, in the integral of (1).

$E_{\max}$ [erg]	$E_{\max}$ [cm^{-1}]	$E_{\max}/kT$	$D(\nu, T)$ [cm^6]	fraction [%]
9.93×10^{-16}	5	0.200	0.103×10^{-54}	21.5
4.965×10^{-15}	25	1.00	0.265×10^{-54}	55.3
6.4545×10^{-14}	325	13.0	0.479×10^{-54}	100

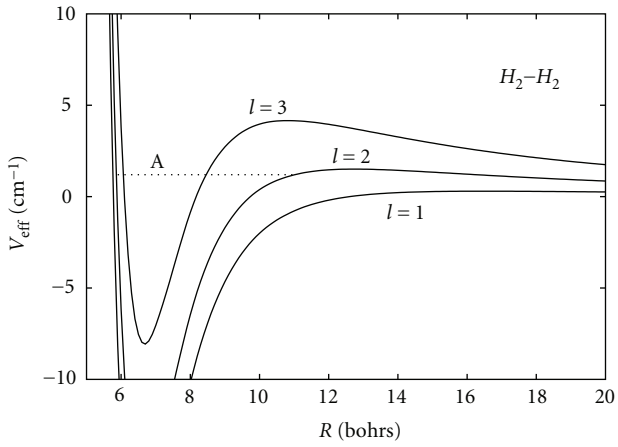

Figure 5: The effective potential for $l = 1, 2, 3$ (isotropic component only). The quasi-bound state or shape resonance energy corresponding to the the feature around $1.2\,\text{cm}^{-1}$ in Figure 4 is indicated with the dotted line.

which is plotted for three values of l in Figure 5. l is the orbital angular momentum corresponding to the classical impact parameter. The reduced mass of the H_2–H_2 pair is indicated with m and the distance between the two diatoms with R. The anisotropic components ($V_{\gamma_1\gamma_2\gamma}(R)$ with not all indices being zero) of the potential are not shown in Figure 5 but they are included in the calculations of the data shown in Figures 1 through 4.

For the $329\,\text{cm}^{-1}$ frequency shift the $S_0(0)$ threshold lies at a collision energy $E = 25.4\,\text{cm}^{-1}$. A feature which is due to a predissociating state (B) is clearly discernible about $3\,\text{cm}^{-1}$ below that threshold in Figure 4, consistent with the value for the bound state $(j_1, j_2, l, J) = (0, 2, 0, 2)$ which is computed with the same potential in [26, 27] Immediately above the threshold two shape resonances (C, D) corresponding to the final rotational state's effective potential are visible.

To investigate the contribution to the depolarized Raman intensity at $380\,\text{cm}^{-1}$ I have carried out test calculations using different upper limits $E_{\max}$ in the energy integral, (1). The corresponding intensities and their fraction of the total are given in Table 1. It turns out that roughly a fifth of the total intensity at that frequency is contained in the feature which corresponds to the shape resonance labeled with an A in Figures 4 and 5. Furthermore, more than half the intensity comes from energies lower than $25\,\text{cm}^{-1}$ which is close to the $S_0(0)$ threshold for $329\,\text{cm}^{-1}$.

5. Conclusion

The depolarized Raman spectra at low temperatures has been analysed. Comparison with an experiment carried out at 50 K [5] verifies satisfactory agreement between the measured and computed spectra. The highly asymmetric $S_0(0)$ line profile at 36 K has been investigated in great detail. The conclusion is that intracollisional interference accounts only for some of the observed asymmetry. The rest stems from the low energy behaviour of the Raman intensity. For example, there is a shape resonance feature which contributes significantly to the intensity for positive detunings ($\nu > 354.4\,\text{cm}^{-1}$).

HD–He with its very shallow potential well, is less likely to show shape resonance features. This is a possible explanation for that the intra-collisional interference theory and the Fano line shape is so successful in describing the infrared spectrum of HD in a He bath [20]. Also, since the dipole of HD is so weak, the total intensities of the allowed spectral lines are small. Previous studies of the HD line shapes focused on the regions a few cm^{-1} from the corresponding transition, compared with $\sim 25\,\text{cm}^{-1} \approx kT$ which are considered here. Thus one expects a smaller role played by threshold effects like that illustrated by comparing the intensities for frequency shifts 329 and $380\,\text{cm}^{-1}$ in Figure 4.

Calculations of low-temperature collision-induced and collision-broadened spectroscopic processes appear to be rather challenging due to resonance features in the cross section. Other methods to handle these are desired and a scheme based on the Breit-Wigner theory [28] similar to that worked out by Bennett et al. [29] for radiative association would likely be useful.

It should also be noted that shape resonances depend strongly on the details of the potential energy surface. This has been investigated in detail for radiative association [30]. The principal aim in this work is to study the mechanisms rather than evaluating accurate light scattering intensity. If high accuracy is needed one should make sure to use the most accurate potential available.

References

[1] B. J. Berne and R. Pecora, *Dynamic Light Scattering*, John Wiley & Sons, New York, NY, USA, 1976.

[2] L. Frommhold, "Collision-induced scattering of light and the diatom polarizabilities," in *Advances in Chemical Physics*, I. Prigogine and S. Rice, Eds., vol. 46, pp. 1–72, John Wiley & Sons, New York, NY, USA, 1981.

[3] M. H. Proffitt, J. W. Keto, and L. Frommhold, "Collision-induced Raman spectra and diatom polarizabilities of the rare gases—an update," *Canadian Journal of Physics*, vol. 59, no. 10, pp. 1459–1474, 1981.

[4] J. van Kranendonk, "Theory of induced infra-red absorption," *Physica*, vol. 23, no. 6–10, pp. 825–837, 1957.

[5] U. Bafile, L. Ulivi, M. Zoppi, F. Barocchi, M. Moraldi, and A. Borysow, "Depolarized-light-scattering spectrum from gaseous hydrogen at 50 K: the density-squared component," *Physical Review A*, vol. 42, no. 11, pp. 6916–6919, 1990.

[6] M. Baranger, "General impact theory of pressure broadening," *Physical Review*, vol. 112, no. 3, pp. 855–865, 1958.

[7] U. Fano, "Pressure broadening as a prototype of relaxation," *Physical Review*, vol. 131, no. 1, pp. 259–268, 1963.

[8] A. M. Arthurs and A. Dalgarno, "The theory of scattering by a rigid rotator," *Proceedings of the Royal Society of London. Series A*, vol. 256, p. 540, 1960.

[9] S. Green, "Rotational excitation in H_2-H_2 collisions: close-coupling calculations," *The Journal of Chemical Physics*, vol. 62, pp. 2271–2277, 1975.

[10] M. Gustafsson, L. Frommhold, X. Li, and K. L. C. Hunt, "Roto-translational Raman spectra of pairs of hydrogen molecules from first principles," *Journal of Chemical Physics*, vol. 130, no. 16, Article ID 164314, 9 pages, 2009.

[11] P. S. Julienne, "Nonadiabatic theory of collision-broadened atomic line profiles," *Physical Review A*, vol. 26, no. 6, pp. 3299–3317, 1982.

[12] J.-M. Hartmann, C. Boulet, and D. Robert, *Collisional Effects on Molecular Spectra*, Elsevier, Amsterdam, The Netherlands, 2008.

[13] A. Borysow and M. Moraldi, "Rototranslational Raman scattering in hydrogen," *Physical Review A*, vol. 40, no. 3, pp. 1251–1261, 1989.

[14] A. P. Kouzov, "Rotational relaxation matrix for fast non-Markovian collisions," *Physical Review A*, vol. 60, no. 4, pp. 2931–2939, 1999.

[15] L. Bonamy and J. V. Buldyreva, "Non-Markovian far-wing rotational Raman spectrum from translational modeling," *Physical Review A*, vol. 63, no. 1, Article ID 012715, 7 pages, 2001.

[16] J. Schäfer and W. E. Köhler, "Low-temperature second virial coefficient of p-H_2 gas obtained from quantum mechanical pair correlation functions," *Zeitschrift für Physik D*, vol. 13, p. 217, 1989.

[17] X. Li, C. Ahuja, J. F. Harrison, and K. L. C. Hunt, "The collision-induced polarizability of a pair of hydrogen molecules," *Journal of Chemical Physics*, vol. 126, no. 21, Article ID 214302, 14 pages, 2007.

[18] W. R. Thorson, J. H. Choi, and S. K. Knudson, "Novel theory of the HD dipole moment. II. Computations," *Physical Review A*, vol. 31, no. 1, pp. 34–42, 1985.

[19] A. R. W. McKellar, "Intensities and the Fano line shape in the infrared spectrum of HD," *Canadian Journal of Physics*, vol. 51, no. 4, pp. 389–397, 1973.

[20] A. R. W. McKellar and N. H. Rich, "Interference effects in the spectrum of HD: II. The fundamental band for HD-rare gas mixtures," *Canadian Journal of Physics*, vol. 62, no. 12, pp. 1665–1672, 1984.

[21] P. G. Drakopoulos and G. C. Tabisz, "Far-infrared rotational spectrum of HD: line shape, dipole moment, and collisional interference," *Physical Review A*, vol. 36, no. 12, pp. 5556–5565, 1987.

[22] R. M. Herman and J. C. Lewis, "Scalar collisional interference parameters for the HD $R_1(0)$ and $R_1(1)$ lines in mixtures with He," in *Spectral Line Shapes 11*, J. Seidel, Ed., vol. 559 of *AIP Conference Proceedings*, pp. 397–399, The American Institute of Physics, New York, NY, USA, 2000.

[23] M. Gustafsson and L. Frommhold, "The HD-He complex: interaction-induced dipole surface and infrared absorption spectra," *Journal of Chemical Physics*, vol. 115, no. 12, pp. 5427–5432, 2001.

[24] M. Gustafsson and L. Frommhold, "Intracollisional interference of R lines of HD in mixtures of deuterium hydride and helium gas," *Physical Review A*, vol. 63, no. 5, Article ID 052514, 6 pages, 2001.

[25] A. Borysow and M. Moraldi, "Effects of the intermolecular interaction on the depolarized rototranslational Raman spectra of hydrogen," *Physical Review A*, vol. 48, no. 4, pp. 3036–3046, 1993.

[26] J. Schäfer and A. R. W. McKellar, "Faint features of the rotational $S_0(0)$ and $S_0(1)$ transitions of H_2: a comparison of calculations and measurements at 77 K," *Zeitschrift für Physik D*, vol. 15, p. 51, 1990.

[27] J. Schäfer and A. R. W. McKellar, "Erratum: Faint features of the rotational $S_0(0)$ and $S_0(1)$ transitions of H_2," *Zeitschrift für Physik D*, vol. 17, no. 3, p. 231, 1990.

[28] G. Breit and E. Wigner, "Capture of slow neutrons," *Physical Review*, vol. 49, no. 7, pp. 519–531, 1936.

[29] O. J. Bennett, A. S. Dickinson, T. Leininger, and F. X. Gada, "Radiative association in Li+H revisited: the role of quasi-bound states," *Monthly Notices of the Royal Astronomical Society*, vol. 341, no. 1, pp. 361–368, 2003.

[30] M. Jurek, V. Spirko, and W. P. Kraemer, "Ab initio determination of the rate coefficient for radiative association of He(^{1}S) + H^+," *Chemical Physics*, vol. 193, no. 3, pp. 287–296, 1995.

Hindawi Publishing Corporation
International Journal of Spectroscopy
Volume 2010, Article ID 936385, 4 pages
doi:10.1155/2010/936385

Research Article

Laser-Induced Optical Breakdown in Methane: Diagnostic Using H-Gamma Line Broadening

Christian G. Parigger[1] and Eugene Oks[2]

[1] *Center for Laser Applications, The University of Tennessee Space Institute, 411 B.H. Goethert Parkway, Tullahoma, TN 37388, USA*
[2] *206 Allison Laboratory, Department of Physics, Auburn University, Auburn, AL 36849, USA*

Correspondence should be addressed to Christian G. Parigger, cparigge@utsi.edu

Received 6 April 2009; Accepted 8 June 2009

Recommended by Elisabeth Dalimier

Measurements and analysis are reported of Stark-broadened profiles of the H-gamma line emitted from plasma formed by Laser-Induced Optical Breakdown (LIOB) in a pulsed methane flow. Electron densities N_e are deduced for 18 instants of time in the range between 0.4 and 2.1 microseconds after LIOB and for 2 different gas pressures. The obtained values of N_e are in a good agreement with the corresponding values found previously from Stark-broadened profiles of the H-alpha and H-beta lines.

1. Introduction

Plasmas formed by a Laser-Induced Optical Breakdown (LIOB) in gases can be diagnosed using the Stark broadening of hydrogen lines. In papers [1, 2], the LIOB was studied in gaseous hydrogen, and the plasmas were diagnosed using H-alpha line in [1] and H-beta line in [2].

In the latest paper [3], the LIOB was studied in a pulsed methane flow; the plasma was diagnosed using time-resolved measurements of profiles of H-alpha, H-beta, and H-gamma-lines. However, in [3] the electron density was deduced from the Stark broadening of only H-alpha and H-beta lines, while the measured widths of the H-gamma line have not been analyzed.

In the present paper we analyze the widths of the H-gamma line measured in [3]. For 18 instants of time in the range between 0.4 and 2.1 μs after the LIOB and for 2 different gas pressures, we deduce the electron density N_e from the Stark broadening of the H-gamma line and compare the results with the corresponding values of N_e obtained from the H-alpha and H-beta lines.

2. Experimental Results

The time-resolved measurements of LIOB comprised typical experimental arrangements for laser-induced breakdown spectroscopy (LIBS): nominal nanosecond Q-switched laser (8 ns, 75 mJ per pulse infrared 1064 nm radiation from a model Continuum YG680-10 Nd:YAG laser), spectrometer (1/2 m model 500 SpectraPro Acton Research Corporation) and intensified linear diode array (model 1460 Princeton Applied Research detector/controller optical multichannel analyzer). The captured time-resolved data, averaged over 100 individual LIOB events, were detector-noise/background corrected, wavelength and detector sensitivity calibrated. Further details of the experimental procedures are summarized in [3].

Individual profiles of the Balmer series lines H-alpha, H-beta, and H-gamma were measured subsequent to optical breakdown. Comparison of the recorded intensities of these lines allows one, in principle, to infer electron temperature, T_e, provided that reasonable complete profiles are recorded. Typical for our LIOB measurements however are incomplete H-beta and H-gamma line profiles due to significant contribution of background radiation early in the methane breakdown, high electron number density, N_e, early in the plasma decay followed by occurrence of molecular spectra that overlap Balmer series lines, particularly from C_2.

Temperature estimates are inferred by using the relative signal-strengths of the three line profiles H-alpha, H-beta, and H-gamma, although several errors in determining T_e are noted. For example, determination of background radiation

Table 1: Measured H-alpha widths.

t_{delay} [μs]	2.7×10^5 Pa: width [nm]	6.5×10^5 Pa: width [nm]
0.4	2.8 ± 0.3	2.7 ± 0.3
0.5	2.4 ± 0.3	2.3 ± 0.3
0.6	2.1 ± 0.3	2.1 ± 0.3
0.7	1.9 ± 0.2	1.9 ± 0.2
0.8	1.7 ± 0.2	1.7 ± 0.2
0.9	1.6 ± 0.2	1.5 ± 0.2
1.0	1.4 ± 0.2	1.4 ± 0.2
1.1	1.3 ± 0.2	1.3 ± 0.2
1.2	1.2 ± 0.1	1.2 ± 0.2
1.3	1.1 ± 0.1	1.1 ± 0.1
1.4	1.0 ± 0.1	1.0 ± 0.1
1.5	1.0 ± 0.1	0.92 ± 0.1
1.6	0.89 ± 0.1	0.87 ± 0.1
1.7	0.86 ± 0.1	0.78 ± 0.1
1.8	0.79 ± 0.1	0.77 ± 0.1
1.9	0.77 ± 0.1	0.69 ± 0.1
2.0	0.73 ± 0.1	0.67 ± 0.1
2.1	0.70 ± 0.1	0.61 ± 0.1

Table 2: Measured H-beta widths.

t_{delay} [μs]	2.7×10^5 Pa: width [nm]	6.5×10^5 Pa: width [nm]
0.4	10.0 ± 0.9	10.0 ± 0.5
0.5	9.0 ± 0.8	8.7 ± 0.5
0.6	8.1 ± 0.7	7.8 ± 0.5
0.7	7.4 ± 0.5	7.3 ± 0.4
0.8	6.8 ± 0.4	6.5 ± 0.4
0.9	6.3 ± 0.4	5.9 ± 0.4
1.0	5.9 ± 0.4	5.4 ± 0.4
1.1	5.3 ± 0.4	5.1 ± 0.3
1.2	5.0 ± 0.3	4.8 ± 0.3
1.3	4.7 ± 0.3	4.5 ± 0.3
1.4	4.4 ± 0.3	4.1 ± 0.3
1.5	4.1 ± 0.3	3.9 ± 0.3
1.6	3.9 ± 0.3	3.7 ± 0.2
1.7	3.8 ± 0.3	3.5 ± 0.2
1.8	3.6 ± 0.2	3.3 ± 0.2
1.9	3.3 ± 0.2	3.1 ± 0.2
2.0	3.1 ± 0.2	2.9 ± 0.2
2.1	2.9 ± 0.2	2.8 ± 0.2

Table 3: Measured H-gamma widths.

t_{delay} [μs]	2.7×10^5 Pa: width [nm]	6.5×10^5 Pa: width [nm]
0.4	11.0 ± 2.0	10.4 ± 2.0
0.5	10.7 ± 2.0	9.5 ± 2.0
0.6	8.7 ± 1.5	8.6 ± 1.5
0.7	8.1 ± 1.5	7.8 ± 1.5
0.8	7.6 ± 1.5	6.7 ± 1.5
0.9	6.7 ± 1.5	6.3 ± 1.5
1.0	6.2 ± 1.5	6.2 ± 1.5
1.1	6.0 ± 1.0	5.8 ± 1.0
1.2	5.8 ± 1.0	5.5 ± 1.0
1.3	5.6 ± 1.0	5.4 ± 1.0
1.4	5.3 ± 1.0	5.1 ± 1.0
1.5	5.2 ± 1.0	5.1 ± 1.0
1.6	5.0 ± 1.0	4.7 ± 1.0
1.7	5.0 ± 1.0	5.0 ± 1.0
1.8	5.0 ± 1.0	4.6 ± 1.0
1.9	5.0 ± 1.0	4.4 ± 1.0
2.0	4.7 ± 1.0	3.6 ± 1.0
2.1	4.6 ± 1.0	3.6 ± 1.0

at a particular time delay from LIOB, or application of sensitivity and wavelength calibrations, or comparison of line-profiles from separate 100-event averages recorded for only one particular Balmer line at a time.

The results for the inferred T_e are in the 10 000 K (time delay 2.1 μs) to 20 000 K (time delay of 0.4 μs) range, using the area of the incomplete H-beta and H-gamma lines and the area of the H-alpha line in constructing Boltzmann plots, analogous as discussed in [1]. For both gas pressures of 2.7×10^5 Pa and 6.5×10^5 Pa, almost identical results are found for T_e. When extending the curve fitting beyond the measured spectral windows used for the three lines, and using the area of these extended profiles, typically 50% higher T_e is found: these temperatures constitute an upper limit of 15 000 K and 30 000 K for time delays of 2.1 μs and 0.4 μs, respectively, with similar results obtained for both pressures.

Tables 1, 2, and 3 show measured FWHM of the H-alpha, H-beta, and H-gamma lines, respectively, for two different gas pressures: 2.7×10^5 Pa and 6.5×10^5 Pa. The data are presented in tabular form for different time delays, t_{delay}, from LIOB. The experimental error bars indicate the estimated total error of determining the FWHM line widths for the Balmer series lines.

3. Analysis

The combined contribution to the FWHM of the instrumental and Doppler broadening (as well as of the fine structure) is negligibly small compared to the measured widths. For example, for the H-gamma line those combined contributions do not exceed 0.14 nm for $t_{delay} = 0.4\,\mu$s, when the experimental FWHM is at least 10.4 nm, and do not exceed 0.11 nm for $t_{delay} = 2.1\,\mu$s, when the experimental FWHM is at least 3.6 nm. A similar situation is for the H-beta and H-alpha lines—except for few largest time delays for the H-alpha line, where those contributions reach up to about 15% of the measured FWHM and should be taken into account.

For each of these three hydrogen lines, for 18 time delays and 2 different gas pressures the values of the electron density N_e were deduced based on the Stark broadening tables and analytical results from [4, 5]. Table 4 shows the values of N_e

Table 4: Deduced N_e for pressure of 2.7×10^5 Pa.

t_{delay} [μs]	H_α N_e [10^{17} cm^{-3}]	H_β N_e [10^{17} cm^{-3}]	H_γ N_e [10^{17} cm^{-3}]
0.4	5.0 ± 0.4	2.9 ± 0.8	2.6 ± 0.7
0.5	3.8 ± 0.4	2.5 ± 0.7	2.5 ± 0.7
0.6	3.0 ± 0.4	2.2 ± 0.6	1.9 ± 0.5
0.7	2.5 ± 0.4	1.9 ± 0.5	1.7 ± 0.5
0.8	2.1 ± 0.3	1.6 ± 0.4	1.5 ± 0.5
0.9	1.9 ± 0.3	1.4 ± 0.4	1.3 ± 0.4
1.0	1.6 ± 0.3	1.3 ± 0.4	1.2 ± 0.4
1.1	1.4 ± 0.2	1.2 ± 0.3	1.1 ± 0.25
1.2	1.3 ± 0.2	1.1 ± 0.3	1.05 ± 0.25
1.3	1.15 ± 0.2	1.0 ± 0.3	1.0 ± 0.28
1.4	1.0 ± 0.2	0.87 ± 0.3	0.95 ± 0.28
1.5	1.0 ± 0.2	0.79 ± 0.3	0.92 ± 0.28
1.6	0.90 ± 0.2	0.76 ± 0.2	0.90 ± 0.28
1.7	0.84 ± 0.1	0.75 ± 0.2	0.90 ± 0.29
1.8	0.72 ± 0.1	0.68 ± 0.2	0.90 ± 0.29
1.9	0.69 ± 0.1	0.60 ± 0.2	0.90 ± 0.29
2.0	0.63 ± 0.1	0.55 ± 0.2	0.80 ± 0.30
2.1	0.58 ± 0.1	0.50 ± 0.2	0.77 ± 0.29

Table 5: Deduced N_e for pressure of 6.5×10^5 Pa.

t_{delay} [μs]	H_α N_e [10^{17} cm^{-3}]	H_β N_e [10^{17} cm^{-3}]	H_γ N_e [10^{17} cm^{-3}]
0.4	4.9 ± 0.8	2.9 ± 0.8	2.4 ± 0.7
0.5	3.6 ± 0.7	2.4 ± 0.7	2.2 ± 0.6
0.6	3.0 ± 0.6	2.1 ± 0.6	1.8 ± 0.5
0.7	2.5 ± 0.5	1.8 ± 0.5	1.6 ± 0.5
0.8	2.1 ± 0.4	1.5 ± 0.4	1.3 ± 0.4
0.9	1.75 ± 0.4	1.3 ± 0.4	1.2 ± 0.4
1.0	1.6 ± 0.4	1.2 ± 0.4	1.2 ± 0.4
1.1	1.4 ± 0.3	1.1 ± 0.3	1.05 ± 0.25
1.2	1.3 ± 0.3	1.0 ± 0.3	1.0 ± 0.26
1.3	1.15 ± 0.3	0.92 ± 0.3	1.0 ± 0.28
1.4	1.0 ± 0.3	0.79 ± 0.3	0.91 ± 0.28
1.5	0.92 ± 0.3	0.76 ± 0.3	0.91 ± 0.28
1.6	0.86 ± 0.3	0.72 ± 0.3	0.78 ± 0.27
1.7	0.70 ± 0.3	0.66 ± 0.3	0.90 ± 0.29
1.8	0.69 ± 0.3	0.60 ± 0.3	0.77 ± 0.28
1.9	0.57 ± 0.3	0.55 ± 0.3	0.71 ± 0.28
2.0	0.55 ± 0.4	0.50 ± 0.4	0.51 ± 0.25
2.1	0.46 ± 0.4	0.48 ± 0.4	0.51 ± 0.25

deduced from these three hydrogen lines for the pressure 2.7×10^5 Pa; Table 5 shows the values of N_e deduced from these three hydrogen lines for the pressure 6.5×10^5 Pa.

The error bars of the deduced N_e are due to several factors as follows. The primary factor is the error bars of the experimental widths. There are two secondary factors: the uncertainty in the temperature and the uncertainty in the reduced mass of the pairs "perturber-radiator". Speaking of the latter, since the discharge occurs in methane (CH4), the perturbers could be not only hydrogen ions (protons) but also carbon ions. The reduced mass is $\mu = 0.5$ for the pairs H-H+ or $\mu = 0.923$ for the pairs H-C+ and H-C++.

4. Conclusions

We demonstrated that time-resolved measurements of profiles of H-alpha, H-beta, and H-gamma lines provide good diagnostics for the LIOB in methane.

The electron densities N_e deduced from the H-gamma and H-beta lines showed generally a good agreement with each other. At $t_{\text{delay}} = 0.4\,\mu$s and $t_{\text{delay}} = 0.5\,\mu$s, the electron density N_e *formally* deduced from the H-alpha line exceeds N_e deduced from the H-beta and H-gamma lines beyond the error bars (while N_e deduced from the H-beta and H-gamma lines agree with each other very well). This is a clear indication that at $t_{\text{delay}} = 0.4\,\mu$s and $t_{\text{delay}} = 0.5\,\mu$s, the H-alpha line experienced a significant self-absorption.

Besides, for the range of $t_{\text{delay}} = 0.6$–$1.2\,\mu$s, the Mean Probable Values (MPVs) of N_e *formally* deduced from the H-alpha line significantly exceed MPV of N_e deduced from the H-beta and H-gamma lines (though the disagreement is within the error bars). Thus it is probable that at $t_{\text{delay}} = 0.6$–$1.2\,\mu$s, the H-alpha still experienced some self-absorption.

We mention that if we would have used the Stark broadening diagnosis-map data from [6], we would have deduced slightly different electron densities. This is because the computational results of paper [6] are based on a simulation model that neglects the direct coupling of the electron and ion microfields taken into account analytically in [4, 5].

We note that for a particular hydrogen line and for a specific time delay, our experimental widths for the higher pressure are generally lower than for the lower pressure. However, generally the higher the pressure is, the higher the expected electron density is. So, there should be some additional broadening mechanism that is more effective at the lower density than at the higher density. Such mechanism could be electrostatic plasma turbulence, that is, some regular or stochastic electrostatic waves in plasmas (see, e.g., [7, 8] and references therein).

Electrostatic waves produce an additional Stark broadening controlled by their amplitude. The collisional damping of electrostatic waves increases with the density, so that their amplitude and the additional Stark broadening decreases with the density.

A future study should analyze this hypothesis in more detail or provide an alternative explanation.

References

[1] C. G. Parigger, D. H. Plemmons, and J. W. L. Lewis, "Spatially and Temporally Resolved Electron Number Density Measurements in a Decaying Laser-Induced Hydrogen Plasma Using Hydrogen-Alpha Line Profiles," *Applied Optics*, vol. 34, p. 3325, 1995.

[2] C. G. Parigger, D. H. Plemmons, and E. Oks, "Balmer series H_β measurements in a laser-induced hydrogen plasma," *Applied Optics*, vol. 42, no. 30, pp. 5992–6000, 2003.

[3] C. G. Parigger, M. Dackman, and J. O. Hornkohl, "Time-resolved spectroscopy measurements of hydrogen-alpha, -beta, and -gamma emissions," *Applied Optics*, vol. 47, no. 31, pp. G1–G6, 2008.

[4] E. Oks, *Stark Broadening of Hydrogen and Hydrogenlike Spectral Lines in Plasmas: The Physical Insight*, Alpha Science International, Oxford, UK, 2006.

[5] E. Oks, "Stark Widths of Hydrogen Spectral Lines in Plasmas: a Highly-Advanced Non-Simulative Semiclassical Theory and Tables," in *Proceedings of the 18th International Conference on Spectral Line Shapes*, vol. 874 of *AIP Conference Proceedings*, p. 5, American Institute of Physics, 2006.

[6] M. A. Gigosos, M. Á. González, and V. Cardeñoso, "Spectrochim," *Acta B*, p. 1489, 2003.

[7] E. Oks, *Plasma Spectroscopy: The Influence of Microwave and Laser Fields*, vol. 9 of *Springer Series on Atoms and Plasmas*, Springer, New York, NY, USA, 1995.

[8] H. R. Griem, *Spectral Line Broadening by Plasmas*, Academic Press, New York, NY, USA, 1964.

Hindawi Publishing Corporation
International Journal of Spectroscopy
Volume 2010, Article ID 371201, 11 pages
doi:10.1155/2010/371201

Research Article

Collision-Induced Infrared Absorption by Molecular Hydrogen Pairs at Thousands of Kelvin

Xiaoping Li,[1] Katharine L. C. Hunt,[1] Fei Wang,[2] Martin Abel,[2] and Lothar Frommhold[2]

[1] *Department of Chemistry, Michigan State University, East Lansing, MI 48824, USA*
[2] *Physics Department, University of Texas, Austin, TX 78712-1081, USA*

Correspondence should be addressed to Lothar Frommhold, frommhold@physics.utexas.edu

Received 21 April 2009; Accepted 18 July 2009

Academic Editor: Chantal Stehle

Collision-induced absorption by hydrogen and helium in the stellar atmospheres of cool white dwarfs causes the emission spectra to differ significantly from the expected blackbody spectra of the cores. For detailed modeling of radiative processes at temperatures up to 7000 K, the existing H_2–H_2 induced dipole and potential energy surfaces of high quality must be supplemented by calculations with the H_2 bonds stretched or compressed far from the equilibrium length. In this work, we describe new dipole and energy surfaces, based on more than 20 000 *ab initio* calculations for H_2–H_2. Our results agree well with previous *ab initio* work (where those data exist); the calculated rototranslational absorption spectrum at 297.5 K matches experiment similarly well. We further report the calculated absorption spectra of H_2–H_2 for frequencies from the far infrared to 20 000 cm^{-1}, at temperatures of 600 K, 1000 K, and 2000 K, for which there are no experimental data.

1. Introduction

It is well known that dense gases of infrared inactive molecules such as H_2 absorb infrared radiation. Absorption continua range from the microwave and far infrared regions of the spectrum to the near infrared and possibly into the visible. Collisionally interacting pairs of hydrogen molecules possess transient electric dipole moments, which are responsible for the observed absorption continua [1, 2]. Planetary scientists understood early on the significance of collision-induced absorption (CIA) for the modeling of the atmospheres of the outer planets [3, 4]. More recently, it was shown that the emission spectrum of cool white dwarf stars differs significantly from the expected blackbody spectrum of their cores: CIA in the dense helium and hydrogen atmospheres suppresses (filters) the infrared emissions strongly [5–10]. Detailed modelling of the atmospheres of cool stars with proper accounting for the collision-induced opacities is desirable, but it has been hampered heretofore by the highly incomplete or nonexisting theoretical and experimental data on such opacities at temperatures of many thousands of kelvin.

Quantum chemical calculations of the induced dipole surfaces of H_2–H_2, H_2–He and other complexes have been very successful [11–14]. Based on such data, molecular scattering calculations accounting for the interactions of the molecular complexes with photons have been undertaken which accurately reproduced the existing laboratory measurements at low temperatures ($T \leq 300$ K or so) [2]. At higher temperatures, virtually no suitable laboratory measurements of such opacities exist, but reliable data are needed. We therefore decided to extend such quantum chemical calculations of the induced dipole (ID) and potential energy surfaces (PES) of H_2–H_2 complexes to highly rotovibrationally excited molecules, as encountered at high temperatures (up to 7 000 K) and photon energies up to ~2.5 eV.

2. *Ab Initio* Calculations of the Induced Dipole and Potential Energy Surfaces

At the temperatures characteristic of cool white-dwarf atmospheres, the CIA spectra depend on transition dipole

matrix elements with vibrational quantum numbers up to $v \approx 7$. To evaluate these matrix elements, we have determined the induced dipoles and interaction energies of pairs of hydrogen molecules with bond lengths ranging from 0.942 a.u. to 2.801 a.u. (1 a.u. = $a_0 = 5.29177249 \cdot 10^{-11}$ m). For comparison, the vibrationally averaged internuclear separation in H_2 is 1.449 a.u., in the ground vibrational state. We have used MOLPRO 2000 [15] to calculate the PES for H_2–H_2 and to calculate the pair ID by finite-field methods, at coupled-cluster single and double excitation level, with triple excitations treated perturbatively [CCSD(T)]. In this work, we have employed MOLPRO's aug-cc-pV5Z(spdf) basis, consisting of (9s 5p 4d 3f) primitive Gaussians contracted to [6s 5p 4d 3f]; this gives 124 contracted basis functions for each of the H_2 molecules. The basis gives accurate energies and properties [16]; yet it is sufficiently compact to permit calculations on H_2 pairs with 28 different combinations of H_2 bond lengths, at 7 different intermolecular separations, in 17 different relative orientations (the orientations listed in Table 1), and at a minimum of 6 different applied field strengths for each geometrical configuration.

In the calculations, the centers of mass of the two H_2 molecules are separated along the Z axis by distances R ranging from 4.0 to 10.0 a.u. The vector **R** joins molecule 2 to molecule 1. The molecular orientations are characterized by the angles $(\theta_1, \theta_2, \varphi_{12})$, where θ_1 is the angle between the Z axis and the symmetry axis of molecule 1, θ_2 is the angle between the Z axis and the symmetry axis of molecule 2, and φ_{12} is the dihedral angle between two planes, one defined by the Z axis and the symmetry axis of molecule 1 and the other defined by the Z axis and the symmetry axis of molecule 2.

Calculations were performed first for two molecules with bond lengths of $r_1 = r_2 = 1.449$ a.u., the ground-state, vibrationally averaged internuclear separation. The interaction energies were evaluated in the absence of an applied field; then the pair dipoles were obtained from finite-field calculations, grouped into three sets of 40. Within each of the sets, the fields were confined to the XY, XZ, or YZ planes, and the two components of the applied field were selected randomly, in the range from 0.001 a.u. to 0.01 a.u., for a total of 120 calculations. For each fixed set of the bond lengths, orientation angles, and intermolecular separation, the total energies were fit (by least squares) to a quartic polynomial in the applied field **F**:

$$E = E_0 - \mu_\alpha F_\alpha - \left(\frac{1}{2}\right)\alpha_{\alpha\beta}F_\alpha F_\beta - \frac{1}{6}\beta_{\alpha\beta\gamma}F_\alpha F_\beta F_\gamma - \frac{1}{24}\gamma_{\alpha\beta\gamma\delta}F_\alpha F_\beta F_\gamma F_\delta - \cdots, \quad (1)$$

where the Einstein convention of summation over repeated Greek subscripts is followed. The coefficients of the linear terms were selected from each fit, to obtain the Cartesian components of the induced dipole moments μ_X, μ_Y, and μ_Z. In Table 1, our results for the components of the pair dipole are given for pairs with $r_1 = r_2 = 1.449$ a.u.

In earlier work on the polarizabilities α for H_2–H_2 [16], we conducted several tests of this fitting procedure: we compared results from quartic fits with 120 different field strengths, quartic fits with 200 different field strengths, and quintic and sixth-order fits with 200 field strengths (at one set of orientation angles and an intermolecular distance of 2.5 a.u., where the differences between the calculations were expected to be magnified); we found excellent agreement among the results from all of the fits. We also compared the results from the random-field calculations with the values obtained analytically, based on calculations with 6 or 8 selected values of the field strengths, for fixed orientation angles and the full range of intermolecular separations. The field values were grouped into the sets $\{f, 2^{1/2}f, 3^{1/2}f, -f, -2^{1/2}f, -3^{1/2}f\}$, $\{f, 2^{1/2}f, 5^{1/2}f, -f, -2^{1/2}f, -5^{1/2}f\}$, and $\{f, 2^{1/2}f, 3^{1/2}f, 5^{1/2}f, -f, -2^{1/2}f, -3^{1/2}f, -5^{1/2}f\}$, with $f = 0.001$, 0.002, 0.003, and 0.004 a.u. At the shortest intermolecular distance ($R = 2.5$ a.u.), the results for $f = 0.001$ a.u. – 0.003 a.u. were affected by numerical imprecision in the hyperpolarization contributions; at larger R, they agreed well with the random-field results. Agreement between the random-field results and the results obtained with $f = 0.004$ a.u. was excellent for all R values. On this basis, we have used random-field fits in the work with $r_1 = r_2 = 1.449$ a.u., but we have used analytic fits with 6 different field values for the computations with r_1 or $r_2 \neq 1.449$ a.u. In [16], we also compared the results obtained via analytic differentiation at the self-consistent field (SCF) level using Gaussian 98 versus the results from our SCF calculations, for the full range of intermolecular separations and three different relative orientations, again with excellent agreement. Basis set superposition error (BSSE) has been shown to be negligible [16], as tested by function counterpoise ("ghost-orbital") methods. BSSE occurs when the pair basis provides a better representation of H_2–H_2 than the single-molecule basis provides for an isolated H_2 molecule. In these calculations, BSSE has been suppressed by the large size of the single-molecule basis.

The interaction mechanisms that determine the induced dipole include classical multipole polarization, van der Waals dispersion, and short-range exchange, overlap, and orbital distortion. At long range, the leading term in the collision-induced dipole comes from quadrupolar induction, which varies as R^{-4} in the separation R between the molecular centers [2]. The next long-range polarization term is of order R^{-6}; it results both from hexadecapolar induction and from the effects of the nonuniformity of the local field gradient (due to the quadrupole moment of the collision partner). The magnitude of the latter term depends on the dipole-octopole polarizability tensor E. At order R^{-7}, back-induction [17, 18] and dispersion [17–21] affect the pair dipole. Back-induction is a static reaction field effect: the field from the permanent quadrupole of molecule 1 polarizes molecule 2, which sets up a reaction field that polarizes molecule 1 (and similarly, with molecules 1 and 2 interchanged). The van der Waals dispersion dipole results from *dynamic* reaction-field effects, combined with the effects of an applied, static field [21], via two physical mechanisms.

Table 1: Cartesian components μ_X, μ_Y, and μ_Z of the H_2–H_2 dipole in a.u. (multiplied by 10^6) with bond lengths $r_1 = r_2 = 1.449$ a.u.

R (a.u.)	4.0	5.0	6.0	7.0	8.0	9.0	10.0
$(\theta_1, \theta_2, \varphi_{12})$				μx			
$(\pi/12, \pi/6, \pi/3)$	48	150	103	63	39	25	16
$(\pi/12, \pi/4, \pi/6)$	−3675	−2393	−1393	−804	−480	−299	−195
$(\pi/12, \pi/3, \pi/6)$	−2790	−1791	−1044	−607	−366	−230	−150
$(\pi/12, 5\pi/12, \pi/6)$	−144	−28	−17	−16	−15	−11	−8
$(\pi/6, \pi/4, \pi/3)$	1417	1294	806	471	280	175	115
$(\pi/6, \pi/3, \pi/4)$	399	562	365	210	121	74	49
$(\pi/6, 5\pi/12, \pi/3)$	2065	1922	1196	695	411	255	167
$(\pi/4, \pi/3, \pi/6)$	1109	879	528	302	177	109	72
$(\pi/4, 5\pi/12, \pi/6)$	3481	2432	1424	815	481	299	195
$(\pi/3, 5\pi/12, \pi/6)$	2555	1804	1062	611	363	226	148
$(7\pi/12, \pi/12, \pi/6)$	−7979	−5226	−3027	−1740	−1037	−648	−424
$(7\pi/12, \pi/6, \pi/4)$	−9089	−5973	−3462	−1988	−1184	−740	−484
$(7\pi/12, \pi/4, \pi/6)$	−11040	−7181	−4151	−2381	−1417	−885	−580
$(7\pi/12, \pi/3, \pi/6)$	−9759	−6345	−3669	−2107	−1255	−785	−515
$(\pi/2, \pi/12, \pi/6)$	−3628	−2337	−1341	−765	−452	−282	−184
$(\pi/2, \pi/6, \pi/3)$	−3575	−2303	−1322	−754	−447	−278	−182
$(\pi/2, \pi/4, \pi/6)$	−7071	−4535	−2606	−1489	−884	−551	−361
				μ_Y			
$(\pi/12, \pi/6, \pi/3)$	−6236	−4288	−2519	−1453	−864	−539	−352
$(\pi/12, \pi/4, \pi/6)$	−3691	−2635	−1566	−908	−542	−338	−221
$(\pi/12, \pi/3, \pi/6)$	−2801	−2088	−1257	−733	−440	−275	−180
$(\pi/12, 5\pi/12, \pi/6)$	−1060	−952	−599	−355	−214	−135	−88
$(\pi/6, \pi/4, \pi/3)$	−5443	−4082	−2455	−1429	−854	−533	−349
$(\pi/6, \pi/3, \pi/4)$	−2847	−2414	−1496	−880	−529	−332	−217
$(\pi/6, 5\pi/12, \pi/3)$	−1427	−1430	−916	−545	−330	−207	−136
$(\pi/4, \pi/3, \pi/6)$	−1008	−1209	−793	−473	−286	−179	−117
$(\pi/4, 5\pi/12, \pi/6)$	419	−239	−224	−145	−90	−57	−37
$(\pi/3, 5\pi/12, \pi/6)$	404	−211	−199	−127	−78	−49	−32
$(7\pi/12, \pi/12, \pi/6)$	−997	−877	−543	−317	−189	−118	−77
$(7\pi/12, \pi/6, \pi/4)$	−2588	−2187	−1342	−780	−464	−290	−189
$(7\pi/12, \pi/4, \pi/6)$	−2416	−1890	−1142	−662	−394	−246	−161
$(7\pi/12, \pi/3, \pi/6)$	−2415	−1757	−1045	−604	−360	−225	−147
$(\pi/2, \pi/12, \pi/6)$	−835	−798	−501	−294	−175	−109	−71
$(\pi/2, \pi/6, \pi/3)$	−2521	−2367	−1481	−865	−515	−321	−210
$(\pi/2, \pi/4, \pi/6)$	−1734	−1570	−976	−569	−339	−211	−138
				μ_Z			
$(\pi/12, \pi/6, \pi/3)$	−15702	−5371	−2141	−1026	−568	−345	−223
$(\pi/12, \pi/4, \pi/6)$	−35330	−12145	−4900	−2374	−1322	−808	−525
$(\pi/12, \pi/3, \pi/6)$	−53105	−18342	−7486	−3664	−2053	−1258	−820
$(\pi/12, 5\pi/12, \pi/6)$	−65061	−22550	−9278	−4573	−2574	−1580	−1032
$(\pi/6, \pi/4, \pi/3)$	−19683	−6793	−2764	−1349	−755	−463	−301
$(\pi/6, \pi/3, \pi/4)$	−37478	−13007	−5355	−2641	−1486	−914	−597
$(\pi/6, 5\pi/12, \pi/3)$	−49514	−17248	−7156	−3553	−2008	−1237	−810
$(\pi/4, \pi/3, \pi/6)$	−17837	−6231	−2596	−1293	−731	−451	−296
$(\pi/4, 5\pi/12, \pi/6)$	−29903	−10485	−4400	−2205	−1253	−774	−509
$(\pi/3, 5\pi/12, \pi/6)$	−12057	−4257	−1805	−913	−522	−323	−213
$(7\pi/12, \pi/12, \pi/6)$	65301	22600	9286	4573	2573	1580	1032
$(7\pi/12, \pi/6, \pi/4)$	49757	17294	7161	3553	2008	1237	810
$(7\pi/12, \pi/4, \pi/6)$	30125	10528	4404	2206	1253	775	510

Table 1: Continued.

R (a.u.)	4.0	5.0	6.0	7.0	8.0	9.0	10.0
$(7\pi/12, \pi/3, \pi/6)$	12133	4272	1807	914	522	323	214
$(\pi/2, \pi/12, \pi/6)$	69310	24042	9916	4898	2761	1697	1109
$(\pi/2, \pi/6, \pi/3)$	53764	18746	7796	3879	2196	1354	887
$(\pi/2, \pi/4, \pi/6)$	34212	11998	5042	2532	1441	891	58

(1) Spontaneous, quantum mechanical fluctuations in the charge density of molecule 1 produce a fluctuating field that acts on molecule 2; then molecule 2 is hyperpolarized by the concerted action of the field from 1 and the applied field **F**. This sets up a field-dependent dynamic reaction field at molecule 1, giving a term in the van der Waals energy that is linear in the applied field **F**. (2) The correlations of the fluctuations in the charge density of molecule 1 are altered by the static field **F** acting on 1; molecule 2 responds linearly to field-induced changes in the fluctuations of the charge density of 1, again giving a term in the van der Waals energy that is linear in the applied field **F**. The precise functional forms of the short-range exchange, overlap, and orbital-distortion effects on the dipole are not known; however, these contributions are expected to drop off (roughly) exponentially with increasing R [2].

The dipole moment of the pair can be cast into a symmetry-adapted form, as a series in the spherical harmonics of the orientation angles of molecules 1 and 2 and the orientation angles of the intermolecular vector:

$$\begin{aligned}\mu_1{}^M(\mathbf{R}, \mathbf{r}_1, \mathbf{r}_2) = (4\pi)^{3/2}\ 3^{-1/2} \sum A_{\lambda_1\lambda_2\Lambda L}(R, r_1, r_2) \\ \times Y_{\lambda_1}{}^{m_1}(\Omega_1) Y_{\lambda_2}{}^{m_2}(\Omega_2) Y_L{}^{M-m}(\Omega_R) \\ \times \langle \lambda_1\lambda_2 m_1 m_2 \mid \Lambda m\rangle \langle \Lambda L m(M-m) \mid 1M\rangle,\end{aligned} \tag{2}$$

where the sum runs over all values of $\lambda_1, \lambda_2, m_1, m_2, \Lambda$ and m; $M = 1, 0$, or -1, corresponding to the dipole components,

$$\begin{aligned}\mu_1{}^1 &= -\left(\frac{1}{2}\right)^{1/2}\left(\mu_X + i\mu_Y\right), \\ \mu_1{}^0 &= \mu_Z, \\ \mu_1{}^{-1} &= \left(\frac{1}{2}\right)^{1/2}(\mu_X - i\mu_Y).\end{aligned} \tag{3}$$

In (2), Ω_1 and Ω_2 denote the orientation angles of molecules 1 and 2, that is, the orientation angles of the z axes of the molecule-fixed frames, Ω_R is the orientation angle of the vector **R** (note that **R** runs from molecule 2 to molecule 1, in this work), and the quantities $\langle \lambda_1\lambda_2 m_1 m_2 \mid \Lambda m\rangle$ and $\langle \Lambda L M(M-m) \mid 1M\rangle$ are Clebsch-Gordan coefficients. Equation (2) follows immediately from the fact that the collision-induced dipole of H_2–H_2 is a first-rank spherical tensor, which is obtained by coupling functions of $\mathbf{r}_1$, $\mathbf{r}_2$, and **R**. Therefore λ_1, λ_2, Λ, L, and the magnitudes of $\mathbf{r}_1$, $\mathbf{r}_2$, and **R** completely determine the dipole expansion coefficients $A_{\lambda_1\lambda_2\Lambda L}(R, r_1, r_2)$.

The dipole coefficients arising from various long-range polarization mechanisms are categorized in Table 2, through order R^{-7}. In this table, Θ denotes the molecular quadrupole moment; $\overline{\alpha}$ is the trace of the single-molecule polarizability; $\alpha_\parallel - \alpha_\perp$ is the polarizability anisotropy, which is equal to $\alpha_{zz} - \alpha_{xx}$ in the molecular axis system, where z is the symmetry axis; Φ is the hexadecapole moment; E is the dipole-octopole polarizability, which has a second-rank spherical tensor component E_2 and a fourth-rank component E_4. The van der Waals dispersion dipole is given by an integral over imaginary frequencies, where the integrand is a product of the polarizability at imaginary frequency $\alpha(i\omega)$ and the dipole-dipole-quadrupole hyperpolarizability $B(0, i\omega)$. The B tensor is a fourth-rank Cartesian tensor with spherical-tensor components of ranks 0, 2, and 4.

For distinct molecules 1 and 2, or for chemically identical molecules that have different bond lengths, all of the dipole coefficients listed in Table 2 are nonzero, although some of the coefficients may be quite small numerically. For chemically identical molecules, when $r_1 = r_2$, the coefficients A_{0001}, $A_{22\Lambda 1}$ with $\Lambda \neq 1$, $A_{22\Lambda 3}$ with $\Lambda \neq 3$, and A_{2245} vanish; the remainder are nonzero. The coefficients $A_{0\lambda\lambda L}$ and $A_{24\Lambda L}$ can be obtained from the coefficients $A_{\lambda 0\lambda L}$ and $A_{42\Lambda L}$ via the relations

$$\begin{aligned}A_{0\lambda\lambda L} &= -\mathcal{P}^{12}\mathrm{A}_{\lambda 0\lambda \mathrm{L}}, \\ A_{24\Lambda L} &= (-1)^{\Lambda+1}\mathcal{P}^{12}A_{42\Lambda L},\end{aligned} \tag{4}$$

where $\mathcal{P}^{12}$ interchanges the labels of molecules 1 and 2. For centrosymmetric molecules such as H_2, the dipole coefficients $A_{\lambda\lambda'\Lambda L}$ vanish unless λ and λ' are both even. Also, due to the Clebsch-Gordan coefficients in (2), nonvanishing contributions are found only if $\Lambda = L-1$, L, or $L+1$. Coefficients with higher values of λ and λ' than those listed are of higher order than R^{-7} at long-range, although they may represent significant short-range overlap effects.

From the dipole values in Table 1, we have obtained a set of A coefficients by least-squares fit (at each R value) to (2), for $r_1 = r_2 = 1.449$ a.u. From the fit, we have been able to determine the coefficients A_{2021}, A_{0221}, A_{2023}, A_{0223}, A_{2211}, A_{2233}, A_{4043}, A_{0443}, A_{4045}, A_{0445}, A_{4221}, A_{2421}, A_{4223}, A_{2423}, A_{4233}, A_{2433}, A_{4243}, A_{2443}, A_{4245}, A_{2445}, A_{4255}, A_{2455}, A_{4265}, A_{2465}, A_{4267}, and A_{2467}. We have kept all of these coefficients, as well as A_{0001} and A_{2201}, in the calculations with unequal bond lengths for molecules 1 and 2. However, for $R \geq 4.0$ a.u and $r_1 = r_2 = 1.449$ a.u., the least squares fit shows that the first ten coefficients are numerically important, while the remaining coefficients are essentially negligible. At $R = 4.0$ a.u., the remaining coefficients do not exceed $7.0 \cdot 10^{-5}$ a.u. in absolute value, and the values drop off

Table 2: Long-range dipole induction mechanisms that contribute to the coefficients $A_{\lambda\lambda'\Lambda L}$ of (2) for a pair of molecules A and B [17, 18].

Induction mechanism	Power law	Properties	Coefficients
Quadrupolar field	R^{-4}	Θ, $\overline{\alpha}$	A_{2023}, A_{0223}
		Θ, $\alpha_\parallel - \alpha_\perp$	$A_{22\Lambda 3}$, $\Lambda = 2, 3, 4$
Hexadecapolar field	R^{-6}	Φ, $\overline{\alpha}$	A_{4045}, A_{0445}
		Φ, $\alpha_\parallel - \alpha_\perp$	$A_{42\Lambda 5}$, $\Lambda = 4, 5, 6$
			$A_{24\Lambda 5}$, $\Lambda = 4, 5, 6$
Nonuniform field gradient	R^{-6}	Θ, E_2	A_{2245}
		Θ, E_4	$A_{42\Lambda 5}$, $\Lambda = 4, 5, 6$
			$A_{24\Lambda 5}$, $\Lambda = 4, 5, 6$
Back-induction	R^{-7}	Θ, $\overline{\alpha}$, $\alpha_\parallel - \alpha_\perp$	A_{0001}
			A_{2021}, A_{0221}
			A_{2023}, A_{0223}
			A_{2221}
			$A_{22\Lambda 3}$, $\Lambda = 2, 3, 4$
			A_{2245}
			A_{4043}, A_{0443}
		Θ, $\alpha_\parallel - \alpha_\perp$	A_{2021}, A_{0221}
			A_{2023}, A_{0223}
			$A_{22\Lambda 1}$, $\Lambda = 0, 1, 2$
			$A_{22\Lambda 3}$, $\Lambda = 2, 3, 4$
			A_{2245}
			A_{4221}, A_{2421}
			$A_{42\Lambda 3}$, $\Lambda = 2, 3, 4$
			$A_{24\Lambda 3}$, $\Lambda = 2, 3, 4$
			$A_{42\Lambda 5}$, $\Lambda = 4, 5, 6$
			$A_{24\Lambda 5}$, $\Lambda = 4, 5, 6$
Dispersion	R^{-7}	$\overline{\alpha}\,(i\omega)$, $B_0(0, i\omega)$	A_{0001}
		$\overline{\alpha}\,(i\omega)$, $B_2(0, i\omega)$	A_{2021}, A_{0221}
			A_{2023}, A_{0223}
		$\alpha_\parallel(i\omega) - \alpha_\perp(i\omega)$, $B_0(0, i\omega)$	A_{2021}, A_{0221}
			A_{2023}, A_{0223}
		$\overline{\alpha}(i\omega)$, $B_4(0, i\omega)$	A_{4043}, A_{0443}
		$\alpha_\parallel(i\omega) - \alpha_\perp(i\omega)$, $B_2(0, i\omega)$	$A_{22\Lambda 1}$, $\Lambda = 0, 1, 2$
			$A_{22\Lambda 3}$, $\Lambda = 2, 3, 4$
			A_{2245}
		$\alpha_\parallel(i\omega) - \alpha_\perp(i\omega)$, $B_4(0, i\omega)$	A_{4221}, A_{2421}
			$A_{42\Lambda 3}$, $\Lambda = 2, 3, 4$
			$A_{24\Lambda 3}$, $\Lambda = 2, 3, 4$
			$A_{42\Lambda 5}$, $\Lambda = 4, 5, 6$
			$A_{24\Lambda 5}$, $\Lambda = 4, 5, 6$

rapidly with increasing R. Table 3 gives our results for A_{2021}, A_{2023}, A_{2211}, A_{2233}, A_{4043}, and A_{4045}; the other numerically significant coefficients are given by the relations $A_{0221} = -A_{2021}$, $A_{0223} = -A_{2023}$, $A_{0443} = -A_{4043}$, and $A_{0445} = -A_{4045}$.

In Table 3, the results are also compared with results from two earlier *ab initio* calculations of the H_2–H_2 dipole with $r_1 = r_2 = 1.449$ a.u., reported by Meyer et al. [12], Meyer et al. [13], and Fu et al. [22]. (The signs in Table 3 follow from our choice of the positive direction of the intermolecular vector **R**.) Meyer et al. [12, 13] used configuration-interaction wave functions including single, double, and triple excitations from a reference Slater determinant, in a (7s 1p) basis of Gaussian primitives on each H center, contracted to [3s 1p] and augmented by a (3s, 2p, 2d) basis at the center of the H–H bond, giving a total of 31 basis functions for H_2 [11]. They performed calculations for 18 relative orientations that provided 9 nonredundant Cartesian dipole components. Fu et al. [22] employed the same basis to generate the CCSD (T) wave functions, in calculations for H_2–H_2 in 13 relative orientations, selected so that $\mu_Y = 0$ in all cases. To find the dipoles, they used finite-field methods, with two fields that were equal in magnitude but opposite in sign. From Table 3,

Table 3: Dipole expansion coefficients $A_{\lambda\lambda' \Lambda L}$ (in a.u., multiplied by 10^6) for H_2–H_2 with $r_1 = r_2 = 1.449$ a.u. Results from this calculation, compared with results of Meyer et al. [13] (MBF), Fu et al. [22] (FZB), long-range results [17, 18] through order R^{-7}(LR), and quadrupole-induced dipole coefficients (QID).

	R (a.u.)	4.0	5.0	6.0	7.0	8.0	9.0	10.0
A_{2021}	This work	9983	2123	407	73	13	4	2
	MBF	10401	2190	429	84	20	7	—
	FZB	10385	2184	427	83	19	6	—
	LR	279	59	16	6	2	1	0
A_{2023}	This work	−20065	−8076	−3725	−1950	−1124	−695	−455
	MBF	−19967	−7953	−3688	−1939	−1119	−692	—
	FZB	−19949	−7946	−3685	−1938	−1118	−692	—
	LR	−19687	−7652	−3603	−1921	−1118	−695	−455
	QID	−17628	−7221	−3482	−1880	−1102	−688	−451
A_{2211}	This work	402	86	18	3	0	0	0
	MBF	332	74	14	2	0	0	—
	FZB	332	74	14	2	0	0	—
	LR	−41	−9	−2	−1	0	0	0
A_{2233}	This work	2020	977	514	289	171	107	70
	MBF	1992	949	498	280	166	104	—
	FZB	1991	949	498	279	166	104	—
	LR	2588	1088	530	288	169	106	70
	QID	2726	1117	538	291	170	106	70
A_{4043}	This work	690	180	42	9	2	0	0
	LR	204	43	12	4	2	1	0
A_{4045}	This work	−845	−283	−97	−37	−16	−8	−4
	MBF	−1523	−450	−135	−47	−19	−9	—
	FZB	−1517	−447	−134	−46	−19	−9	—
	LR	−1040	−273	−91	−36	−16	−8	−4

it is apparent that the results of Fu et al. (FZB) [22] agree well with the earlier results given by Meyer et al. (MBF) [13].

For the largest coefficients, A_{2023} and A_{0223}, our results are in excellent agreement with both of the earlier calculations: The percent differences between our results and those of Meyer et al. [13] are largest at $R = 5.0$ a.u. (1.52%) and $R = 6.0$ a.u. (0.99%); the remaining differences in these two coefficients average to 0.48%. We have obtained results at $R = 10.0$ a.u., which were not given previously. The differences between our values for A_{2233} and those of Meyer et al. [13] are typically ∼3% (smaller at $R = 4.0$ a.u.). Differences in the values of A_{2021} and A_{0221} are ∼5% or less at short range ($R \leq 6.0$ a.u.), where these coefficients have their largest values. At longer range, the absolute discrepancies are smaller, although the differences are larger on a relative basis. The principal differences in the dipole coefficients are attributable to the inclusion of A_{4043} and A_{0443} in our work; this affects the values of A_{4045}, A_{0445}, and A_{2211} (to a lesser extent).

In Table 3, the *ab initio* values of the coefficients are also compared with values based on the quadrupole-induced dipole model (QID) and the long range model (LR), which is complete through order R^{-7}. The LR calculations include hexadecapolar induction, back-induction, and van der Waals dispersion effects, in addition to quadrupolar induction. The QID and LR calculations are based on the value of the H_2 quadrupole computed by Poll and Wolniewicz [23], the value of Θ interpolated to $r = 1.449$ a.u. given by Visser et al. [24], the hexadecapole computed by Karl et al. [25], the polarizabilities and E-tensor values given by Bishop and Pipin [26], and the dispersion dipoles computed from the polarizability and dipole-dipole-quadrupole polarizability at imaginary frequencies, also given by Bishop and Pipin [27].

The coefficient A_{2023} depends primarily on the quadrupole-induced dipole: the difference between the QID approximation and our result is ∼12% at $R = 4.0$ a.u., ∼10.6% at $R = 5.0$ a.u., ∼6.5% for $R = 6.0$ a.u., and smaller at larger R. The QID model gives remarkably good values for this coefficient, even when R is quite small. Agreement with the full long-range model is somewhat better, with errors of ∼5.25% at $R = 5.0$ a.u. and only 1.88% at $R = 4.0$ a.u. Quadrupole-induced dipole effects are also present in the coefficient A_{2233}; this coefficient fits the QID and LR models quite well for $R \geq 6.0$ a.u., but the percent errors in these approximations are larger than those in A_{2023} for $R = 4.0$ and 5.0 a.u. It should be noted that the back-induction and dispersion contributions have the same sign in A_{2023} but opposite signs in A_{2233}.

At long range the values of A_{4045} and A_{0445} depend on hexadecapolar induction, which varies as R^{-6}; there are no other contributions through order R^{-7}. We find strong agreement between the values of these coefficients and the hexadecapole-induced dipole terms (which determine LR),

for $R \geq 5.0$ a.u.; short-range effects become significant when R is reduced to 4.0 a.u. In contrast, A_{2021}, A_{0221}, A_{2211}, A_{4043}, and A_{0443} seem to reflect the short-range exchange, overlap, and orbital distortion effects predominantly. For these coefficients, the leading long-range terms of back-induction and dispersion vary as R^{-7}; and they contribute with opposite signs in each case, further reducing the net effect of the long-range polarization mechanisms, in these particular dipole coefficients.

As noted above, we have carried out calculations with 28 different combinations of bond lengths in molecules 1 and 2. *Ab initio* calculations have been completed for pairs with each bond length combination, in each of the 17 relative orientations, at each of 7 separations between the centers of mass, and for at least six values of the applied field in the X, Y, or Z direction.

In the work of Meyer et al. on the absorption spectra of H_2–H_2 pairs in the fundamental band, results for the Cartesian components of the pair dipoles are listed for four nonredundant pairs of bond lengths, (r_o, r_o), (r_o, r_-), (r_o, r_+), and (r_-, r_+), with $r_o = 1.449$ a.u., $r_- = 1.111$ a.u., and $r_+ = 1.787$ a.u. [13]. Fu et al. [22] augmented this set by the addition of a larger bond length, $r_{++} = 2.150$ a.u., and reported results for all ten nonredundant pairs of configurations with the bond lengths drawn from the set $\{r_o, r_-, r_+, r_{++}\}$. In the current work, we have included r_o, three bond lengths smaller than r_o (1.280 a.u., 1.111 a.u., and 0.942 a.u.), and four bond lengths larger than r_o (1.787 a.u., 2.125 a.u., 2.463 a.u., and 2.801 a.u.), in order to examine new portions of the dipole surface, particularly those that may become significant for photon absorption at higher temperatures. The specific nonredundant length combinations used in the calculations are (r_1, r_2) = (2.801, 2.125), (2.801, 1.787), (2.801, 1.449), (2.801, 1.280), (2.801, 1.111), (2.801, 0.942), (2.463, 2.125), (2.463, 1.787), (2.463, 1.449), (2.463, 1.280), (2.463, 1.111), (2.463, 0.942), (2.125, 1.787), (2.125, 1.449), (2.125, 1.280), (2.125, 1.111), (2.125, 0.942), (1.787, 1.449), (1.787, 1.280), (1.787, 1.111), (1.787, 0.942), (1.449, 1.449), (1.449, 1.280), (1.449, 1.111), (1.449, 0.942), (1.280, 1.111), (1.280, 0.942), and (1.111, 0.942), with all bond lengths in a.u.

To illustrate the results for pairs with one or both bond lengths displaced from r_o (the averaged internuclear separation in the ground vibrational state of H_2), in Table 4 we list our values for the dipole expansion coefficients when $r_1 = 1.787$ a.u. and $r_2 = 1.449$ a.u., and we compare with the values given earlier by Fu et al. [22]. In general, we find excellent agreement. The values of A_{0001}, A_{2021}, A_{0221}, A_{2023}, A_{0223}, A_{2233}, A_{2243}, and A_{2245} agree quite closely, particularly given the extension of the basis set and the corrections for hyperpolarization effects included in the current work. A few of the coefficients show larger differences, based on differences in the fitting procedures. In the current work, we have omitted the coefficients A_{2221} and A_{2223}, which were included by Fu et al.; this contributes to the difference in the fitted values of A_{2211}. On the other hand, we have included A_{4043} and A_{0443}, which were omitted by Fu et al. [22]; this probably accounts for the difference in the values of A_{4045} and A_{0445} shown in Table 4. Our inclusion of A_{4221}, A_{2421}, A_{4223}, A_{2423}, A_{4243}, A_{2443}, A_{4245}, A_{2445}, A_{4265}, A_{2465}, A_{4267}, and A_{2467} in the fitting procedure also causes slight shifts in the values of the other coefficients.

No previous results are available for comparison when one or both of the molecules in the pair have bond lengths of 0.942 a.u., 1.280 a.u., 2.125 a.u, 2.463 a.u., or 2.801 a.u. In Table 5, we provide results for one such combination of bond lengths, with $r_1 = 2.463$ a.u. and $r_2 = 1.787$ a.u. The coefficients listed in the top line of each set (and the corresponding coefficients for other pairs of bond lengths) were used in generating the rototranslational and vibrational spectra. These were obtained from fits that included 26 dipole coefficients all together (with A_{2211} and A_{2233}, but not A_{2221} and A_{2223}); immediately below those results in each set, we list values obtained from fits with 27 dipole coefficients (including A_{2221} and A_{2223}, but not A_{2211}). We find that the coefficients A_{0001}, A_{2021}, A_{2023}, A_{2243}, A_{2245}, A_{4043}, and A_{4045} are numerically "robust;" these coefficients are little affected by the difference in the fitting procedure. The coefficients A_{0221}, A_{0223}, A_{2233}, A_{0443}, and A_{0445} show greater sensitivity, although the agreement tends to improve as the separation between the molecular centers R increases (particularly for A_{0223} and A_{2233}). The full results for the new potential energy surface and the pair dipoles, with individual H_2 bond lengths ranging from 0.942 a.u. to 2.801 a.u., will be reported and analyzed in a subsequent paper. However, here we note that the coefficients A_{2023}, A_{0223}, A_{2233}, A_{4045}, and A_{0445} appear to be dominated by long-range induction mechanisms, specifically quadrupolar induction for A_{2023}, A_{0223}, and A_{2233}, hexadecapolar induction for A_{4045} and A_{0445}, and E-tensor induction for A_{2245}. When the logarithms of the absolute values of these coefficients are plotted versus the logarithms of the separations R between the molecular centers of mass, over the range from 8.0 a.u. to 10.0 a.u., the slopes are -4.20 for A_{2023}, -4.08 for A_{0223}, and -3.995 for A_{2233}, all close to the quadrupolar-induction value of -4. Similarly, the slopes are -6.42 for A_{4045} and -6.34 for A_{0445}, close to the value of -6 for hexadecapolar induction; and the slope is -5.84 for A_{2245}, close to the value of -6 for E-tensor induction [17].

3. About the Spectra

The absorption spectrum is a quasicontinuum, consisting of many thousand highly diffuse, unresolved "lines," corresponding to rotovibrational transitions from an initial state $\{\nu_1, j_1, \nu_2, j_2\}$, to a final state $\{\nu_1', j_1', \nu_2', j_2'\}$, of the binary collision complex. Under the conditions encountered in cool stellar atmospheres, vibrational quantum numbers ν from 0 to about 5 occur with significant population numbers, with rotational quantum numbers j up to 20 or so, for H_2 molecules.

The isotropic potential approximation (IPA), which neglects the anisotropic terms of the intermolecular potential, is used for the calculation of the spectra [2]. Each "line" requires as input the matrix elements of the spherical dipole components [2]

$$\langle \nu_1 j_1 \nu_2 j_2 \mid A_{\lambda_1\lambda_2\Lambda L}(R, r_1, r_2) \mid \nu_1' j_1' \nu_2' j_2' \rangle, \qquad (5)$$

Table 4: Dipole expansion coefficients $A_{\lambda\lambda'\Lambda L}$ (in a.u., multiplied by 10^6) for H_2–H_2 with $r_1 = 1.787$ a.u. and r_2=1.449 a.u. The results from this calculation are compared with the results of Fu et al. (FZB), [22].

	R (a.u.)	4.0	5.0	6.0	7.0	8.0	9.0	10.0
A_{0001}	This work	−22960	−5786	−1241	−203	−10	13	9
	FZB	−21869	−5518	−1232	−231	−29	6	—
A_{2021}	This work	20653	4618	928	168	26	2	1
	FZB	21290	4688	963	194	45	15	—
A_{0221}	This work	−10595	−2394	−486	−95	−16	−1	−2
	FZB	−11028	−2450	−508	−108	−28	−10	—
A_{2023}	This work	−32456	−12335	−5392	−2735	−1554	−957	−624
	FZB	−32287	−12113	−5368	−2749	−1568	−966	—
A_{0223}	This work	23916	10071	4764	2525	1459	905	591
	FZB	23778	9865	4685	2488	1439	889	—
A_{2211}	This work	733	166	37	7	0	−2	0
	FZB	528	126	26	3	0	0	—
A_{2233}	This work	3079	1497	789	443	260	161	106
	FZB	2952	1415	750	423	253	158	—
A_{2243}	This work	−316	−242	−150	−88	−55	−34	−23
	FZB	−375	−263	−148	−83	−49	−30	—
A_{2245}	This work	416	180	86	39	19	10	5
	FZB	433	184	72	29	13	6	—
A_{4043}	This work	1981	529	123	29	8	3	1
A_{0443}	This work	−623	−185	−43	−9	0	1	0
A_{4045}	This work	−2079	−684	−224	−84	−35	−16	−9
	FZB	−3956	−1129	−322	−108	−43	−20	—
A_{0445}	This work	989	364	131	53	23	12	5
	FZB	1559	524	169	61	25	11	—

and the isotropic component of the intermolecular potential for the initial (unprimed) state

$$\langle \nu_1 j_1 \nu_2 j_2 \mid V_{000}(R, r_1, r_2) \mid \nu_1 j_1 \nu_2 j_2 \rangle; \quad (6)$$

the potential for the final state is given by a similar expression, where all rotovibrational quantum numbers are primed. The line shape calculations proceed with these expressions as described elsewhere [2]. In (5), (6), as above, R designates the intermolecular separation and r_1, r_2 the intramolecular separations. The indices $\lambda_1\lambda_2\Lambda L$ are the expansion parameters of the spherical dipole components in (2).

Figure 1 shows the calculated absorption coefficient $\alpha(\nu; T)$, normalized by the numerical density ρ squared, at the temperature T of 297.5 K, and frequencies ν from 0 to 3000 cm^{-1} (the "rototranslational band"). Laboratory measurements [28] are shown for comparison (•). Good agreement of theory and measurements is observed.

We note that similarly good agreement of theory and measurement was previously observed, based on an earlier *ab initio* ID surface and a refined intermolecular potential [2, 12]. In the present work, a more complete induced dipole surface has been obtained and used, although the extension has not significantly affected the rototranslational band, shown in Figure 1. Additionally, a new potential energy surface has been obtained and used in the current work. This new potential surface (as well as the new ID surface) accounts for highly rotovibrationally excited H_2 molecules; and the new surfaces will be essential for our high-temperature opacity calculations—but again, the extensions of the potential surface are of little consequence for the rototranslational band, Figure 1, near room temperature.

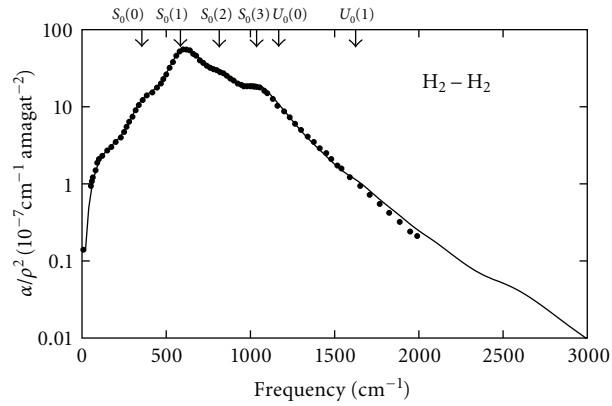

Figure 1: The calculated absorption spectrum of pairs of molecular hydrogen in the rototranslational band of H_2, at the temperature of 297.5 K, and comparison with laboratory measurements (• from [28]).

The new potential surface is believed to be accurate in the repulsive region of the interaction, but it is not as

Table 5: Dipole expansion coefficients $A_{\lambda\lambda'\Lambda L}$ (in a.u., multiplied by 10^6) for H_2-H_2 with $r_1 = 2.463$ a.u. and $r_2 = 1.787$ a.u. Results from the fit used to calculate the spectra (top line in each set) are compared with an alternate fit, which includes A_{2221} and A_{2223}, but not A_{2211}.

R (a.u.)	4.0	5.0	6.0	7.0	8.0	9.0	10.0
A_{0001}	−67727	−18429	−4357	−863	−119	8	14
	−65778	−19365	−4616	−960	−112	22	25
A_{2021}	61278	16009	3620	734	126	12	−3
	61859	15730	3543	705	128	16	0.5
A_{0221}	−23618	−6192	−1472	−322	−60	−9	−1
	−14285	−4351	−1033	−235	−47	−10	−1
A_{2023}	−77947	−28920	−11520	−5413	−2954	−1786	−1157
	−78659	−28577	−11425	−5378	−2956	−1791	−1161
A_{0223}	47485	20508	9741	5119	2948	1819	1185
	53866	22606	10265	5251	2955	1809	1178
A_{2211}	2759	674	164	37	4	−2	−1
A_{2221}	9063	937	201	10	16	8	7
A_{2223}	3803	2494	642	187	1	−19	−15
A_{2233}	6468	3571	1978	1144	678	424	278
	−2544	1369	1441	1024	666	430	282
A_{2243}	−1604	−788	−575	−362	−223	−143	−94
	−1711	−737	−561	−357	−223	−143	−95
A_{2245}	4102	1139	545	266	129	66	35
	4222	1082	530	260	129	67	36
A_{4043}	8512	2914	742	175	45	14	5
	8404	2966	756	181	44	13	4
A_{0443}	−1310	−616	−178	−41	−8	0	1
	−1531	−510	−149	−30	−8	−2	−1
A_{4045}	−7655	−3106	−984	−339	−134	−62	−32
	−7534	−3165	−1000	−345	−133	−61	−31
A_{0445}	2393	1086	415	162	70	33	17
	2640	968	382	150	71	35	19

extensively modeled in the well region, and at long range (dispersion part). Nevertheless, the measurements of the absorption spectra are as closely reproduced by the new *ab initio* input, Figure 1, as they are by the earlier advanced models. Apparently, the collision-induced absorption spectra arise mainly through interactions in the repulsive part of the potential, which is certainly consistent with previous observations [2].

The new opacity calculations of the fundamental and H_2 overtone bands [29] show similar agreement with measurements. Figure 2 shows the calculated normalized absorption coefficients over a frequency band ranging from the microwave region of the spectrum to the visible. In these calculations, we have used the exact equilibrium populations for the initial states, which at 2000 K consist of $v = 0$, 1, and 2, with many different rotational states, including highly excited states. For the final states (after a photon of energy up to 2.5 eV has been absorbed), we have included much higher rotovibrational states of the molecules. We have accounted for all of these states rigorously, using the new intermolecular potential and induced dipole surfaces.

The coarse structures seen in the spectrum correspond roughly to the rototranslational band (peak near 600 cm^{-1}), the fundamental band of H_2 (peak near 4200 cm^{-1}), and the first through fourth overtone bands of H_2 (remaining peaks). Unfortunately, no measurements exist for these high-frequency data, but we feel that the results shown are of comparable reliability to the results in Figure 1.

Calculations of the type shown supplement previous estimates, especially at the highest frequencies [10, 30]. Presently, we are attempting calculations of H_2–H_2 opacities at still higher temperatures (up to 7000 K). Moreover, similar calculations are planned for H_2-He and H_2-H collisional complexes.

4. Conclusion

We report opacity calculations of collisional H_2–H_2 complexes for temperatures of thousands of kelvin and a frequency range from the microwave to the visible regions of the electromagnetic spectrum. The calculations are based on new *ab initio* induced dipole and potential energy surfaces of rotovibrating H_2 molecules, and are intended to facilitate modeling the atmospheres of cool stars. Agreement with earlier theoretical work and laboratory measurements, where these exist, is excellent.

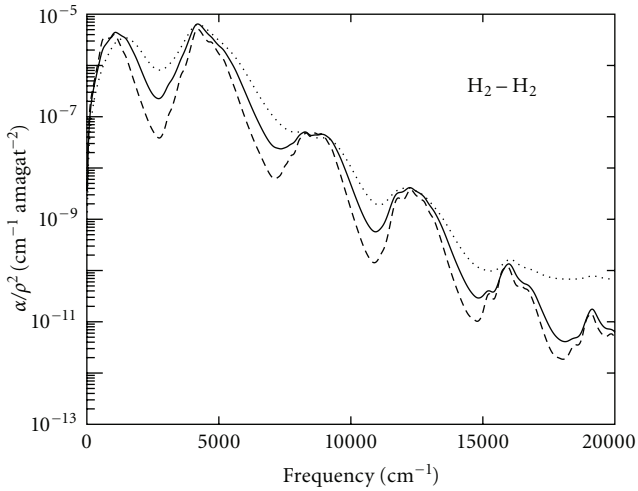

Figure 2: Calculated absorption spectrum of pairs of molecular hydrogen, from the far infrared to the visible, at the temperatures of 600 K (dashes), 1000 K (solid line), and 2000 K (dotted).

Acknowledgments

This work has been supported in part by the National Science Foundation Grants AST-0709106 and AST-0708496 and by the National Natural Science Foundation of China Grant NSFC-10804008.

References

[1] H. L. Welsh, "Pressure induced absorption spectra of hydrogen," in *MTP International Review of Science. Physical Chemistry, Series One, Vol. III: Spectroscopy*, A. D. Buckingham and D. A. Ramsay, Eds., chapter 3, pp. 33–71, Butterworths, London, UK, 1972.

[2] L. Frommhold, *Collision-Induced Absorption in Gases*, Cambridge University Press, Cambridge, UK, 2006.

[3] L. M. Trafton, "The thermal opacity in the major planets," *Astrophysical Journal*, vol. 140, p. 1340, 1964.

[4] L. M. Trafton, "Planetary atmospheres: the role of collision-induced absorption," in *Molecular Complexes in Earth's, Planetary, Cometary, and Interstellar Atmospheres*, A. A. Vigasin and Z. Slanina, Eds., pp. 177–193, World Scientific, Singapore, 1998.

[5] J. Mould and J. Liebert, "Infrared photometry and atmospheric composition of cool white-dwarfs," *Astrophysical Journal*, vol. 226, pp. L29–L33, 1978.

[6] P. Bergeron, D. Saumon, and F. Wesemael, "New model atmospheres for very cool white dwarfs with mixed H/He and pure He compositions," *Astrophysical Journal*, vol. 443, no. 2, pp. 764–779, 1995.

[7] B. M. S. Hansen, "Old and blue white-dwarf stars as a detectable source of microlensing events," *Nature*, vol. 394, no. 6696, pp. 860–862, 1998.

[8] D. Saumon and S. B. Jacobson, "Pure hydrogen model atmospheres for very cool white dwarfs," *Astrophysical Journal*, vol. 511, no. 2, pp. L107–L110, 1999.

[9] P. Bergeron, S. K. Leggett, and M. T. Ruiz, "Photometric and spectroscopic analysis of cool white dwarfs with trigonometric parallax measurements," *The Astrophysical Journal, Supplement Series*, vol. 133, no. 2, pp. 413–449, 2001.

[10] A. Borysow, U. G. Jørgensen, and Y. Fu, "High-temperature (1000–7000 K) collision-induced absorption of H_2 pairs computed from the first principles, with application to cool and dense stellar atmospheres," *Journal of Quantitative Spectroscopy and Radiative Transfer*, vol. 68, no. 3, pp. 235–255, 2001.

[11] W. Meyer and L. Frommhold, "Collision-induced rototranslational spectra of H_2-He from an accurate *ab initio* dipole moment surface," *Physical Review A*, vol. 34, no. 4, pp. 2771–2779, 1986.

[12] W. Meyer, L. Frommhold, and G. Birnbaum, "Rototranslational absorption spectra of H_2-H_2 pairs in the far infrared," *Physical Review A*, vol. 39, no. 5, pp. 2434–2448, 1989.

[13] W. Meyer, A. Borysow, and L. Frommhold, "Absorption spectra of H_2-H_2 pairs in the fundamental band," *Physical Review A*, vol. 40, no. 12, pp. 6931–6949, 1989.

[14] W. Meyer, A. Borysow, and L. Frommhold, "Collision-induced first overtone band of gaseous hydrogen from first principles," *Physical Review A*, vol. 47, no. 5, pp. 4065–4077, 1993.

[15] H.-J. Werner, P. J. Knowles, J. Almlöf, et al., *MOLPRO, Version 2000.1*, Universität Stuttgart, Stuttgart, Germany and Cardiff University, Cardiff, UK, 2000.

[16] X. Li, C. Ahuja, J. F. Harrison, and K. L. C. Hunt, "The collision-induced polarizability of a pair of hydrogen molecules," *Journal of Chemical Physics*, vol. 126, no. 21, Article ID 214302, 2007.

[17] J. E. Bohr and K. L. C. Hunt, "Dipoles induced by long-range interactions between centrosymmetric linear molecules: theory and numerical results for $H_2 \ldots H_2$, $H_2 \ldots N_2$, and $N_2 \ldots N_2$," *The Journal of Chemical Physics*, vol. 87, no. 7, pp. 3821–3832, 1987.

[18] X. Li and K. L. C. Hunt, "Transient, collision-induced dipoles in pairs of centrosymmetric, linear molecules at long range: Results from spherical-tensor analysis," *The Journal of Chemical Physics*, vol. 100, no. 12, pp. 9276–9278, 1994.

[19] K. L. C. Hunt, "Long-range dipoles, quadrupoles, and hyperpolarizabilities of interacting inert-gas atoms," *Chemical Physics Letters*, vol. 70, no. 2, pp. 336–342, 1980.

[20] L. Galatry and T. Gharbi, "The long-range dipole moment of two interacting spherical systems," *Chemical Physics Letters*, vol. 75, pp. 427–433, 1980.

[21] K. L. C. Hunt and J. E. Bohr, "Effects of van der Waals interactions on molecular dipole moments: The role of field-induced fluctuation correlations," *The Journal of Chemical Physics*, vol. 83, no. 10, pp. 5198–5202, 1985.

[22] Y. Fu, Ch. Zheng, and A. Borysow, "Quantum mechanical computations of collision-induced absorption in the second overtone band of hydrogen," *Journal of Quantitative Spectroscopy and Radiative Transfer*, vol. 67, no. 4, pp. 303–321, 2000.

[23] J. D. Poll and L. Wolniewicz, "The quadrupole moment of the H_2 molecule," *The Journal of Chemical Physics*, vol. 68, no. 7, pp. 3053–3058, 1978.

[24] F. Visser, P. E. S. Wormer, and W. P. J. H. Jacobs, "The nonempirical calculation of second-order molecular properties by means of effective states. III. Correlated dynamic polarizabilities and dispersion coefficients for He, Ne, H_2, N_2, and O_2," *The Journal of Chemical Physics*, vol. 82, no. 8, pp. 3753–3764, 1985.

[25] G. Karl, J. D. Poll, and L. Wolniewicz, "Multipole moments of hydrogen molecule," *Canadian Journal of Physics*, vol. 53, pp. 1781–1790, 1975.

[26] D. M. Bishop and J. Pipin, "Dipole, quadrupole, octupole, and dipole octupole polarizabilities at real and imaginary frequencies for H, He, and H_2 and the dispersion-energy coefficients for interactions between them," *International Journal of Quantum Chemistry*, vol. 45, pp. 349–361, 1993.

[27] D. M. Bishop and J. S. Pipin, "Calculation of the dispersion-dipole coefficients for interactions between H, He, and H_2," *The Journal of Chemical Physics*, vol. 98, no. 5, pp. 4003–4008, 1993.

[28] G. Bachet, E. R. Cohen, P. Dore, and G. Birnbaum, "The translational rotational absorption spectrum of hydrogen," *Canadian Journal of Physics*, vol. 61, no. 4, pp. 591–603, 1983.

[29] M. Abel and L. Frommhold, To be published.

[30] A. Borysow, U. G. Jørgensen, and Ch. Zheng, "Model atmospheres of cool, low-metallicity stars: The importance of collision-induced absorption," *Astronomy and Astrophysics*, vol. 324, no. 1, pp. 185–195, 1997.

Hindawi Publishing Corporation
International Journal of Spectroscopy
Volume 2010, Article ID 804506, 8 pages
doi:10.1155/2010/804506

Research Article

Plasma Temperature Determination of Hydrogen Containing High-Frequency Electrodeless Lamps by Intensity Distribution Measurements of Hydrogen Molecular Band

Zanda Gavare, Gita Revalde, and Atis Skudra

Institute of Atomic Physics and Spectroscopy, University of Latvia, 4 Skunu Street., Riga LV-1050, Latvia

Correspondence should be addressed to Zanda Gavare, zanda.gavare@gmail.com

Received 15 April 2009; Revised 29 July 2009; Accepted 23 September 2009

Academic Editor: Chantal Stehle

The goal of the present work was the investigation of the possibility to use intensity distribution of the Q-branch lines of the hydrogen Fulcher-α diagonal band ($d^3\Pi_u^- \rightarrow a^3\sum_g^+$ electronic transition; Q-branch with $v = v' = 2$) to determine the temperature of hydrogen containing high-frequency electrodeless lamps (HFEDLs). The values of the rotational temperatures have been obtained from the relative intensity distributions for hydrogen-helium and hydrogen-argon HFEDLs depending on the applied current. The results have been compared with the method of temperature derivation from Doppler profiles of He 667.8 nm and Ar 772.4 nm lines. The results of both methods are in good agreement, showing that the method of gas temperature determination from the intensity distribution in the hydrogen Fulcher-α (2-2)Q band can be used for the hydrogen containing HFEDLs. It was observed that the admixture of 10% hydrogen in the argon HFEDLs significantly reduces the gas temperature.

1. Introduction

The high-frequency electrodeless lamps (HFEDLs) are well known as a bright radiators of narrow and intense spectral lines in wide spectral range from vacuum ultra violet to infrared. These lamps are widely used in Atomic Absorption Spectroscopy for the determination of metal concentrations [1, 2], and they are of interest in plasma-surface interaction investigations due to lack of electrodes [3, 4]. For the application of HFEDLs and for the discharge plasma modeling it is important to estimate the plasma parameters in the lamps. It is of particular importance to determine and control the gas temperature, since this parameter plays an important role for many relevant plasma processes. In our previous work for the discharge gas temperature estimation in HFEDLs we used the high-resolution spectroscopy method of the emission spectral line shape measurements using Fabry-Perot interferometer and Zeeman spectrometer and nonlinear spectral line shape modeling [5]. However, the method of the line shape modeling is very complicated due to the necessity to solve the incorrect inverse task [6]. It is of great interest to find other methods and verify their applicability for the determination of plasma temperature in HFEDLs. In the case of hydrogen containing plasmas, one of the commonly used techniques for the determination of gas temperature is based on the measurements of the intensity distribution in the rotational bands of hydrogen molecule [7–18], for instance, (0-0), (1-1), (2-2), and (3-3) Q-branches of Fulcher-α ($d^3\Pi_u^- \rightarrow a^3\Sigma_g^+$) electronic transition [9–18]. The determination of the gas temperature from measured intensity distribution in rotational bands is based on a certain theoretical model, which involves series of assumptions about the mechanism of the excitation-deexcitation of rotational-vibrational (vibronic) levels of hydrogen. According to this model, the translational gas temperature may be in equilibrium with rotational temperature determined from either upper or lower energy level depending on processes in plasma under study [8, 12, 14].

For example, as it was shown by Tomasini et al. [12], in the case of hydrogen containing microwave discharge the ground state rotational temperature can be used at pressure of 0.5 Torr to derive the gas temperature, while at higher pressure (1 Torr) the authors observed discrepancy between temperature obtained from the Doppler broadening

and rotational temperature derived from the ground state energies.

Garg et al. [14] compared temperature values obtained from hydrogen Fulcher-α (0-0)Q-branch with those derived from the rotational band of N_2 molecule. They found that in the microwave plasma at pressure 10 Torr, the H_2 rotational temperatures derived using upper and lower level rotational constants are far from equilibrium with translational temperature and they do not accurately represent the translational temperature under their experimental conditions.

Iordanova [17] used the ground state rotational temperature of hydrogen molecule to derive temperature of the RF (excited at 27 MHz frequency) inductively driven H_2 plasma in the pressure range 26–60 mTorr, estimating that in this pressure range and at gas temperatures 300–900 K the characteristic time between heavy particle collisions is much longer than the radiation lifetime of the excited state, which means that the rotational distribution in the excited state is an image of the rotational distribution in the ground state.

Lebedev and Mokeev [18] used Fulcher-α (2-2)Q-branch to determine the microwave plasma temperature at pressures 1–8 Torr. They argued that at pressure 1 Torr the collision frequency ν_{coll} is much smaller than the radiative destruction frequency ν^* ($\nu_{\text{coll}} \ll \nu^*$), concluding that under their experimental conditions the gas temperature can be derived from the ground state rotational energies.

In each particular case, the relation between the rotational and translational temperatures needs to be verified. One way to establish the relationship between both temperatures is the comparison of the rotational temperature with that obtained by other methods, for example, the rovibrational bands of N_2 molecule [14] or Doppler broadening of the lines [12].

The Fulcher-α Q-branches have been used for the plasma temperature determination in different kinds of discharges; however for the diagnostics of the high-frequency electrodeless discharge lamps (excited at about 100 MHz frequency) it was not used before. Therefore, the goal of the present work was to investigate the possibility to use relative intensities of the Q-branch lines of the hydrogen Fulcher-α diagonal band ($d^3\Pi_u^- \rightarrow a^3\Sigma_g^+$ electronic transition; Q branch with $\nu = \nu' = 2$) in spectroscopic diagnostics of hydrogen containing HFEDLs. In this paper, the H_2 rotational temperature was obtained from the intensity measurements of Fulcher-α (2-2) Q-branch, and the results were compared with the temperature derived from the measurements of Doppler broadening of Ar and He atomic lines.

2. Experiment

The plasma sources under study was helium HFEDLs with hydrogen ($p_{He} \approx 0.9$ Torr, $p_{H2} \approx 0.1$ Torr) and argon HFEDLs with hydrogen ($p_{Ar} \approx 0.9$ Torr, $p_{H2} \approx 0.1$ Torr) manufactured at the *Institute of Atomic Physics and Spectroscopy, University of Latvia*. The cylindrical lamps with diameter of 2 cm and the length of 4 cm were placed into an induction coil and an inductive coupled discharge was exited by means of a high-frequency field of about 100 MHz frequency. The power of the discharge was changed, changing the applied current i into the coil in the region 80–200 mA. The gas temperature dependence from the current i in the induction coil was investigated.

The gas temperature of hydrogen and helium or argon containing HFEDL has been measured by two methods: using the relative intensities of the hydrogen (2-2)Q branch of Fulcher-α band and using the temperature derivation from Doppler profile of He 667.8 nm (He I 2^1P–3^1D) and Ar 772.4 nm (Ar I $1s_5$–$2p_7$) lines.

2.1. Experimental Setup for the Rotational Temperature Determination. The light from the lamp was imaged on the entrance slit of the spectrometer (*JobinYvon SPEX 1000 M*, grating 1200 l · mm^{-1}, focal length 1 m) and detected by means of a charge-coupled device matrix detector (2048 × 512 *Thermoelectric Front Illuminated UV Sensitive CCD Detector, Simphony*). With this detector a spectral range of about 15 nm can be recorded at one time. The resolving power of the system spectrometer-CCD camera was ~136 pixels · nm^{-1}. The entrance slit was set at 30 μm. In Figure 1 the experimental setup for the temperature measurements is shown.

The emission spectra of the discharge under study have been recorded in the wavelength range λ = 620–630 nm, containing first five lines of the (2-2)Q branch of the Fulcher-α band system of the hydrogen molecule. Figure 2 shows an example of the recorded emission spectra of hydrogen containing HFEDL.

2.2. Experimental Setup for the Gas Temperature Determination from the Line Profile. The experimental setup for the spectral line shape registration by means of the Fabry-Perot interferometer is shown in Figure 3. The light, collected from the lamp, is transmitted through the pressure-scanned interferometer, focused on a monochromator, amplified and registered by means of a photomultiplier. Line profiles of He 667.8 nm (or Ar 772.4 nm) line were recorded using mirrors with a dielectric coating and a 1.4 cm spacer (free spectral range of 0.36 cm^{-1}).

The experimental work was organised in the following way. First, the measurement session was performed to obtain the gas temperature from the Fulcher-α band system of hydrogen (the first session). The first five lines Q_1–Q_5 could be distinguished and their intensity measured. The second session of measurements was performed to derive the temperature from the Doppler profile of helium or argon lines. After the second measurement session the control measurements of the lamp spectra was made (the control session).

3. Theoretical

3.1. Rotational Temperature Determination. The determination of the rotational temperature is based on the measurements of relative intensity distributions in the vibronic bands of Fulcher-α system; in this case, rovibronic line (Q_1–Q_5) intensities of Q-branch of the hydrogen Fulcher-α diagonal band ($d^3\Pi_u^-$ ($\nu = 2$) $\rightarrow$ $a^3\Sigma_g^+$ ($\nu' = 2$)electronic transition)

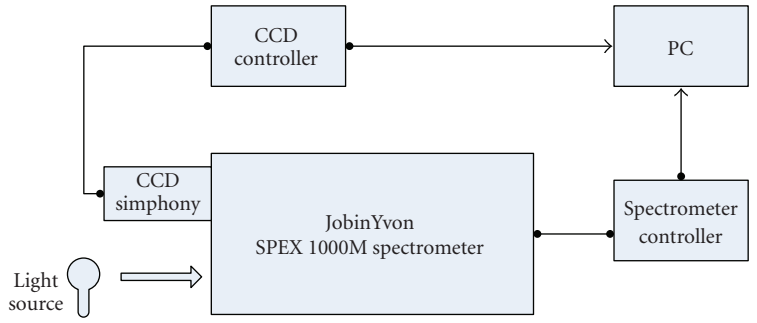

Figure 1: The experimental setup for the measurements of gas temperature using H_2 Fulcher-α (2-2)Q band.

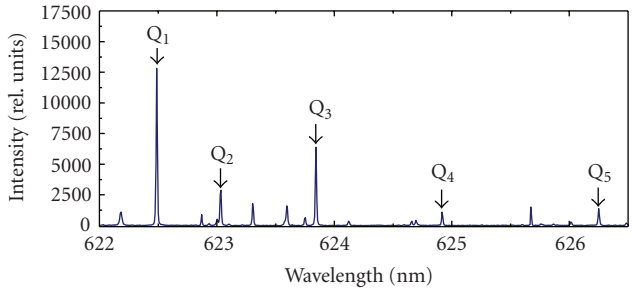

Figure 2: Example of a typical emission spectra of the hydrogen containing plasma of HFEDL recorded at applied current i = 80 mA, in the wavelength region containing five lines of the (2-2)Q branch of the Fulcher-α band system of the H_2 molecule.

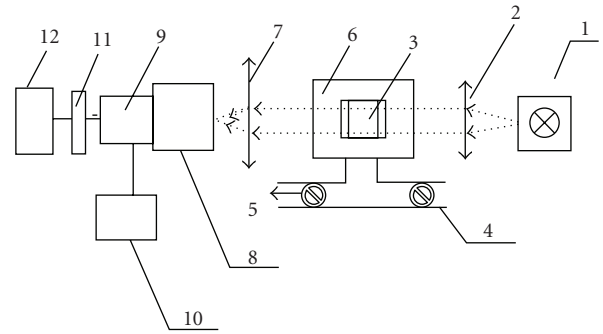

Figure 3: Experimental setup for spectral line profile measurements based on a pressure scanned Fabry-Perot interferometer. 1: Lamp inside the generator; 2: lens; 3: Fabry-Perot interferometer; 4, 5: capillary; 6: vacuum chamber; 7: lens; 8: monochromator; 9: photomultiplier; 10: power supply; 11: amplifier; 12: PC.

have been used. The transition diagram for these lines is shown in Figure 4.

The method of the determination of the gas temperature is described in detail in [8–10, 16, 19–21].

According to this model, the translational gas temperature may be in equilibrium with rotational temperature determined from either upper or lower energy level depending on processes in plasma under study [8, 12, 14, 16].

(i) The rotational temperature determined from the excited upper level can be equal to the translational temperature if the rotational relaxation time from the upper to the lower level is much smaller than the radiative lifetime (the destruction frequency of the $d^3\Pi_u$ state ν^* is lower than the neutral species rotational mixing collision frequency ν_{coll}, $\nu^* < \nu_{\text{coll}}$), and equilibrium between the rotational distribution and the neutral velocity distribution is achieved.

(ii) If the upper level is only populated by direct electron impact from the ground state, then the upper level rotational distribution is the image of the lower level rotational distribution. In this case the rotational temperature obtained from the lower level can be considered as a valid estimation of translational temperature. This condition is satisfied for low-pressure plasmas [14, 17].

It is necessary to mention that for the precise temperature derivation from the Fulcher-α bands it is necessary to take into account the excitation rate and vibrational distribution, for example, as it was done in [19–21]. Kado et al. in their work [19] show that there is a small discrepancy between values of rotational temperature derived with and without taking into account the vibrational excitation. However within the framework of this study we will use simple model with the following assumptions [8–10, 16]:

(1) the population distribution in the ground $X^1\Sigma_g^+$ ($v'' = 0$) vibronic state obeys Boltzmann's law (with the rotational temperature equal to gas temperature T_g);

(2) the excited states are populated mainly via electron collisions from the ground $X^1\Sigma_g^+$ ($v'' = 0$) vibronic state;

(3) the transitions with a change in angular momentum $|\Delta N| \geq 2$ may be neglected, and the rate coefficients are assumed to be independent of the rotational quantum number;

(4) the effective lifetime of the excited state does not depend on the rotational quantum number and is much shorter than the relaxation time of rotational levels.

In addition to the previous assumptions, if we assume that the rovibronic transition probability of the Q lines of

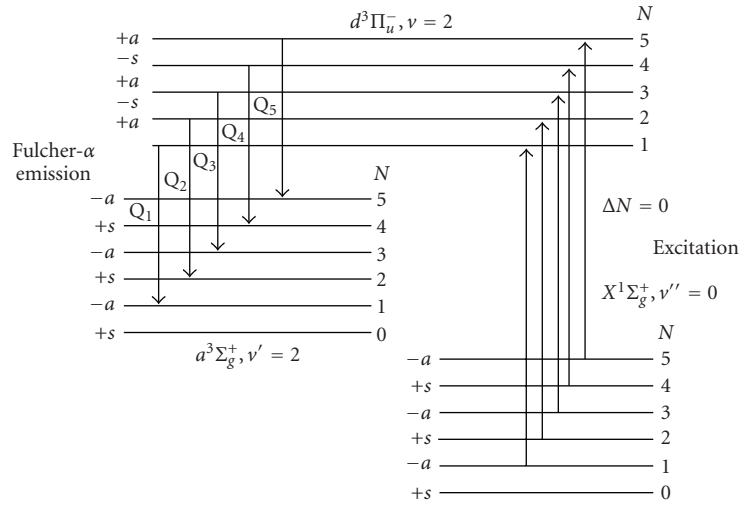

Figure 4: The transition diagram of the first five lines of hydrogen Fulcher-α (2-2)Q band.

Table 1: Transition parameters for the first five lines of (2-2)Q branch of Fulcher-α band of hydrogen molecule [22–24].

Line	E_{X0N}, K	N	$g_{a,s}$	λ, nm
Q_1	170,50	1	3	*622.4815*
Q_2	509,80	2	1	*623.0258*
Q_3	1015,10	3	3	*623.8391*
Q_4	1681,60	4	1	*624.9150*
Q_5	2503,80	5	3	*626.2495*

Fulcher-α (2-2) band does not depend on the rotational quantum number, the population of the level $d^3\Pi_u^-$ ($v = 2$, N) is related to the rotational temperature in the following way:

$$\frac{N_{nvN}}{g_{a,s}\cdot(2N+1)} \propto \frac{I^{nvN}_{n'v'N'}}{\left(\nu^{nvN}_{n'v'N'}\right)^3\cdot g_{a,s}\cdot(2N+1)} \propto \exp\left(-\frac{E_{X0N}}{T_{\text{rot}}}\right), \tag{1}$$

where N_{nvN} is the population of the level $d^3\Pi_u^-$ ($v = 2$, N), $I^{nvN}_{n'v'N'}$ is measured intensity of a spectral line, $\nu^{nvN}_{n'v'N'}$ is wavenumber of the radiative transition (in cm^{-1}), $g_{a,s}$ is statistical weight of the $d^3\Pi_u^-$ ($v = 2, N$) level, N is rotational quantum number, E_{X0N} is rotational energy of the ground state (in K), and T_{rot} is the temperature (in K). From (1) one may conclude that it is possible to determine the rotational temperature (equal to the gas temperature) by measuring the line intensities and knowing the transition parameters. The transition parameters for the lines of (2-2)Q branch of Fulcher-α band can be seen in Table 1 [22–24].

To determine the plasma temperature the formula (1) can be expressed through the logarithm in the following way:

$$\ln\left(\frac{I^{nvN}_{n'v'N'}}{\left(\nu^{nvN}_{n'v'N'}\right)^3\cdot g_{a,s}\cdot(2N+1)}\right) = -\frac{E_{X0N}}{T_{\text{rot}}} + \text{const}, \tag{2}$$

where in *const* all factors, which do not depend on the rotational quantum number, are combined. For the determination of the gas temperature it is necessary to plot the dependence of the logarithm of the reduced line intensity (left side of (2)) on the molecular rotational energy in the ground state E_{X0N}. A typical semilogarithmic plot of the Fulcher-α (2-2)Q branch lines is shown in Figures 5(a) and 5(b) for hydrogen-helium and hydrogen-argon HFEDLs, respectively. The temperature then can be obtained by applying the linear fit.

The linearity of these plots (Figure 5) indicates the Boltzmann distribution over the rotational levels. It can be seen that the point corresponding to the line Q_5 is higher (especially for the Ar + H_2 HFEDL, see Figure 5(b)), indicating the deviation from the Boltzmann distribution for this rotational level. The difference is only about 5%; yet it was excluded from the plots of Ar + H_2 HFEDL.

3.2. Gas Temperature Determination from the Line Profile. The gas temperature of the plasma under study has been obtained from the Doppler widths of the shapes of spectral lines (He 667.8 nm or Ar 772.4 nm), measured using Fabry-Perot interferometer.

The problem is that spectral line profile, registered by means of the interferometer, differs significantly from the real one. The observed distribution $f(x)$ is given by a convolution:

$$f(x) = \int_{-\infty}^{+\infty} f''(x-y)\cdot f'(y)\,dy + \xi(x), \tag{3}$$

where $f''(x)$ is the real profile of a spectral line, $f'(x)$ is the instrument function, and $\xi(x)$ is the function characterizing random errors. To determine the real spectral line profile $f''(x)$ (in our case—the real Doppler profile), it is necessary to solve the inverse task (see (3)). We used another method—the line fitting by means of a nonlinear multiparameter chi-square fit. It was assumed that the form of the experimental

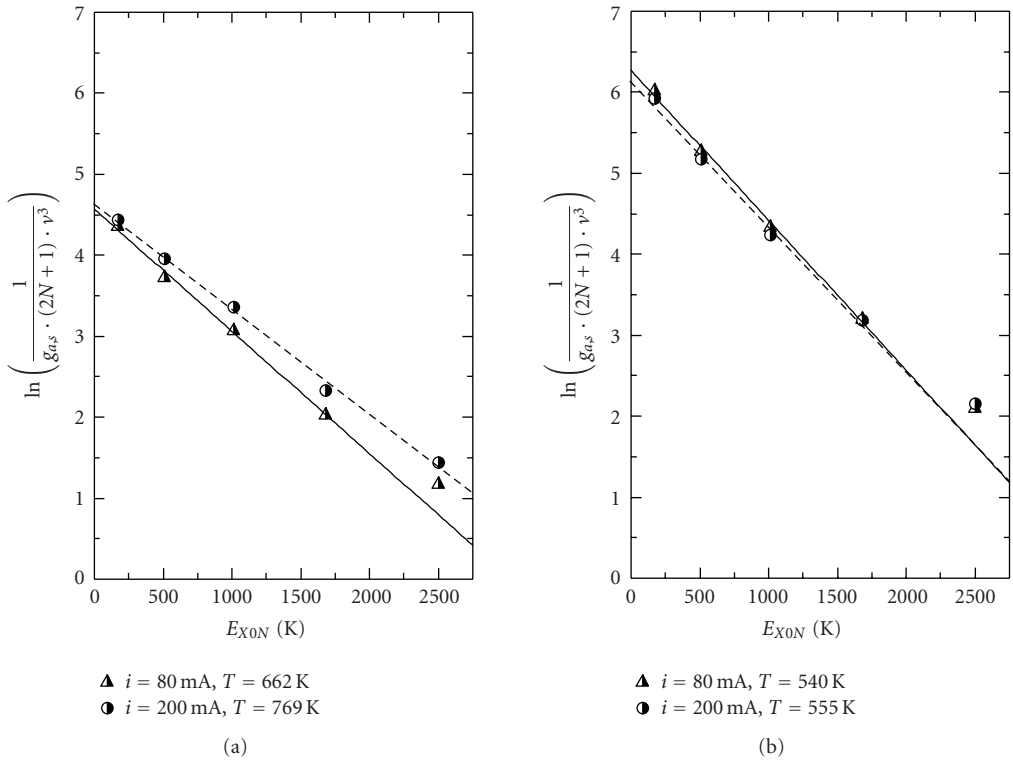

Figure 5: The semilogarithmic plot of scaled intensity of Fulcher-a (2-2)Q lines versus rotational energy of the molecular hydrogen ground state: (a) He + H_2 HFEDL and (b) Ar + H_2 HFEDL, at i = 80 mA and i = 200 mA.

profile can be approximated by the Voigt function, which is a convolution of the Gaussian and Lorentz functions:

$$V(a,\omega) = \frac{a}{\pi}\int_{-\infty}^{+\infty}\frac{\exp(-z^2)\,dz}{a^2+(\omega-y)^2},$$

$$a = \frac{\Delta\nu_L}{\Delta\nu_G}\sqrt{\ln 2}, \qquad \omega = \frac{2(\nu-\nu_0)}{\Delta\nu_G}\sqrt{\ln 2}, \tag{4}$$

$$z = \frac{(\nu-\nu')}{\Delta\nu_G}\sqrt{\ln 2},$$

where $V(a,\omega)$ is Voigt function describing the real line profile, $\Delta\nu_L$ is the Lorentzian width, $\Delta\nu_G$ is the Gaussian full-width at half-maximum (FWHM), ν_0 is line-center frequency, and ν is frequency. The profiles were fitted and deconvoluted from the Lorentz function, mainly composed of the instrumental function in our case, to obtain the real Doppler profile. In the case of helium and argon discharges we can neglect the effect of self-absorption which often has to be taken into account [5]. An example of experimental profile of He 667.8 nm line is shown in Figure 6.

The gas temperature has been calculated by well-known formula:

$$T = \mu\cdot\left(\frac{\Delta\lambda_D}{\lambda_0}\cdot\frac{1}{7,16\cdot 10^{-7}}\right)^2, \tag{5}$$

where T is gas temperature (K), $\Delta\lambda_D$ is Doppler width (FWHM), λ_0 is wavelength at the centre of the line, and μ is atomic mass of the species (in this case—atomic mass of helium or argon).

4. Results and Discussion

4.1. He and H_2 HFEDLs. In Figure 7 one may see the comparison of the temperature for the He and H_2 HFEDL, obtained by means of the two methods: using the intensities of the H_2 rotational lines of the (2-2)Q branch of the Fulcher-α band system and using the Doppler broadening of He 667.8 nm line.

The gas temperature ranging from 630 K to 740 K was obtained, depending on the applied current (80–200 mA). Relative uncertainty of the obtained temperature values using both methods is less than 10% (the uncertainties were obtained averaging results from the repeated measurements, the dispersion is due to the variances in the line intensities from measurement to measurement), and the difference between the results of both methods does not exceed 10%, too.

These results show that in the case of hydrogen containing helium-HFEDL the rotational distribution of the excited state can be considered as the image of the rotational distribution of the ground state.

The results of both methods coincide within experimental error, showing that the method of the gas temperature determination using molecular Fulcher-α (2-2)Q band of the hydrogen can be successfully used for the spectroscopic diagnostics of hydrogen containing HFEDLs. It is necessary to point out that there is a slight discrepancy between the rotational temperature and gas temperature at the applied current of 100 mA; however this difference is just about 75 K.

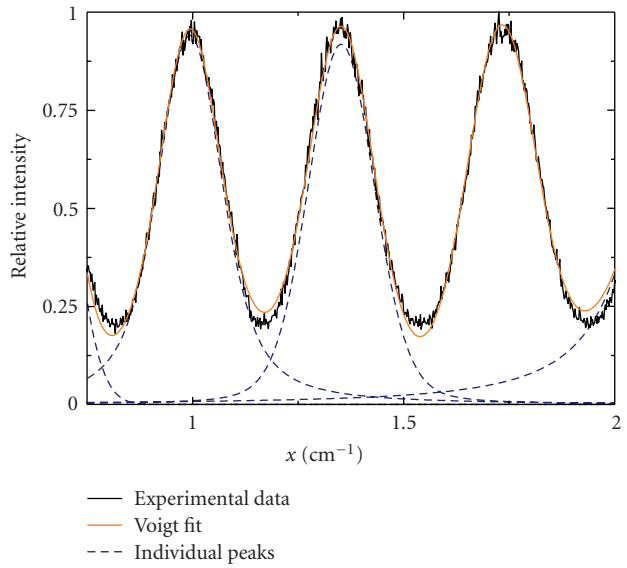

Figure 6: An example of experimental profile of helium emission line with wavelength 667.8 nm registered by means of Fabry-Perot interferometer at the applied current $i = 100$ mA. The profile fitting with the Voigt function has been performed. Obtained gas temperature from the Doppler width was equal to 628 ± 34 K.

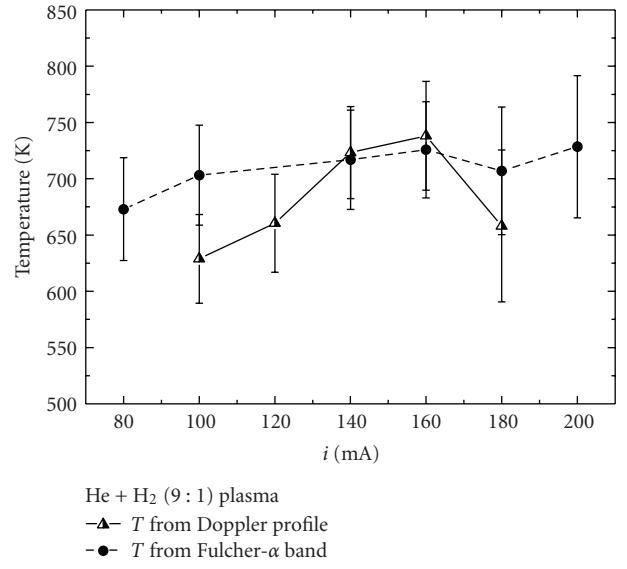

Figure 7: The temperature dependence on the applied current for the He + H_2 (9 : 1) HFEDL. Temperature values obtained using H_2 Fulcher-α (2-2)Q band are compared with the ones obtained from Doppler profile of helium emission line with wavelength 667.8 nm.

4.2. Ar and H_2 HFEDLs. Concerning Ar and H_2 HFEDL, we used this lamp to estimate the gas temperature difference of argon HFEDL in the presence of hydrogen admixture and without it. As mentioned before, initially the HFELD was filled with 0.9 Torr Ar and 0.1 Torr H_2. In Figure 8(a) one may see the emission spectra of the Ar + H_2 HFEDL recorded during the first measurement session, which consisted from

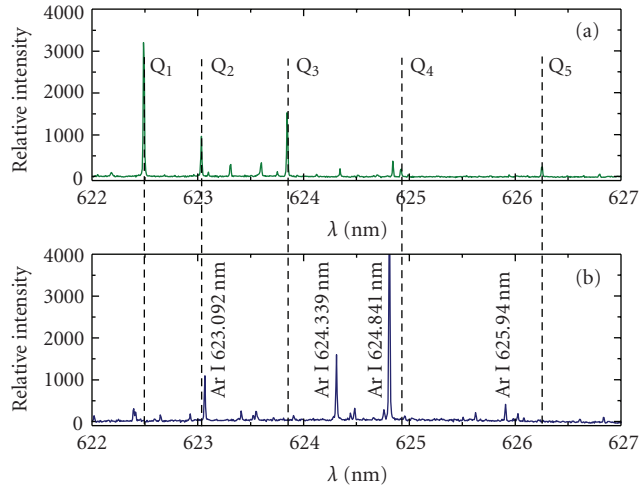

Figure 8: The emission spectra of the Ar HFEDL recorded at applied current $i = 100$ mA, in the wavelength region 622–627 nm: (a) argon disharge with admixture of hydrogen (9 : 1) with hydrogen Fulcher-α (2-2)Q first five lines (first measurement session); (b) pure argon discharge without hydrogen (the control session).

several repeated measurements to assess experimental uncertainties. From this session we estimated the gas temperature using the rotational line spectrum of hydrogen. Later we operated the HFEDL so long until the hydrogen was diffused out from the lamp through the walls. The diffusion of the hydrogen was indicated registering the spectra in the same spectral region as before. The lamp spectra showed at the end that the Fulcher-α (2-2)Q band could not be detected anymore (Figure 8(b)). Due to the fact that hydrogen was lost from the lamp during measurements, also visually one could observe the changing color of the discharge. The gas temperature using the Doppler broadening of argon lines was estimated during the second measurement session.

In the Figure 9 the dependence of the estimated gas temperature in dependence of the applied current is shown for two cases described before. The Line 1 indicates the temperature dependence for argon and hydrogen discharge plasma, estimated from the H_2 rotational lines of the (2-2)Q branch of the Fulcher-α band system during the first measurement session. Line 2 indicates the temperature for argon plasma after degassing of hydrogen, estimated from the Doppler broadening of Ar spectral line of 772.4 nm wavelength during the second measurement session.

The temperature of argon discharge with admixture of hydrogen was estimated about 620 K and changes not significantly by varying the applied current. Temperature estimated during second measurement session from Doppler broadening was changed from 620 K up to 1050 K (at applied current 180 mA) because of the hydrogen loses, namely, the plasma temperature was increased. During the second session the plasma content was changed and at the end only argon plasma was present.

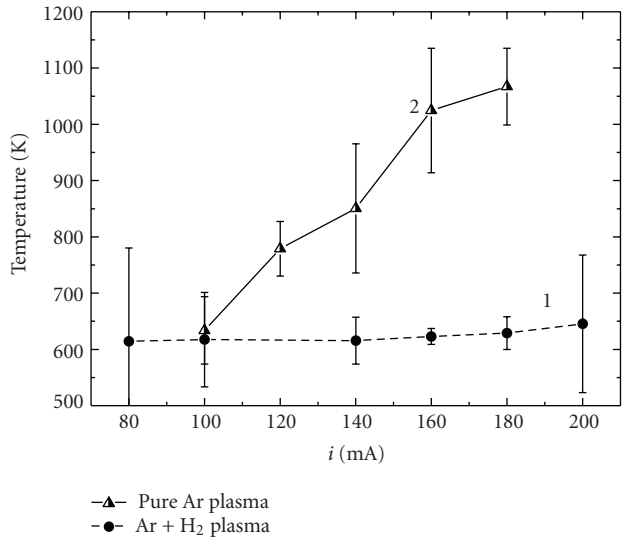

Figure 9: The temperature dependence on the applied current for the Ar and H_2 containing HFEDL. Temperature values obtained using Fulcher-α (2-2)Q band are compared with ones obtained from Doppler profile of argon emission line with wavelength 772.4 nm. Line 1 is temperature of Ar + H_2 (9 : 1) plasma obtained from Fulcher-α (2-2)Q band; Line 2 is temperature of pure Ar plasma obtained from the Doppler profile.

The difference between the temperatures of plasma with 10% admixture of hydrogen and pure argon plasma increases with increasing applied current.

So the results, shown in Figure 9, allow concluding that the addition of about 10% hydrogen in argon plasma causes the significant decrease of the gas temperature. The observation of argon emission quenching by the addition of hydrogen has been reported elsewhere [11, 25–28]. For instance, in [25, Page 349] it was mentioned that the addition of hydrogen quenches the argon's excited states, and in one of our previous articles [11] we reported the observation of the similar phenomenon in the microwave Ar + H_2 plasma, where the increase of the hydrogen percentage in the Ar plasma decreased the population of resonant and metastable states of Ar.

In addition, authors of [26] report the temperature decrease with increasing the percentage of hydrogen in the argon plasma (DC plasma).

One of the possible mechanisms involved in the cooling of the plasma is quenching of excited argon atoms by hydrogen molecules in the ground state, leading to excitation with subsequent dissociation of H_2 [27, 28]. Nevertheless it needs to be verified by detailed analysis of excitation and deexcitation processes in this kind of plasma.

5. Conclusion

From the results of our measurements we can conclude that it is possible to use relative intensities of the (2-2)Q branch of hydrogen Fulcher-α band for the gas temperature determination also in hydrogen containing high-frequency electrodeless lamps. The gas temperatures, obtained from Fulcher-α (2-2)Q band, are in good agreement with the ones obtained from the Doppler broadening of emission lines, but it is necessary to investigate further the applicability of this method for HFEDLs in the variety of experimental conditions.

Our experiments show that adding 10% of hydrogen in the argon high-frequency electrodeless discharge lamps significantly reduces the plasma temperature comparing to temperature of the plasma without hydrogen.

Acknowledgment

The work was partly supported by Latvian Council of Science Grant no. 05.1866.

References

[1] A. Ganeev, Z. Gavare, V. I. Khutorshikov, et al., "High-frequency electrodeless discharge lamps for atomic absorption analysis," *Spectrochimica Acta B*, vol. 58, no. 5, pp. 879–889, 2003.

[2] G. Revalde, N. Denisova, Z. Gavare, and A. Skudra, "Diagnostics of capillary mercury-argon high-frequency electrodeless discharge using line shapes," *Journal of Quantitative Spectroscopy and Radiative Transfer*, vol. 94, no. 3-4, pp. 311–324, 2005.

[3] A. Skudra, G. Revalde, Z. Gavare, J. Silinsh, N. Zorina, and B. Polyakov, "Study of the high-frequency inductive coupled discharge plasma interaction with walls," *Plasma Processes and Polymers*, vol. 4, supplement 1, pp. S1026–S1029, 2007.

[4] A. Skudra, N. Zorina, Z. Gavare, M. Berzins, and D. Erts, "Light source inner surface changes depending on treatment," *Physica Status Solidi C*, vol. 5, pp. 915–917, 2008.

[5] A. Skudra and G. Revalde, "Mathematical modelling of the spectral line profiles in the high-frequency discharge," *Journal of Quantitative Spectroscopy and Radiative Transfer*, vol. 61, no. 6, pp. 717–728, 1999.

[6] G. Revalde, A. Skudra, N. Zorina, and S. Sholupov, "Investigation of Hg resonance 184.9 nm line profile in a low-pressure mercury-argon discharge," *Journal of Quantitative Spectroscopy and Radiative Transfer*, vol. 107, no. 1, pp. 164–172, 2007.

[7] V. Schulz-von der Gathen and H. F. Döbele, "Critical comparison of emission spectroscopic determination of dissociation in hydrogen RF discharges," *Plasma Chemistry and Plasma Processing*, vol. 16, no. 4, pp. 461–486, 1996.

[8] S. A. Astashkevich, M. Käning, E. Käning, et al., "Radiative characteristics of 3p $\sum$, Π; 3d Π^-, Δ^--states of H_2 and determination of gas temperature of low pressure hydrogen containing plasmas," *Journal of Quantitative Spectroscopy and Radiative Transfer*, vol. 56, no. 5, pp. 725–751, 1996.

[9] T. Gans, V. Schulz-von der Gathen, and H. F. Döbele, "Time dependence of rotational state populations of excited hydrogen molecules in an RF excited plasma reactor," *Plasma Sources Science and Technology*, vol. 10, no. 1, pp. 17–23, 2001.

[10] M. Abdel-Rahman, T. Gans, V. Schulz-von der Gathen, and H. F. Döbele, "Space and time resolved rotational state populations and gas temperatures in an inductively coupled hydrogen RF discharge," *Plasma Sources Science and Technology*, vol. 14, no. 1, pp. 51–60, 2005.

[11] Z. Gavare, D. Goett, A. V. Pipa, J. Roepcke, and A. Skudra, "Determination of the number densities of argon metastables in argon-hydrogen plasma by absorption and self-absorption methods," *Plasma Sources Science and Technology*, vol. 15, no. 3, pp. 391–395, 2006.

[12] L. Tomasini, A. Rousseau, G. Gousset, and P. Leprince, "Spectroscopic temperature measurements in a H_2 microwave discharge," *Journal of Physics D*, vol. 29, no. 4, pp. 1006–1013, 1996.

[13] A. V. Pipa, *On determination of the degree of dissociation of hydrogen in non-equilibrium plasmas by means of emission spectroscopy*, Ph.D. thesis, University of Greifswald, Greifswald, Germany, 2004.

[14] R. K. Garg, T. N. Anderson, R. P. Lucht, T. S. Fisher, and J. P. Gore, "Gas temperature measurements in a microwave plasma by optical emission spectroscopy under single-wall carbon nanotube growth conditions," *Journal of Physics D*, vol. 41, no. 9, Article ID 095206, 2008.

[15] G. Lj. Majstorović, "Spectroscopic study of hydrogen rotational, vibrational and translational temperatures in a hollow cathode glow discharge," *Journal of Physics: Conference Series*, vol. 133, Article ID 012022, 2008.

[16] G. Lj. Majstorović, N. M. Šišović, and N. Konjević, "Rotational and vibrational temperatures of molecular hydrogen in a hollow cathode glow discharge," *Plasma Sources Science and Technology*, vol. 16, no. 4, pp. 750–756, 2007.

[17] S. Iordanova, "Spectroscopic temperature measurements in hydrogen inductively-driven plasmas at low pressures," *Journal of Physics: Conference Series*, vol. 113, no. 1, Article ID 012005, 2008.

[18] Yu. A. Lebedev and M. V. Mokeev, "Gas temperature in the plasma of a low-pressure electrode microwave discharge in hydrogen," *Plasma Physics Reports*, vol. 29, no. 3, pp. 226–230, 2003.

[19] Sh. Kado, D. Yamasaki, B. Xiao, et al., "On the anomalous characteristics in the P and R branches in a hydrogen fulcher band," *Journal of Plasma and Fusion Research*, vol. 7, pp. 54–58, 2006.

[20] B. Xiao, Sh. Kado, Sh. Kajita, and D. Yamasaki, "Rovibrational distribution determination of H_2 in low temperature plasmas by Fulcher-α band spectroscopy," *Plasma Physics and Controlled Fusion*, vol. 46, no. 4, pp. 653–668, 2004.

[21] E. Surrey and B. Crowley, "Spectroscopic measurement of gas temperature in the neutralizer of the JET neutral beam injection system," *Plasma Physics and Controlled Fusion*, vol. 45, no. 7, pp. 1209–1226, 2003.

[22] H. M. Crosswhite, Ed., *The Hydrogen Molecule Wavelength Tables of Gerhard Heinrich Dieke*, Wiley-Interscience, New York, NY, USA, 1972.

[23] S. A. Alexander and R. L. Coldwell, "Spectroscopic constants of H_2 using Monte Carlo methods," *International Journal of Quantum Chemistry*, vol. 100, no. 6, pp. 851–857, 2004.

[24] I. Dabrowski, "The Lyman and Werner bands of H_2," *Canadian Journal of Physics*, vol. 62, pp. 1639–1664, 1984.

[25] H. Yasuda, *Luminous Chemical Vapor Deposition and Interface Engineering*, Surfactant Science, CRC Press, Boca Raton, Fla, USA, 2004.

[26] I. Ishii, T. G. Beuthe, J. S. Chang, et al., "The influence of hydrogen gas mixtures on the argon thermal plasma temperature," *Research Reports of the Faculty of Engineering, Tokyo Denki University*, vol. 46, pp. 11–22, 1998.

[27] A. Bogaerts, "Hydrogen addition to an argon glow discharge: a numerical simulation," *Journal of Analytical Atomic Spectrometry*, vol. 17, no. 8, pp. 768–779, 2002.

[28] A. Bogaerts, Z. Chen, and R. Gijbels, "Glow discharge modelling: from basic understanding towards applications," *Surface and Interface Analysis*, vol. 35, no. 7, pp. 593–603, 2003.

Hindawi Publishing Corporation
International Journal of Spectroscopy
Volume 2010, Article ID 627571, 6 pages
doi:10.1155/2010/627571

Research Article

Absorption Line Profile of the $^5S_2^o - ^5P_1$ Transition of Atomic Oxygen and Its Application to Plasma Monitoring

K. Sasaki,[1] Y. Okumura,[2] and R. Asaoka[2]

[1] *Plasma Nanotechnology Research Center, Nagoya University, Nagoya 464-8603, Japan*
[2] *Department of Electrical Engineering and Computer Science, Nagoya University, Nagoya 464-8603, Japan*

Correspondence should be addressed to K. Sasaki, sasaki@nuee.nagoya-u.ac.jp

Received 15 April 2009; Accepted 27 May 2009

Recommended by Roland Stamm

The line profile of the $^5S_2^o - ^5P_1$ transition of atomic oxygen was measured by diode laser absorption spectroscopy. As a result, it was found that the absorption line profile had a wing component in the wavelength range detuned from the line center and was not fitted with a Gaussian function. The wing component was considered to be originated from dissociative excitation of molecular oxygen. We fitted the absorption line profile with the superposition of two Gaussian functions corresponding to high and low translational temperatures. We propose that the ratio of the high-temperature to low-temperature components is useful for monitoring the relative degree of dissociation of molecular oxygen in oxygen-containing plasmas. The ratio of the high-temperature to low-temperature components was compared with the survival ratio of molecular oxygen, which was evaluated from the lifetime of $O(^5S_2^o)$ in the afterglow of pulsed discharges.

1. Introduction

Low-pressure plasmas with electron densities below 10^{13} cm^{-3} are widely used for various material processing such as dry etching and plasma-enhanced chemical vapor deposition. The spectral line profiles of atoms and molecules in low-pressure, low-density plasmas are governed by Doppler broadening, which represents the velocity distribution function of atoms and molecules in plasmas. Since collisions among neutral species in plasmas used for material processing are frequent, it is expected that the velocity distribution functions of atoms and molecules are approximated by Maxwellian functions with widths corresponding to the species temperatures. However, there are several processes which deviate the velocity distribution functions of neutral species from Maxwellian functions.

Spectral profiles of hydrogen Balmer lines have been investigated intensively by optical emission spectroscopy, and many authors have reported the existence of large Doppler broadening in their spectral line profiles [1–10]. The existence of large Doppler broadening means that the velocity distribution function of emitting species contains a high-energy component. A possible mechanism for the production of the high-energy component is collision between molecular hydrogen and ions. Another process for explaining the existence of the high-energy component is dissociative excitation of molecular hydrogen. This is because electron impact dissociation of a diatomic molecule is divided into two steps. The first step is electron impact excitation to an electronic state having a repulsive potential curve without changing the distance between nuclei. The second step is automatic separation of nuclei along the repulsive potential curve. Since the energy of the dissociated state is lower than that of the repulsive potential curve immediately after electron impact excitation, atoms produced after dissociation have kinetic energies corresponding the energy difference.

A reason why the investigations of the spectral line profiles are concentrated in atomic hydrogen may be the smallest mass number. Since the spectral resolution of optical emission spectroscopy is not high, atomic hydrogen, which has the widest Doppler broadening width (the smallest mass number), is suitable for investigating the spectral line profile by optical emission spectroscopy. In this work, we examined the spectral line profile of the $^5S_2^o - ^5P_1$ transition of atomic oxygen by diode laser absorption spectroscopy. Since diode laser absorption spectroscopy has a much finer resolution than optical emission spectroscopy, we can examine the

detailed structure of the spectral line profile. In addition, we propose a method for monitoring the relative degree of dissociation of molecular oxygen in oxygen-containing discharges from the spectral line profile of the $^5S_2^o - ^5P_1$ transition. The plasma processing industry requires a simple, economical technique which is applicable to the monitoring of plasma processing tools. The proposed method has a potential as a plasma monitoring tool because of the compactness, simplicity, and the economical price of a diode laser.

2. Experiment

The plasma source and the system for diode laser absorption spectroscopy are the same as those used in a previous work [11], where we evaluated the gas temperatures in hydrogen plasmas from the absorption line profile of the Balmer-α line. We used pure oxygen at pressures from 30 to 100 mTorr for discharge in this experiment. Helicon-wave plasmas were produced by applying rf power at 13.56 MHz to a helical antenna wound around a glass discharge tube of 1.6 cm inner diameter. The plasma column with the same diameter as the glass tube was confined radially by the uniform magnetic field along the cylindrical axis of a vacuum chamber. The strength of the magnetic field was adjusted to be 70 G to avoid the distortion of the spectral line profile due to the Zeeman effect. The plasmas were produced in a pulsed mode with a discharge duration of 40 milliseconds and a repetition frequency of 2 Hz to avoid the overheating of the plasma source.

A commercial diode laser (TOPTICA, DL100) beam was injected into the plasma from the radial direction of the cylindrical vacuum chamber. The wavelength of the diode laser beam was tuned around the line center of the $^5S_2^o - ^5P_1$ transition (777.539 nm). The tuning of the laser wavelength was triggered at 15 milliseconds after the initiation of the pulsed discharge, when the plasma reached the steady-state condition. Sweeping the laser wavelength for ± 20 pm needed 20 milliseconds. The wavelength tuning of the diode laser beam was monitored using a spectrum analyzer. The power of the diode laser beam was attenuated below 10 μW to avoid saturation. The laser beam transmitted through the plasma was detected using a photomultiplier tube via a monochromator.

3. Absorption Line Profile and the Interpretation

For the sake of comparison, we produced an argon plasma and measured the absorption line profile of the $4s[3/2]_2^o$–$4p[3/2]_2$ transition at a wavelength of 763.510 nm. Figure 1 shows the absorption line profile of the $4s[3/2]_2^o$–$4p[3/2]_2$ transition observed at an argon pressure of 30 mTorr and an rf power of 1.5 kW. The open circles illustrated in Figure 1(a) represent the experimental result, and the solid curve shows the data fitting using a Gaussian function corresponding to a temperature of 0.066 eV. Figure 1(b) shows the difference between the experimental result and the data fitting. The difference

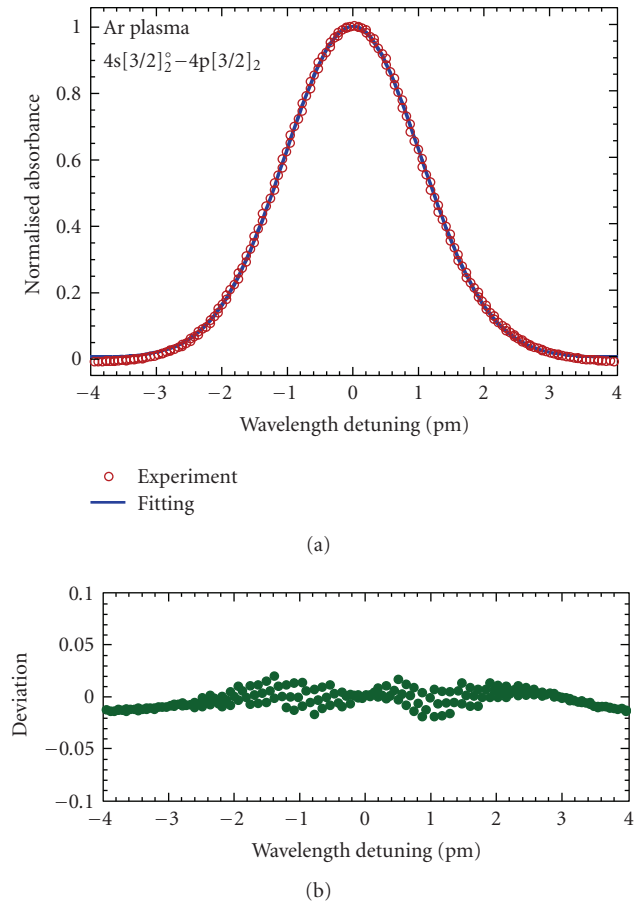

Figure 1: Absorption line profile of the $4s[3/2]_2^o$–$4p[3/2]_2$ transition of argon observed at an rf power of 1.5 kW and a pressure of 30 mTorr. The open circles illustrated in (a) show the experimental result, and the solid curve is the data fitting using a Gaussian function with a temperature of 0.066 eV. The difference between the experimental result and the data fitting is shown in (b).

shown in Figure 1(b) is fairly small, and the absorption line profile of the $4s[3/2]_2^o$–$4p[3/2]_2$ transition was approximated well by a Gaussian function.

Figure 2 shows the absorption line profile of the $^5S_2^o - ^5P_1$ transition of atomic oxygen observed in an oxygen plasma produced at an oxygen pressure of 30 mTorr and an rf power of 1.5 kW. The solid curve shown in Figure 2(a) represents a Gaussian profile corresponding to a temperature of 0.12 eV. It is clearly understood from Figure 2 that the absorption line profile of the $^5S_2^o - ^5P_1$ transition was not approximated by a Gaussian function. The comparison between the experimental result and the data fitting indicates that the velocity distribution function of the metastable $^5S_2^o$ state of atomic oxygen had a high-energy component. Figure 3 shows the data fitting of the same experimental absorption line profile with the superposition of two Gaussian functions corresponding to temperatures of 0.072 and 0.37 eV. The absorption line profile of the $^5S_2^o - ^5P_1$ transition observed experimentally was approximated well by the superposition of two Gaussian functions.

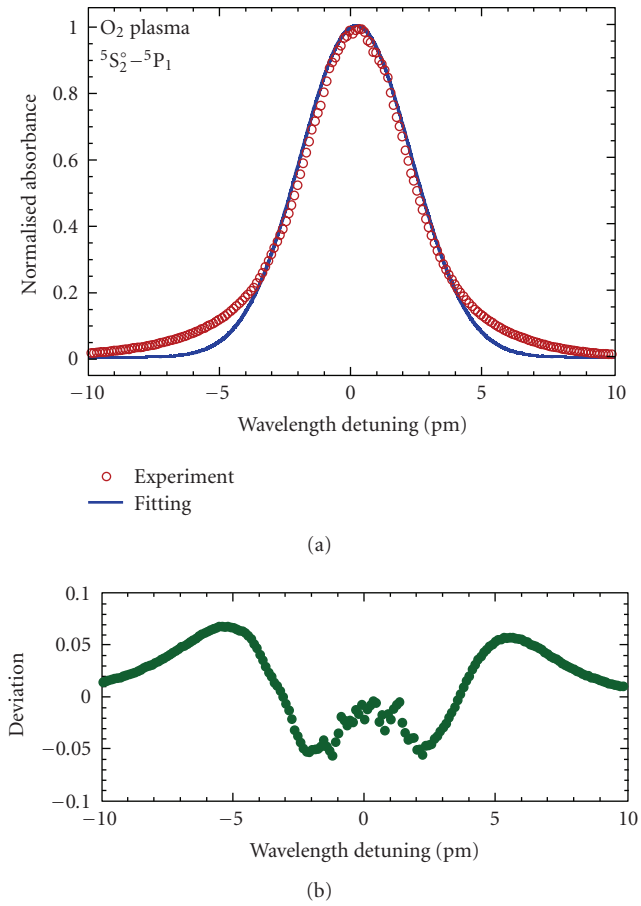

Figure 2: Absorption line profile of the ${}^5S_2^o - {}^5P_1$ transition of atomic oxygen observed at an rf power of 1.5 kW and a pressure of 30 mTorr. The open circles illustrated in (a) show the experimental result, and the solid curve is the data fitting using a Gaussian function with a temperature of 0.12 eV. The difference between the experimental result and the data fitting is shown in (b).

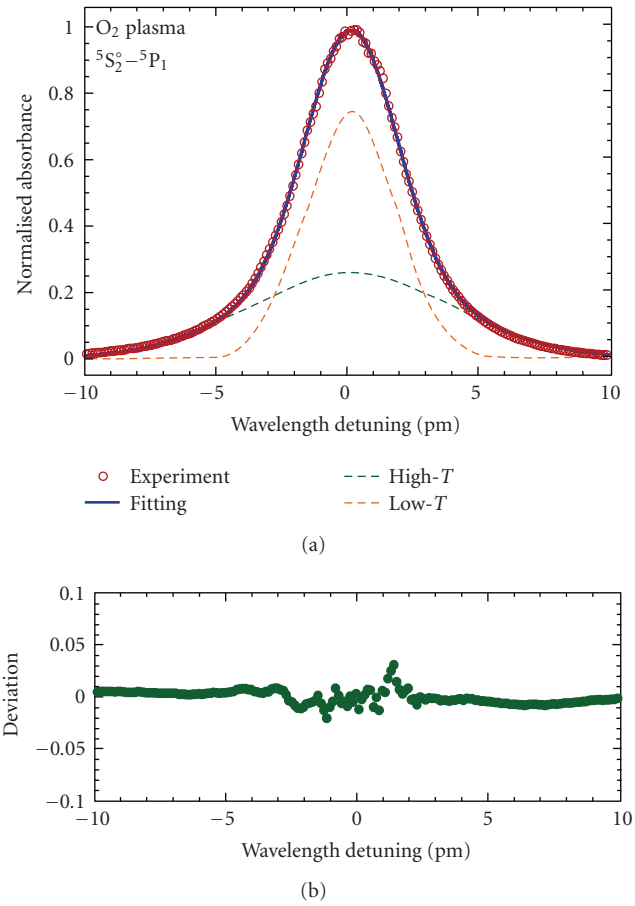

Figure 3: The same experimental absorption line profile as that shown in Figure 2 and the data fitting using the superposition of two Gaussian functions with temperatures of 0.072 and 0.37 eV. The difference between the experimental result and the data fitting is shown in (b).

There is a possibility that the temperatures of positive ions are higher than those of neutral species. In addition, there is a possibility that the velocity distribution function of positive ions has a high-energy component which is originated from the reflection of positive ions in the sheath. Therefore, charge exchange collision between positive ions and neutral species is a possible mechanism for the generation of the high-energy component in the velocity distribution function of neutral species. However, the experimental result that the absorption line profile of the $4s[3/2]_2^o$–$4p[3/2]_2$ transition of argon was approximated well by a Gaussian function indicates that the velocity distribution function of the metastable $4s[3/2]_2^o$ state of argon is thermalized completely, and the high-energy component originated from charge exchange collision is negligible in this plasma source.

A reasonable mechanism for explaining the high-energy component observed in the absorption line profile of the ${}^5S_2^o - {}^5P_1$ transition of atomic oxygen is dissociative excitation. In this interpretation of the spectral line profile, the low-energy component in the velocity distribution function of $O({}^5S_2^o)$ is produced by the three-step process represented by

$$O_2 + e \longrightarrow O({}^3P^o, \text{fast}) + O({}^3P^o, \text{fast}) + e, \quad (1)$$

$$O({}^3P^o, \text{fast}) + M \longrightarrow O({}^3P^o, \text{slow}) + M, \quad (2)$$

$$O({}^3P^o, \text{slow}) + e \longrightarrow O({}^5S_2^o, \text{slow}) + e. \quad (3)$$

Since the lifetime of $O({}^3P^o)$ is much longer than the reciprocal of the collision frequency, the velocity distribution function of $O({}^3P^o)$ is thermalized, and the high-energy component ($O({}^3P^o, \text{fast})$ in (1)) becomes negligible via elastic collision processes (2). On the other hand, the high-energy component in the velocity distribution function of $O({}^5S_2^o)$ is considered to be produced by dissociative excitation:

$$O_2 + e \longrightarrow O({}^5S_2^o, \text{fast}) + O({}^3P^o, \text{fast}) + e. \quad (4)$$

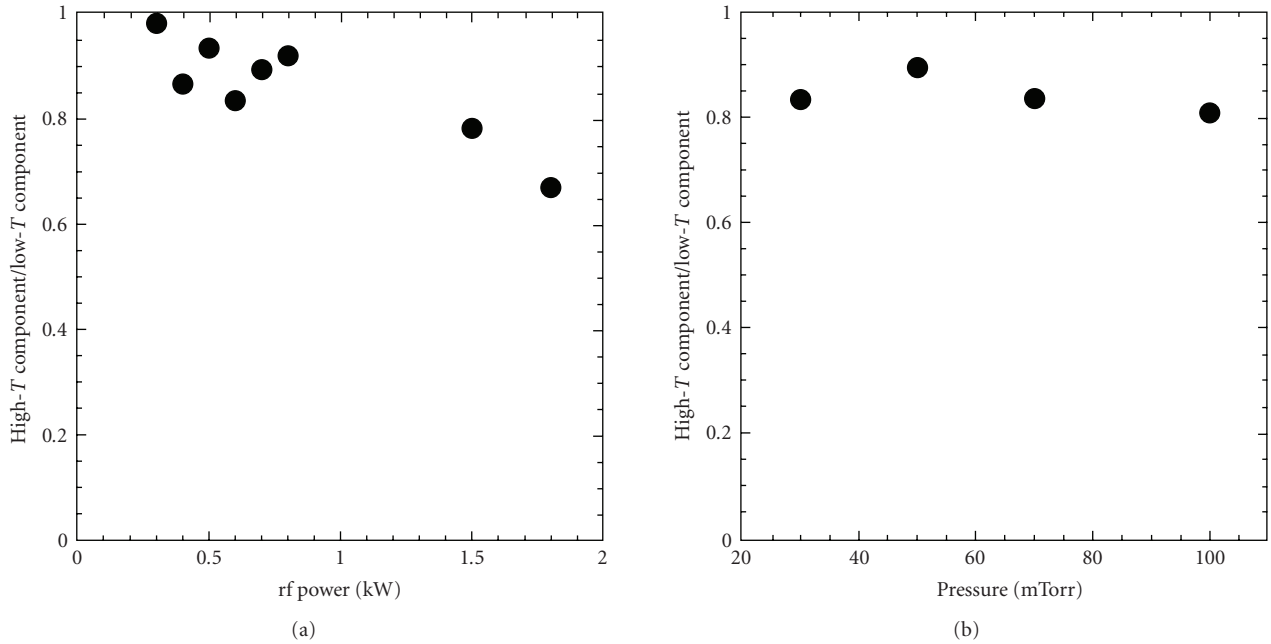

Figure 4: The density ratio of the high-temperature to low-temperature components as functions of (a) the rf power and (b) the oxygen pressure.

Since the lifetime of $O(^5S_2^o)$ is determined by the loss processes described below and is much shorter than the lifetime of $O(^3P^o)$, the high-energy component ($O(^5S_2^o, \text{fast})$ in (4)) is expected to survive in the velocity distribution function.

4. Application to the Monitoring of Degree of Dissociation

According to the aforementioned production processes, the densities of the slow (low-energy) and fast (high-energy) components in the velocity distribution function are given by

$$[O(^5S_2^o, \text{slow})] = \tau k_{\text{ex}}[O]n_e, \tag{5}$$

$$[O(^5S_2^o, \text{fast})] = \tau k_{\text{diss}}[O_2]n_e, \tag{6}$$

respectively, where τ is the lifetime of $O(^5S_2^o)$, n_e is the electron density, and [X] stands for the density of species X. The rate coefficients for (3) and (4) are represented by k_{ex} and k_{diss}, respectively. Therefore, the density ratio of molecular oxygen to atomic oxygen is evaluated by

$$\frac{[O_2]}{[O]} = \frac{k_{\text{ex}}}{k_{\text{diss}}} \frac{[O(^5S_2^o, \text{fast})]}{[O(^5S_2^o, \text{slow})]}. \tag{7}$$

The relative values of $[O(^5S_2^o, \text{slow})]$ and $[O(^5S_2^o, \text{fast})]$ are estimated by integrating the two Gaussian functions with low and high temperatures in the absorption line profile of the $^5S_2^o - ^5P_1$ transition, respectively. Hence, if we ignore the variation of $k_{\text{ex}}/k_{\text{diss}}$ with respect to the discharge conditions, the relative variation of $[O_2]/[O]$ is roughly evaluated by $[O(^5S_2^o, \text{fast})]/[O(^5S_2^o, \text{slow})]$. We evaluated $[O(^5S_2^o, \text{fast})]$ and $[O(^5S_2^o, \text{slow})]$ at various discharge conditions from the absorption line profiles. The ratio $[O(^5S_2^o, \text{fast})]/[O(^5S_2^o, \text{slow})]$ is plotted in Figure 4 as functions of the rf power and the discharge pressure.

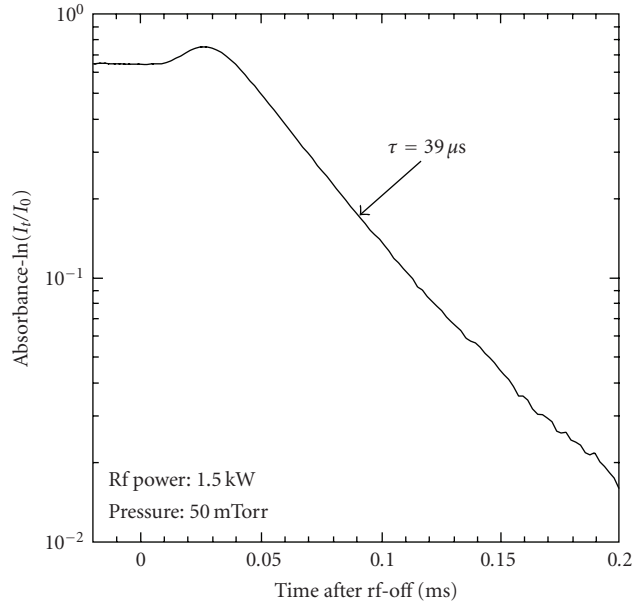

Figure 5: Temporal variation of the absorbance at the line center of the $^5S_2^o - ^5P_1$ transition in the afterglow phase of a pulsed discharge at an rf power of 1.5 kW and a pressure of 50 mTorr.

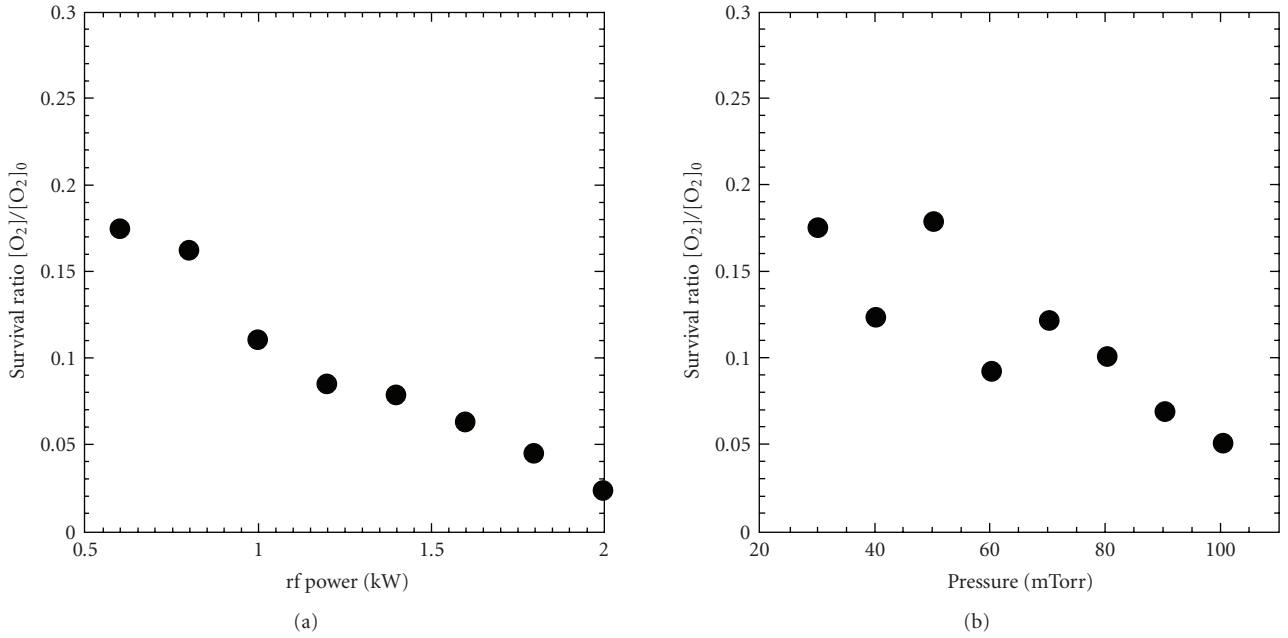

FIGURE 6: Survival ratio of O_2 as functions of (a) the rf power and (b) the oxygen pressure. The O_2 density before discharge ($[O_2]_0$) was evaluated from the gas pressure, and the survived O_2 density ($[O_2]$) was evaluated from the lifetime of $O(^5S_2^o)$ in the afterglow phase.

5. Comparison with Degree of Dissociation Evaluated from Lifetime of $O(^5S_2^o)$

The major loss processes of $O(^5S_2^o)$ are diffusion, spontaneous emission, and collisional quenching with O_2, and the lifetime τ in (5) and (6) are given by

$$\frac{1}{\tau} = k_q[O_2] + \frac{1}{\tau_d} + \frac{1}{\tau_r}, \tag{8}$$

where k_q is the rate coefficient for collisional quenching, τ_d is the diffusion time constant, and τ_r is the radiative lifetime. The values of k_q and $1/\tau_r$ are given in literature [12, 13] as $k_q = 2.2\times10^{-10}\,\mathrm{cm^3/s}$ and $1/\tau_r = 5.6\times10^3\,\mathrm{s^{-1}}$. The diffusion time constant of O atoms in O_2 plasmas produced in the plasma source used in this experiment has been examined in a previous work and was estimated as $1/\tau_D < 2\times10^3\,\mathrm{s^{-1}}$ at pressures higher than 30 mTorr [14, 15]. Therefore, the dominant term in the right-hand side of (8) is $k_q[O_2]$, and the O_2 density can be estimated by measuring the lifetime of $O(^5S_2^o)$.

Figure 5 shows the temporal variation of the absorbance at the line center ($-\ln(I_t/I_0)$ with I_0 and I_t being the incident and transmitted laser intensities, resp.) in the afterglow phase of a pulsed discharge at an rf power of 1.5 kW and a pressure of 50 mTorr. The slight increase in the absorbance immediately after the termination of the rf power may be due to the production of $O(^5S_2^o)$ by recombination reactions. After that, the absorbance decreased exponentially as shown in Figure 5, and the decay time constant was evaluated to be $\tau = 39$ microseconds, corresponding to $[O_2] \simeq 1.2\times10^{14}\,\mathrm{cm^{-3}}$. Since the O_2 density before the discharge was $[O_2]_0 = 1.6\times10^{15}\,\mathrm{cm^{-3}}$, the survival ratio of O_2 in the discharge was evaluated to be $[O_2]/[O_2]_0 \simeq 0.07$.

The survival ratio of O_2 thus evaluated is plotted in Figure 6 as functions of the rf power and the pressure. It is reasonable that the survival ratio decreases with the rf power as shown in Figure 6(a). The ratio of $[O(^5S_2^o, \mathrm{fast})]/[O(^5S_2^o, \mathrm{slow})]$ shown in Figure 4(a) also decreases with the rf power. Hence, the monitoring of the relative degree of dissociation from the absorption line profile of the $^5S_2^o$–$^5P_1$ transition is expected to work rather nicely, provided that a smaller survival ratio of O_2 directly means a higher O atom density. On the other hand, according to Figure 6(b), the survival ratio of O_2 decreases with the pressure, while the ratio of $[O(^5S_2^o, \mathrm{fast})]/[O(^5S_2^o, \mathrm{slow})]$ shown in Figure 4(b) is roughly constant. A possible explanation for this discrepancy is the increase in k_{ex}/k_{diss} in (7) with the pressure. This is because k_{ex}/k_{diss} decreases with the electron temperature since the threshold electron energy for (4) is higher than that for (3). Since the electron temperature is usually a decreasing function of the pressure, it is expected that the decrease in the survival ratio of O_2 is compensated by the increase in k_{ex}/k_{diss}, resulting in the roughly constant $[O(^5S_2^o, \mathrm{fast})]/[O(^5S_2^o, \mathrm{slow})]$ with the pressure. Further investigation is necessary to evaluate the discharge conditions where this method is applicable.

6. Conclusions

In this work, we investigated the absorption line profile of the $^5S_2^o$–$^5P_1$ transition of atomic oxygen by diode laser absorption spectroscopy. The Doppler broadened absorption line profile had a wing component corresponding to a high-energy tail in the velocity distribution function of the metastable $^5S_2^o$ state and was fitted by the superposition of

two Gaussian functions with high and low temperatures. The comparison with the absorption line profile of the $4s[3/2]_2^o$–$4p[3/2]_2$ transition of argon suggests that the origin of the high-energy component in the absorption line profile of the $^5S_2^o$–$^5P_1$ transition is electron impact dissociative excitation of O_2. We propose a method for monitoring the relative degree of dissociation of O_2 by the ratio of the high-temperature to low-temperature components in the absorption line profile. The relative degree of dissociation estimated by the proposed method was compared with the survival ratio of O_2 evaluated from the lifetime of the $^5S_2^o$ state. As a result, a reasonable agreement was obtained in the rf power dependence of the relative degree of dissociation, but the agreement was insufficient in the pressure dependence.

References

[1] K. Ito, N. Oda, Y. Hatano, and T. Tsuboi, "Doppler profile measurements of balmer-α radiation by electron impact on H_2," *Chemical Physics*, vol. 17, no. 1, pp. 35–43, 1976.

[2] R. S. Freund, J. A. Schiavone, and D. F. Brader, "Dissociative excitation of H_2: spectral line shapes and electron impact cross sections of the Balmer lines," *The Journal of Chemical Physics*, vol. 64, no. 3, pp. 1122–1127, 1976.

[3] G. Baravian, Y. Chouan, A. Ricard, and G. Sultan, "Doppler-broadened H_α line shapes in a rf low-pressure H_2 discharge," *Journal of Applied Physics*, vol. 61, no. 12, pp. 5249–5253, 1987.

[4] T. Ogawa, N. Yonekura, M. Tsukada, et al., "Electron-impact dissociation of water as studied by the angular difference doppler profiles of the excited hydrogen atom," *Journal of Physical Chemistry*, vol. 95, no. 7, pp. 2788–2792, 1991.

[5] S. A. Bzenic, S. B. Radovanov, S. B. Vrhovac, Z. B. Velikic, and B. M. Jelenkovic, "On the mechanism of Doppler broadening of H_β after dissociative excitation in hydrogne glow discharges," *Chemical Physics Letters*, vol. 184, no. 1–3, pp. 108–112, 1991.

[6] J. M. Ajello, S. M. Ahmed, and X. Liu, "Line profile of H Lyman-β emission from dissociative excitation of H_2," *Physical Review A*, vol. 53, no. 4, pp. 2303–2308, 1996.

[7] M. Andrieux, J. M. Badie, M. Ducarroir, and C. Bisch, "The evolution of the translational energy of hydrogen atoms in a 2 MHz inductively coupled plasma deposition reactor," *Journal of Physics D*, vol. 31, no. 12, pp. 1457–1464, 1998.

[8] O. P. Makarov, J. M. Ajello, P. Vattipalle, I. Kanik, M. C. Festou, and A. Bhardwaj, "Kinetic energy distributions and line profile measurements of dissociation products of water upon electron impact," *Journal of Geophysical Research A*, vol. 109, no. A9, article A09303, 2004.

[9] J. Jovović, N. M. Šišović, and N. Konjević, "Doppler spectroscopy of hydrogen Balmer lines in a hollow cathode water vapour and argon-water vapour glow discharge," *Journal of Physics D*, vol. 41, Article ID 235202, 2008.

[10] J. Kipritidis, J. Khachan, M. Fitzgerald, and O. Shrier, "Absolute densities of energetic hydrogen ion species in an abnormal hollow cathode discharge," *Physical Review E*, vol. 77, no. 6, Article ID 066405, 9 pages, 2008.

[11] M. Aramaki, Y. Okumura, M. Goto, S. Muto, S. Morita, and K. Sasaki, "Measurements of gas temperature in high-density helicon-wave H_2 plasmas by diode laser absorption spectroscopy," *Japanese Journal of Applied Physics*, vol. 44, no. 9A, pp. 6759–6763, 2005.

[12] T. Mori, K. Kanou, K. Mizuta, T. Kuramasu, Y. Ishikawa, and S. Arai, "Reactions of highly excited oxygen atoms ($2p^3 3s$,^{5} S) with simple gas molecules," *The Journal of Chemical Physics*, vol. 97, no. 12, pp. 9094–9098, 1992.

[13] NIST Atomic Spectra Database, http://physics.nist.gov/PhysRefData/ASD/index.html.

[14] J. Matsushita, K. Sasaki, and K. Kadota, "Dynamic variation of the sticking coefficient of oxygen atoms in helicon-wave excited high-density oxygen plasmas," *Japanese Journal of Applied Physics*, vol. 36, no. 7, pp. 4747–4751, 1997.

[15] R. C. Reid, J. M. Prausnitz, and T. K. Sherwood, *The Properties of Gases and Liquids*, McGraw-Hill, New York, NY, USA, 1977.